University of Nottingham
UK | CHINA | MALAYSIA

IMPACT OF MOISTURE ON ESTIMATING GAS IN PLACE FOR SHALES: CHARACTERISATION AND SIMULATION STUDIES ON KEROGENS

By

Wei Li

Thesis submitted to the University of Nottingham for the degree of Doctor of Philosophy

May/2022

ABSTRACT

Moisture in shale can affect the gas in place (GIP) estimated from the sum of free and adsorbed gas, which are also affected by the residual oil. Four shales (two China shales (SH1, SH2), and two UK shales (BS3, GH4)) were selected to reveal these impacts by illustrating their influence on the porosity and methane adsorption capacity. Kerogen (K1, K2, and GHK3, isolated from shales SH1, SH2, and GH4), the primary contributor to adsorbed gas, was selected as the target of laboratory characterisation and molecular simulation studies. Shales and their kerogens have been investigated, both dry and moisture equilibrated at 95% relative humidity (R.H.). Their methane adsorption capacities are obtained from high-pressure adsorption, and pore textures characterised primarily by low-pressure gas (N_2, CO_2) sorption. Type II kerogen micropore-scale models (matrix and slits (0.5, 1.0, 1.5, and 2.0 nm)) have been constructed for the molecular simulations. Results from Grand Canonical Monte Carlo (GCMC) and molecular dynamic (MD) simulations are compared with the experimental results.

Isolated kerogens account for 59-83% and 42-67% of the methane adsorption capacities for the shales dry and at 95% R.H., respectively. However, the isolated kerogens could adsorb more methane than the organic matter in the shales. More than 50% of methane equilibrium adsorption quantity (Qm), surface area (SA), and nanopore volume (<100 nm) of the kerogens and shales are reduced at 95% R.H.. The low-pressure gas sorption results suggest water can block most micropores less than 1.3 nm, and vastly reduce accessible pores for gas transport. The greater proportional losses in SA and pore volume compared to the Qm is probably due to ice forming at -196 °C in the low-pressure N_2 analysis. Failure to consider moisture overestimates the total GIP by 32-38% for shales (SH1 and SH2) investigated.

As well as maturation, oil from contaminant drilling mud fluids can also be present in shales. The oils extracted in low yield from the overmature shales (SH1 and SH2, <0.5 wt.% TOC) arise from oil-based drilling mud, while the much higher yields from the lower maturity UK shales (BS3 and GH4, 1.1-2.5 wt.% TOC) is mainly oil generated by maturation. After extraction, minimal changes (<5%) in total nanopore volume (<100 nm) were observed for the dry over mature shales, but significant increases (95 and 176%) were observed for the dry lower maturity shales. More than 60% of the extracted oil resides in micro and mesopores, and removal could unblock the micropore necks and enlarge the accessible meso and macropore volume. The Qm increased after oil extraction for both the dry and wet shales, especially for

lower maturity shales. Henry's Law was used to show that there were no significant amounts of dissolved methane in oils for the dry shales. Extracting oil from shales prior to determining the porosity and methane adsorption capacity can lead to the GIP being over-estimated for moisture equilibrated shales, particularly for oil-window shales where an overestimation of 22% was obtained for the shale investigated here.

The micropore volume (V_{micro}) and Qm of dry K1, K2, and GHK3 (10-75 mm^3/g TOC, and 21.3-75.8 mg/g TOC) are comparable with dry overmature (KIID) simulated kerogens (19-261 mm^3/g TOC, and 36.5-148 mg/g TOC). The higher values from the simulation are observed as all the pores in GCMC are accessible. Both experiment and simulation suggest Type I(a) isotherms are attributable to small micropores, while Type I (b) isotherms arise from larger micropores. The increase of moisture leads to the decrease of Qm and V_{micro}. When the moisture content of KIID (matrix and slits) is 4-24wt.%TOC, kerogen simulated models have the same Qm (61-75%), and V_{micro} (88-93%) reductions as wet 95%R.H. isolated kerogens, suggesting up to 56% of the moisture is in the micropore of K1, K2, and GHK3.

The relative coordination number (C_r) from the MD simulation indicates water has a stronger affinity than methane for the same functional groups. The preferred function groups for methane only exist at extremely low pressure, and the affinity becomes much weaker at higher pressures with no significant differences among the functional groups considered. Compared with the sorption sites around functional groups, micropores are regarded as the key control for methane adsorption kerogens, as a positive correlation between V_{micro} and Qm is observed with R^2>0.96. In contrast, certain functional groups, such as carboxyl (COOH) are the preferred sorption sites for water via the solid H-bonds. The selected functional groups provide initial sorption sites for water, with the water cluster size controlled by micropore volume. Water reduces the methane adsorption capacity of kerogen presenting as 'rapid', 'gentle', and 'slow' stages with increased moisture content in simulation. The 'rapid' reduction is due to water adsorbed in ultra-micropores (<0.7 nm), the 'gentle' reduction arises from water condensing, and filling of the remaining micropores at the highest moisture is related to the 'slow' Qm reduction stage. Therefore, water reduces the methane adsorption capacity of kerogen by occupying and blocking pores rather than competing directly for sorption sites with methane.

Keywords: Methane adsorption; porosity; water; kerogen; molecular simulation.

ACKNOWLEDGMENTS

First and foremost, I would like to express my sincere gratitude to my supervisors, Prof. Colin Snape and Dr. Lee Stevens, for their invaluable guidance, continuous support, and insightful comments at every stage of my Ph.D. For me, they are more than supervisors, they are role models, they are my good friends in the UK, cheering me up all the time. I am grateful for their trust and recognition. It is a great honour and luck for me to meet them and be their students. My Ph.D. experience has become vivid and wonderful because of them.

Secondly, I would express my sincere gratitude and love to my family, my parents, my sister, my brother, my nephews, and my Sasha. It is their unwavering support and company that make my being the person I am today. They are the meaning I am fighting for. I would also like to thank my best friends in China, Cui, Bo, and Heng. It is their friendship and encouragement in the past few years that let me know I would never be alone. A special thank goes to Dr. Clement Uguna, Dr. William Meredith, Dr. Xin Liu, and my colleagues in the Energy Technologies Building for their help in the lab.

Last but not least, my gratitude extends to the Faculty of Engineering, for the financial support of the Faculty of Engineering Research Excellence Ph.D. Scholarship, to undertake my study at the University of Nottingham. The AAPG Foundation Grants-in-Aid Program (2021) and the William Spackman Student Research Award from TSOP (2021) are especially acknowledged for additional research funds.

This acknowledgement represents the end of my three and half years Ph.D. life, while it is also the starting sign of my further academic career. I hope, one day, I will be able to help others as others helped me.

PUBLICATIONS AND CONFERENCES

Journal papers

1. **Li, W.,** Stevens, L. A., Meredith, W., Uguna, C. N., Vane, C. H., Zhang, B., ... & Snape, C. E. (2022). The effect of oil extraction on porosity and methane adsorption for dry and moisture-equilibrated shales. **Fuel**, 316, 123304.
2. **Li, W.,** Stevens, L. A., Uguna, C. N., Vane, C. H., Meredith, W., & Snape, C. E. (2021). Comparison of the impact of moisture on methane adsorption and nanoporosity for over mature shales and their kerogens. **International Journal of Coal Geology**, 237, 103705.
3. **Li, W.,** Pang, X., Snape, C., Zhang, B., Zheng, D., & Zhang, X. (2019). Molecular simulation study on methane adsorption capacity and mechanism in clay minerals: Effect of clay type, pressure, and water saturation in shales. **Energy & Fuels**, 33(2), 765-778. (MSc, China university of petroleum, Beijing)
4. **Li, W.**, Pang, X., Zhao, Z., Xu, Y. (2018). Evaluation on the conventional and unconventional oil and gas resources in K1qn1 of Songliao basin, **China Offshore Oil and Gas**, (05), 46-54. (MSc, China university of petroleum, Beijing)
5. Tang, L., Song, Y., Jiang, Z., Pang, X., Li, Z., Li, Q., **Li, W.,** Tang, X., Pan, A. (2019). Influencing factors and mathematical prediction of shale adsorbed gas content in the Upper Triassic Yanchang Formation in the Ordos Basin, China. Minerals, 9(5), 265.
6. Zheng, D., Pang, X., Luo, B., Chen, D., Pang, B., Li, H., ... & **Li, W.** (2021). Geochemical characteristics, genetic types, and source of natural gas in the Sinian Dengying Formation, Sichuan Basin, China. Journal of Petroleum Science and Engineering, 199, 108341.

International conferences

1. European Geosciences Union **(EGU)** General Assembly 2022, May 23-27th, 2022, **Oral presentation**, Vienna, Austria & online.
2. The Society for Organic Petrology **(TSOP)** 37th Annual Meeting 2021, September 12-14th, 2021, **Oral presentation**, online.
3. American Association of Petroleum Geologists (**AAPG**) 2020 Annual Convention & Exhibition, October 1st, 2020, **Poster**, online.

CONTENTS

List of Figures

List of Tables

Abbreviations

Abbreviations/Symbols	Meaning
GIP	Gas in place
TOC	Total organic matter content
3D	Three-dimensional
VR	Vitrinite reflectance
Ultra-micropore	Pores with the pore size less than 0.7 nm
Super-micropore	Pores with the pore size in the range of 0.7-2.0 nm
Narrow micropores	Pores with the pore size less than 1.0 nm
Micropore	Pores with the pore size less than 2.0 nm
Mesopore	Pores with the pore size in the range of 2-50 nm
Macropore	Pores with the pore size larger than 50 nm
Nanopore	Pores with the pore size smaller than 100 nm
V_{micro}	micropore volume
V_{meso}	mesopore volume
V_{macro}	macropore volume
V_{nano}	nanopore volume
GCMC	Grand Canonical Monte Carlo
MD	Molecular dynamic
TEM	Transmission Electron Microscopy
SEM	Scanning Electron Microscope
XRCT	X-ray computed tomography
MIP	Mercury intrusion porosimetry
EA	Elemental analysis
TGA	Thermal gravimetric analyser
XRD	X-ray crystallography
HP	Helium pycnometry
GC-MS	Gas Chromatography-Mass Spectrometry
BGS	British Geological Survey
SH1	China shale1
SH2	China shale2
BS3	Bacconsall shale
GH4	Grange Hill shale
K1	Kerogen isolated from SH1
K2	Kerogen isolated from SH2
GHK3	Kerogen isolated from Grange hill shale
HCl	Hydrochloric acid
HF	Hydrofluoric acid
DCM	Dichloromethane
R.H.	Relative humidity
KNO_3	Potassium nitrate
KOH	Potassium hydroxide
$MgCl_2$	Magnesium chloride
$Mg(NO_3)_2$	Magnesium nitrate hexahydrate
KI	Potassium iodide

HI	Hydrogen Index
OI	Oxygen Index
PI	Production Index
PC	Pyrolysable Carbon
FID	Flame ionization detector
CO_2	Carbon dioxide
IR	Infra-red
TCD	Thermal conductivity detector
P	Pressure
BR	Bitumen reflectance
YAG	Yttrium Aluminium Garnet
EI	Electron ionization
CI	Chemical ionization
m/z	mass/charge
SCAN	Full-scan mass detection
SIM	Selected ion monitoring
VdW	Van der Waals forces
BET	Brunaue-Emmett-Teller model
NLDFT	Non-local density functional theory
DSL	Dual site Langmuir model
Q	Adsorbed gas
SA	Surface area
BJH	Barrett-Joyner-Halenda
BET	Brunauer-Emmett-Teller
HK	Horvath-Kawazoe
DR	Dubinin–Radushkevich
DFT	Density functional theory
P/P_0	Relative pressure
PSD	Pore size distribution
HPVA	High-Pressure Volumetric Analyser
BSE	Backscattered electrons
SE	Secondary electrons
ff	Force field
COMPASS	Condensed-phase Optimized Molecular Potentials for Atomistic Simulation Studies
NVE	Micro-canonical ensemble
NVT	Canonical ensemble
mVT	Macro-canonical ensemble
NPT	Isothermal-isobaric ensemble
KIIA	Immature kerogen
KIIB	Early mature (beginning of the oil window) kerogen
KIIC	Middle-late mature (middle to end of the oil window) kerogen
KIID	Over mature (gas window) kerogen
CH_4	Methane
N_2	Nitrogen

CO_2	Carbon dioxide
$g(r)$	Relative number density
Cr	Relative coordination number
OM	Organic matter
THF	Tetrahydrofuran
CS_2	Carbon disulfide
TIC	Total ion chromatograms
EIC	Single ion chromatograms
EMO	Enhanced-mineral oil
NMR	Nuclear magnetic resonance
MPSD	Micropore size distribution
Qm	Maximum methane adsorption capacity

CHAPTER 1 INTRODUCTION

1.1 Research background and motivation

1.1.1 Shale and shale gas

Shale, fine-grained sedimentary rock, is composed of a mix of flakes of quartz, clay minerals (above 40%), and organic matter (usually less than 10%) (Jones, Hughes et al. 1989, Curtis 2002, Schön 2011, Caineng, Guosheng et al. 2013). Shale generates hydrocarbons (natural gas and petroleum) as a source rock as well as storing hydrocarbons in reservoirs (Curtis 2002, Ambrose, Hartman et al. 2012, Curtis, Cardott et al. 2012, Clarke, Turner et al. 2018). Shale gas reserve evaluation is important for helping to secure natural gas supply (Curtis, Cardott et al. 2012, Gasparik, Ghanizadeh et al. 2012, Whitelaw, Uguna et al. 2019). Shale is heterogeneous with variations in composition and structure from the nanoscale to microscale, resulting in the pore system differing dramatically between shales (Curtis, Ambrose et al. 2010, Loucks, Reed et al. 2010, Milner, McLin et al. 2010, Milliken, Rudnicki et al. 2013, Ma, Fauchille et al. 2017). Shale gas is stored as adsorbed, free, and dissolved gas (Curtis 2002, Jarvie, Hill et al. 2007, Ross and Bustin 2008, Rexer, Mathia et al. 2014, Chen, Jiang et al. 2017). It is believed that most adsorbed gas is adsorbed in micropores, and free gas is stored in the larger meso and macropores, making the pore texture and networks significant factors for shale gas reserve evaluation (Chalmers and Bustin 2007, Curtis, Ambrose et al. 2010, Ambrose, Hartman et al. 2012, Rexer, Mathia et al. 2020). The total organic matter content (TOC), kerogen type, and maturity are three critical parameters for shale evaluation as they control the hydrocarbon generation and the pore network development (Tissot 1984, Curtis 2002).

1.1.2 Organic matter in shale and pore texture

1.1.2.1 Kerogen type

Organic matter in sedimentary rocks is divided into extractable and insoluble organic matter. Kerogen is commonly defined as the macromolecular organic matter insoluble in organic solvents, while the extractable organic matter is known as bitumen, which can be dissolved in organic solvent (Tissot 1984, Vandenbroucke and Largeau 2007, Curtis, Ambrose et al. 2010) (Hunt 1979, Durand 1980). About 70-90 % of the total organic matter is contributed by

kerogen (Dow 1977). Kerogen has a reticular three-dimensional (3D) structure and no fixed chemical formula, which is mainly composed of carbon (C), hydrogen (H), oxygen (O), and smaller amounts of nitrogen (N) and sulfur (S) (Vandenbroucke and Largeau 2007). The average element content (mass percentage) of 427 kerogen samples from all over the world was 76.4% C, 6.3% H, and 11.1% O, and these three elements accounted for 93.8 % of the total mass (Durand 1980).

Kerogen can be classified mainly into three types based on provenance, as indicated by specific macerals. It is can also be classified based on H/C and O/C ratios, as defined in the Van Krevelen diagram (Figure 1-1 A). Each type has a distinct bearing on what kind of petroleum, if any, will be produced (Tissot, Durand et al. 1974, Tissot 1984). (1) Type I kerogen has an original high H/C ratio and a low O/C ratio (atomic H/C ratio is between 1.25-1.75, atomic O/C ratio is between 0.026-0.12). It includes algae-rich sediments from the lacustrine deposition environment, which is rich in aliphatic structures. (2) Type II kerogen has relatively high H/C ratios and low O/C ratio (atomic H/C ratio is between 0.65-1.25, atomic O/C ratio is between 0.04-0.13). Type II kerogen is predominately derived from plankton, some contribution from algae, deposited in the marine environment. (3) Type III kerogen has a high original oxygen content and a relatively low H/C ratio (atomic H/C ratio is between 0.05-1.12, atomic O/C ratio is between 0.05-0.30). Type III kerogen arised from higher plants and terrestrial humic material accumulated in nonmarine or paralic environments, and they are mainly deposited in the terrestrial environment, which is predominated by aromatic structure. Kerogen includes the reworked and oxidized material that can be defined as Type IV kerogens (Tissot, Durand et al. 1974, Dow 1977, Tissot 1984) (Figure 1-1 B).

1.1.2.2 Kerogen maturity

The thermal maturity of organic matter refers to a source rock being exposed to heat over geological timescales, which are categorized as thermally immature, mature (oil window), high mature (wet gas window), and post/over mature (dry gas window) rocks in terms of capability to generate hydrocarbons (Tissot and Welte 2013, Bernard and Horsfield 2014). It follows the evolution path shown in the Van Krevelen diagram (Figure 1-1 A), the H/C and O/C atomic ratios of kerogen decrease with the increased maturity and the bury depth. Increasing maturity causes structural simplification as oil is converted into light hydrocarbons, including

wet gas, and ends at dry gas (McCarthy, Rojas et al. 2011) (Figure 1-1 B). The maturity can be identified through the measurement of the vitrinite reflectance (VR) (%Ro), and the Rock-Eval parameter (T_{max}) (Vassoyevich, Korchagina et al. 1970, Tissot 1984, Jarvie, Hill et al. 2007). Although the burial depth and temperature are related to the maturity stages, they are not used to identify maturity since each basin has different geothermal and pressure gradients (Moses 1961, Tissot and Welte 2013). As Figure 1-1 B shows, boundaries between maturity stages vary according to kerogen type. Time-temperature relationships and the mixing of various sources of organic matter may alter these boundaries. Approximately immature shales with VR, usually less than 0.5% Ro, may generate biogenic natural gas. Mature shales with VRs ranging from 0.5 to 1.2% Ro are in the 'oil window', and most oil is generated at this stage. High maturity shales, with VR in the range of 1.2-2% Ro are in the 'gas window', which generates mainly relatively wet gas. Overmature shales (VR>2% Ro) will generate only dry gas (Tissot and Welte 2013, Bernard and Horsfield 2014, Dayal and Mani 2017).

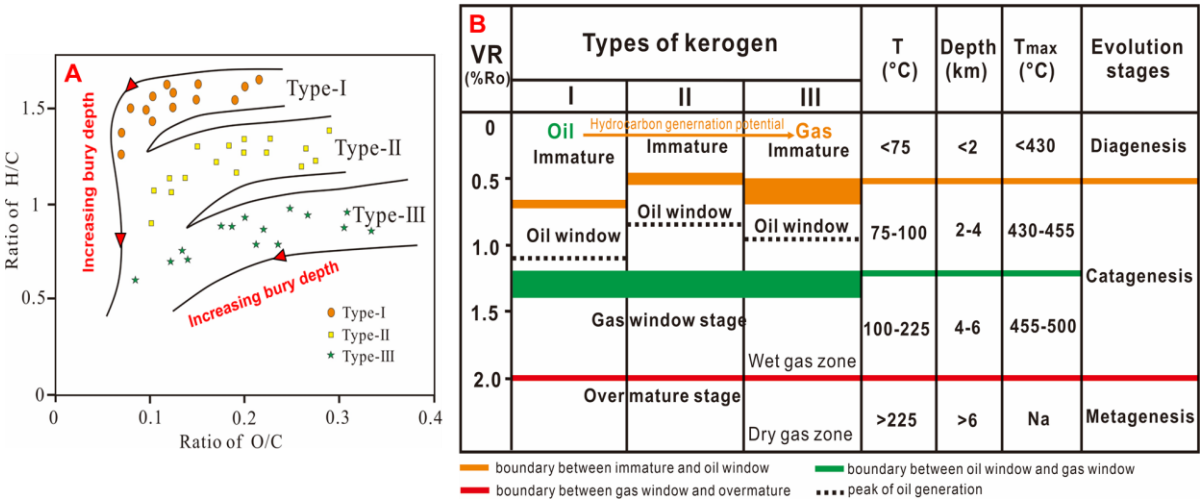

Figure 1-1. A) Van Krevelen diagram of different types of kerogen (modified after Van Krevelen., 1961) (Krevelen 1961), B) Summary of the evaluation parameters of maturity for different kerogen (Types I, II, and III) (Tissot 1984, Tissot and Welte 2013).

1.1.2.3 Classification of shale pores

The complex heterogeneity pore network at multiple scales is the key to fluid transport and storage in shales (Ross and Bustin 2008, Cristancho-Albarracin, Akkutlu et al. 2017, Chen, Kang et al. 2018). As Figure 1-2 indicates, the pores in shale can be classified into three types based on where the pores develop 1) interparticle pores (between particles like mineral-mineral and mineral-organic matter), 2) intraparticle pores (within discrete particle boundaries), 3)

organic matter pores (pores developed in organic matter) (Loucks, Reed et al. 2010, Slatt and O'Brien 2011, Loucks, Reed et al. 2012, Zhang, Ellis et al. 2012). The organic matter intraparticle pores are related to the thermal maturation of organic matter during hydrocarbon generation and may form a connected pore network (Loucks, Reed et al. 2009, Zou, Dong et al. 2010, Loucks, Reed et al. 2012, Bernard and Horsfield 2014). The organic pores make a significant contribution to the total pore volume of shale, particularly to the micropores and small mesopores (Ambrose, Hartman et al. 2010, Sondergeld, Ambrose et al. 2010, Milliken, Rudnicki et al. 2013, Tian, Pan et al. 2013, Kuila, McCarty et al. 2014). Pores in shale are widely distributed with a much smaller size (nanometer scale) than the pores within conventional carbonate and sandstone reservoirs (micrometer scale) (Loucks and Ruppel 2007, Javadpour 2009, Nelson 2009, Zou, Dong et al. 2010, Caineng, Rukai et al. 2011, Chalmers, Bustin et al. 2012). According to the IUPAC classification, the nanometer-scaled (<100 nm) pores of shales are subdivided into three categories based on the pore size: macropores (>50 nm), mesopores (2–50 nm), and micropores (<2 nm) (Thommes, Kaneko et al. 2015).

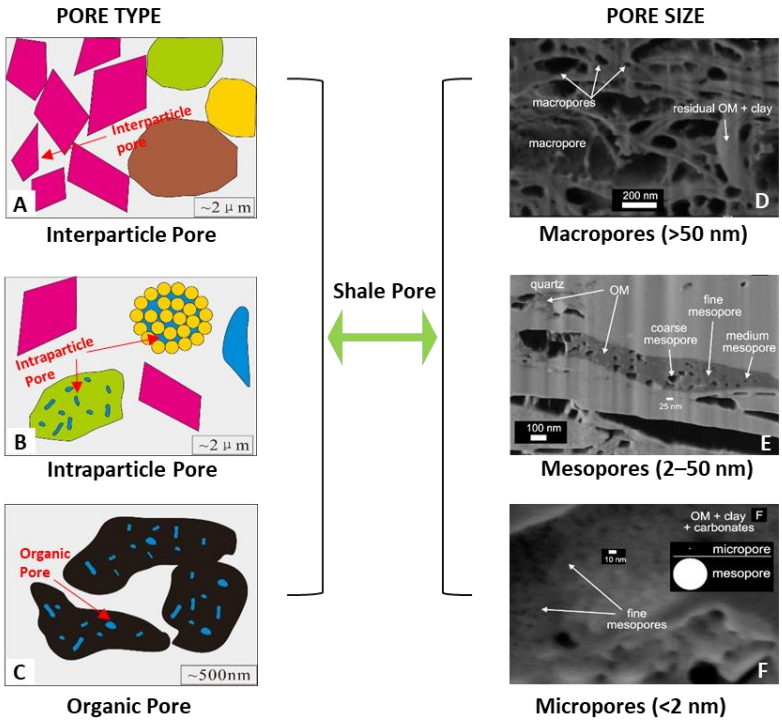

Figure 1-2. The classification of pore type and pore size (Figures D, E, and F are from Chalmer, (2012)).

1.1.3 Background and motivation

Shale gas in place (GIP) is usually estimated from the sum of adsorbed and free gas, which is stored in the shale pores (Curtis 2002, Ambrose, Hartman et al. 2012, Tang, Ripepi et al. 2016, Li, Stevens et al. 2021). Moisture and residual oil in shales under reservoir conditions adversely affect gas adsorption and porosity (Curtis 2002, Ross and Bustin 2008, Heller and Zoback 2014, Mohnhoff, Littke et al. 2016, Cao, Han et al. 2019, DiStefano, McFarlane et al. 2019, Qi, Ju et al. 2019, Whitelaw, Uguna et al. 2019, Li, Stevens et al. 2021). Shale GIP estimation without considering moisture leads to a vast overestimation (Whitelaw, Uguna et al. 2019, Li, Stevens et al. 2021). However, the impact of extracted oil has never been studied at moisture-equilibrated (wet) conditions, although both initial (Guo 2013, Gasparik, Bertier et al. 2014, Rexer, Mathia et al. 2014, Wang, Zhu et al. 2016) and solvent extracted (Löhr, Baruch et al. 2015, Whitelaw, Uguna et al. 2019) shales have been used to relate key factors impact on the methane adsorption capacity. Therefore, considering the effect of water and residual oil for GIP estimation is necessary for evaluating shale gas resources.

Kerogen is considered to store most adsorbed gas (Ross and Bustin 2009, Zhang, Ellis et al. 2012, Gasparik, Bertier et al. 2014). Moisture exists under reservoirs conditions and has a profound negative influence on gas adsorption capacity (Ji, Zhang et al. 2012, Heller and Zoback 2014, Jin and Firoozabadi 2014, Zolfaghari, Dehghanpour et al. 2017). The impact of moisture on methane adsorption for shales and coals by laboratory experiments have been addressed (Joubert, Grein et al. 1973, Ross and Bustin 2007, Gasparik, Bertier et al. 2014, Zou, Rezaee et al. 2018, Whitelaw, Uguna et al. 2019). Hydrophilic clays are believed to be the main mineral that adsorbs water in shale, decreasing methane adsorption in several studies (Heller and Zoback 2014, Tang, Ripepi et al. 2017, Zolfaghari, Dehghanpour et al. 2017). Recent experimental results reveal that the amount of water absorbed in shale is positively related to the content of organic matter (Cheng, Tian et al. 2017, Sang, Liu et al. 2019, Bai, Kang et al. 2020), making water adsorption in organic matter of shale being significant. Whereas, up to date, the relationship between the impact of moisture on methane adsorption capacities and pore characteristics of isolated kerogens by laboratory experiments has not yet been related. With the development of computer simulations, molecular simulation studies have become an exemplary method for studying gas adsorption behaviours and analysing the adsorption mechanism (Collell, Galliero et al. 2014, Huang, Ning

et al. 2018, Li, Pang et al. 2019). Methane adsorption in a moist kerogen matrix has been studied by molecular simulation (Zhao, Li et al. 2017, Huang, Ning et al. 2019, Gong, Shi et al. 2020), the simulation results of which are compared with data from coal, shale, or dry kerogen (Zhao, Li et al. 2017, Huang, Ning et al. 2019, Gong, Shi et al. 2020), due to the limited laboratory experiments on wet kerogen.

The motivation for this project is to provide guidance for accurate shale gas resource estimation by revealing the impacts of water and residual oil on the methane adsorption and nano porosity of shale. Promoting the development of molecular simulation on kerogen by comparing the results with experimental data to predict, and provide a solid foundation for further simulation studies on kerogen.

1.2 Research gaps and objectives

1.2.1 Research gaps

The research gaps identified are:

(1). Methane adsorption capacities are generally measured from dry shales for the GIP estimation leading to overestimations. The impact of residual oil on wet shales and the GIP estimation has not been addressed.

(2). The contribution of kerogen to methane adsorption is only stated in dry conditions. Molecular simulations about wet kerogens are verified by experiments data from wet shales, wet coals, or dry kerogens, due to the lack of laboratory experiments on wet kerogens.

(3). Molecular simulation and laboratory experiments on kerogen are studied separately. A throughout comparison between the results from simulation and experiments is needed, and the mechanism of moisture impact on methane adsorption on kerogen remains unclear.

1.2.2 Research aim and the objectives

The overall aim is to identify how moisture impacts on methane adsorption capacity of shale through combining laboratory experiments and molecular simulation methods on kerogens. Illustrating moisture impact on the nanopore characteristics, especially micropore, of kerogen becomes another unneglected aim as it is significant for explaining the adsorption behaviour and mechanism.

To achieve this aim, the following objectives were identified:

(1). To investigate the basic geochemical parameters of shale and kerogen, as well as the methane adsorption capacity and nanopore characteristics of the initial and extracted selected shales at dry and wet conditions by laboratory experiments.

(2). To determine the methane adsorption capacity of kerogen at dry and wet conditions by high-pressure methane adsorption (laboratory experiments) and Grand Canonical Monte Carlo (GCMC) (molecular simulation) methods.

(3). To determine the micropore characteristics of kerogen at dry and wet conditions by low-pressure gas sorption (BET measurement) (laboratory experiments) and dummy probes measurement (molecular simulation) methods.

(4). To analyse the selectivity of water and methane on different functional groups of kerogens by molecular dynamic (MD) simulation to study the sorption sites of methane and water.

1.3 Thesis organization

1.3.1 Research content

The research mainly consists of three activities (Figure 1-3): high-pressure methane adsorption capacity, pore characterization, and molecular simulation (MD and GCMC). The experiments provide input data for simulation. The simulation illustrates the gas adsorption behaviour and mechanism. The final comparison of simulation and experiment verifies the simulation, making the further results-driven from simulation more reliable.

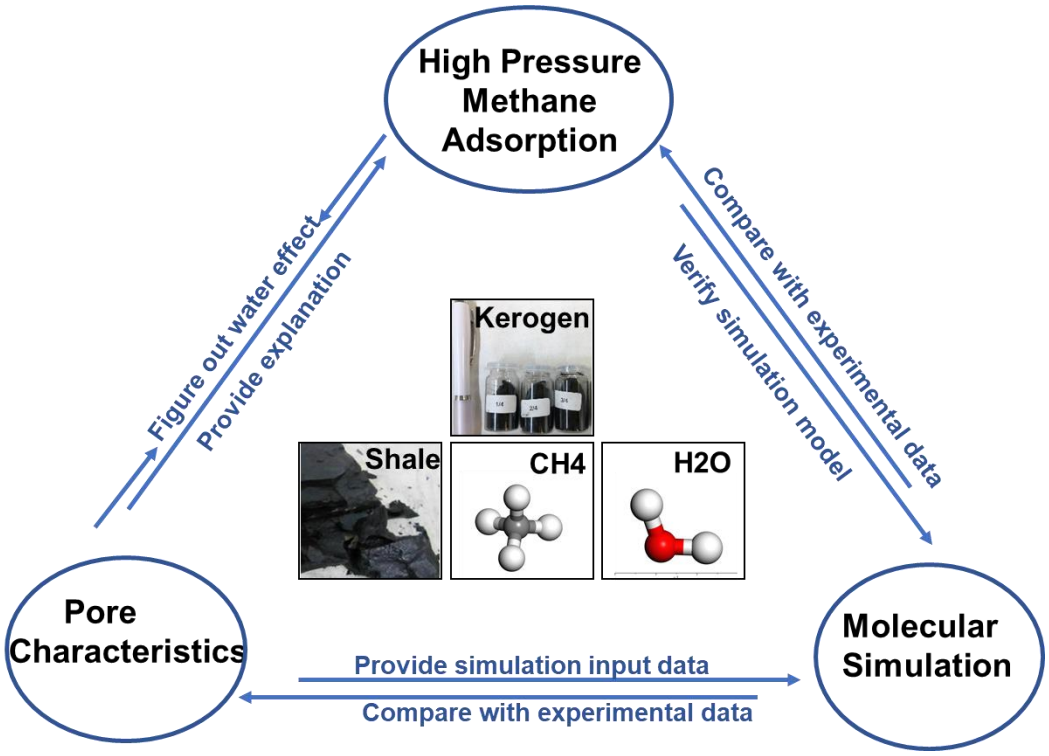

Figure 1-3. The main research contents and their correlations

Figure 1-4 is the flowchart of the techniques used in this study, comprising sample preparation, experiments on both dry and wet samples, and molecular simulation. The key methods used are:

(1). Solvent extraction and demineralization are applied to the initial shales to obtain the extracted shales and kerogens. All these samples are prepared both in dry and wet states for characterisation.

(2). Low-pressure gas (N_2, CO_2) sorption for dry and wet shales and kerogens is the main experiment for characterising the pore structure of samples in this study, which is also supported by the Transmission Electron Microscopy (TEM) for kerogen, Scanning Electron Microscope (SEM) for shales, X-ray computed tomography (XRCT) for shales, mercury intrusion porosimetry (MIP) for shales and kerogens.

(3). High-pressure methane adsorption has been applied on dry and wet kerogens and shales to measure their methane adsorption capacity. In addition, basic analysis including, elemental analysis (EA) for shales and kerogens, thermal gravimetric analyser (TGA) for shales and kerogens, helium pycnometry (HP) for dry and wet shales and kerogens, vitrinite reflectance (VR) test for shales and kerogens, and Rock-eval for shales, are adopted to determine total

organic carbon content (TOC), composition, skeletal density (dry and wet), maturity (%Ro, Tmax), and standard thermal assessment parameters, respectively.

(4). The experiment data provide the input data for simulated models construction, as well as verify the models. GCMC and MD simulation is carried out on kerogen matrix and slit (0.5, 1.0, 1.5, and 2.0 nm) models to get the methane adsorption capacity, micropore characteristic, the adsorption behaviour, and the selectivity of water and methane molecules in kerogen.

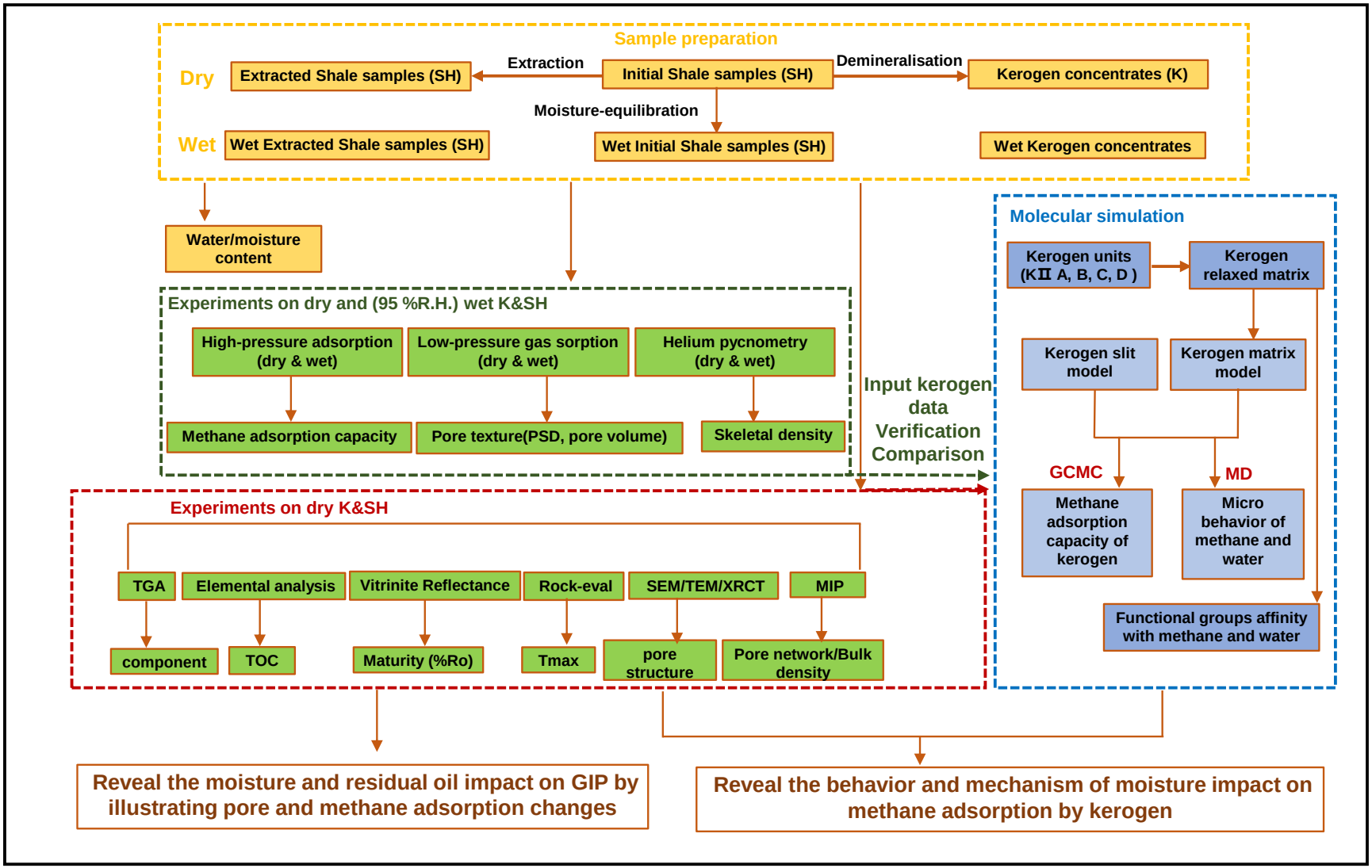

Figure 1-4. Flowchart of the experimental and simulated methods.

1.3.2 Thesis layout

This thesis is divided into six further chapters after the introduction, which are outlined below.:

1) Chapter 2 Methodologies, including sample preparation, laboratory experiments (basic analysis techniques, high-pressure methane adsorption, and experiments of pore characterization), and molecular simulation methods. The principles of the technique used are summarised together with the experimental procedures.
2) Chapters 3-6 are the main contents. Each chapter is presented with a short summary, literature review for this chapter, the methods referred from chapter 2, the results and discussion, and the chapter conclusions. Chapter 3 is about the moisture impact on methane adsorption capacity and the nano porosity of shales and their isolated kerogen. The moisture impact on GIP and the contribution of kerogen on adsorbed shale gas are revealed in this chapter.
3) Chapter 4 discusses the residual oil impact on methane adsorption and nano porosity of dry and wet shales. Significantly, the combined effects of residual oil and water on shales GIP estimation are revealed, which can provide guidance for the GIP estimation of how to select and carry out the proper procedure for the selected shale.
4) Chapter 5 describes the molecular simulation on dry kerogens, the results from which are compared with experimental results on dry isolated kerogen. Chapter 5 reveals the critical factor of the methane adsorption capacity of dry kerogen with different maturity, as microporosity and the chemical surface (functional groups) are the two significant factors.
5) Chapter 6 covers the molecular simulation on wet kerogen. The behaviour and mechanism of moisture impact on methane adsorption are revealed by combing and comparing the results from simulations and experiments.
6) Chapter 7 is the conclusion chapter, where all the key findings are summarized, the novelty of the research is discussed, and future work is suggested.
7) Appendices A, B, and C are for Chapters 2, 5, and 6, respectively.

CHAPTER 2 METHODS

The geological background, sample selection and preparation, the principle and procedure of laboratory experiments, and molecular simulation methods applied in this study are illustrated in this chapter.

2.1 Geological setting of the China and UK shales for study

The shales used were collected from two areas, the Sichuan Basin in China and the Bowland Basin in the UK. Shale gas exploration and development have been conducted in five sedimentary basins (regions) of 11 provinces in China by more than 20 domestic and foreign enterprises, with Sichuan Basin as the most prospering area for shale gas production (Caineng, Dazhong et al. 2016). Sichuan Basin, with an area of 1.81×10^5 km^2, is a marine–continental complex superimposed basin located in the south of China (Dai, Zou et al. 2014, Wang and LI XQ 2016). The study area is situated in the south part of the Sichuan Basin (Figure 2-1 A), well developing the Upper Ordovician Wufeng Formation and Lower Silurian Longmaxi Formation shale (Figure 2-1 B) (Dai, Zou et al. 2014). The substantial-high-quality shale from Wufeng-Longmaxi Formation is the main target for shale gas exploration in Sichuan (Dong, Shi et al. 2018, Tang, Song et al. 2019). Typically, colossal thickness (about 400-600 m), rich organic matter (TOC >2.0%), and high maturity (VR range from 1.8 to 4.2 %Ro) are the characteristic of Wufeng-Longmaxi Formation shale (Fan, Tang et al. 2014, Dong, Shi et al. 2018).

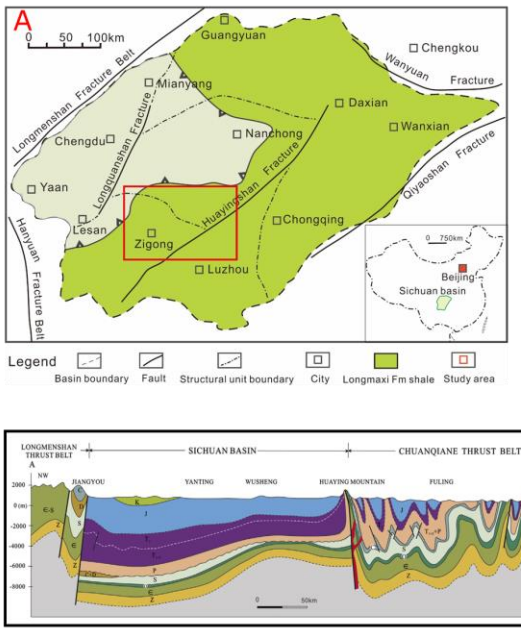

Chronostratigraphic			Lithostratigraphic			Thickness (m)	Sedimentary environment
Eonthem	Erathem	System	Formation	Member	Code		
Lower Paleozoic	Silurian	Lower	Longmaxi	Upper	S_1l	0~450	Continental shelf
				Lower			
	Ordovician	Upper	Wufeng		O_3W	5~25	Continental shelf
		Middle	Linxiang Baota		O_2b	20~80	Continental shelf
		Lower	Dachengsi		O_1d	131~280	Restricted marine -mudflat
			Lyuohanpo		O_1l		
	Cambrian	Mid-Upper	Xixiangchi		ϵ_{2-3}	191~259	Restricted marine -tidal flat
		Lower	Yuxiansi		ϵ_1y	212~246	Restricted marine -intertidal
			Jiulaodong		ϵ_1j	409~514	Open marine -continental shelf
Neoproterozoic	Sinian	Upper	Dengying	4th	Z_2dn	0~400	Restricted marine -tidal flat
				3rd		0~70	
				2nd		300~1000	
				1st		30~500	

B

Figure 2-1. A) The location of the study area in Sichuan Basin, B) Stratigraphic column of Sichuan Basin, modified from (Dai, Zou et al. 2014), C) Cross section of Sichuan Basin (Zou, 2015).

Considerable effort has been undertaken to expand the inventory of shale gas resources in Europe (Gasparik, Ghanizadeh et al. 2012, Song, Littke et al. 2017, Gorshkov and Khomyakov 2019). Although progress has been made on shale in laboratory research (Whitelaw, Uguna et al. 2019, Rigby, Jahan et al. 2020, Li, Stevens et al. 2022), the exploration of the UK shale gas is in the initial stage (Andrews 2013, Stephenson 2016). The geology background of the UK shale is complex. As one of the most prospective areas in the UK, the Pennine Basin consists of a variety of sub-basins separated by blocks, including the Widmerpool Gulf and Bowland Basin (Aitkenhead 2002). The UK shale samples in this study are from Bowland Basin, which is the central part of the UK (Figure 2-2 A), and experienced a complex tectonic history (Church and Gawthorpe 1994, Fraser and Gawthorpe 2003). Bowland covers much of northern England from Nottinghamshire to Lancashire and North Yorkshire (Gawthorpe 1987, Fraser and Gawthorpe 2003, Andrews 2013), which contains a basin-wide source rock for oil and gas (Gawthorpe 1987, Andrews 2013).

The sedimentary strata of the Bowland Basin are illustrated in Figure 2-2 B. The targeted formation in this study is the 'Bowland-Hodder Formation', which includes the shale of Bowland Formation together with the Hodder Mudstone Formation, from Visean to the early Namurian age of Carboniferous (Andrews 2013). The depositional environment of the Bowland-Hodder Formation is typically a marine environment, in lakes or swamps along sea or lake margins (Passey, Bohacs et al. 2010). The TOC of the Bowland-Hodder shale usually range from 1 to 3 %, but some higher one can reach 8 % (Andrews 2013).

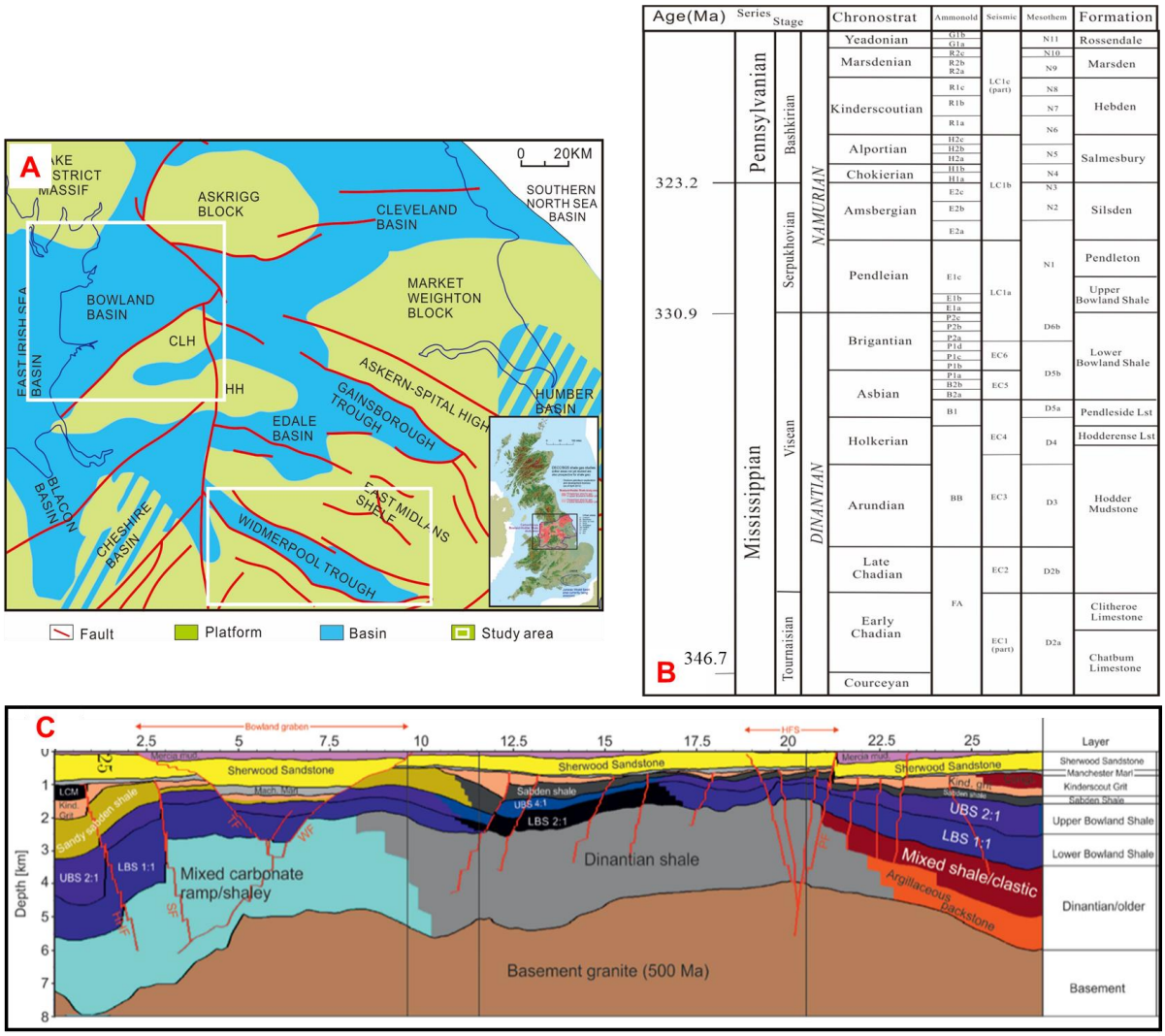

Figure 2-2. A) The location of the Bowland basin, UK, modified after (Andrews 2013) and (Fraser and Gawthorpe 2003), B) The carboniferous chronostratigraphic column of Bowland Basin, modified from Huw Clarke (2018) (Clarke, Turner et al. 2018), C) Cross-section of Bowland Basin (Lohdia et al, in press)

2.2 Sample Selection and Preparation

The twenty-five core shales collected from Ordovician-Lower Silurian Wufeng-Longmaxi Formation, south of Sichuan Basin, China. Fourteen shales with higher TOC (>2 %) are organic-rich shales. Two shales from different drilling wells, with a depth of 4119 m for shale 1 (SH1) and 4098 m for shale 2 (SH2), were selected from the organic-rich shales for kerogen isolation and solvent extraction, considering their higher available amount (>296 g) (Appendix A, Table A1). Two UK shales (supplied by the British Geological Survey (BGS) core store in Keyworth, Nottingham) collected from the Carboniferous Bowland Basin, Bacconsall (BS3) and Grange Hill shales (GH4) with the depth of 2143 and 3113 m, are chosen for the solvent extraction. Grange Hill shale is selected for the kerogen isolation as it was available in larger amounts.

To minimize the effect of heterogeneity, all the prepared core shales were crushed, mixed, and sized into bulk chunks (>4 mm), 2-4 mm particles, 250 μm to 2 mm particles, and fine powder (<250 μm) first (Figure 2-3), then allocated for each experiment as the required size and mass which is illustrated in below methods. The adsorption capacity of shale is influenced by particle size, where milling can destroy or create pores in shale (Gasparik, Bertier et al. 2014, Rexer, Mathia et al. 2014). Thus, shale samples prepared for the gas adsorption experiment were not crushed into powder but using particles with a size range of 2-4 mm, which can keep the interconnectivity between macro, meso, and micropores.

2.2.1 Kerogen Isolation

Three kerogen concentrates, K1, K2, and GHK3 isolated from SH1, SH2, and GH4 shales (Figure 2-3), respectively, were prepared by standard demineralisation procedures (Guthrie and Pratt 1994, Rexer, Mathia et al. 2014), which was carried out by BGS. Shale samples (60 g each of SH1 and SH2, 50-60 g for GH4) were crushed into the fine powder (<250 μm) and treated with 37% hydrochloric acid (HCl) at 25 °C for 12 hours to remove carbonates. The HCl-treated shales were washed with distilled water before using 40% hydrofluoric acid (HF) treatment at 25 °C for 48 hours to remove aluminosilicate minerals. Samples were washed with distilled water and treated with 37% HCl again to make sure to remove the fluorapatite, which can precipitate after HF treatment (Guthrie and Pratt 1994). After decanting the acid, the powdered residue was then repeatedly washed six times with distilled water to remove the

acid and reach pH 7. Samples were then freeze-dried (at −5 °C) for 6 hours and dried at ambient temperature. After drying, 7.21, 6.55, and 3.58 g of K1, K2, and GHK3 were obtained, and the yield of kerogen concentrate can be calculated by Equation (2-1).

$$Y = \frac{M_{kerogen}}{M_{shale}} \times 100\% \quad (2\text{-}1)$$

Where, Y is the yield of kerogen in %, $M_{kerogen}$ is the mass of kerogen, (g), M_{shale} is the mass of shale for isolation (g).

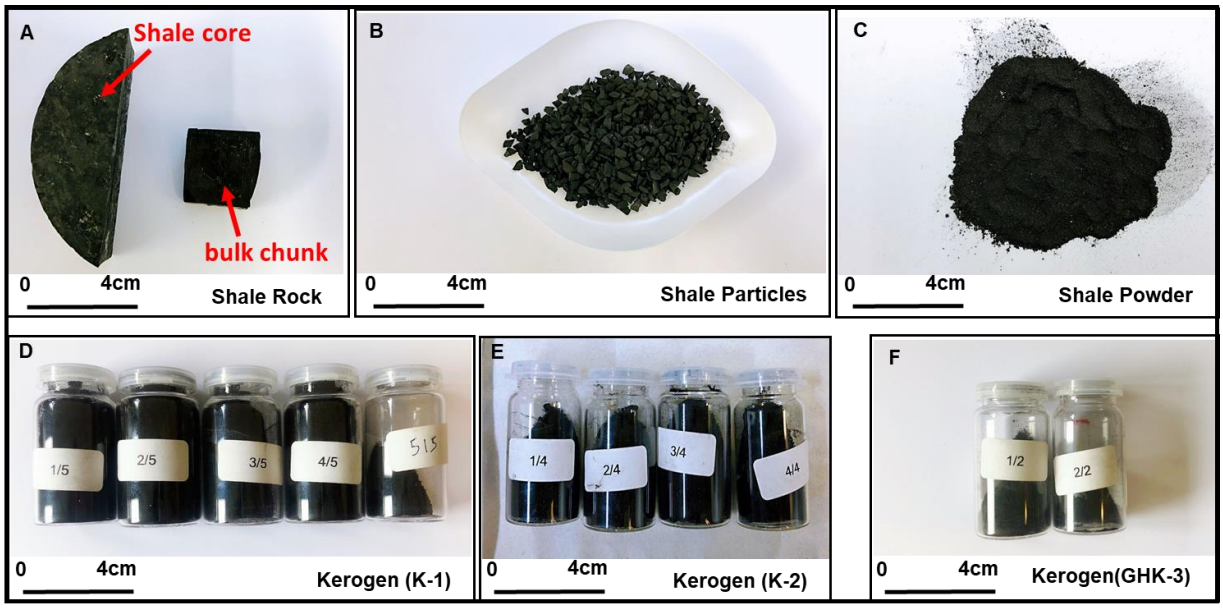

Figure 2-3. Shale and kerogen samples. A) shale core rock before any preparation and shale bulk chunks, B) shale particles with the size of 2-4 mm, C) shale powder with the size of <250 µm, D), E) and F) are kerogen samples of K1, K2, and GHK3, respectively.

2.2.2 Shale soxhlet extraction

Two China shales (SH1 and SH2) and two UK shales (BS3 and GH4) are selected for the soxhlet extraction. Soxhlet solvent extraction was carried out on 20 g of shale using both the 2-4 mm and <250 µm fractions to ensure the particle size has a limited impact on the oil yields in this study. Samples were loaded into the pre-cleaned thimble and plugged with cotton wool to ensure samples remained in the thimble during extraction (Figure 2-4 A). A mixture of 186 mL dichloromethane (DCM) and 14 mL methanol was used as the extraction solvent. Extraction was carried out for 120 hours at 40 °C (Figure 2-4 B), and zeolite was added to the solvent to prevent 'bumping'. After extraction, the solvent was removed using a rotary evaporator at 35 °C under 400 mbar pressure (Figure 2-4 C). The remaining solvent (about 2 mL) was then collected into a pre-weighed vial and dried at 25 °C until no weight change for obtaining oil

mass. The extracted organics yield was calculated by the mass of oil and sample TOC. The extracted shales were dried in a fume hood for 24 hours, before drying in a vacuum oven (<0.5 mbar) at 120 °C for 48 hours. Duplicate extractions for each shale were carried out to collect the remaining solvent (about 2 mL) without drying, which was prepared for the GC-MS analysis. The (initial) shales are the shales without solvent extraction, while the extracted shale is called 'ext' shale in Chapter 4.

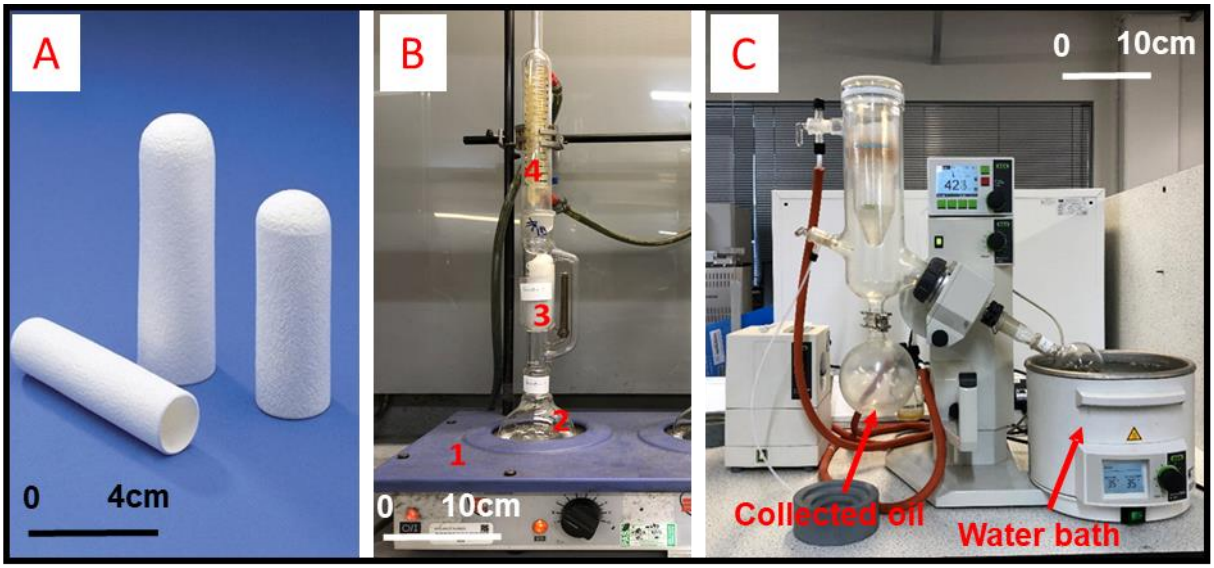

Figure 2-4. A) Fibers and Cotton Linters thimbles, B) Soxhlet extractor, 1 is the heater, 2 is the 250 ml round bottom flask, 3 is the tube extractor, 4 is the condenser pipe, C) Distill oil from the extraction solvent by a rotary evaporator in the water bath.

2.2.3 Dry and Moisture-Equilibrated Sample Preparation

The shales and kerogen concentrates were first dried at 120 °C in a vacuum oven (<0.5 mbar) (Figure 2-5 A) for 48 hours to get the dry sample and dry mass. In order to get the wet samples at a specific relative humidity (R.H.), these pre-dried samples are placed in a vacuum desiccator containing the specific saturated salt solution at a controlled temperature of 20 °C for 48 hours (Figure 2-5 B) (Young 1967, Zolfaghari, Dehghanpour et al. 2017). The salts used in this study are present in Table 2-1. The 95 % R.H. moisture equilibrated (wet) samples were prepared by saturated potassium nitrate (KNO_3) solution (8 g KNO_3/10 mL H_2O), which are the wet samples used for the helium pycnometry, high-pressure methane adsorption, and low-pressure gas adsorption experiments. The 10, 30, 50, and 70 % R.H. moisture equilibrated samples are prepared by saturated potassium hydroxide (KOH) solution(14 g KOH/10 mL H_2O), magnesium chloride ($MgCl_2$) solution (5 g $MgCl_2$/10 mL H_2O), magnesium nitrate hexahydrate

($Mg(NO_3)_2$) solution (18.7 g $Mg(NO_3)_2$/10 mL H_2O), and potassium iodide (KI) solution (15 g KI/10 mL H_2O) (Young 1967, Zolfaghari, Dehghanpour et al. 2017). All the R.H. is in the range of ±2% R.H. as the lab temperature will fluctuate slightly. A logger in the desiccator was used to monitor the R.H. and the temperature (Figure 2-5 C). The moisture content for the wet samples was calculated from the mass difference (Equation 2-2) of moisture equilibrated samples and after drying under a vacuum. The water volume uptake in shales at 95 % R.H. is calculated from the moisture contents and densities by Equation 2-3.

$$W = \frac{M_{water}}{M_{dry}} \tag{2-2}$$

$$S_w = \frac{V_{water}}{V_{dry\ pore}} = 1 - \frac{\rho_{dry\ sk}}{\rho_{dry\ sk} - \rho_{dry\ bulk}} + \frac{\rho_{dry\ sk} \times \rho_{dry\ bulk} \times (1+W)}{\rho_{wet\ sk} \times (\rho_{dry\ sk} - \rho_{dry\ bulk})} \tag{2-3}$$

Where, W is the moisture content, M_{dry} is the mass of the dry sample, M_{water} is the mass of the water, S_w is the water volume uptake, V_{water} is the volume of the water in the pore, $V_{dry\ pore}$ is the total pore volume in the dry sample, $\rho_{dry\ bulk}$ is the bulk density of the dry sample from mercury intrusion porosimetry (MIP) at 0.03 bar (Section 2.5.3), $\rho_{dry\ sk}$ and $\rho_{wet\ sk}$ are the skeletal densities of the dry and wet samples obtained from helium pycnometry (Section 2.3.4).

Table 2-1. Salts for moisture equilibrated sample at different relative humidity.

Salt	Relative humidity %	Salt concentration
Potassium hydroxide (KOH)	10	14g/100H_2OmL
magnesium chloride ($MgCl_2$)	30	5g/10H_2OmL
Magnesium nitrate hexahydrate ($Mg(NO_3)_2$)	50	18.7g/10 H_2OmL
Potassium Iodide (KI)	70	15g/10H_2OmL
Potassium nitrate (KNO_3)	95	8g/10H_2OmL

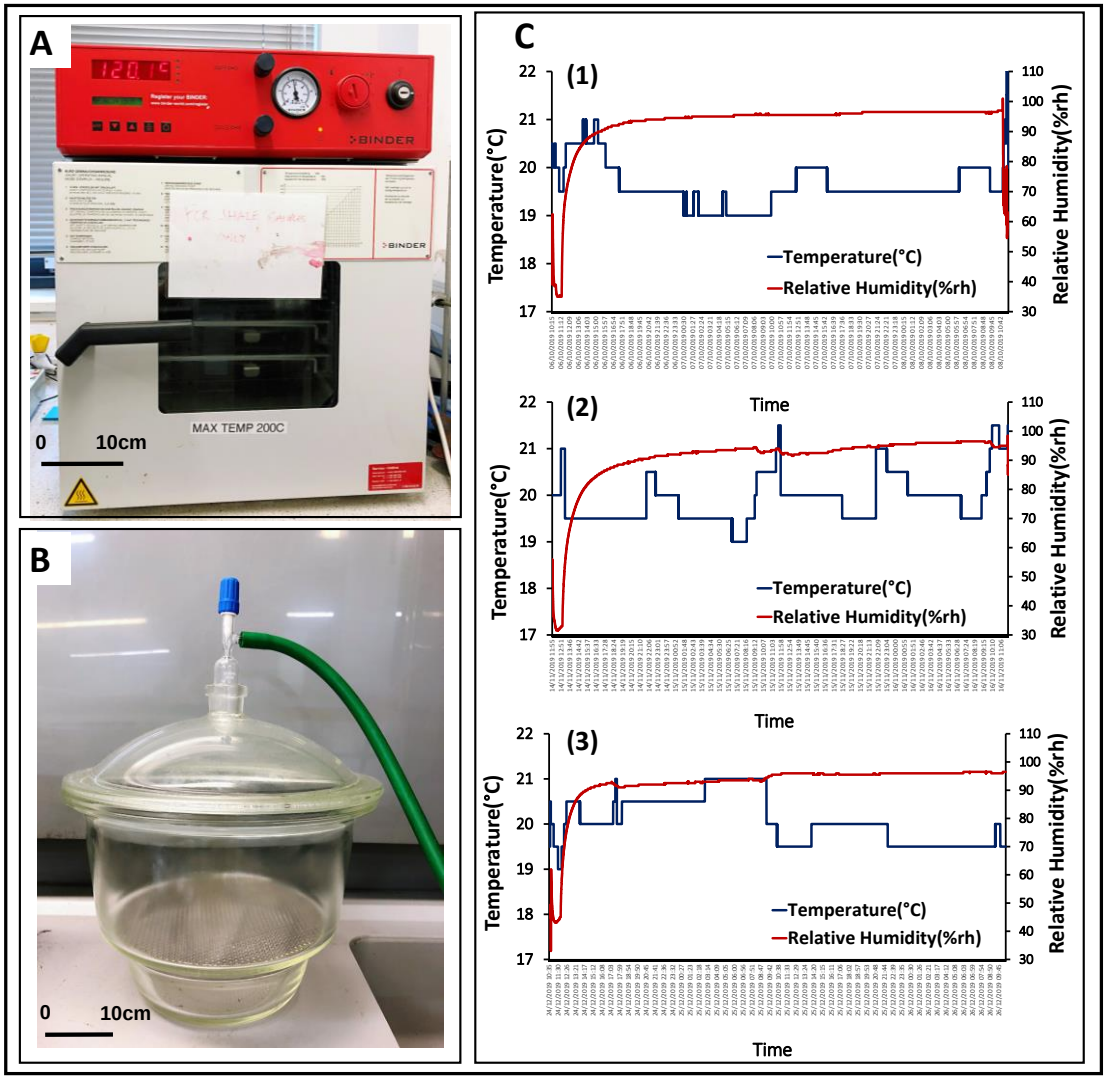

Figure 2-5. A) the vacuum oven used for dry samples, B) the vacuum desiccator used for the moisture equilibrated sample, C) the relative humidity and temperature in the vacuum desiccator used for 95±2% R.H. moisture equilibrated samples preparation recorded by the logger. (1), (2), and (3) corresponding to humidity experiments carried out in triplicate.

2.3 Basic analysis techniques

2.3.1 Rock-eval pyrolysis

2.3.1.1 The principle

Rock-Eval pyrolysis is a well-known technique for rapid geochemical characterisation, used to evaluate the petroleum-generative potential and thermal maturity of rocks (Peters 1986, Peters and Cassa 1994). It is a pyrolysis method that involves heating a small amount of sample in an inert atmosphere (either Helium (He) or Nitrogen (N_2)), presenting the hydrocarbons within the sample as the released gaseous state. In Rock-eval pyrolysis, the

heating of powdered rock samples is divided into three stages. The parameters most frequently reported are S1, S2, S3, S4, T_{max}, and TOC, together with several derived parameters (e.g. Hydrogen Index (HI), Oxygen Index (OI), Production Index (PI), and Pyrolysable Carbon (PC)) (Tissot 1984, Lafargue, Marquis et al. 1998).

Stage one is heating the sample to 300 °C in an inert atmosphere in order to liberate all the free organic compounds (bitumen) without causing significant decomposition of kerogen. The amount of free hydrocarbons obtained in this stage is recorded as the S1 (mg Hc/g rock) (Figure 2-6). The hydrocarbons were detected by a flame ionization detector (FID), as the gaseous hydrocarbons produce ions during the combustion when they come into contact with the flame. And the proportional generation of the ions is indicative of their corresponding hydrocarbon concentration within the shale (Nicholson and Swingler 1980, McCarthy, Rojas et al. 2011). The second stage is increasing the temperature steadily to a maximum (550−600 °C) in an inert atmosphere to crack pyrolytic products from the insoluble organic matter (kerogen), during which all the kerogen capable of generating petroleum is converted into hydrocarbons, which are quantified by the FID and recorded as the S2 (mg Hc/g rock) (Figure 2-6). S2 is used to estimate the remaining hydrocarbon generating potential of the sample. T_{max} is the temperature at which the maximum amount of S2 hydrocarbons is generated, which can be used to indicate maturity. T_{max} at 400-430 °C, 435-455 °C, and >455 °C represent the immature, mature, and high mature stages, while it is not a good indicator for the overmature shale since most hydrocarbons are driven out of kerogen before the test (Tissot 1984, Tissot and Welte 2013). The carbon dioxide (CO_2) from kerogen cracking is released and detected by an infra-red (IR) cell, which is recorded as the S3 (mg CO_2/g rock). S3 indicates the amount of oxygen in the kerogen and can be used to calculate the OI. The third stage is determining the residual organic carbon after pyrolysis by oxidation under oxygen (O_2) in a second oven to get the S4 (mg Carbon/g rock) (Lafargue, Marquis et al. 1998). The TOC (Equation 2-4), HI (Equation 2-5), OI (Equation 2-6), PI (Equation 2-7), and PC (Equation 2-8) are calculated by the following equations (Peters 1986, Peters and Cassa 1994, Lafargue, Marquis et al. 1998):

$$TOC = [0.083 \cdot (S_1 + S_2) + S_4]/10 \quad (2\text{-}4)$$

$$HI = (100 \cdot S_2)/TOC \quad (2\text{-}5)$$

$$OI = (100 \cdot S_3)/TOC \quad (2\text{-}6)$$

$$PI = S_1/(S_1 + S_2) \quad (2\text{-}7)$$

$$PC = 0.083 \cdot (S_1 + S_2) \quad (2\text{-}8)$$

Where, HI, Hydrogen Index, indicates the amount of hydrogen compared to the TOC, which can be used to determine the source rock potential for production; OI, Oxygen Index, similar to HI, can indicate the comparative amount of oxygen compared to TOC; PI, Production Index, is used to characterize the evolution level of the organic matter; PC, Pyrolyzable Carbon, corresponds to the carbon content of hydrocarbons volatilized and pyrolyzed during the analysis.

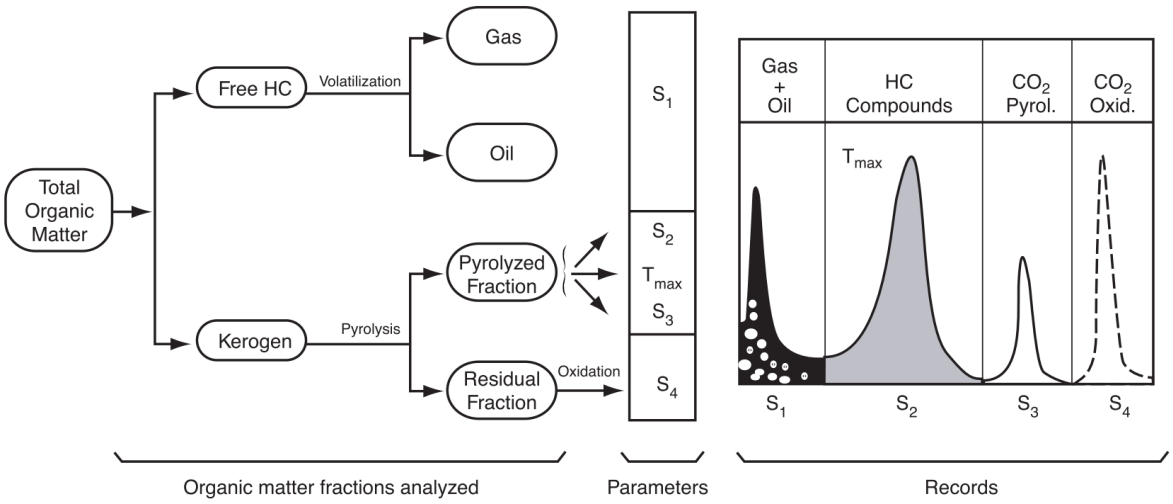

Figure 2-6. The diagram presents the different organic matter fractions in analysed rocks, the corresponding parameters, and their recordings by rock-eval pyrolysis (Lafargue, Marquis et al. 1998).

2.3.1.2 Experimental procedure

Rock-eval pyrolysis was carried out by the British Geological Survey (BGS) by Vinci Technologies Rock-Eval 6 standard instrument, which can be heated up to 850 °C controlled by a thermocouple located in contact with the sample. 60 mg shale powder (<250 µm) loaded into the sampler. The pyrolysis oven is heated up and kept isothermally at 300 °C for 3 mins to get S1. Then the temperature was increased from 300 to 650 °C steadily at a heating rate of 25°C /min to obtain S2 (hydrocarbon generated from kerogen) and S3 (released CO_2 produced from kerogen breakdown), both in an N_2 atmosphere. The oxidation stage was achieved by heating at 300 °C for 1 min and then from 300 to 850 °C at 20 °C/min and held at 850 °C for 5 min in oxygen (O_2). The residual carbon released as CO_2, forms the S4 peak (Uguna,

Carr et al. 2016). The TOC results of two UK shales (BS3 and GH4) are obtained from the Rock-eval pyrolysis.

2.3.2 Thermal Gravimetric Analysis (TGA)

2.3.2.1 The principle

Thermogravimetric Analysis (TGA) is a technique to measure a sample's thermal stability and volatile components by monitoring sample mass changes over time at the controlled temperature and atmosphere (Earnest 1988, Zafeiropoulos 2011). A typical TGA consists of a precision balance with a platinum pan located inside a furnace with a programmable control temperature. Standard gases like Nitrogen (N_2), Argon (Ar), Helium (He), Carbon dioxide (CO_2), and Hydrogen (H_2) are used for controlling the atmosphere. The temperature is generally increased at a constant rate (10-250 °C/min) to incur a thermal reaction. A variety of pressures, including a high vacuum, high pressure, constant pressure, or controlled pressure, can be held in different TGAs.

2.3.2.2 Experimental procedure

The thermal properties of three kerogen samples are tested by SDT Q 600 TGA. The proximate analysis of the samples was carried out in triplicate by TGA to get the fraction of moisture, volatiles, fixed carbon, and ash contents by the following methods. Samples were heated to 110 °C at a ramp rate of 20 °C/min in N_2 gas with a flow rate of 100 mL/min, 1bar, and were held isothermally at a temperature of 110 °C for 30 minutes to remove water. Then samples were heated from 110 to 950 °C at a ramp rate of 20 °C/min in N_2 gas with a flow rate of 100 mL/min, 1bar, and samples were held isothermally at 950 °C for 30 minutes to remove the volatiles material. After that, the gas was switched from N_2 to air at a 100 mL/min flow rate for another 30 minutes to burn the fixed carbon, leaving the ash content on the sample pan. The TGA results of the three kerogen samples are shown in Appendix A, Table A2. The ash contents of which are applied to obtain the kerogen ash-free density for comparison with the simulated kerogen density in Chapters 5 and 6.

2.3.3 Elemental Analysis (EA)

2.3.3.1 The principle

The Elemental analysis (EA), commonly referred to as CHNS analysis, provides a rapid method to determine the Carbon (C), Hydrogen (H), Nitrogen (N), and Sulfur (S) in organic matrices and other types of materials by utilizing a high-temperature combustion technique. This combustion can be carried out under both static conditions (introduction of a set volume of oxygen) or dynamic conditions (a constant flow of oxygen) for a set period (ASTM D5291) (uk 2006). The basic principles are converting the C, H, N, and S present in the sample to CO_2, H_2O, NO_X, SO_2, respectively, in the furnace containing pure oxygen by the combustion process (combustion temperature can range from 600 to 1450 °C). Then these combustion products are separated by a chromatographic column. The inert gas (eg. He) sweeps the combustion products through overheated (600 °C) purity copper to remove any excess oxygen present from the combustion process and convert NO_x to N_2. All the gases, N_2, CO_2, H_2O, and SO_2, are detected by the thermal conductivity detector (TCD), which gives an output signal proportional to the concentration of the individual components of the mixture.

2.3.3.2 Experimental procedure

Elemental analysis was conducted by Leco CHN/S 628 instrument to measure C, H, N, and S contents, in order to obtain the total organic carbon (TOC) in the shale and kerogen samples. Up to 3 g of the powdered shales (particle size <250 µm) were treated using enough HCl with a concentration of 1 mol/L for 24 hours to remove carbonates. The samples were then washed with distilled water six times to remove the acid and reach pH 7. After carefully decanting the water from the samples, the samples were dried in the vacuum oven (<0.5 mbar) for 48 hrs at 120 °C. The TOC contents were measured by CHN 628 using vacuumed dried 120 mg shale (after acid wash), and 75 mg kerogens, respectively. Each sample is wrapped in tin foil and then combusted in a chamber with enough pure oxygen at 950 °C. The Leco 628S analyser for S content uses 250 mg kerogen at 1350 °C. All the elemental analyses were carried out in triplicate.

2.3.4 Helium Pycnometry (HP)

2.3.4.1 The principle

There are two types of density associated with shale and kerogen samples in this study, envelope (or bulk) density and skeletal density, which are calculated from the bulk volume and the skeletal volume (Figure 2-7 A). The bulk density is determined for porous materials when pore spaces within the material are included in the volume measurement (Figure 2-7 A). Skeletal density is the ratio of the mass of solid material to the sum of the volumes of the solid material and closed pores within the material (Figure 2-7 A) (ASTM D3766).

Helium Pycnometry (HP) measures the skeletal volume of material by gas displacement using the volume-pressure relationship of Boyle's Law (Webb 2001). As the inert gas, Helium (He) is used as the displacement medium that can go into the open pores but not the closed pore (Figure 2-7 A). The equipment has two chambers, a sample chamber and a reference chamber (Figure 2-7 B), the volumes of which are known as V_{sc} and V_{rc}. The sample is placed in a sample chamber before analysis, and the pressure of both chambers is at atmosphere pressure (P_1). Then He is purged into the sample chamber, and the pressure is measured as P_2. After that, gas in the sample chamber is expanded into the reference chamber, and the pressure is measured as P_3 (Figure 2-7 B). Then the volume of the sample (V_s) can be calculated by Equations (2-9) and (2-10). The skeleton density is determined by the sample weight and the sample skeletal volume measured (Equation 2-11).

$$P_2 \cdot (V_{sc} - V_s) = P_3 \cdot (V_{sc} + V_{rc} - V_s) \quad (2\text{-}9)$$

$$V_s = \frac{P_3 \cdot V_{sc} + P_3 \cdot V_{rc} - P_2 \cdot V_{sc}}{P_3 - P_2} \quad (2\text{-}10)$$

$$\rho = \frac{m}{V_s} \quad (2\text{-}11)$$

V_{sc} is the sample chamber volume; V_{rc} is the reference chamber volume; P_2 is the pressure when the sample chamber is full of He; P_3 is the pressure when the sample chamber and reference chamber are connected; V_s is the sample skeletal volume; m is the sample mass; ρ is the sample skeleton density.

2.3.4.2 Experimental procedure

The skeletal density of dry and wet samples was measured by a Micromeritics Helium pycnometer (AccuPyc II 1340) (Figure 2-7 C). The pre-dried and pre-wetted shale (about 3.5

g) and kerogen (about 1.5 g) were weighed and loaded into the 10 cm^3 cell with a 3.5 cm^3 sample chamber (Figure 2-7 D). The sample needs to fill at least two-thirds of a cup to obtain satisfactory results. Helium is purging at a pressure of 1.34 bar (19.5 psig) at 20 °C to the sample chamber (P_2). A successive evacuation (20 cycles purges) is applied to drive the air out before measuring the dry samples with 20 cycles of He dosing applied. A run sequence of 20 cycles of He dosing without purge evacuation is used for wet samples. The density is accepted as the correct one once the standard deviation is less than ± 0.01 g/cm^3.

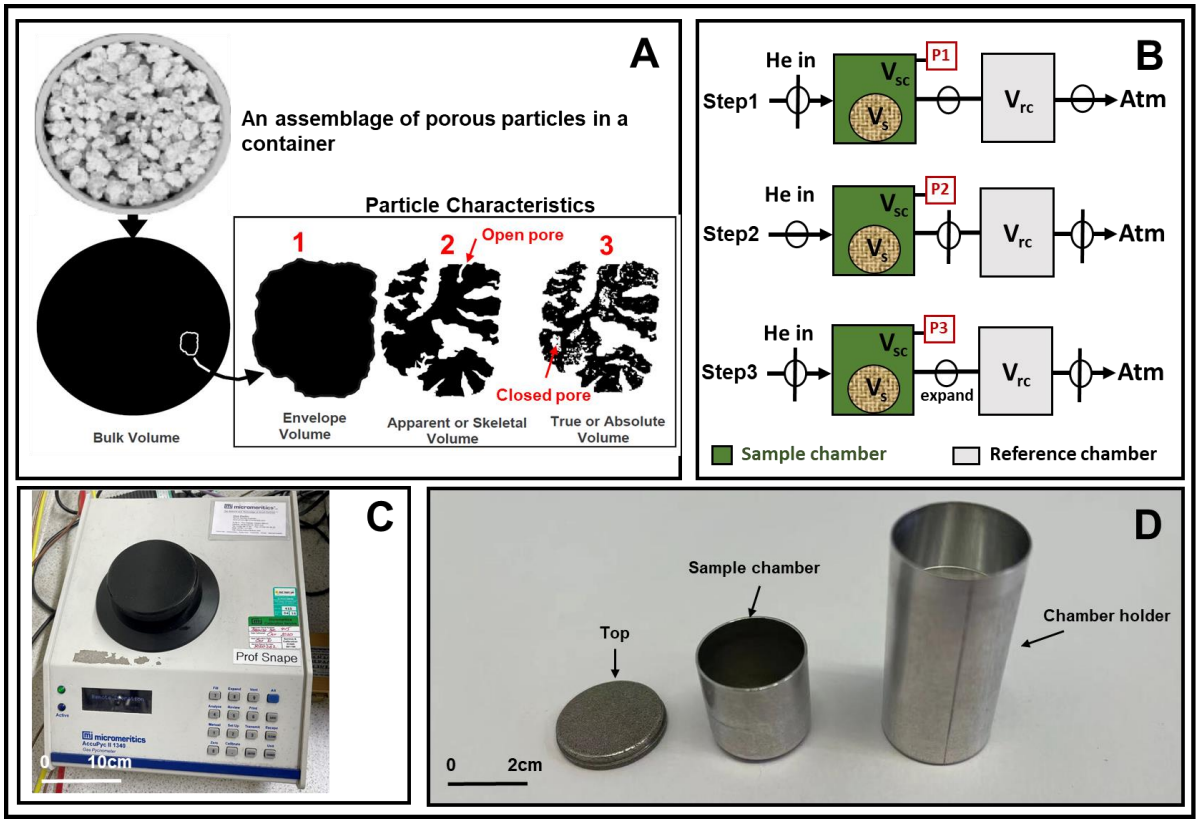

Figure 2-7. A) An illustration diagram of various sample volume types and helium pycnometry, 1) is the particle bulk volume within the envelope, the density calculated from this volume is bulk density, 2) is the apparent/skeletal volume which minus the 'external' volume and volume of open pores, the density calculated from this volume is skeletal density, and 3) is the volume within the envelope minus both open and closed pores, modified from (Webb 2001), B) the volume and pressure change for the Helium Pycnometry measurements, C) the Micromeritics helium pycnometer (AccuPyc II 1340), D) the sample holder and chamber for the Helium Pycnometry.

2.3.5 Vitrinite Reflectance (VR)

2.3.5.1 The principle

Vitrinite reflectance (VR) (%Ro) is used to quantify the thermal maturity of sedimentary shales by measuring the proportion of incident white light reflected from the plane polished surface of the vitrinite maceral at 500X magnification under oil immersion by microscope (Barker and Pawlewicz 1986, Carr 1999). Vitrinite is the remains of woody materials, commonly found in source reservoir rocks (Barker and Pawlewicz 1986). Reflectance and fluorescence of other macerals such as solid bitumen and amorphous organic matter can also provide an independent means to assess thermal maturity and hydrocarbon generation potential (Kibria, Das et al. 2020). The major physical manifestation of maturation is the increase in VR, as with the increase of temperature and pressure (generally a function of depth), progressive changes such as aromatization, condensation, and rearrangement of the vitrinite molecular structure have occurred (Levine and Davis 1984, Mukhopadhyay 1994, Carr 1999). The characteristic of vitrinite include 1) ubiquitous presence (most shale, except overmature shales), 2) the homogenous appearance when viewed under the incident light microscope, and 3) the constant physical and chemical changes under increasing thermal stress making vitrinite being the main parameter for the determination of maturity (Levine and Davis 1984, Mukhopadhyay 1994, Carr 1999). While the vitrinite might not be easy to view for the overmature shale, due to its absence, then the bitumen reflectance (BR) can be used to calculate the VR by Equation (2-12) (Schoenherr, Littke et al. 2007).

$$\mathrm{VR} = \frac{\mathrm{BR}+0.2443}{1.0495} \qquad (2\text{-}12)$$

2.3.5.2 Experimental procedure

The VR measurements were conducted by using a LEICA DM4500P microscope. Initial shales (around 1.5 g) were crushed to 250 µm-2 mm particles, mounted in epoxy resin, polished, and immersed in oil before measuring. Calibration was carried out using a Zirconian standard (3.13% Ro), a blank (0% Ro), and the calibration was checked using a Yttrium Aluminium Garnet (YAG) standard (0.89% Ro) to ensure a linear calibration. Measurement was carried out in non-polarized light, which was a white light source of 12 V 100 W halogen lamp with a LED illumination slider 29 x 11.5 mm in the incident light axis. The wavelength used was 546

nm in oil immersion, and the data (between 16 and 32 points count were taken depending on the number of recognisable vitrinite available for measurement in each sample, the variation of these data is within 10%) were collected randomly via the Hilgers Fossil Man system connected to the LEICA DM4500P microscope. The UK shale vitrinite reflectance (%Ro) was obtained directly, the data of which is compared with Tmax, and they all present same maturity stages. And the China shale vitrinite reflectance (VR) was converted from the reflectance of bitumen (BR) by Equation (2-12) (Schoenherr, Littke et al. 2007) to indicate the maturity of shales, due to their higher maturity vitrinite was not easy to observe.

2.3.6 Gas Chromatography-Mass Spectrometry.

2.3.6.1 The principle

The Gas Chromatography-Mass Spectrometry (GC-MS) instrument is a technique used to separate chemical mixtures (by GC) and identify the components at a molecular level (by MS) (Figure 2-8) according to their volatility and mass (Sparkman, Penton et al. 2011, Hübschmann 2015). In the GC system (Figure 2-8), the sample is heated to vapor state immediately after injection, which will be carried by the pure carrier gas (He, H_2, N_2, or Ar) to pass through the GC column to separate the different components. The separation of the molecules is promoted by the difference in relative affinity between the molecules and the column as the sample travels the length of the column. The oven is heated to the pre-set temperature during the separation, and the components come out of the column at different times (called the retention time), then reach the GC detector, with each chemical component recorded on a chromatogram. The height and area of each peak are directly proportional to the concentration of the compound within the sample. As the separated substances emerge from the column, they flow into the MS. These molecules are broken into charged, unique ionized fragments (ions) by the ionization source like Electron ionization (EI), Chemical ionization (CI), and Electrospray ionization. Electron Ionization (EI) source is the popular ionization source, with 70 ev commonly chosen as the electron energy as the ion signal is most intense at around 70 ev. These ions with different mass/charge (m/z) travel through the magnetic field, filtered based on their mass, which is recorded by the MS detector (Sparkman, Penton et al. 2011).

MS is typically utilized in two ways: Electron ionization with full-scan mass detection (SCAN) and selected ion monitoring (SIM). Full-scan mass detection is an untargeted approach and is capable of potentially detecting all the fragment ions. It is widely used in MS for relatively volatile samples that are thermally stable and have relatively low molecular weight. Identification of unknown compounds can be achieved by comparison of their full mass spectrum with a mass spectral library or database. SIM is a targeted approach and will only identify the compounds for which specific acquisition parameters are entered into the analytical method. SIM is considered to be more sensitive compared to full-scan methods for the component that the SIM method is designed to detect (Sparkman, Penton et al. 2011, Nair and Clarke 2016).

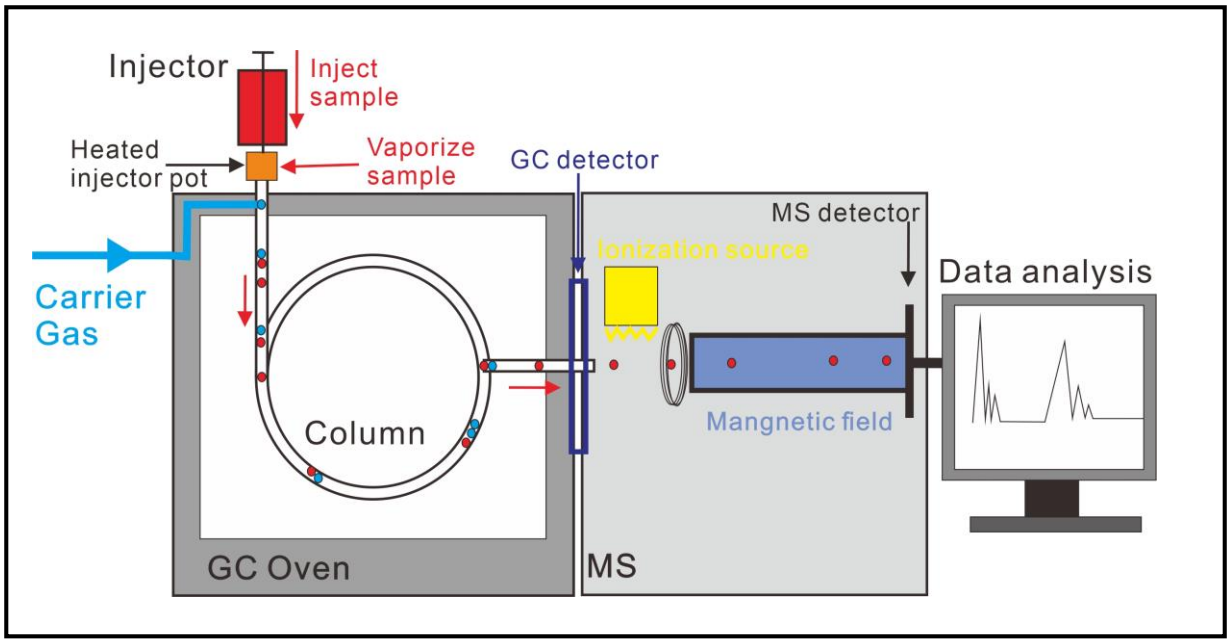

Figure 2-8. Schematic of GC-MS.

2.3.6.2 Experimental procedure

Extracted oils from the shales (by the method in Section 2.2.2) were analysed by gas chromatography-mass spectrometry (GC-MS) using an Agilent GC-MS (7890B GC; 5977A-mass selective detector (MSD)) in splitless mode. Product separation was performed on an HP-5MS column (30 m × 250 µm × 0.25 µm). The GC oven temperature was initially held at 50 °C for 0.5 min, then heated to 300 °C at a rate of 4 °C/min, where it was held for 5 minutes. The MS (with EI of 70 eV) was scanned by SCAN mode in the mass range of m/z 40–400, with an ion

source temperature of 200 °C. Individual compounds were identified using a NIST 14 MS library and published data.

2.4 Gas adsorption technique

2.4.1 The theory of gas adsorption

2.4.1.1 Gas adsorption interactions

Gas adsorption is defined as the enrichment of molecules, atoms, or ions around an interface, which can be divided into physisorption and chemisorption based on the different features (Thommes, Kaneko et al. 2015) (Table 2-2). Chemisorption, typically presented as monolayer and unreversible, is not included in this research. The adsorption heat is larger (50-200 or more KJ/mol), and the intramolecular forces mainly mean the formation of chemical bonds (Rouquerol, Rouquerol et al. 2013). Physisorption, as a general phenomenon, occurs whenever the adsorbate is brought into contact with the surface of a solid (the adsorbent) by the intermolecular forces mainly involving Van der Waals forces (VdW) and hydrogen bonds (H-bond). Monolayer (includes selected and full cover) and multiple layers of adsorption can form with low adsorption heat (less than 40 KJ/mol), and the whole adsorption process is reversible as desorption, for physisorption (Figure 2-9) (Bruch 1983, Rouquerol, Rouquerol et al. 2013, Thommes, Kaneko et al. 2015).

Table 2-2. Different features between physisorption and chemisorption

Features	Interaction	The heat of adsorption (KJ/mol)	Reversibility	Adsorption layer
Physisorption	Intermolecular	<40	Yes	Mono/Multilayer
Chemisorption	Intramolecular	50-200 or more	No	Monolayer

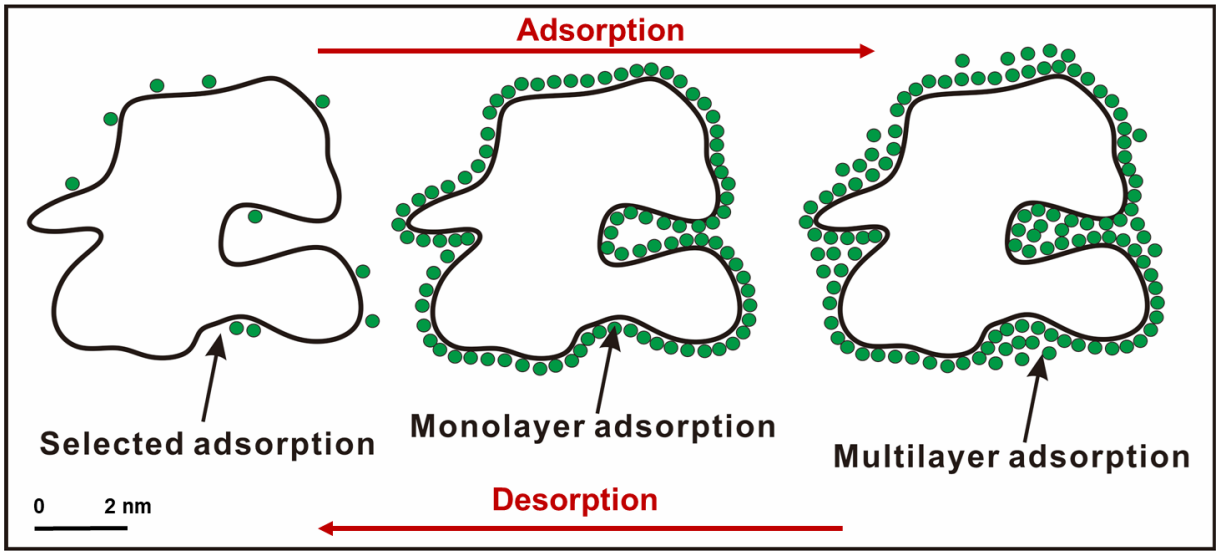

Figure 2-9. The adsorption and desorption process for physisorption, from monolayer (selected and full cover) to multiple layers adsorption.

VdW is a universal nonspecific interaction between atoms or molecules. As a weak force (roughly 10^2-10^3 times weaker than chemical force), it decreases with distance (Dzyaloshinskii, Lifshitz et al. 1961, Winterton 1970, Levy 2007). VdW can be classified into orientation (electrostatic), induction, and dispersion forces. Orientation force, known as dipole-dipole force, results from the interaction of the dipole moments of two polar molecules (Figure 2-10). Induction force exists between the charged or polar molecule with another non-polar or polar molecule due to the former inducing a dipole in the latter (Figure 2-10 B). Dispersion force is a temporary attraction force in all atoms and molecules. It results from the constant motion of the electrons developing a temporary dipole when its electrons are distributed unsymmetrically about the nucleus, making this atom or molecule can affect the other atom and molecule (Figure 2-10 C) (Dzyaloshinskii, Lifshitz et al. 1961, Winterton 1970, Parsegian 2005). Polar molecules (like water (H_2O- H_2O) molecules) include all three VdW. The induction and dispersion forces exist between polar and nonpolar molecules (like between H_2O and CH_4) molecules), whereas only dispersion forces exist between non-polar molecules (like between CH_4-CH_4 molecules). Therefore, most molecules have dispersion force. Only the polar molecules are predominated by Orientation force.

The H-bond (X-H···Y) is a primarily electrostatic force of attraction, which can vary in strength from weak (1-2 KJ/mol) to strong (161.5 KJ/mol) force (Emsley 1980, Larson and McMahon 1984). It is the attractive interaction between a hydrogen (H) atom covalently bound to a

more electronegative atom or group (X), like nitrogen (N), oxygen (O), fluorine (F), Carboxylic acid (COO-), and another electronegative atom (Y) bearing a lone pair of electrons—the hydrogen bond acceptor. H-bonds usually are stronger than VdW and weaker than chemical bonds (Martin and Derewenda 1999, Labinger and Bercaw 2002).

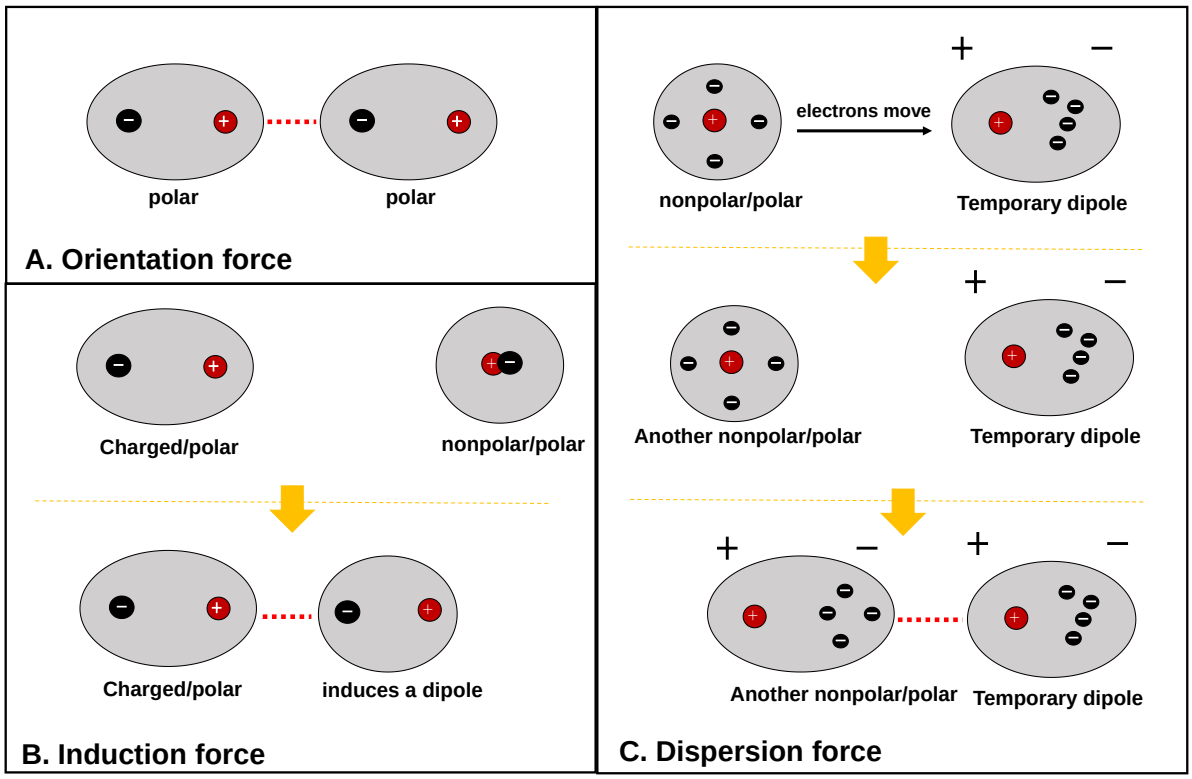

Figure 2-10. Schematic of Orientation force (A), Induction force (B), and Dispersion force (C) for Van der Waals forces.

2.4.1.2 Gas adsorption isotherms and hysteresis loops

Adsorption isotherms are direct results of gas adsorption within various pores. The isotherms are classified into six types by IUPAC, which are closely related to pore structures (Thommes, Kaneko et al. 2015) (Figure 2-11). Microporous materials like activated carbons, molecular sieve zeolites and certain porous oxides can give Type I isotherms. Type I(a) isotherms are contributed by microporous materials having mainly small micropores (of width <1 nm) due to the micropore filling at the low pressure, while Type I(b) isotherms are given by the materials that have pore size distributions over a broader range, including larger micropores (of width >1 nm) and possibly narrow mesopores (of width <2.5 nm). Reversible Type II isotherms occur by the physisorption of most gases on nonporous or macroporous

adsorbents. The knee point (B) indicates the beginning of the middle almost linear section, corresponding to the completion of monolayer coverage. A less distinctive B shows the significant overlap of monolayer coverage and the onset of multilayer adsorption. There is no identifiable monolayer formation in the Type III isotherm, and the adsorbed molecules are gathered around the most favourable sites on the surface of non-porous or macroporous material by the relatively weak (adsorbate-adsorbent) interactions. Mesoporous adsorbents like oxide gels, industrial adsorbed, and mesoporous molecular sieves can provide Type IV isotherms. The adsorption isotherm located in the low-middle relative pressure area is similar to Type II but ends with a final saturation plateau as the typical feature at high relative pressure. Type IV(a) isotherm indicates the capillary condensation is accompanied with hysteresis, which occurs when the pore width is bigger than a particular size (this size is dependent on the adsorption system and temperature, e.g., for N_2 in cylindrical pores at -196 °C, the hysteresis starts when the pore size is bigger than 4 nm), and the hysteresis shapes in IV(a) have a relationship with pore networking (Section 2.4.1.2, Table 2-3). Type IV(b) isotherm is completely reversible, normally formed by the smaller width mesopores. Water adsorption on hydrophobic microporous and mesoporous material can form Type V isotherm, which is very similar to Type III at the low relative pressure range, with molecular clustering is followed by the pore filling at a higher relative pressure range. Type VI isotherm is reversible, and it is representative of layer-by-layer adsorption on a highly uniform nonporous surface (Sing 1985, Webb and Orr 1997, Thommes, Kaneko et al. 2015). The application of these isotherms includes predicting the gas adsorption capacity (like methane adsorption capacity in shale) by high-pressure gas sorption experiment, as well as analysing the pore characterization by low-pressure gas (N_2, and CO_2) sorption (Sing 1985, Webb and Orr 1997, Gasparik, Ghanizadeh et al. 2012, Thommes, Kaneko et al. 2015).

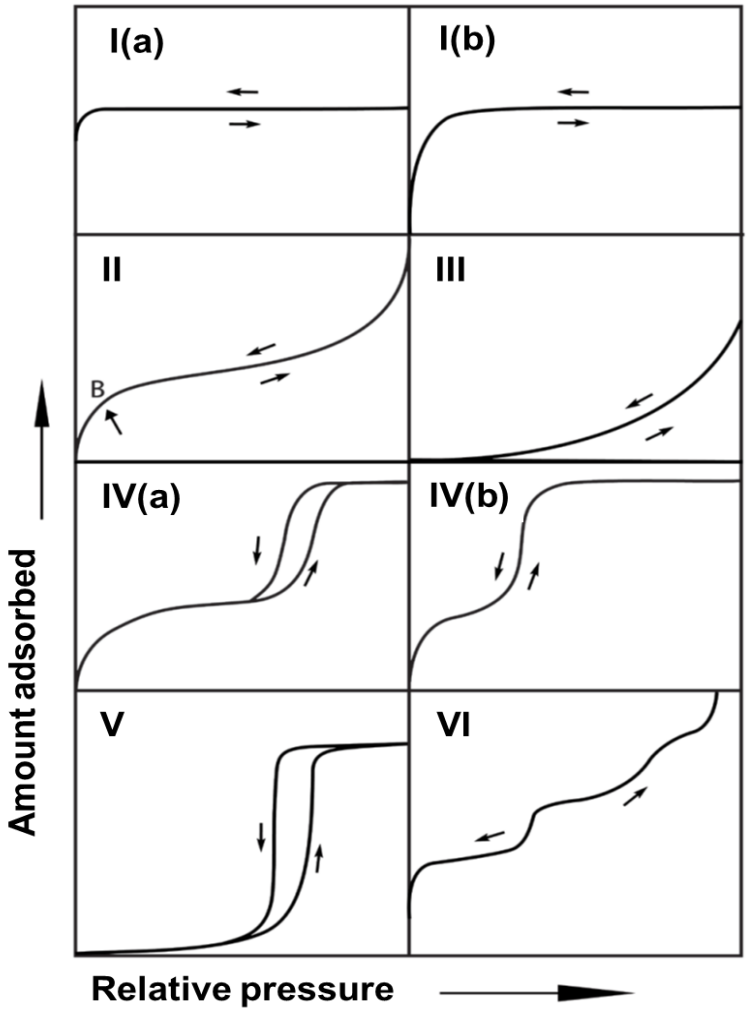

Figure 2-11. Classification of physisorption isotherms (Thommes, Kaneko et al. 2015).

The hysteresis loops are mainly divided into six types (Figure 2-12), located in the multilayer range of the isotherms, associated with capillary condensation and adsorption metastability (delayed condensation), where the pore geometry and network can impact the type of hysteresis (Thommes, Kaneko et al. 2015). The characteristics and usual interpretations for each hysteresis are listed in Table 2-3. H1 is given by the uniform mesopores or ink-bottle pores with similar pore neck size to pore size. H2 is given by the pores with complex pore networks, with H2(a) relating to pores with narrow pore necks, and H2(b) associated with the pores having wider pore necks. H3 is given by the non-rigid aggregates of plate-like particles, H4 is often found with aggregated crystals of zeolites, some mesoporous zeolites, and micro-mesoporous carbons, and the unusual H5 can be found in the pore containing both open and partially blocked mesopores like plugged hexagonal templated silicas (Thommes, Kaneko et al. 2015).

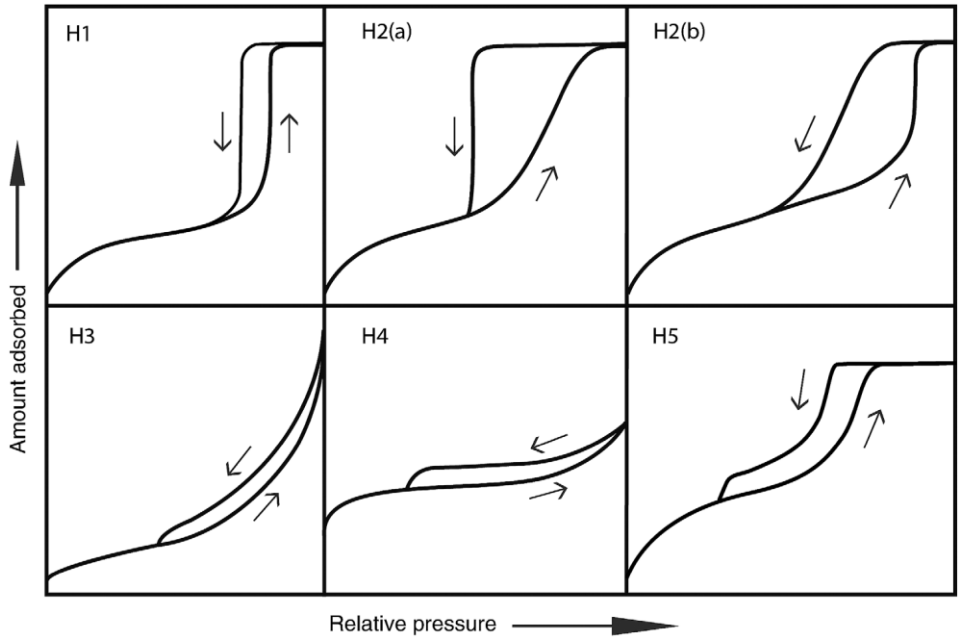

Figure 2-12. Classification of hysteresis loops for adsorption isotherms (Thommes, Kaneko et al. 2015).

Table 2-3. Characteristics and interpretation of hysteresis loop types (Thommes, Kaneko et al. 2015).

Hysteresis type	Characteristics	Usual interpretation
H1	Nearly vertical and parallel adsorption and desorption branches with narrow loop due to the delayed condensation.	Uniform mesopores (e.g. templated silicas) or ink-bottle pores where the width of neck is similar to the pore size (e.g. 3D ordered mesoporous carbons)
H2(a)	Sloping adsorption and nearly vertical desorption branch, associated with pore-blocking	Pores with narrow range pore necks (e.g. silica gels)
H2(b)	Same adsorption branch as H2(a), with desorption branch slope decreases gradually, associated with pore blocking	Pores linked with larger necks (e.g. mesocellular silica foams and mesoporous silicas after hydrothermal treatment)
H3	Adsorption branch similar to Type II, and the desorption branch lower limit is located at the cavitation-induced relative pressure	Non-rigid aggregates of plate-like pores (e.g. certain clays)
H4	Similar to H3, but Underlying type I isotherm	Slit-like pores for the aggregated crystals of zeolites, mesoporous zeolite, and micro-mesoporous carbons
H5	Unusual to see, the desorption branch has similar shape like adsorption branch but delayed	Associated with certain pore structures containing both open and partially blocked mesopores (e.g. plugged hexagonal templated silicas)

2.4.1.3 Gas adsorption models

Various models are applied to represent and predict the gas adsorption isotherms. As far as this research is concerned, the henry law, Langmuir, dual-site Langmuir model, Brunaue-Emmett-Teller model (BET), and the NLDFT models are the applied models in this study, with their detailed introduction analysed below.

Henry law

Henry's law states that at a constant temperature, the amount of adsorbed/dissolved gas is directly proportional to the partial pressure of its gas phase. The proportionality factor is called Henry's law constant (Sander 2014). It was formulated by the English chemist William Henry (Henry 1803). Henry's law equation is shown as (Equation 2-13).

$$Q_a = K_{xa} \cdot P_a \quad (2\text{-}13)$$

P_a is the partial vapour pressure of gas; K_{xa} is Henry's constant, whose value is related to temperature, solute, and solvent. The henry's constants of methane used in this study for water (NIST Chemistry WebBook, SRD 69) and crude oil (Ma, Hua et al. 2002) at 25 °C are 0.0013 and 0.0167 mol/(kg·bar); Q_a is the dissolve/adsorbed gas quantity.

Langmuir and Dual site Langmuir model

Langmuir model is widely applied to describe the gas adsorption phenomenon, especially with Type I isotherms. It can provide a good fit of the measured data up to intermediate pressures (Langmuir 1918). It explains adsorption by assuming 1) an adsorbate behaves as an ideal gas at isothermal conditions; 2) the surface of the sorbent is homogenous, and all the binding sites are uniformly distributed, having the same affinity, and no interaction between adjacent adsorbed molecules; 3) the gas is adsorbed as a monolayer, each active site interacts with only one adsorbate molecule; 4) the adsorption and desorption are reversible processes in this model (Langmuir 1918, Aguilar-Armenta, Patiño-Iglesias et al. , Gasparik, Bertier et al. 2014, Baur, Katz et al. 2020).

The Langmuir model can be presented as Equation (2-14), it is normally used to predict the maximum amount of gas (gas adsorption capacity) at a specified pressure and temperature

in researches about methane adsorption in shale (Chalmers and Bustin 2007, Gasparik, Ghanizadeh et al. 2012, Gasparik, Bertier et al. 2014, Chen, Kang et al. 2018).

$$Q_a = Q_m(\frac{b \cdot P}{1+b \cdot P}) \quad (2\text{-}14)$$

Q_a is the quantity of gas adsorbed at pressure P, Q_m is the maximum adsorbed gas content, which is the quantity of gas adsorbed when the entire surface is covered with a monomolecular layer for the Langmuir model, b is a constant related to the adsorption energy.

Classical Langmuir assumes the adsorbent is homogenous, which is not sufficient to describe the gas adsorption on a heterogeneous surface, where the adsorption energy at each site varies depending on the local chemistry and structure. The dual-site Langmuir model (Equation 2-15) with the most simplified case is developed to address heterogeneous adsorbents, where two different adsorption sites are available. The most favourable sites will be filled first, followed by the less favourable sites (Tang, Ripepi et al. 2016). The dual-site Langmuir model applied in shale research provides more accurate results, where each site can be modelled by a separate equilibrium constant (Whitelaw, Uguna et al. 2019, Li, Stevens et al. 2021).

$$Q_a(P,T) = Q_m \times \left[(1-\alpha)\frac{b_1 \cdot P}{1+b_1 \cdot P} + \alpha\frac{b_2 \cdot P}{1+b_2 \cdot P}\right] \quad (2\text{-}15)$$

Where, Q_a is the absolute adsorption quantity; Q_m is the maximum adsorbed gas content, which is the quantity of gas adsorbed when the entire surface is covered with a monomolecular layer for the dual-site Langmuir model; b_1 and b_2 are the temperature-dependent equilibrium constants, which is related to the adsorption energy of sorption sites 1 and 2; b_1 and b_2 are weighted by a coefficient (α); α is the fraction of the second type of site ($0 < \alpha < 1$); P is the pressure and T is the temperature.

Brunaue-Emmett-Teller (BET)

BET model (Equations 2-16, and 2-17), is an advanced multilayer adsorption model, which was developed from the Langmuir monolayer model by Brunaue-Emmett-Teller (1938) (McMillan and Teller 1951). The main assumption for BET models is that the forces for the gas condensation are also responsible for the binding energy of multilayer sorption. It has been widely applied as a semi-empirical tool for the investigation of the characteristics of porous adsorbents, such as surface area (Webb 2001).

$$Q_a = \frac{Q_{ml} \cdot C \cdot P}{(P_0 - P) \cdot \left[1 + (C-1) \cdot \frac{P}{P_0}\right]} \quad (2\text{-}16)$$

$$C \propto exp \frac{E_1 - E_L}{RT} \quad (2\text{-}17)$$

Where, C is a constant, must be positive, can be represented by equation (2-17); Q_a is the absolute adsorption quantity; Q_{ml} is the quantity of gas adsorbed when the entire surface is covered with a monomolecular layer; P_0 is the saturation pressure of the gas; E_1 is the heat of adsorption of the first layer, E_L is the heat of liquefaction of the adsorptive, which means E_L is that for the second and higher layers and is equal to the heat of liquefaction or heat of vaporization; R is the gas constant; P is the pressure, and T is the temperature.

This BET model is the most widely used procedure for evaluating the surface area of porous material, and the BET equation in the linear form is applied as Equation (2-18) (Thommes, Kaneko et al. 2015). A straight line can be plotted by $(P/P^\circ)/(Q_a(1 - P/P^\circ))$ *vs.* P/P°, with intercept of $(1/Q_{ml} \cdot C)$, and slope of $((C-1)/(Q_{ml} \cdot C))$. Therefore, the values of C and Q_{ml} can be obtained by the plotted straight line. Once the Q_m (the gas monolayer adsorbed molecules quantity/amount/volume) is obtained, the surface area (SA) of the samples can be determined using the area occupied by the monolayer adsorbate molecule, which can be calculated by Equation (2-19), once the cross-sectional area (σ, e.g. 0.162 nm^2 for N_2 at -196°C, 0.170 nm^2 for CO_2 at 0°C (Thommes, Kaneko et al. 2015)) of a single adsorbed gas molecule and the molecular gas mass (M, e.g. 28 g/mol for N_2, 44 g/mol for CO_2) are known. N_A is the Avogadro constant (6.023×10^{23} molecules/mole).

$$\frac{P/P^\circ}{Q_a(1-P/P^\circ)} = \frac{1}{Q_{ml} \cdot C} + \frac{C-1}{Q_{ml} \cdot C}\left(\frac{P}{P^\circ}\right) \quad (2\text{-}18)$$

$$SA = \frac{Q_{ml} \cdot \sigma \cdot N_A}{M} \quad (2\text{-}19)$$

Non-local density functional theory (NLDFT)

Barrett, Joyner, and Halenda (BJH) model (Barrett, Joyner et al. 1951) is used widely for porosity characterization of mesoporous materials without distinguishing the pore structure morphologies, the precision of which is reduced or not applicable for the microporous materials (Thommes, Kaneko et al. 2015). Although other methods like Horvath-Kawazoe (HK), t-plot, Dubinin–Radushkevich (DR) can describe the micropore (Thommes, Kaneko et al. 2015), applying these methods in combination with BJH does not provide a continuous pore size distribution.

Density functional theory (DFT) based on the fundamental principles of statistical mechanics, is considered as a more reliable mathematical method in quantum physics for the pore size analysis over the complete nanopore range (Seaton and Walton 1989, Landers, Gor et al. 2013, Thommes and Cychosz 2014). It describes the distribution of adsorbed molecules in pores with different shapes (e.g., slit, cylinder and spherical geometries and hybrid shapes) on a molecular level as the fluid-solid interaction potential is dependent on the pore model, and thus provides detailed information about the local fluid-structure near the adsorbent surface (Landers, Gor et al. 2013, Thommes and Cychosz 2014, Thommes, Kaneko et al. 2015). Based on the chosen pore shapes and the selected adsorbed gas, non-local-density functional theory (NLDFT) generates 'kernel' (Figure 2-13), a series of theoretical isotherms ($N(P/P^{\circ}, W)$), to indicate the amount of gas adsorbed as a function of pore size (W) and relative pressure (P/P°), at a specific temperature first. Then calculating the pore size distribution function ($f(W)$) based on the solution of the general adsorption isotherm (GAI) equation (Equation 2-20), which is generated by correlating the experimental adsorption isotherm ($N(P/P^{\circ})$) with the kernel (Landers, Gor et al. 2013, Thommes, Kaneko et al. 2015). It is included in commercial software and is also featured in international standards (such as ISO 15901-3). Other models/theories calculate the PSD from the isotherms, while NLDFT calculates the PSD by plotting the theoretical isotherms by assuming PSD first and then comparing these isotherms with the experiment isotherms. To obtain a reasonably accurate evaluation of the pore size distribution, a compatible and the representative chosen kernel is needed to be consistent with the experimental adsorptive/adsorbent system (Thommes, Kaneko et al. 2015).

$$N\left(\frac{P}{P^{\circ}}\right) = \int_{W_{min}}^{W_{max}} N(\frac{P}{P^{\circ}}, W) \cdot f(W) dw \qquad (2\text{-}20)$$

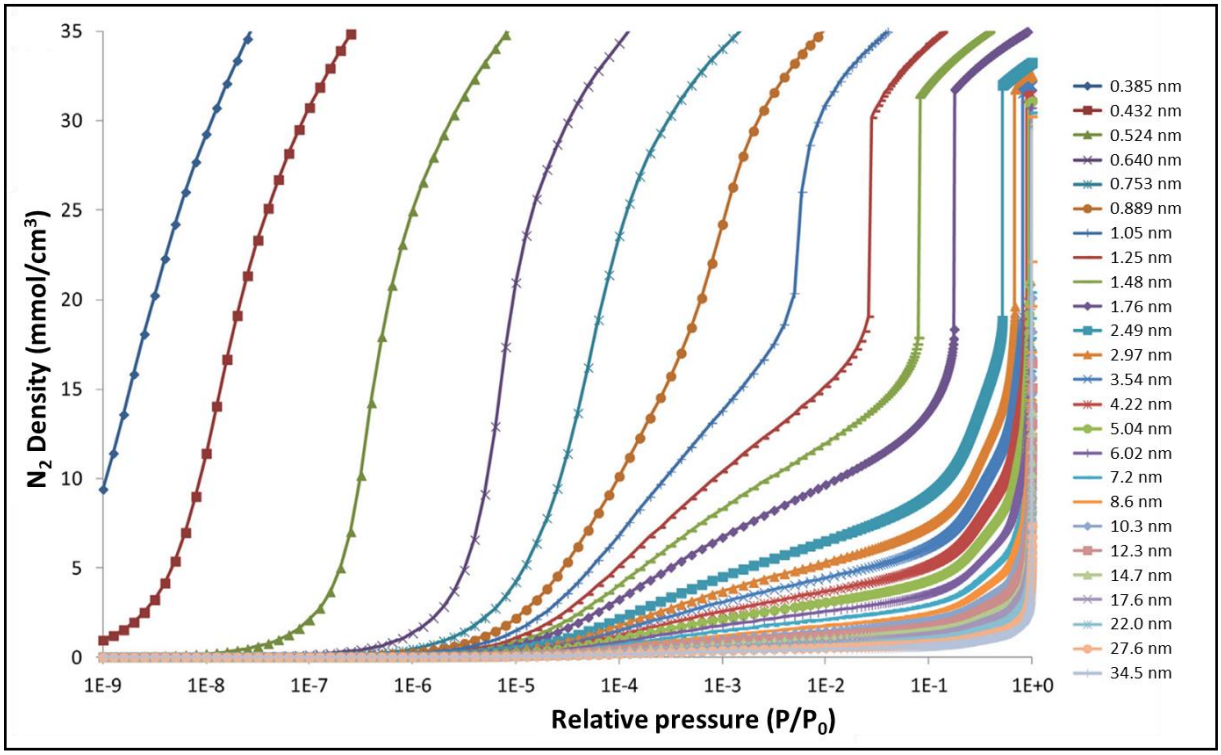

Figure 2-13. Kernels of selected equilibrium nitrogen (N_2) at -196°C adsorption isotherms in slit-shaped carbon pores, calculated using NLDFT (Landers, Gor et al. 2013).

2.4.2 High-pressure methane adsorption

2.4.2.1 The principle of the High-Pressure Volumetric Analyser (HPVA)

A High-Pressure Volumetric Analyser (HPVA) (Figure 2-14 A) is designed to obtain high-pressure gas (hydrogen, methane, and carbon dioxide) adsorption isotherms by employing the static volumetric method using the ideal gas law at a single pressure. The volumetric technique consists of dosing a known amount of gas (Q_{Dose}) into analysis sample cell, measuring the gas amount in sample cell after equilibrium was reached (Q_{eq}), and then calculating the excess adsorbed gas amount (Q_{ade}) by Equation (2-21).

Firstly, the gas is dosing from valves 6 or 7, and 3 (Figure 2-14 B) into the reference cell or the manifold volume (V_m, is the known volume) to equilibrate, and the temperature and pressure in the manifold are recorded as P_{mA} and T_{mA}. Then the gas is dosed into the sample cell by opening valve 1. After equilibrium was reached, the P_{mB} and T_{mB} are recorded as the pressure and temperature in the manifold after dosing. The known amount of gas dosed (Q_{Dose}) into sample cell can be calculated by Equation (2-22).

Secondly, after the gas was expanded into the sample cell (9 in Figure 2-14 B), and reached equilibrium. The equilibrium pressure and temperature (P_s and T_s) in sample cell are recorded by the transducer (11 in Figure 2-14 B). The gas amount in the sample cell after equilibrium (Q_{eq}) was calculated by Equation (2-23). The analysis free space of the cell with samples in experiments (V_{fs}) is calculated by Equation (2-24) with the known sample mass, density, and free space for the blank cell (V_f). The measurement of blank free space (V_f) is carried out before experiments (Equation 2-25 and 2-26), where the system first pulls a vacuum on the manifold and sample cell, and the helium (approximately 1.2 bar) is dosed into the manifold, reaching equilibration. After that, the helium is dosed into the sample cell. The pressure and temperature of the manifold before (P_{mA}, and T_{mA},) and after dosing (P_{mB}, and T_{mB},) helium into sample cell, and the equilibrium pressure and temperature (P_s, and T_s,) in sample cell are recorded.

For an experiment, this process is repeated at given pressure intervals using a typical adsorbate (in this case, methane) until the maximum pre-selected pressure is achieved. Each of the resulting equilibrium points (gas quantity adsorbed and equilibrium pressure) is then plotted to provide an isotherm. The thermophysical properties (density, compressibility) of methane at any given experimental temperature and pressure condition are obtained from REFPROP 8.0 software based on the database of the U.S. National Institute of Standards and Technology (NIST).

$$Q_{ade} = Q_{Dose} - Q_{eq} \tag{2-21}$$

$$Q_{Dose} = \frac{P_{mA} \cdot V_m}{T_{mA} \cdot Z_A \cdot R} - \frac{P_{mB} \cdot V_m}{T_{mB} \cdot Z_B \cdot R} \tag{2-22}$$

$$Q_{eq} = \frac{P_s \cdot V_{fs}}{T_s \cdot Z_s \cdot R} \tag{2-23}$$

$$V_{fs} = V_f - \frac{m_s}{\rho_s} \tag{2-24}$$

$$V_f = \frac{Q_{Dose'} \cdot T_{s'} \cdot Z_{s'} \cdot R}{P_{s'}} \tag{2-25}$$

$$Q_{Dose'} = \frac{P_{mA'} \cdot V_m}{T_{mA'} \cdot Z_{A'} \cdot R} - \frac{P_{mB'} \cdot V_m}{T_{mB'} \cdot Z_{B'} \cdot R} \tag{2-26}$$

Where, Q_{ade} is the excess gas adsorbed by samples; Q_{Dose}/$Q_{Dose'}$ is the gas amount dosed into the sample cell; Q_{eq} the gas amount in the sample cell after equilibrium; m_s is the mass of the sample; ρ_s is the density of samples; Z_A / $Z_{A'}$ and Z_B / $Z_{B'}$ are the gas compressibility

at $P_{mA}/P_{mA'}$ and $T_{mA}/T_{mA'}$, and $P_{mB}/P_{mB'}$ and $T_{mB}/T_{mB'}$; R is the gas constant; $Z_s/Z_{s'}$ is the gas compressibility at $P_s/P_{s'}$ and $T_s/T_{s'}$.

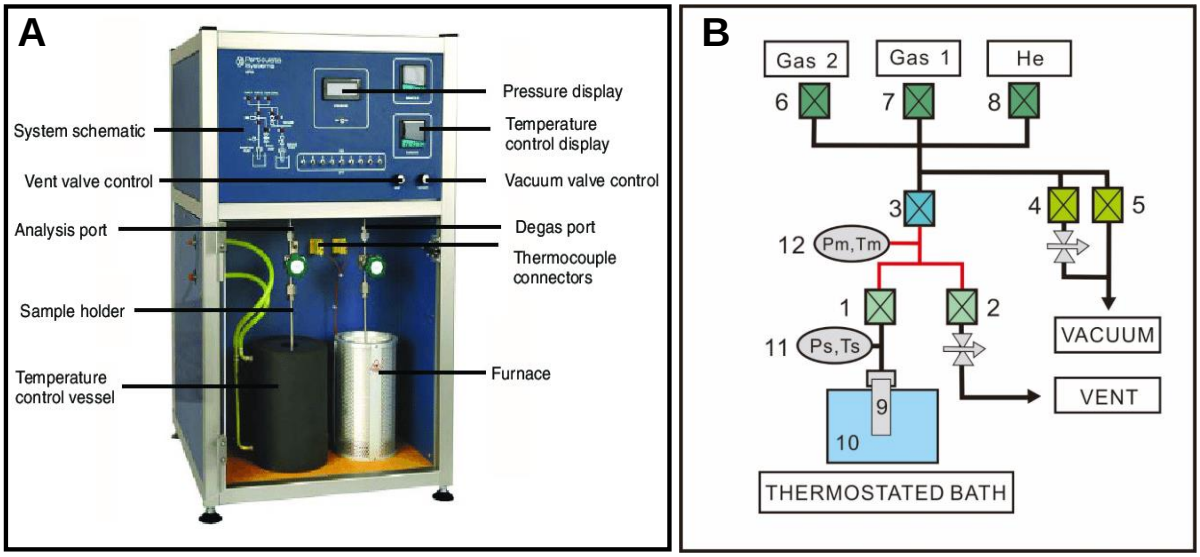

Figure 2-14. A) Particulate Systems High-Pressure Volumetric Analyser (HPVA-100), B) Schematic of the standard HPVA system, 1,2,3,4,5,6,7,8, are valves, 9 is stainless measuring cell, 10 is the thermostatic bath, 11, 12 are temperature and pressure transducers.

The gas adsorption capacity of shale is represented by the gas adsorption quantity (Q), which is controlled by the temperature (T), gas pressure (P), and the adsorption potential (E) between the gas and the solid ($Q = f(T, P, E)$). The gas quantity measured (directly) by the volumetric or gravimetric sorption measurement is the excess adsorption quantity (Q_{ade}), which is necessary to convert to absolute adsorption quantity (Q_a) by Gibbs equation (Equation 2-27) (Sircar 1999), as this is the fundamental thermodynamic property (Brandani, Mangano et al. 2016). The difference between the excess adsorption quantity and the absolute adsorption quantity is determined by the gas density (ρ_g) and adsorbed pore volume (V_a) at corresponding temperature and pressure (Figure 2-15 A, B), and their difference is significant at high pressure (Tang, Ripepi et al. 2016) (Figure 2-15 B).

$$Q_a = Q_{ade} + (V_a \times \rho_g) \quad (2\text{-}27)$$

Where, Q_a is the absolute adsorption quantity; Q_{ade} is the excess adsorption quantity; V_a is the pore volume for gas to adsorb into, which is micropore volume here; ρ_g is the density of the bulk gas.

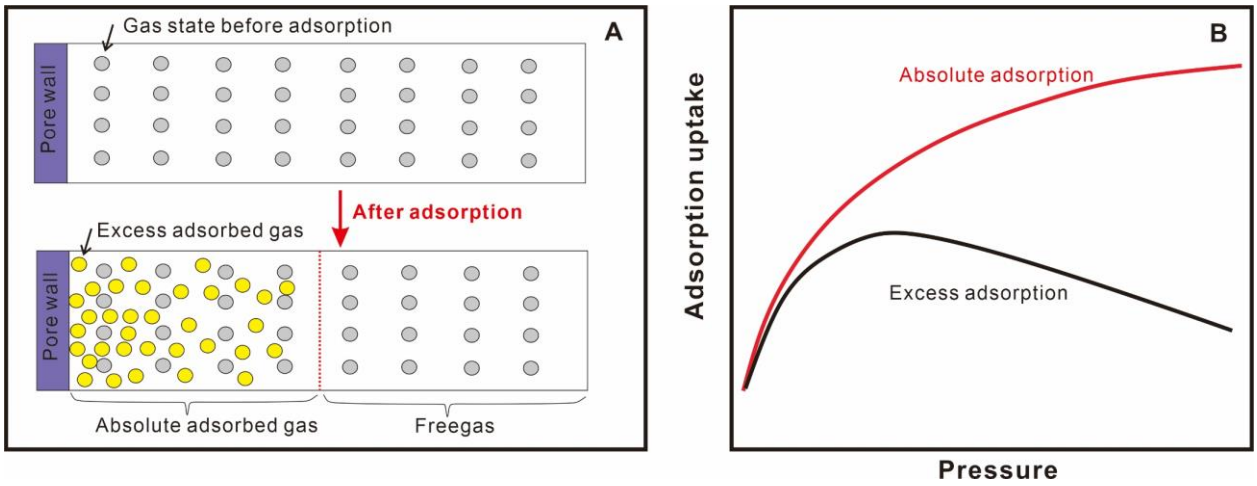

Figure 2-15. A) Gas adsorbed states before and after adsorption, B) The difference between the excess adsorption and the absolute adsorption isotherms.

2.4.2.2 Exerimental procedure

High-pressure methane adsorption measurements were performed using a Particulate Systems High-Pressure Volumetric Analyzer (HPVA-100) (pressures up to 105 bar and temperatures up to 500 °C) (Figure 2-14 A). Approximately 10 g of pre-treated 95 %R.H. moisture-equilibrated shale (2-4 mm) and 3 g of 95 %R.H. moisture-equilibrated kerogen concentrate (<250 µm) were weighed and loaded into the 10 cm^3 stainless steel sample cell and sealed. The helium free space (V_f) calibration was done before analysis on an empty sample cell (Equations 2-25 and 2-26). For wet (95 %R.H.) samples, the methane adsorption isotherms were acquired from 1.2 to 105 bar at 25 °C. Here, the external valve linking the analysis cell to the instrument manifold remained closed until the analysis or manifold pressure reached 1.4 bar, then opened, the pressure settled to 1.2 bar, avoiding samples being subjected to a vacuum on the high-pressure instrument. The mass deviation of wet samples before and after analysis was less than ±0.0018%, verifying the moisture is still in the sample. For dry adsorption isotherms, the samples were degassed at 120 °C for 48 hours before starting the methane adsorption method. A pre-evacuation was carried out for 45 minutes to reach a vacuum set point of 0.013 bar on the high-pressure instrument before pressure dosing, and then with a gas adsorption isotherm was generated from 0 to 105 bar. The pressure reaching equilibrium in this study is defined as pressure variation less than 0.001bar over 7 mins, with an average equilibration taking around 40 mins. Helium pycnometry (Section 2.3.4) was used to measure the skeletal density of wet and dry samples for the manual calculation of the analysis free space (Equation 2-24) to obtain exact gas

sorption results, as an automatic free space test by helium on the instrument would expose the moisture equilibrated samples to a vacuum which would remove the moisture. The adsorption isotherms of blank cell correction were carried out on both dry and wet sample data.

Each sample was analysed in triplicate to assess errors. The excess adsorption quantity is obtained by the volumetric sorption measurement; therefore, it is necessary to convert to absolute adsorption quantity by the Gibbs equation (Equation 2-27) (Sircar, 1999; Tang et al., 2016). The HPVA can measure the adsorption up to 105 bar, whereas the adsorbed gas quantities at higher pressures can be predicted by the dual-site Langmuir model which is for heterogeneous adsorbents (Tang et al., 2016; Whitelaw et al., 2019). The equation for the dual-site Langmuir can be written in the above form (Equation 2-15).

2.4.3 Low-pressure gas sorption experiment

2.4.3.1 The principle of low-pressure gas sorption

As an application of the gas adsorption theory, the low-pressure gas adsorption experiment also normally known as 'BET' measurement, is an essential tool for the characterization of porous solids and fine powders. It is used to quantify the amount of various subcritical fluids at different relative pressure (P/P_0, P is the absolute equilibrium pressure, and P_0 is the saturation pressure), and to obtain the pore surface area, pore size distribution, and pore volume based on varies models (Labani, Rezaee et al. 2013, Thommes, Kaneko et al. 2015). Different theories like Brunauer-Emmett-Teller (BET), Barrett-Joyner-Halenda (BJH), t-plot, Dubunin-Radushkevich (DR), Dubinin-Astakhov (DA), G. Horváth-K. Kawazoe (H-K) and Dollimore-Heal (DH) are applied to get the specific surface area (SSA), pore size distribution (PSD), pore volume, and other parameters (Barrett, Joyner et al. 1951, Horváth and Kawazoe 1983, Webb and Orr 1997, Thommes, Kaneko et al. 2015).

In order to get the realistic adsorbed gas quantity, the selected adsorbed probe gas (adsorbate) should follow the following conditions: 1) The gas molecules are relatively inert to ensure that there is no chemical interaction with the adsorbent; 2) In order to allow sufficient gas to adsorb to the surface of the solid, the solid must be cooled during the measurement, usually to the boiling point of the adsorbed gas, so the coolant is relatively easy to obtain; 3) Meet the conditions of use of the ideal gas equation. Therefore, the gases

like nitrogen (N_2) and krypton (Kr) at -196 °C, argon (Ar) at -186 °C or at -196 °C, carbon dioxide (CO_2) at -78 °C or 0 °C can be applied. N_2 and CO_2 are widely used for probing the meso-macro pores and micropores, considering their price and availability. Kr is normally used for the samples with the SA less than 0.5 m^2/g, and Ar is too expensive for this study.

2.4.3.2 Exerimental procedure

Low-pressure gas sorption experiments were carried out for both dry and 95% R.H. moisture equilibrated (wet) samples by a Micromeritics Surface Area and Porosity Analyser (ASAP 2420). For shale samples, 4 g particles (2-4 mm) were used for the low-pressure N_2 sorption experiments, 2 g for CO_2 adsorption, and about 1 g of the powdered kerogen concentrates (<250 μm) for both N_2 and CO_2 sorption. All the dry samples were degassed under high vacuum (<0.013 mbar) at 120 °C for 48 hours prior to analysis, and a pre-evacuation of 3 hours on the low-pressure instrument to reach the vacuum setpoint (0.013 bar) to start the isotherm. The pressure equilibrium interval for the low-pressure gas sorption in this study was set to 30 s (time taken to measure pressure in the sample tube), and the pressure can only move to the next pressure point when the change in pressure per interval (30 s) is less than 0.01%, with the equilibration time for per pressure step ranging between 40-60 mins. The warm and cold analysis free space corrections were carried out based on the sample mass and density on this instrument, which is the same as the correction for the high-pressure methane adsorption method (Section 2.4.2, Equation 2-24, 2-25 and 2-26).

For low-pressure N_2 sorption, the prepared wet samples were frozen first in liquid N_2 for 30 minutes, before manually evacuating the sample tube and starting the analysis. This ensures moisture-equilibrated samples are not exposed to vacuum at warmer temperatures on the low-pressure instrument. The mass deviation of wet samples before and after analysis was less than ±0.0020%, verifying the moisture is still in the samples. The analysis for both dry and wet samples was performed in a liquid N_2 bath (-196 °C), with the relative pressure (P/P_0, P is the absolute equilibrium pressure, and P_0 is the saturation pressure) from 10^{-7} until 0.995 P/P_0. CO_2 adsorption isotherms were acquired from 6×10^{-5} to 3.5×10^{-2} P/P_0 (absolute pressure is from 0.002 to 1.2 bar) at 0 °C with the same pressure equilibration setting as N_2 adsorption, to characterise the ultra-microporous structure (<0.8 nm) of dry shale and kerogen concentrates (Liu, Sun et al. 2015, Whitelaw, Uguna et al. 2019). CO_2 adsorption was not

carried out for wet samples because the experimental temperature is 0 °C which could not hold the moisture in the sample under low pressure.

Brunauer-Emmett-Teller (BET) theory was used to calculate the SA, where the P/P_0 between 0.05 and 0.2 of N_2 adsorption and P/P_0 between 0.025 and 0.030 of CO_2 adsorption was selected to get a positive BET 'C' parameter (Brunauer, Emmett et al. 1938, Thommes, Kaneko et al. 2015). With the development of density functional theory and computer simulation approaches, the whole range of micro and mesopores can be probed with commercially available models such as Non-Local Density Functional Theory (NLDFT) (Rouquerol, Llewellyn et al. 2007, Qi, Tang et al. 2017). NLDFT method based on the carbon slit pore model is applied to calculate the PSD from 0.33 to 100 nm in this study by combining both N_2 and CO_2 isotherms using Microactive software (Micromeritics Microactive Software V5.01).

2.5 Other experiments for pore characterisation

Characterising the pore texture of shale and kerogen is critical for understanding methane adsorption capacity and providing input data for kerogen model construction in simulation. Low-pressure gas (N_2, CO_2) sorption experiments (stated in Section 2.4.3) is the major method for pore characterisation of kerogens and shales, which is also supported by other experiments, including Field Emission Scanning Electron Microscopy (FE-SEM), Transmission Electron Microscopy (TEM), X-ray Computed Tomography (XRCT), and high-pressure mercury intrusion porosimetry (MIP) in this research. SEM and TEM with relatively high resolution are widely used in shale to get the 2D images of the nano-scale. They can identify macropores, mesopores, and even micropores (by TEM) in an organic matter clearly (Loucks, Reed et al. 2009, Chalmers, Bustin et al. 2012, Tian, Pan et al. 2013, Kuila, McCarty et al. 2014, Wang, Zhu et al. 2014). XRCT presents the 3D pore network of shale from a larger scale (μm) (Whitelaw, Uguna et al. 2019). Low-pressure gas adsorption and MIP (penetration of fluids) can be used for the measurement of open pores and the pore networks, providing precise quantitative measurement in shale studies (Ross and Bustin 2009, Clarkson, Solano et al. 2013, Tian, Pan et al. 2013, Klaver, Hemes et al. 2015).

2.5.1 SEM and TEM

2.5.1.1 The principle

Electron microscope (EM) is working based on a stream of high voltage electrons (formed by the electron source and accelerated in a vacuum using a positive electrical potential) to magnify the object's image based on the interactions between electrons and the atoms in the sample (Piazzesi 1973, Zhou, Apkarian et al. 2006). Electron microscopes employ an electron beam for imaging. In transmission electron microscopy (TEM), signals such as the transmitted electrons are detected, which will give information on the sample's inner structure. In scanning electron microscope (SEM), two types of signal are typically detected: the backscattered electrons (BSE) and the secondary electrons (SE). BSE is reflected back after elastic interactions between the beam and the sample, coming from deeper regions of the sample and providing imaging carries composition information of the sample. Moreover, BSE images can also provide valuable information on crystallography, topography, and the magnetic field of the sample. In contrast, SE originates from the atoms of the sample, which is very useful for the inspection of the topography of the sample's surface (Zhou, Apkarian et al. 2006, Akhtar, Khan et al. 2018, Kannan 2018)(Figure 2-16).

Instead of using an electron beam to scan the sample like SEM, TEM collects the beam of electrons that passes through the specimen and analyzes the internal structure of the specimen in the form of images (Williams and Carter 1996, Kannan 2018) (Figure 2-16). Compared to SEM, TEM has higher requirements in terms of sample preparation and analysis conditions. The sample for the TEM has to be very thin to allow electrons to travel through the specimen, often less than one hundred nanometers, since the electron has a poor penetrating capability and gets absorbed in a thick sample (Williams and Carter 1996, Frank 2013, Kannan 2018).

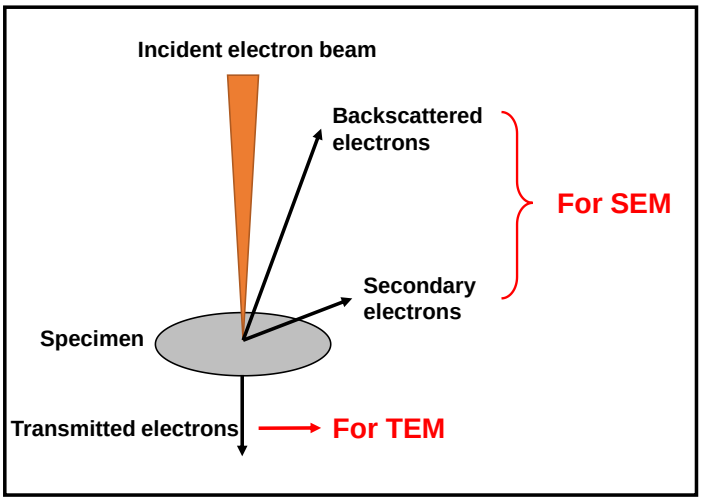

Figure 2-16. Schematic of the electron beam working for SEM and TEM.

2.5.1.2 Exerimental procedure of SEM

The shales (with a particle size of 2-4 mm) have been embedded in EpoFix resin and polished to a 1 micron diamond polish by Fischione Model 1010 Low Angle Argon Ion Beam Miller and Polisher. Then, the samples were coated with a 15 nm conductive layer by PELCO conductive carbon paste. The samples were imaged using a JEOL 7100F FEG-SEM equipped at 15 KV and 10 mm working distance, with either backscatter electron or secondary electron images. All the high-resolution FE-SEM images were processed using Image J-1.53a software (developed at National Institutes of Health and the LOCI, University of Wisconsin) (Abràmoff, Magalhães et al. 2004).

2.5.1.3 Exerimental procedure of TEM

Kerogen fine grounded powder (particle size <300 nm) samples are dry-deposited onto holey carbon film supports (EM Resolutions Ltd). Then the samples are analyzed using a JEOL 2100F FEGTEM operating at 200 KV, equipped with a Gatan Orius camera and Gatan Digital Micrograph software to get the TEM images of kerogen.

2.5.2 X-ray Computed Tomography (XRCT)

2.5.2.1 The principle

The X-ray Computed Tomography (XRCT) technique is well applied to obtain the shale pore network as it can produce 3D image of a material's internal structure at a spatial resolution by a non-destructive process (Figure 2-17) (Colletta, Letouzey et al. 1991, Ma, Fauchille et al.

2017, Arif, Mahmoud et al. 2020). XRCT shows the spatial distribution of different particles within the shale system, including the pores, as each element has a different attenuation of X-rays (Hounsfield 1973, Landis and Keane 2010). The lack of attenuation of X-rays is presented for pores within the shales as the only thing to pass through is the air present, which has a much lower attenuation compared to solid objects. Other particles composed of the shale, such as organic matter and different minerals, have a much higher and different attenuation rate. Each component is defined during analysis with thresholds, with separate parts of shale based on their attenuation (Whitelaw, Uguna et al. 2019). The 3D images are generated via a series of 2D slices by rotating the sample through 360° around a central axis without destroying the sample (Landis and Keane 2010, Ma, Fauchille et al. 2017, Arif, Mahmoud et al. 2020).

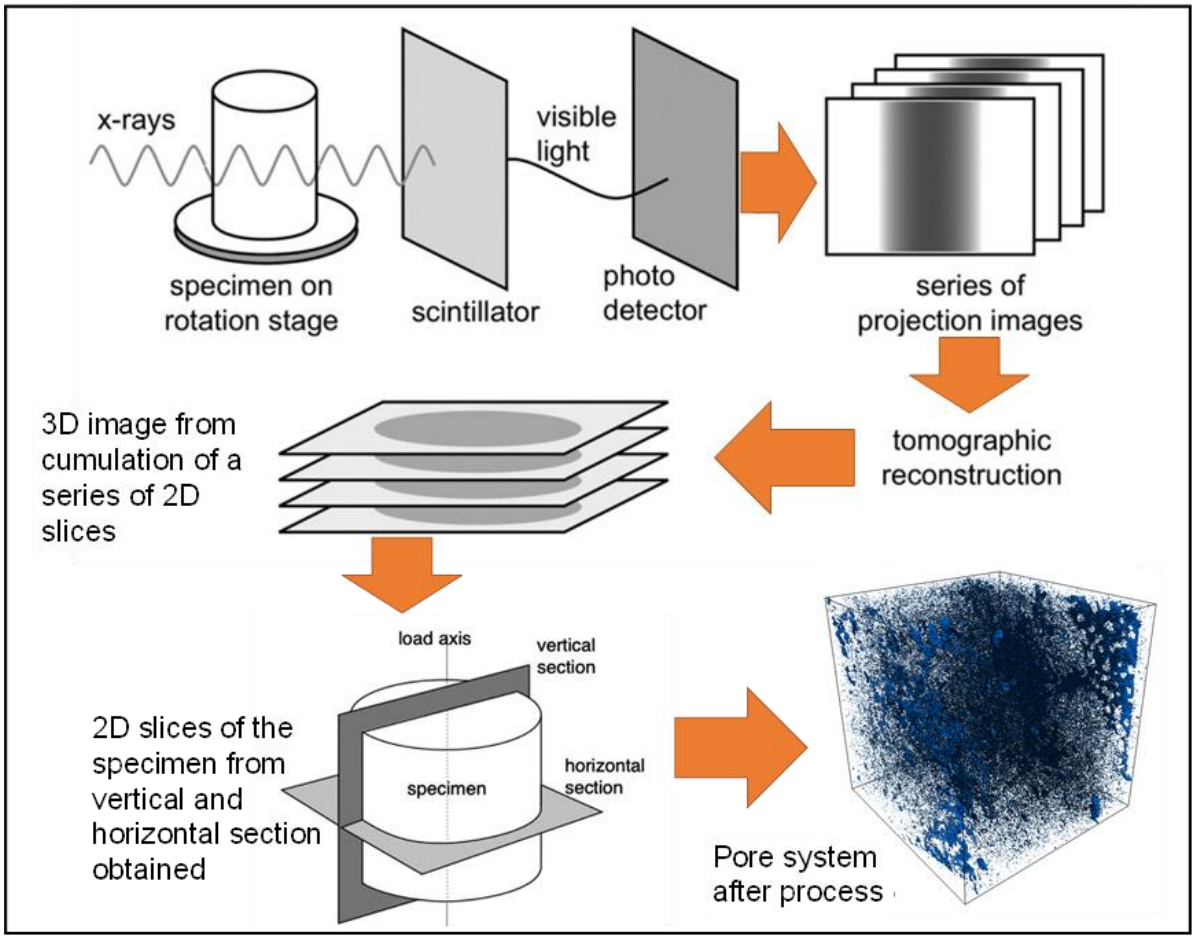

Figure 2-17. Schematic illustration of XRCT acquisition and reconstruction processes. A series of 2D XRCT images are acquired and mathematically reconstructed to produce a 3D image. (Modified from (Landis and Keane 2010)).

2.5.2.2 Exerimental procedure of XRCT

XRCT on the shales was conducted by an Xradia Zeiss Versa XRM500 CT system with a maximum electron acceleration of 160 kV. Scan parameters were kept constant between measurements, using the following setup: source voltage 80 kV, source current 88 µA, exposure time 4s and geometric magnification 0.4×; with a pixel size of 2.5 µm. The reconstructed pixel size limits the minimum detectable pore size, as it is generally accepted that the minimum detectable pore size is approximately that of a few pixels. These scans captured the entire cross-section of the x–y plane, but to avoid edge effects from the top and bottom surfaces. The images were captured using a 2 x 2 camera binning mode over a 180-degree rotation span. 3D data was reconstructed from the 2D radiographs using a filtered back-projection algorithm. The data was analysed using Avizo Fire 9 software (Thermo Scientific™) with segmentation by the Otsumethod (Otsu 1979). Analysis was performed to characterise porosity in terms of volume, size, and the pore networks. XRCT with a 2.5 µm resolution combined with 3D image analysis offers the chance to visualize the pores system and quantify the geometrical characterisation of 3D features and volume fraction using image analysis routines.

2.5.3 Mercury Intrusion Porosimetry (MIP)

2.5.3.1 The principle

MIP can provide a wide range of information about a sample, including the pore size distribution (PSD), total pore volume or porosity, the simple pore surface area, and the bulk density (Giesche 2006). Mercury is the non-wetting liquid with higher surface tension (surface tension is the tendency of liquid surfaces to try to shrink into the minimum surface area possible (Kirkwood and Buff 1949, Rigby and Edler 2002)) and a larger contact angle (>90°) (Figure 2-18 A). It will not wet most substances and will not spontaneously penetrate pores by capillary action unless forced by the application of external pressure (Figure 2-18 B) (Donaldson, Chilingarian et al. 1985, Webb and Orr 1997, Giesche 2006). Accurate contact angles and surface tension between sample and mercury are needed for getting correct results. MIP measures the mercury injected volume at different pressures, and the equilibrated pressure is inversely proportional to the pore size. Lower pressure (typically 0.0069 bar/1 psia) is required to apply mercury into large macropores, whereas higher

pressures are needed to force mercury into smaller pores (when the pressure end at 4136.85 bar/60000 psia, the mercury can intrude into the pores with a diameter/width of 4-2 nm) (Donaldson, Chilingarian et al. 1985, Giesche 2006, Malik, Smith et al. 2016, Rigby 2018).

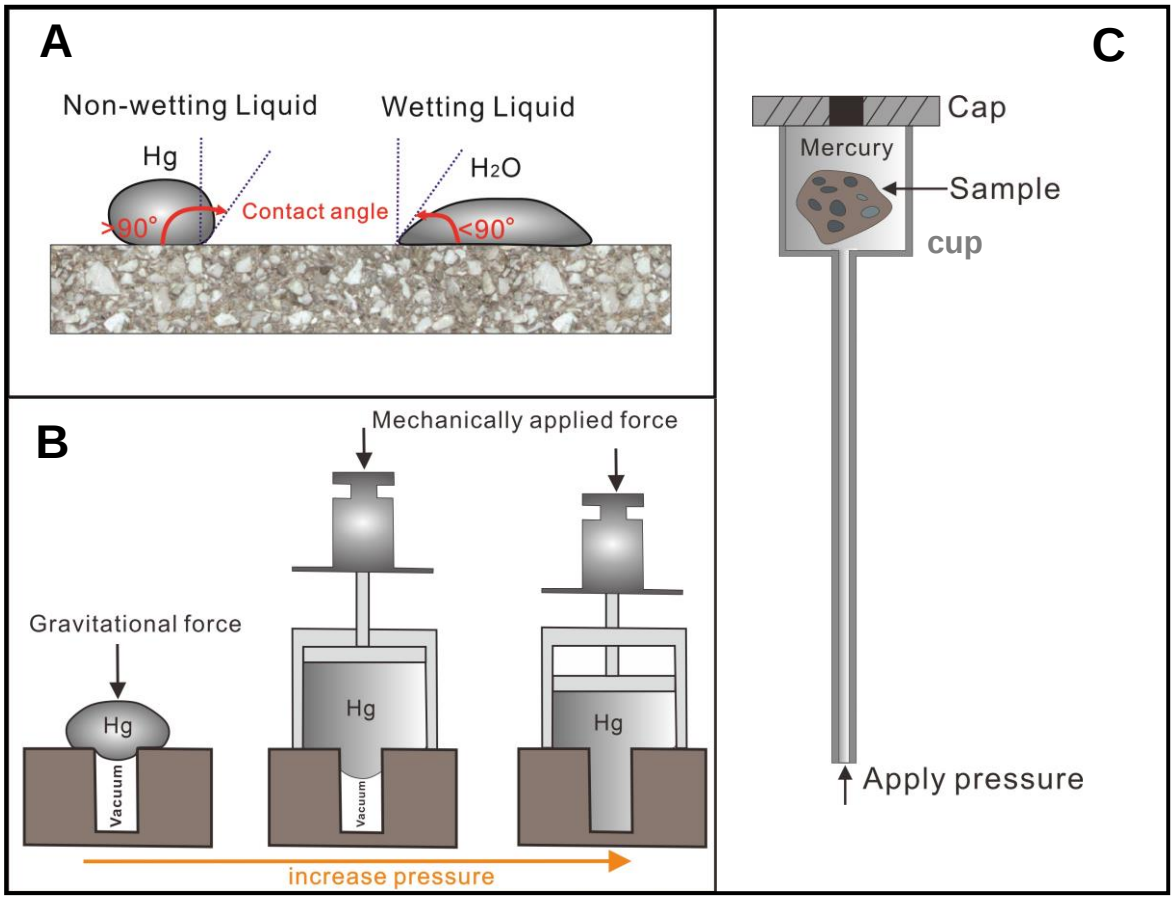

Figure 2-18. Schematic of MIP. A) is the contact angle difference between non-wetting and wetting liquid, B) is the intrusion of mercury when pressure applied, C) is the penetrometer for the MIP measurement.

To obtain the pore size from the pressure versus intrusion data, the following equations are used. The magnitude of mercury resisting force (f_R) can be represented by Equation (2-28). The externally applied force (f_{Ext}) to force mercury into the pores can be calculated from Equation 2-29). At equilibrium, just before the resistive force is overcome, the Equation is (2-30), with Equations 2-31 and 2-32, also called the Washburn equation (Washburn 1921), to calculate the pore diameter (D) for cylinder and pore width (W) for slits pore from pressure. Therefore, each pressure can get the corresponding pore diameter/pore width.

$$f_R = \pi D\gamma \cos\theta \quad (2\text{-}28)$$

$$f_{Ext} = PA = P\pi D^2/4 \quad (2\text{-}29)$$

$$-\pi D\gamma \cos\theta = \pi D^2 P/4 \quad (2\text{-}30)$$

$$D = -4\gamma \cos\theta \,/P \tag{2-31}$$

$$W = -2\gamma \cos\theta \,/P \tag{2-32}$$

Where, f_R is the mercuy resisting force; f_{Ext} is the externally applied force; D is the pore diameter for cylinder pores; W is the pore with for slits pores; γ is the surface tension of mercury; θ is the contact angle; P is the pressure; A is the area that pressure applied, it is also a pore's circular cross-section.

The bulk density is acquired by the total bulk volume of the sample (before any pores are filled with mercury) and the mass (Equation 2-33). The bulk sample volume is found by subtracting the mercury volume from the empty penetrometer volume (Figure 2-18 C) (Equation 2-34). The void volume occupied by the mercury can be calculated by Equation (2-35), and the percent porosity (φ) of the sample is found from Equation (2-36).

$$\rho_{bulk} = W_s / V_{bulk\,S} \tag{2-33}$$

$$V_{bulk\,S} = V_p - V_{Hg} \tag{2-34}$$

$$V_{Hg} = W_{Hg} / \rho_{Hg} \tag{2-35}$$

$$\varphi = \left(1 - \frac{\rho_{bulk}}{\rho_{skelton}}\right) \times 100\% \tag{2-36}$$

Where, ρ_{bulk} is the bulk density of the sample; W_s is the weight of the sample; $V_{bulk\,S}$ is the bulk volume of sample; V_p is the volume of the empty penetrometer; V_{Hg} is the volume occupied by the mercury; W_{Hg} is the weight of the mercury; ρ_{Hg} is the mercury density; $\rho_{skelton}$ is the skeletal density of the sample (from helium pycnometry).

2.5.3.2 Experimental procedure

A Micromeritics Autopore IV Series Automated Mercury Porosimeter equipment was used to obtain the bulk density and the porosity of shale samples. 2 g initial shale particles (2-4 mm) (for PSD) and bulk shales (for the bulk density and porosity) were vacuumed dry at a temperature of 120 °C for 48 hours in a vacuum oven (<0.5 mbar), and loaded into the pre-weighed clean solid penetrometer with a 5 cm^3 bulb and 0.392 cm^3 stem volume, then sealed, lubricated, and weighed again to gain a combined weight of the penetrometer and the shale. The intrusion of mercury was recorded from 0 to 4137 bar (0 to 60000 psia). The penetrometer was vacuumed for 30 minutes and filled with mercury first. Then, the low-

pressure mercury intrusion stage starts with the pressure rising from 0.5 to 1.38 bar (20 psia). After that, the penetrometer is then placed onto the high-pressure analysis port. Pressure is increased from 1.38 bar (20 psia) to 4137 bar (60000 psia) in incremental steps and subsequently reduced to 1.03 bar (15 psia), with 30 seconds as the pressure equilibration time. During the whole process, the pressure and volume changes are measured, which can form isotherms. The MIP can provide a wide pore size measure range from 2-4 nm to 400 μm, depending on the form of the Washburn equation used. Correction methods were applied by running a blank penetrometer to remove any intrusion seen from the penetrometer itself (Malik, Smith et al. 2016). The volume of mercury entering the shale pores at a given pressure can be converted to pore volume and size using the Washburn equation (Equation 2-32) for slit/angular-shaped pores. A contact angle of 151.5° for intrusion and extrusion of mercury and surface tension of 475.5 mN/m for mercury intrusion and extrusion in shale was used (Wang, Javadpour et al. 2016).

2.6 Molecular simulation

2.6.1 The principle

2.6.1.1 Grand canonical Monte Carlo (GCMC) and Molecular Dynamics (MD) simulation

Molecular simulation is a microcosmic theoretical approach to studying the structure and properties of molecular systems by computer simulations (Frenkel and Smit 2001, Sadus 2002). In contrast to quantum chemistry, the detailed electronic structure of each molecule is not considered in such simulations (Ungerer, Lachet et al. 2006). It is based on the assumption that classical mechanics can be used to describe the motions of atoms and molecules, including Grand canonical Monte Carlo (GCMC) and Molecular Dynamics (MD) simulations (Frenkel and Smit 2001, Dubbeldam, Torres-Knoop et al. 2013).

The GCMC method is a stochastic strategy that relies on probabilities and addresses equilibrium properties through the statistic method (Sadus 2002, Ungerer, Lachet et al. 2006). It is widely applied in simulation research to predict the gas adsorption isotherms (Mosher, He et al. 2013, Collell, Galliero et al. 2014, Fan, Tang et al. 2014, Sharma, Namsani et al. 2015, Li, Pang et al. 2019). In GCMC simulation, transitions between different configurations are achieved by (1) generating a trial configuration randomly, (2) evaluating an ‘acceptance

criterion' by calculating the change in energy and other properties in the trial configuration, and (C) comparing the 'acceptance criterion' to another random configuration, and (D) accepting or rejecting the trial configuration. A new configuration is generated typically by displacing, exchanging, removing, or adding a molecule, which will only be accepted if it is more 'favourable' than the existing state. If the attempted change is rejected, then the old state is counted as the new state (Sadus 2002).

In contrast, MD simulations generate a new configuration by applying Newton's equations on the motion of the molecules (Frenkel and Smit 2001, Sadus 2002). The basic principle of MD simulation is using potential functions as a force field to express the interactions between molecules, getting the force of each molecule to simulate the movement of micro-particles, and then getting the macroscopic properties of the whole system (Frenkel and Smit 2001, Dubbeldam, Torres-Knoop et al. 2013). MD simulation can analyze the physical movements of atoms and molecules, while the trajectories of atoms and molecules can be determined numerically by solving Newton's equations of interacting particles (Ungerer, Lachet et al. 2006).

Progress has been made on methane adsorption in shale achieved by GCMC and MD methods (Liu and Wilcox 2010, Mosher, He et al. 2013, Fan, Tang et al. 2014, Sharma, Namsani et al. 2015, Huang, Ning et al. 2018). GCMC is an effective method to study the gas adsorption capacity, while MD simulation can get the gas adsorption behaviours for analyzing the adsorption mechanism (Collell, Galliero et al. 2014, Huang, Ning et al. 2018, Li, Pang et al. 2019).

2.6.1.2 Force field

Force-field is a set of empirical functions used to describe the interatomic interactions in molecular systems. It works at the atomic level, ignoring the details of electron-electron and electron-nucleon interactions (Sun 1998, Frenkel and Smit 2001, Sadus 2002). The parameters for the energy functions could be derived from experiments in physics and chemistry, calculations in quantum mechanics, or both (Sun 1998). Various force fields are developed with different applications and limitations, and the reliability of simulation results is closely related to the force field. The Universal force field (Uff), the polymer consistent force field (pcff), consistent-valence force field (cvff), Condensed-phase Optimized Molecular Potentials

for Atomistic Simulation Studies (COMPASS) force fields are the typical force fields applied (Mayo, Olafson et al. 1990, Rappé, Casewit et al. 1992, Sun 1998, Lille 2004). Uff is the general-purpose force field that covers all elements on the periodic table, with simple calculation functions and generic parameters (Rappé, Casewit et al. 1992). Two force fields, pcff and COMPASS, are the consistent force fields developed to obtain a higher accuracy for particular systems. All the consistent force fields apply the same calculation functions but with different parameters. The cvff, is a generalized valence force field, widely used for the system with larger organic molecules, such as proteins (Dauber‐Osguthorpe, Roberts et al. 1988, Gaedt and Höltje 1998, Sun 1998). COMPASS is selected for the force field in this research, as it has broad coverage in covalent molecules, including most common organics, small inorganic molecules, and polymers. COMPASS enables accurate and simultaneous prediction of gas-phase properties and condensed phase properties (equation of state, cohesive energies, and so on) for a broad range of molecules and polymers. It is also the first high-quality force field to consolidate parameters of organic and inorganic materials (Sun 1998, Sun, Ren et al. 1998). Although there are different functions forms and parameters in these force fields, the potential energy types for interactions are consistent. As Equation 2-37 shows, the total potential energy (E_{total}) of a system can be expressed as a sum of bond (E_{bond}), the cross term ($E_{Crossterm}$), and non-bond interactions ($E_{non-bond}$).

The bond energy is presented as Equation 2-38 (Figure 2-19 A), including the bond angle bending, bond stretching, dihedral angle torsion, and inversion energy. The cross term energy is considered for higher accuracy, and it includes the following: stretch-stretch, stretch-bend-stretch, bend-bend, torsion-stretch, torsion-bend-bend, bend-torsion-bend, and stretch-torsion-stretch. The non-bond energy (Equation 2-39) includes Van der Waals energy (E_{Van}), Coulomb energy ($E_{coulomb}$) and hydrogen bond energy (E_H) (Figure 2-19 B). In COMPASS force field, van der Waals (vdW) force is expressed by LJ-9–6 function (Equation 2-40), the electrostatic force is calculated by the Coulombic equation (Equation 2-41), and hydrogen bond impact is considered in the above forces.

$$E_{total} = E_{bond} + E_{Crossterm} + E_{non-bond} \quad (2\text{-}37)$$

$$E_{bond} = E_{bond\ stretching} + E_{angle} + E_{torsion} + E_{inversion} \quad (2\text{-}38)$$

$$E_{nonbond} = E_{van} + E_{coulomb} + E_H \quad (2\text{-}39)$$

$$E_{van} = \mathrm{D}_0 \left[2 \cdot \left(\frac{R_0}{R_{ij}} \right)^9 - 3 \cdot \left(\frac{R_0}{R_{ij}} \right)^6 \right] \quad (2\text{-}40)$$

$$E_{coulomb} = \sum ij \, \frac{q_i q_j}{R_{ij}} \quad (2\text{-}41)$$

Where, E_{bond} is the bond force, E_{angle} is the bond angle bending energy, $E_{bond\ stretching}$ is bond stretching energy, $E_{torsion}$ is the dihedral angle torsion energy, $E_{inversion}$ is inversion energy, also called out-of-plane interactions terms, which are part of nearly all forcefields for covalent systems energy. $E_{nonbond}$ is the non-bond energy, E_{Van} is the van der Waals force, $E_{coulomb}$ is the Coulomb force, E_H is the hydrogen bond energy, R_{ij} is the distance between the atoms i and j, D_0 is the equilibrium L-J well depth, R_0 is the equilibrium distance, q_i , q_j are the charges of the atoms (i and j) in the system.

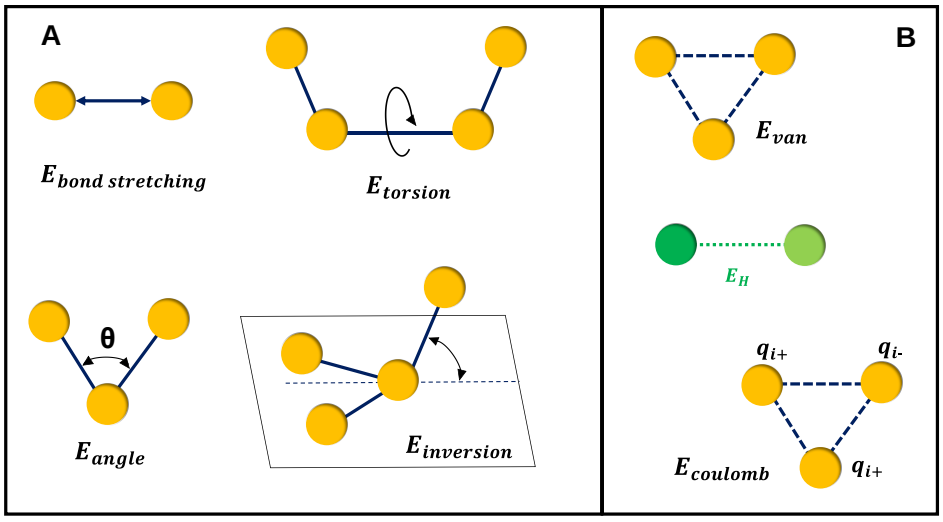

Figure 2-19. The schematic of potential energy in molecular systems, A) is the bonds energies, including bond angle bending, bond stretching, dihedral angle torsion, and inversion energy. B) is the non-bonds energies, including the Van der Waals energy, Coulomb energy, and hydrogen bond energy.

2.6.1.3 Statistical ensemble

The statistical ensemble is introduced by statistical methods to describe the statistical regularity of thermodynamic systems, which are set to control the equilibrium conditions of particles. It is defined as a collection of various states of the system which contain different positions and the velocities of the particles in the molecular dynamics simulation (Frenkel and Smit 2001, Ungerer, Lachet et al. 2006). According to the conditions and states of the system, the statistical ensemble is normally divided into the micro-canonical ensemble (NVE),

canonical ensemble (NVT), macro-canonical ensemble (mVT), and isothermal-isobaric ensemble (NPT) (Frenkel and Smit 2001, Ungerer, Lachet et al. 2006). The N, V, T, P, m, and E indicate the particle number (N), global volume (V), temperature (T), pressure (P), chemical potential (m) and energy (E). The NVT is applied for a system at imposed volume and temperature, where the number of particles (N) and the global volume (V) is identical for all system states belonging to the ensemble, but the total energy is a fluctuating variably in this ensemble. The imposed/constant temperature does not mean that every system state is at temperature (T), but that the energies of the system states are displaying a specific distribution (Ungerer, Lachet et al. 2006). The other ensembles are defined similar way. When T is fixed, the energy fluctuates. When P is fixed, the volume fluctuates. When the chemical potential (m) is fixed, the molecules' corresponding number (N) fluctuates. The N, V, and E in the NVE ensemble are constant, adopted when the simulation is in an environment without heat exchange. The heat exchange and particle exchange can be carried out in mVT, as it is an open system, as the m, V, and T of each sample in the system remain unchanged, with the energy (E) and particle number (N) are variable. The N, P, and T remain constant in the NPT system, in which the system volume can change based on the T, P conditions. The NPT and NVT are the more common ensemble applied in the simulation for gas adsorption in kerogen (Jin and Firoozabadi 2014, Sui and Yao 2016, Zhang and Cao 2016, Li, Pang et al. 2019). The control of temperature is carried out by controlling the particle's velocity.

2.6.2 The procedures for molecular simulation

2.6.2.1 Simulation setup

Molecular simulations were carried out by BIOVIA Materials Studio software. Kerogen molecule unit and force field are the essential input data for initialising simulation. The pore texture of isolated kerogen from the experiment is used for constructing kerogen models. And other information like temperature, pressure and moisture contents from experiments are the input data for setting up the simulation conditions. The all-atom COMPASS force field (Sun 1998) is selected as the force field used in this research. It is a widely used high-quality force field to consolidate parameters of organic materials in kerogen research (Sui and Yao 2016, Huang, Ning et al. 2018, Gong, Shi et al. 2020). The force field of each atom was checked

before simulation to ensure the appropriate force field was assigned correctly based on the molecule structure.

The COMPASS force field includes the bonded and non-boned interactions. The bond energy is shown in Equation 2-38. The van der Waals (vdW) force and the electrostatic force in the non-bond interactions between pairs of atoms are expressed by LJ-9–6 function (Equation 2-40) and the Coulombic function (Equation 2-41) as stated above. The temperature and the pressure are, respectively, controlled by the Nosé−Hoover thermostat and barostat (Nosé and Klein 1983, Nosé 1984, Nosé 1984, Hoover 1986). The summation method of vdW and electrostatic forces are atom-based and Ewald (Frenkel and Smit 2001, Tesson and Firoozabadi 2019), with a cut-off distance of 1.55 nm. It is worth noting that the dissolved methane in water, as well as the swelling of kerogen, is not considered in this simulation study due to their limited effect (Van Bergen, Spiers et al. 2009, Wang, Su et al. 2018).

2.6.2.2 Kerogen model construction

Type II kerogen molecular units used in this study were developed by Ungerer (Ungerer, Collell et al. 2015) based on the elemental and functional analysis data of kerogen (Kelemen, Afeworki et al. 2007). Figure 2-20 A, B, C, and D show the immature (KIIA), early mature (beginning of the oil window) (KIIB), middle-late mature (middle to end of the oil window) (KIIC), and overmature (gas window) (KIID) kerogen, with chemical formulas of $C_{252}H_{294}O_{24}N_6S_3$, $C_{234}H_{263}O_{14}N_5S_2$, $C_{242}H_{219}O_{13}N_5S_2$, and $C_{175}H_{102}O_9N_4S_2$, respectively. The four thermal maturity stages used to construct the molecules are in Figure 2-20 E on a van Krevelen diagram.

Kerogen matrix and slit models are constructed based on the kerogen molecular units (Figure 2-20) after a series of molecular dynamic (MD) simulations using the BIOVIA Materials Studio software. The basic procedure starts from a low-density configuration. It is compressed under typical reservoir conditions (Collell, Ungerer et al. 2014, Huang, Ning et al. 2018), the pressure and temperature of which are more than 600 bar and 100 °C for the three isolated kerogens considering their burial depth (3113-4119 m), and the average geothermal and pressure gradients (Tang, Ripepi et al. 2016, Li, Zhou et al. 2018, Li, Stevens et al. 2021).

Initial kerogen models (KIIA, KIIB, KIIC, and KIID) with a low density of 0.1 g/cm^3 were constructed by 10-13 pre-optimized kerogen units (Figure 2-20 F), the number of which is

determined to guarantee 1) a similar system size (final kerogen cell size is 3.85, 3.70, 3.68, and 3.52 nm) bigger than twice of cut-off distance (3.10 nm), and 2) computational workload (Huang, Ning et al. 2018). Geometry optimisation was applied to find the local minimal energy structure. In addition, a relaxation time of 1 ns from 500 to 100 °C with the NVT ensemble (0.5 ns) and NPT ensemble (0.5 ns) was conducted for obtaining the global minimum energy structure. After that, a total of 1.5 ns dynamic simulation was carried out with the NPT ensemble for equilibration (1 ns) and production (0.5 ns) to obtain the final stable condensed kerogen matrix model (Figure 2-20 G). The total 2.5 ns dynamic simulation time is sufficient to reach equilibration, as the convergence and equilibration of density are reached (Figure 2-20 H). The final kerogen matrix models have a cell size bigger than twice the cut-off distance (3.1 nm), with periodic boundary conditions in X, Y, and Z directions.

Kerogen slit models with pore sizes (width) of 0.5±0.2, 1.0±0.2, 1.5±0.2, and 2.0±0.2 nm were constructed for KIID (Figure 2-20 I). The slit pores are over the range of ±0.2 nm of the stated width due to the unevenness of the kerogen molecules (Figure 2-20). The molecular simulation includes uncertainty from the simulated software or/and the initial setting for each simulation (such as the velocity, direction, and location of particles). To reduce the uncertainty (Huang, Ning et al. 2018), the above kerogen models are built in triplicate, and the simulation results of these models are averaged to represent more 'realistic' results. Kerogen matrix and slit models with different moisture contents (0, 0.6, 1.2, 2.4, 3.6, 6, 9, 12, 15, 18, 21, 24, 27, 30, 36 and 42 wt.%TOC) are constructed by water adsorption to obtain the moist ('moist' is used for kerogens in simulation, to distinguish from 'wet' for the isolated kerogens used experimentally). The kerogen models are built in triplicate, and the average simulation data of the triplicated models are applied to represent the authentic results.

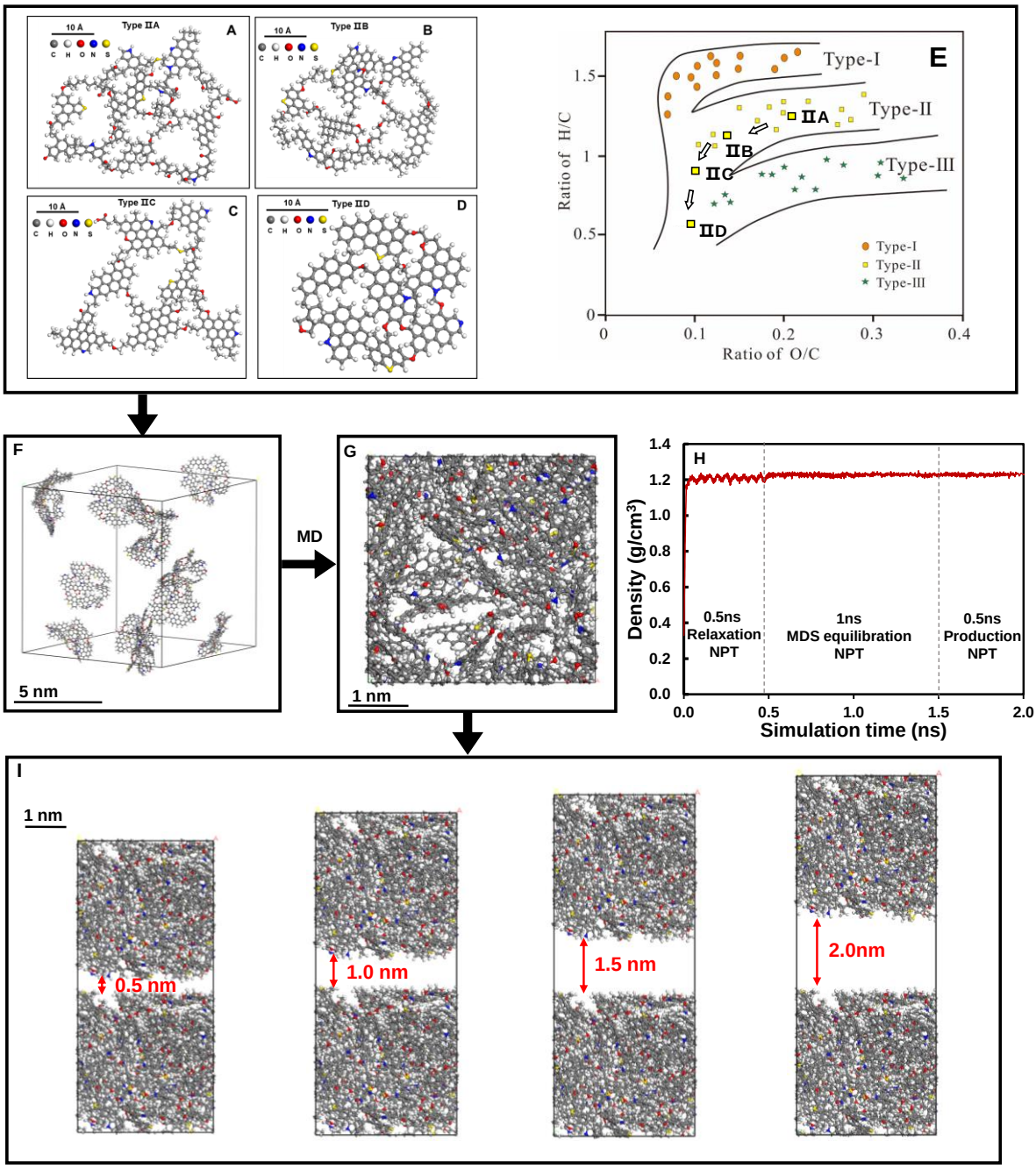

Figure 2-20. A) The immature kerogen molecular unit (KIIA), $C_{252}H_{294}O_{24}N_6S_3$; B) The early-mature (at the beginning of the oil window) kerogen molecular unit (KIIB), $C_{234}H_{263}O_{14}N_5S_2$; C) The middle-late mature (at middle to end of oil window stage) kerogen molecular unit (KIIC), $C_{242}H_{219}O_{13}N_5S_2$; D) The overmature kerogen molecular unit (KIID), $C_{175}H_{102}O_9N_4S_2$; E) The maturity stages of different kerogen units in Van Krevelen diagram. Modified from (Ungerer, Collell et al. 2015) and (Kelemen, Afeworki et al. 2007); F) The KIID low density relaxed kerogen model; G) The KIID final condensed kerogen matrix model; H) The density variation of KIID kerogen in dynamic simulation with NPT ensemble, I) the KIID kerogen slit pore models.

2.6.2.3 GCMC for methane adsorption

The GCMC method was used to simulate the methane adsorption in the kerogen dry and moist matrix and slit models. A total of 2×10^7 Monte Carlo steps was performed at each pressure step to obtain the methane adsorption isotherms, with the first 1×10^7 Monte Carlo steps used for equilibration and relaxation, and the last 1×10^7 Monte Carlo steps used for producing the adsorption amount. The fugacity in GCMC is converted to pressure with the fugacity coefficient (Equation 2-42), which is calculated by Equation (2-43) and (2-44), with the relation between pressure (P) and molar volume (V_m) in Equation (2-44) calculated by the Peng-Robinson equation (Equation 2-45). The other parameters in Peng-Robinson equation are calculated by Equations (2-46), (2-47), (2-48), and (2-49) (Mathias and Copeman 1983, Huang, Ning et al. 2018). The maximum simulation pressure was set at 300 bar, which is enough for isotherms to approach equilibrium. The equilibrium absolute adsorption methane amount (Qm) from the simulation was fitted and predicted by the dual-site Langmuir model (Equation 2-15) (Tang, Ripepi et al. 2016), which is the same model applied for the experimental laboratory data. The methane adsorption was simulated at two temperatures for the kerogen matrices, 25 and 100 °C. For the slit models, GCMC is applied at 25 °C for comparison with experimental data. The water adsorption (for constructing moist kerogen models) in simulated dry kerogen are obtained by the GCMC method with same parameter used for methane adsorption in GCMC.

$$\varphi = \frac{\mathrm{F}}{\mathrm{P}} \tag{2-42}$$

$$\ln\varphi = \ln\left(\frac{\mathrm{F}}{\mathrm{P}}\right) = \frac{1}{RT}\cdot\int_0^{P_r}\left(V_m - V_m^{ideal}\right)dP_r = \int_0^{P_r}\left(\frac{Z-1}{P_r}\right)dP_r \tag{2-43}$$

$$\mathrm{Z} = \frac{\mathrm{P}\cdot V_m}{\mathrm{R}\cdot\mathrm{T}} \tag{2-44}$$

$$\mathrm{P} = \frac{\mathrm{R}\cdot T}{V_m - b} - \frac{a\cdot\alpha}{V_m^2 + 2\cdot b\cdot V_m - b^2} \tag{2-45}$$

$$a = 0.457235\cdot\frac{(R\cdot T_c)^2}{P_c} \tag{2-46}$$

$$b = 0.077796\cdot\frac{R\cdot T_c}{P_c} \tag{2-47}$$

$$\alpha = (1 + k\cdot(1 - T_r^{0.5}))^2 \tag{2-48}$$

$$k = 0.37464 + 1.54226\cdot\omega - 0.26992\cdot\omega^2 \tag{2-49}$$

Where, φ is the fugacity coefficient; F is the fugacity; P is the pressure; V_m is the molar volume; V_m^{ideal} is the ideal molar volume; R is the universal gas constant; T is the

temperature; a is the attraction parameter; b is the van der Waals covolume; α is the scaling factor; k is the characteristic constant; P_c is the critical pressure for the component of interest; T_c is the critical temperature for the component of interest; P_r and T_r are the pressure and temperature other than the critical ones; ω is the acentric factor for the component of interest.

The heat of adsorption is a good indicator of the strength of the interaction between methane molecules and the kerogen model. It can be obtained by the Clausius Chapeyron equation (Equation 2-50) (Pan, Ritter et al. 1998, Builes, Sandler et al. 2013).

$$H_{ad} = RT^2 \left(\frac{\partial \ln P}{\partial T}\right)_Q \tag{2-50}$$

Where, H_{ad} is the adsorption heat at the absolute adsorption amount of Q; R is the universal gas constant; Q is the absolute adsorbed methane amount; P is the pressure; T is the temperature.

2.6.2.4 Probe measurement for pore volume

The micropore volume in the simulation is measured by the dummy Connolly probes, the diameter of which can vary (Figure 2-21). The measured surface of a solid (Figure 2-21 B) can be defined as 1) van der Waals surface formed by the outer part of the van der Waals spheres of the surface atoms, 2) Connolly surface, which is probe accessible surface and known in simulation studies. 3) The R-distance surface, which is located at a distance of R from the Connolly surface (Thommes, Kaneko et al. 2015). A given-sized probe molecule is randomly inserted into the kerogen model and then rolled over the van der Waals surface (Figure 2-21 B1) to obtain the probe-Connolly surface (Figure 2-21 B2), and the regions wrapped by the detected surface (Connolly surface) are identified as the free pore volumes in this simulation. (Connolly 1983, Thommes, Kaneko et al. 2015, Huang, Ning et al. 2018). In this simulation, the micropore size distribution (MPSD) of kerogen models is obtained by the micropore volume measured by dummy probes with different diameters (d) from 0.10 to 2.0 nm. The dummy probes with various diameters can be compared with the gas molecules having the same kinetic diameter, like d=0.26 nm for Helium (He), d=0.33 nm for carbon dioxide (CO_2), d=0.36 nm for Nitrogen (N_2), and d=0.38 nm for methane (CH_4) molecule (Aguilar-Armenta, Patiño-Iglesias et al. 2003, Ismail, Khulbe et al. 2015, Tesson and Firoozabadi 2019). The micropore volume (V_{micro}) for dry simulation kerogen is measured by 0.33 nm (CO_2) probe, and for moist

kerogen is measured by 0.36 nm (N_2) probe, which are used to compare with the results of dry and wet isolated kerogen measured by low-pressure CO_2 and N_2 adsorption through the NLDFT model (Section 2.4.3).

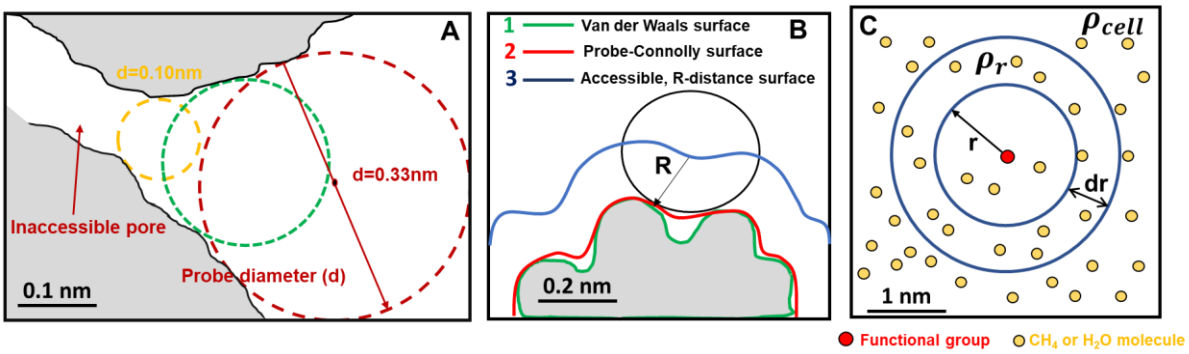

Figure 2-21. A) Schematic diagram of pore volume measurement by different probes, the probe diameters (d) range from 0.10 to 2.0 nm in this study, B) diagram of van der Waals (1), Connolly probe accessible (2), and the accessible, R-distance (3) surfaces of an adsorbent (modified from (Thommes, 2015) (Thommes, Kaneko et al. 2015)), C) diagram depicting methane or water molecules around a functional group for calculating relative number density and coordination number.

2.6.2.5 Molecular dynamic simulation

MD simulation can reveal the behaviour and mechanism of methane adsorption in kerogen. A relaxed kerogen matrix with low density (0.1 g/cm^3) was used for the selectivity analysis of methane and water on different functional groups to eliminate the impact of matrix pore structure. Different amounts (5, 10, 25, 50, 75, 100, 150, 200, 250, 300) of methane and water molecules are loaded on a relaxed kerogen matrix first before MD simulation. The number of methane and water molecules from 5 to 300 is used to represent the density and pressure changes for methane (0.0002-0.0124 g/cm^3, 0.3-18.5 bar at 25 °C, 0.4-23.6 bar at 100 °C) (Figure 2-22 A) and different moisture contents (0.3, 0.7, 1.7, 3.3, 5.0, 6.6, 10, 13, 17 and 20 wt.% TOC) (Figure 2-22 B) in kerogen models. A total of a 2.0 ns MD simulation with NVT ensemble was applied at 25 °C and 100 °C. The simulated results of the last 1.0 ns were used after the simulation had stabilized. The relative number density ($g(r)$) of methane/water around a specific functional group and the relative coordination number (C_r) are obtained after dynamic analysis by Equations 2-51 and 2-52, which are good indicators for the affinity of methane and water with the function group.

$$g(r) = \frac{\rho_r}{\rho_{cell}} = \frac{\frac{dN}{4\pi r^2 dr}}{\frac{N}{V_{cell}}} \quad (2\text{-}51)$$

$$C_r = \frac{\sum dN}{N} = \frac{g(r)\cdot 4\pi r^2 dr}{V_{cell}} \quad (2\text{-}52)$$

Where, $g(r)$ is the relative number density, ρ_r is the number density of methane/water around the particular functional group, ρ_{cell} is the number density of methane/water in the simulation cell, dN is the amount of methane/water around the functional group when the measured distance is r with the measured thickness of dr (Figure 2-21 C), N is the number density of methane/water in the cell, V_{cell} is the volume of the cell, C_r is the relative coordination number.

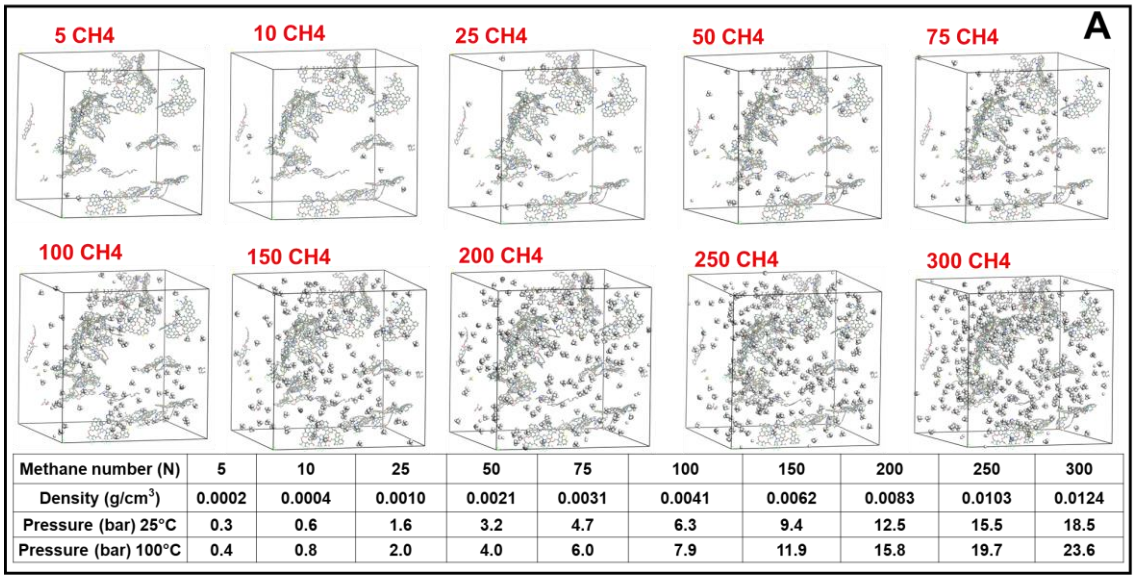

Methane number (N)	5	10	25	50	75	100	150	200	250	300
Density (g/cm^3)	0.0002	0.0004	0.0010	0.0021	0.0031	0.0041	0.0062	0.0083	0.0103	0.0124
Pressure (bar) 25°C	0.3	0.6	1.6	3.2	4.7	6.3	9.4	12.5	15.5	18.5
Pressure (bar) 100°C	0.4	0.8	2.0	4.0	6.0	7.9	11.9	15.8	19.7	23.6

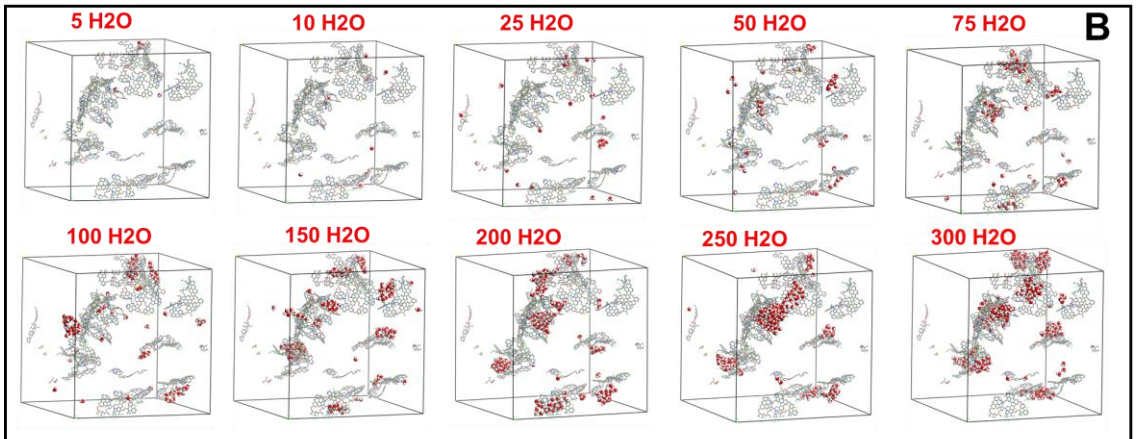

Water number (N)	5	10	25	50	75	100	150	200	250	300
Moisture content (wt.% TOC)	0.3	0.7	1.7	3.3	5.0	6.6	10	13	17	20

Figure 2-22. KIID relaxed kerogen matrix with methane (A) and water (B) molecules after dynamic simulation at 25°C.

CHAPTER 3 COMPARISON OF THE IMPACT OF MOISTURE ON METHANE ADSORPTION AND NANOPOROSITY FOR OVER MATURE SHALES AND THEIR KEROGENS.

3.1 Summary

Moisture in shales under reservoir conditions adversely affects gas adsorption and nanoporosity and is also likely to impact on the contribution that kerogen makes to the methane adsorption capacity. To investigate these phenomena, two over mature shales from the Wufeng-Longmaxi Formation, south of Sichuan basin, and their kerogens isolated by demineralisation were investigated at dry and 95% relative humidity (R.H.) by high-pressure methane adsorption, and low-pressure nitrogen (N_2) and carbon dioxide (CO_2) sorption. The kerogen concentrates account for 59-83% and 42-67% of the methane adsorption capacities for the shales dry and at 95% R.H. respectively. However, the isolated kerogens could adsorb more methane than the organic matter in the shales because their shallower adsorption isotherms indicate large micropores and small mesopores not evident for the shales. Methane adsorption capacities of the kerogens and shales reduced by 50-75% at 95% R.H.. This compares with the reductions in surface area (SA) and pore volume of 81-82% and 48-59%, respectively, for the kerogens and 98-99% for both SA and pore volume of the shales at 95% R.H.. Water can block most micropores less than 1.3 nm, reducing the micropores volume and blocking the micropore necks connecting the larger pores, and vastly reducing accessible pores for gas transport. The greater proportional losses in SA and pore volume compared to the methane adsorption capacities is probably due to ice forming at -196 °C in the low-pressure N_2 analysis. Failure to take moisture into account for free and adsorbed methane overestimates the total gas in place (GIP) by 32-38% for the shales investigated.

3.2 Literature review

Shale gas is stored in adsorbed, free and dissolved states and it is often estimated from the sum of the adsorbed and free gas in the pores (Curtis 2002, Jarvie, Hill et al. 2007, Ross and Bustin 2008, Rexer, Mathia et al. 2014, Chen, Jiang et al. 2017). The adsorbed gas can be significant under reservoir conditions, estimated as 20-85% of the total gas in organic-rich shales (Curtis 2002, Ross and Bustin 2008, Adesida, Akkutlu et al. 2011, Heller and Zoback

2014). Kerogen, the organic matter insoluble in alkali, non-oxidizing acids and organic solvents in shales (Hunt 1979, Durand 1980), is considered to store much of the gas since methane adsorption capacity of shale generally increases with increasing total organic content (TOC) (Ross and Bustin 2009, Zhang, Ellis et al. 2012, Gasparik, Bertier et al. 2014). In addition to the kerogen, the major minerals in shales including quartz, clays and calcite are also believed to provide porosity for shale gas to adsorb in different extents (Ross and Bustin 2009, Gasparik, Ghanizadeh et al. 2012, Loucks, Reed et al. 2012, Gasparik, Bertier et al. 2014, Ma, Fauchille et al. 2017, Peng, Milliken et al. 2019, Peng, Milliken et al. 2020). Gasparik (2012) reported no correlation between TOC and dry adsorption capacity for some shales, suggesting that the sorption capacities of the minerals can be significant.

To investigate methane adsorption on isolated kerogens, Hu (2014) chose two kerogens of different maturity (vitrinite reflectance (VR) of 0.58 and 2.01% Ro), and found that the more mature kerogen had a much higher adsorption capacity. Methane adsorption experiments on organic-rich shales and their isolated kerogens were conducted at different temperatures under dry conditions to study the impact of different parameters on gas adsorption but not including moisture (Zhang, Ellis et al. 2012, Rexer, Mathia et al. 2014, Li, Zhou et al. 2018). Fan (2014) found that 43-57% of the methane adsorption in dry shales was accounted for by the kerogen, confirming that kerogen has a much larger methane adsorption capacity than minerals. Rexer et al (2014) compared kerogen and shale using low-pressure nitrogen (N_2) and carbon dioxide (CO_2) and high-pressure methane isotherms and identified that the vast majority sorption of methane occurs in the pores less than 6 nm, and kerogen accounts for about 50% total measured adsorbed methane in dry shales investigated. Although these studies confirm that kerogen accounts for much of the methane adsorption capacity in shale, the impact of moisture present has not been addressed.

Moisture always exists under reservoirs conditions and has a profound negative influence on gas adsorption capacity (Ji, Zhang et al. 2012, Heller and Zoback 2014, Jin and Firoozabadi 2014, Zolfaghari, Dehghanpour et al. 2017). Some studies have addressed the impact of moisture on methane adsorption for shales and coals (Joubert, Grein et al. 1973, Ross and Bustin 2007, Gasparik, Bertier et al. 2014, Zou, Rezaee et al. 2018, Whitelaw, Uguna et al. 2019). Joubert (1973) found methane adsorption capacity for coals decreased with increasing humidity, although there was a 'critical value' of moisture above which no change in

adsorption capacity occurred. High critical values were thought to relate to high coal oxygen contents since there is a strong interaction between the polar water molecule and the surface oxygen complexes (Joubert, Grein et al. 1973, Day, Sakurovs et al. 2008). The critical moisture content of shale is approximately 75% R.H. (Gasparik, Bertier et al. 2014). Ross and Bustin (2007) compared the isotherms of dry shales with moisture equilibrated shales from the Lower Jurassic Gordondale Member and showed that methane adsorbed in dry shales (0.5–4.0 cm^3/g) were much larger than that in moisture equilibrated shales (0.1–1.6 cm^3/g). Reductions of 20-85% in methane adsorption capacities have also been reported by Merkel (2016) and Whitelaw et al (2019) at high R.H., the latter finding that moisture reduced pore volume by over 90%. In contrast, Zou (2018) reported much smaller reductions of less than 20% in methane adsorption capacity and 30% in pore volume because their degassing of the 84% R.H. shales and standardised pre-evacuation procedures for the low and high-pressure instruments is likely to have removed any free and weakly adsorbed water, resulting in the moisture being considerably less than 84% R.H. when the experiments started. Moisture adsorbed on hydrophilic clay minerals is considered to be main reason for the decreasing methane adsorption in a number of studies (Liming, Junli et al. 2012, Heller and Zoback 2014, Jin and Firoozabadi 2014, Zolfaghari, Dehghanpour et al. 2017, Zou, Rezaee et al. 2018).

Methane adsorption in shale and kerogen is clearly related to pore structure, mainly pore surface area (Liming, Junli et al. 2012, Rexer, Mathia et al. 2014, Li, Pang et al. 2019). Molecular simulation was used to study the impact of different pore sizes on methane adsorption and other gases (e.g. CO_2, N_2) in kerogen (Xiong, Liu et al. 2017, Huang, Ning et al. 2018, Zhao, Li et al. 2018). In addition to molecular simulation, some experimental studies on kerogens have focused on methane adsorption, but without investigating the pore size distribution (PSD) (Zhang, Ellis et al. 2012, Fan, Tang et al. 2014, Hu 2014, Li, Zhou et al. 2018, Pang, Tian et al. 2019). Other studies have only addressed pore characterization without considering methane adsorption (Adesida, Akkutlu et al. 2011, Chen, Hu et al. 2013, Cao, Song et al. 2015, Ji, Song et al. 2017, Wang, Tian et al. 2018). Only a few studies (Rexer, Mathia et al. 2014, Xiong, Liu et al. 2017) have investigated both methane adsorption and pore structure but only under dry conditions.

This is the first to relate methane adsorption capacities and pore characteristics of shales and their isolated kerogens, both dry and equilibrated at 95% R.H., and to compare the impact of

moisture on methane adsorption capacity and nanoporosity for kerogens and shales. Furthermore, this research provides new guidance on accounting for moisture to estimate gas in place (GIP) for shales. This is often estimated from the total amount of free gas obtained from the total porosity and adsorbed gas content measured from methane adsorption (Tang, Ripepi et al. 2016, Li, Zhou et al. 2018). GIP based on the accessible pore volume and methane adsorption of dry shales without taking moisture into account is overestimated (Tang, Ripepi et al. 2016, Li, Zhou et al. 2018), since moisture exists in shale reservoirs (Feng, Li et al. 2018) (Loucks and Ruppel 2007, Merkel, Fink et al. 2015).

3.3 Experiments and Methods

Two China shale samples, SH1 and SH2 (Section 2.1, Figure 2-1) were selected for kerogen isolation by method in Section 2.2.1. Dry and moisture-equilibrated kerogen concentrates and shales were prepared (by method in Section 2.2.3) for the high-pressure methane adsorption (2.4.2), low-pressure gas sorption (2.4.3), and Helium pycnometry (2.3.4) for the methane adsorption capacity, pore texture, and skeletal density. Dry shales are prepared for the vitrinite reflectance (2.3.5), elemental analysis (2.3.3), X-ray Computed Tomography (XRCT) (2.5.2), field emission scanning electron microscopy (FE-SEM) (2.5.1.2), and mercury intrusion porosimetry (MIP) (2.5.3) to obtain the maturity, TOC, mineral composition, visible pore structure, and bulk density.

3.4 Results and discussion

3.4.1 TOC, maturity, mineral compositions, and moisture content

The TOC, maturity, compositions and physical properties of the two shales and their isolated kerogen concentrates are presented in Table 3-1. SH1 (5.1%) has a higher TOC than SH2 (2.4%). Combining the kerogen concentrate yields for SH1 and SH2 of 12.0 and 10.9 wt.%, respectively, with TOCs of 36.0 and 18.7%, indicates that the K1 and K2 account for 86% and 83% of the TOC in the SH1 and SH2, since K1 provides 4.4 wt.% TOC for SH1 (5.1 wt.%), and K2 provide 2.0 wt.% for SH2 (2.4 wt.%), indicating the demineralization process did not cause significant kerogen weight loss. The Ro of SH1 and SH2 are 2.95 and 2.58%, suggesting the shales are all thermally over matured. XRD result shows clay mineral content of SH1 (18.4%)

is much lower than SH2 (35.8%), while the quartz content of 55.4% for SH1 is higher than that of 41.7% for SH2. For the 95% R.H. moisture equilibrated samples, the kerogen concentrates adsorb much more water (15.5 and 13.0 wt.%) than the shales (1.50 and 1.22 wt.%), due to their higher SA and pore volumes. Considering the yield, the moisture content provided by K1 and K2 (1.86 and 1.42 wt.%) for shales are even higher than the moisture content of SH1 and SH2, which could in part arise from demineralisation opening inaccessible pores in the shales or the moisture may not reach all organic matter pore in shale.

Table 3-1. TOC, maturity (Ro), mineral compositions and moisture contents of the shales.

Sample Name	Moisture (Wt.%)	TOC(Wt.%)	Ro(%)	Yield (wt.%)	Mineral (%)					
					Clay	Quartz	Plagioclase	Calcite	Dolomite	Pyrite
SH1	1.48±0.14	5.1±0.1	2.95	-	18.4	55.4	3.1	4	14.9	4.1
SH2	1.22±0.10	2.4±0.1	2.58	-	35.8	41.7	6.9	4.4	6.9	4.3
K1	15.5±2.9	36.3±1.4	-	12						
K2	13.0±1.2	18.7±0.2	-	10.9						

The mean of moisture content and TOC are from triplicate experiments (2.2.3) and (2.3.3), and the errors represent the dispersion of a dataset relative to its mean.

3.4.2 Pore structure from XRCT and FE-SEM

Figure 3-1 is the XRCT 3D image of the pore network and pore distribution of SH1 and SH2. The pore in shales is varied from micro to the nanoscale, with scattered distribution to form a complex pore network. FE-SEM can observe pores larger than 100 nm in shales (Loucks, Reed et al. 2009, Zou, Dong et al. 2010, Loucks, Reed et al. 2012, Milliken, Rudnicki et al. 2013). As Figure 3-2 indicates that shale is heterogenous from composition to pore structure, there are more pores in the organic matter than the pores in the clay minerals. Figure 3-2 shows that the region of most organic matter is in the range of 5-20 µm, surrounded by minerals (Figure 3-2 A) and a large number of macropores in the organic matter (Figure 3-2 A). Intra-particle macropores in the organic matter are evident (Figure 3-2 B, C) with irregular shapes (Figure 3-2 B), with only a few pores larger than 500 nm (Figure 3-2 D). The most minerals contain inter-particle pores (Figure 3-2 C).

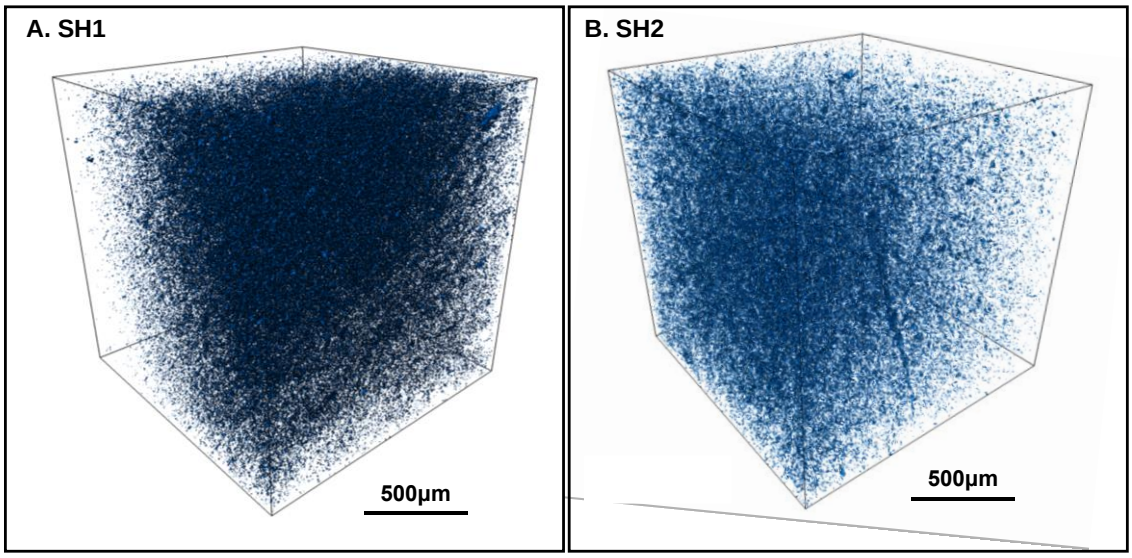

Figure 3-1. The 3D image of SH1 (A) and SH2 (B) pore network from XRCT.

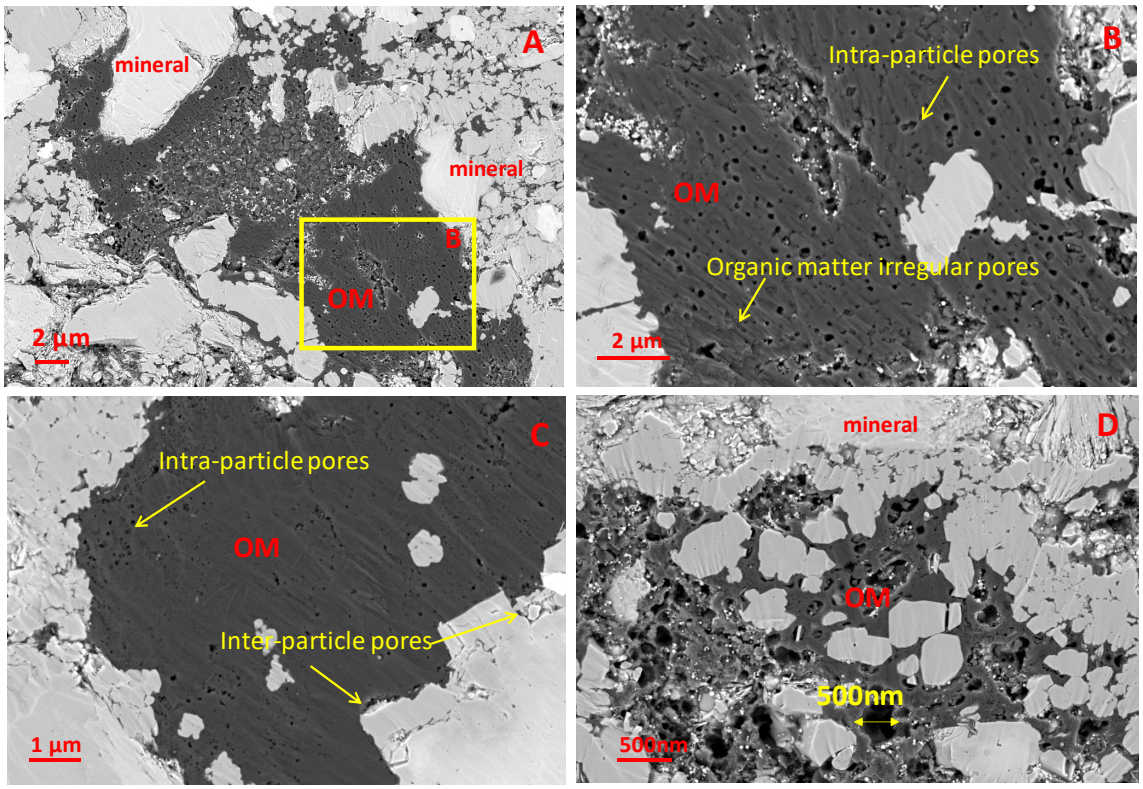

Figure 3-2. FE-SEM backscattered electron images of organic matter and macropores in shales. A) Minerals and organic matter (OM) distribution in SH2, B) is the enlarged figure of A, OM irregular pores in SH2, C) Intra-particle pores and inter-particle pores in SH1, D) The size of OM pores in SH2.

3.4.3 Methane adsorption capacities of the shales and kerogen concentrates

3.4.3.1 Moisture impact on methane adsorption capacity

Figure 3-3 indicates that the dry kerogen concentrates and shales have much higher methane adsorption capacities than their wet counterparts. Approximately 75 and 61% of the equilibrium methane adsorption capacities are lost for K1 and K2, respectively (K1 reducing from 27.3 mg/g to 6.9 mg/g, and K2 from 16.7 mg/g to 6.6 mg/g, Table 3-2). The same pattern is found for the shale samples, with approximately 50 and 66% of equilibrium methane capacities of the dry shales being lost (SH1 reducing from 4.0 mg/g to 2.0 mg/g, and SH2 from 3.1 mg/g to 1.1 mg/g wet, Table 3-2). The level of reduction for the shales is consistent with previous studies (Gasparik, Bertier et al. 2014, Merkel, Fink et al. 2016, Whitelaw, Uguna et al. 2019). A significant decrease in adsorption capacity of 40-60% was observed between the dry and moisture equilibrated shale samples studied by Gasparik et al. (2014). Merkel et al. (2016) found that Lacustrine shales lose 20-80% of initial dry adsorption capacity upon full moisture equilibration (97% R.H.). Whitelaw et al. (2019) also found that the equilibrated methane adsorption amount dropped by 27% after the shale samples were equilibrated at 50% R.H..

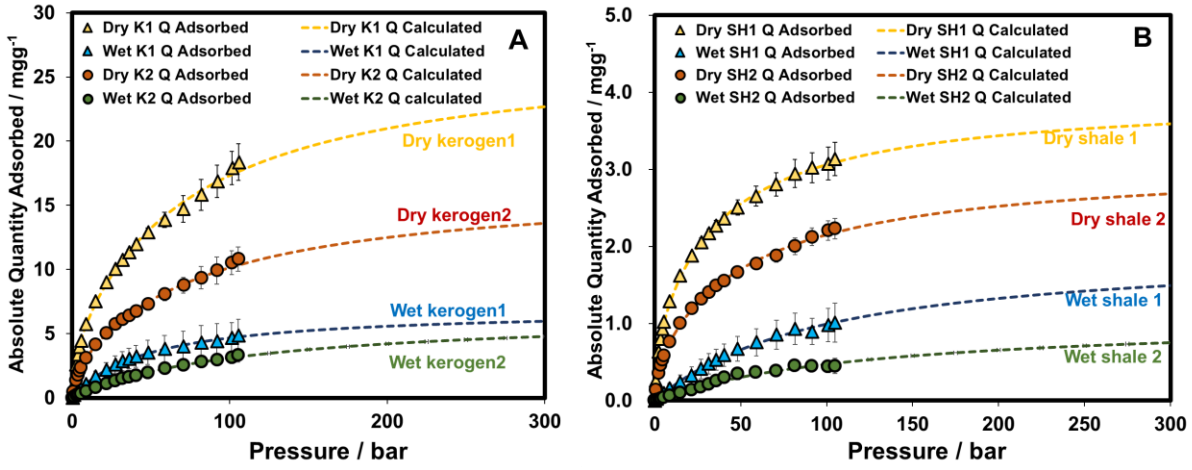

Figure 3-3. Comparison of absolute methane adsorption isotherms of dry and wet (95% R.H.) kerogen concentrates and shales at 25 °C. A) dry and wet kerogen concentrates, B) dry and wet shales. Each sample was analysed in triplicate by HPVA, the data points are the mean from triplicate experiments, and the error bars represent the dispersion of a dataset relative to its mean.

The dry shales have slightly steeper isotherms (Type Ia) than their kerogen counterparts (Type Ib) (Figure 3-3), suggesting that isolated kerogens have higher proportion of larger micropores and smaller mesopores, which can be accessed by demineralisation, as the steeper uptake at low pressure are mainly contributed by narrow micropores (<1 nm) (Thommes, Kaneko et al. 2015) . The isotherm shapes of wet samples are less steep than the dry ones (Figure 3-3), indicating higher pressure and more energy are required to adsorb the same amount. This suggests that moisture preferentially reduces adsorption on the smaller micropores as intuitively expected, by blocking the accessible micropores, occupying/changing the adsorption sites or swelling clays (for shale) and blocking the access.

3.4.3.2 Contribution of kerogen concentrates to the methane adsorption capacities of the shales

The methane adsorption capacities for the kerogen concentrates and corresponding shales are compared in Table 3-2, which lists the contributions of the kerogen concentrates made to methane adsorption capacities for the shales under dry and wet conditions. The contributions from the kerogen concentrates to the methane adsorption capacities are calculated from the yields of kerogen concentrates from shales using Equation 3-1, and these are expressed as a percentage using Equation 3-2.

$$Q_{contribution} = Y_K \times Q_K \quad (3\text{-}1)$$

$$R_K = 100\% \times (Q_{contribution}/Q_{SH}) \quad (3\text{-}2)$$

Where, $Q_{contribution}$ is the quantity of methane adsorbed by the kerogen concentrates per gram shale; Y_K is the yield of kerogen concentrate; Q_K is the methane adsorption quantity of the kerogen concentrate; R_K is the percentage that the kerogen concentrate contributes to the methane adsorption in shale; Q_{SH} is the methane adsorption quantity of shale.

As expected, Table 3-2 indicates that kerogen concentrates have greater methane adsorption capacities than shales, both under dry and wet conditions. For the dry samples, the equilibrium adsorbed methane quantity for K1 is 27.3 mg/g, which is about 7 times higher than that for the SH1 (4.0 mg/g). The equilibrium adsorbed methane quantity of K2 (16.7 mg/g) is more than 5 times higher than that of SH2 (3.1 mg/g). K1 and K2 account for 83 and 59% of the equilibrium methane uptakes for the dry shales, respectively. The high content of clay minerals in SH2 could account for kerogen concentrates (K2), contributing less on

methane adsorption under dry conditions. These contributions are higher than those of about 50% reported in other studies (Fan, Tang et al. 2014, Rexer, Mathia et al. 2014) probably because the kerogens in this research are from overmatured shales, which are likely to contain more pores for methane adsorption.

Table 3-2. Methane adsorption capacities of the kerogen concentrates and shales, and the contributions made by kerogen concentrates to the capacities of the shales.

	Dry sample 1				Dry sample 2			
Pressure (bar)	Q_{K1} (mg/g)	Q_{SH1} (mg/g)	K1-$Q_{contribution}$ (mg/g)	R_{K1} (%)	Q_{K2} (mg/g)	Q_{SH2} (mg/g)	K2-$Q_{contribution}$ (mg/g)	R_{K2} (%)
5	4.0±0.1	0.9±0.1	0.5±0.1	52±1	2.1±0.1	0.5±0.1	0.2±0.1	43±1
50	13±0.3	2.5±0.1	1.6±0.1	62±4	7.5±0.3	1.7±0.1	0.8±0.1	48±4
100	17.4±1.2	3.1±0.2	2.1±0.1	68±10	10.2±0.9	2.2±0.1	1.1±0.1	51±7
150	19.6±1.4	3.3±0.2	2.4±0.2	71±10	11.6±0.9	2.4±0.1	1.3±0.1	53±7
300	22.7±1.6	3.6±0.2	2.7±0.2	76±11	13.6±1.0	2.7±0.2	1.5±0.1	55±8
Qm	27.3±1.8	4.0±0.3	3.3±0.2	83±12	16.7±1.2	3.1±0.2	1.8±0.1	59±9
	Wet sample 1				Wet sample 2			
Pressure (bar)	Q_{K1} (mg/g)	Q_{SH1} (mg/g)	K1-$Q_{contribution}$ (mg/g)	R_{K1} (%)	Q_{K2} (mg/g)	Q_{SH2} (mg/g)	K2-$Q_{contribution}$ (mg/g)	R_{K2} (%)
5	0.7±0.2	0.1±0.1	0.09±0.02	90±24	0.3±0.1	0.04±0.01	0.04±0.01	87±11
50	3.5±0.9	0.7±0.2	0.42±0.10	64±23	2.0±0.2	0.30±0.04	0.22±0.02	73±9
100	4.7±1.1	1.0±0.2	0.56±0.13	57±20	3.1±0.4	0.48±0.07	0.34±0.05	72±18
150	5.3±1.2	1.2±0.3	0.63±0.15	53±21	3.8±0.5	0.58±0.13	0.41±0.06	70±20
300	6.0±1.4	1.5±0.3	0.72±0.17	48±20	4.8±0.7	0.75±0.17	0.52±0.07	69±19
Qm	6.9±1.6	2.0±0.4	0.83±0.19	42±18	6.6±0.9	1.1±0.24	0.71±0.10	67±18

Q_K and Q_{SH} is the absolute methane quantity adsorbed by kerogen concentrate, and shale from HPVA result, Q (<105 bar) is the absolute methane quantity converted from excess methane quantity by Equation (2-27) in 2.4.2, Q (>105 bar) is the absolute methane quantity obtained from dual-site Langmuir model (Equation (2-15) in 2.4.1.3), $Q_{contribution}$ is the methane amount adsorbed by kerogen per gram of shale, calculated based on Equation 3-1. R is the percentage kerogen concentrate contribution to the methane adsorption capacity of the shale calculated by Equation 3-2. Q_m is the predicted maximum methane amount adsorbed (monolayer capacity) when the isotherm reach equilibrium. The data points are the mean from triplicate experiments and the errors represent the dispersion of a dataset relative to its mean.

Due to the different isotherm profiles, at low pressure (5 bar), the dry kerogen concentrates nominally account for much less of the methane adsorption for the dry shales, 52 and 43% for SH1 and SH2, respectively. The ratio of the kerogen concentrate contribution increases with pressure. Most of methane adsorption of the dry shales takes place at a relatively low-pressure range due to the higher proportion of small micropores (Table 3-2). Moreover, dry

kerogens, as discussed earlier (section 3.4.3.1), with larger micropores and small mesopores could have higher methane adsorption capacities than the organic matter in shales.

For the wet samples, the methane adsorption capacities of the kerogen concentrates are about 4-6 times higher than corresponding shales. K1 and K2 account for 42 and 67% respectively, of the methane adsorbed in the wet shales, which are different from the corresponding dry contributions. This could be due to the methane adsorption capacity of the isolated kerogen concentrates are reduced differently by water compared with those of the organic matter within the shales. The data suggest that some organic matter within shales could be 'shielded' from water as most organic matter in shale are surrounded by less porous minerals (section 3.4.2, Figure 3-2 FE-SEM), and methane can still adsorb on the unwet organic matter surface. Whereas water can wet most of the organic matter in the isolated kerogen concentrate, having a strongly negative impact on their adsorption capacity. Moreover, in contrast to the dry samples, the apparent contributions of the kerogen concentrates to the methane adsorption capacities of the shales decrease with increasing pressure. Although moisture reduces the accessible micropores for methane adsorption for both shales and kerogen concentrates and results in shallower isotherms (Figure 3-3), the micropores in kerogen concentrates dominate methane adsorption in wet shales at low pressure (5 bar) with contribution ratios for K1 and K2 are 90 and 87% respectively (Table 3-2), indicating minimal adsorption on minerals (Li, Li et al. 2016, Li, Pang et al. 2019).

3.4.4 Pore characterization of the shales and kerogen concentrates

3.4.4.1 Moisture impact on low-pressure gas sorption isotherms

The low-pressure gas isotherms of the dry (N_2, CO_2) and wet (N_2) kerogen concentrates and shales are compared in Figure 3-4 and Figure 3-5. The CO_2 adsorption isotherms (Figure 3-5) are Type I(b) and the N_2 sorption isotherms are Type IV(a) with a hysteresis loop (Figure 3-4), a steeper gas uptake at low relative pressure arises from a higher proportion narrow micropores (Thommes et al., 2015). This confirms that the shales and kerogen concentrates contain mesopores and macropores, with the N_2 isotherms showing adsorption at a low relative pressure ($P/P_0<0.1$) from micropores. The CO_2 isotherms show adsorption solely associated with micropores for both the shales and kerogen concentrates.

The quantity of adsorbed N_2 and shape of the hysteresis patterns of the dry and wet shales and kerogen concentrates are slightly different. For the dry shales (Figure 3-4 A), the hysteresis loop is similar to hysteresis type H2 based on the classification of the hysteresis (Sing 1985) which suggests the pores are very complex, with pore shapes including ink-bottle pores comprising necks and windows, inhomogeneous cylinder, slit and sphere pores, and other irregular pores (Sing 1985, Thommes, Kaneko et al. 2015). The obvious desorption plateau in H2 hysteresis means there is pore-blocking or shielding from a narrow range of pore necks/windows, as cavitation occurs between 0.4-0.5 P/P_0, indicating these necks and windows are all approximately <4 nm. This phenomenon still exists for wet shales (Figure 3-4 B) having same isotherm and hysteresis types, but at a reduced pore volume or quantity of adsorbed N_2, indicating water is blocking a large majority of the pore and neck/window volume. The low-pressure hysteresis below 0.42 P/P_0 could be associated with the swelling of clay minerals (Bertier, Schweinar et al. 2016), which could affect the desorption in this pressure range.

For the dry kerogen concentrates (Figure 3-4 C), the hysteresis loop is very similar to type H3 (Sing 1985, Thommes, Kaneko et al. 2015), and the adsorption of N_2 increase rapidly at low relative pressure range (<0.1 P/P_0), this indicates most of the pores are micro and mesopores with slit shape pore geometry. Pore necks/windows exist in kerogen concentrates with a large pore width ranging between 4-100 nm, as desorption isotherms decrease gradually, with the addition of necks/windows pores <4 nm (cavitation). However, most of these neck and window pores are blocked or filled when kerogen concentrates are equilibrated with moisture at 95% R.H. reducing interconnectivity (shown in Figure 3-4 D, with little or no hysteresis for K1 and K2), and reducing N_2 adsorption. Another key difference between isotherms of kerogen concentrates and shales is that shales show greater hysteresis than kerogen concentrates, both wet and dry, which suggests that the hysteresis (narrow pore necks/windows) are mostly attributed by minerals or interfaces between minerals and kerogen.

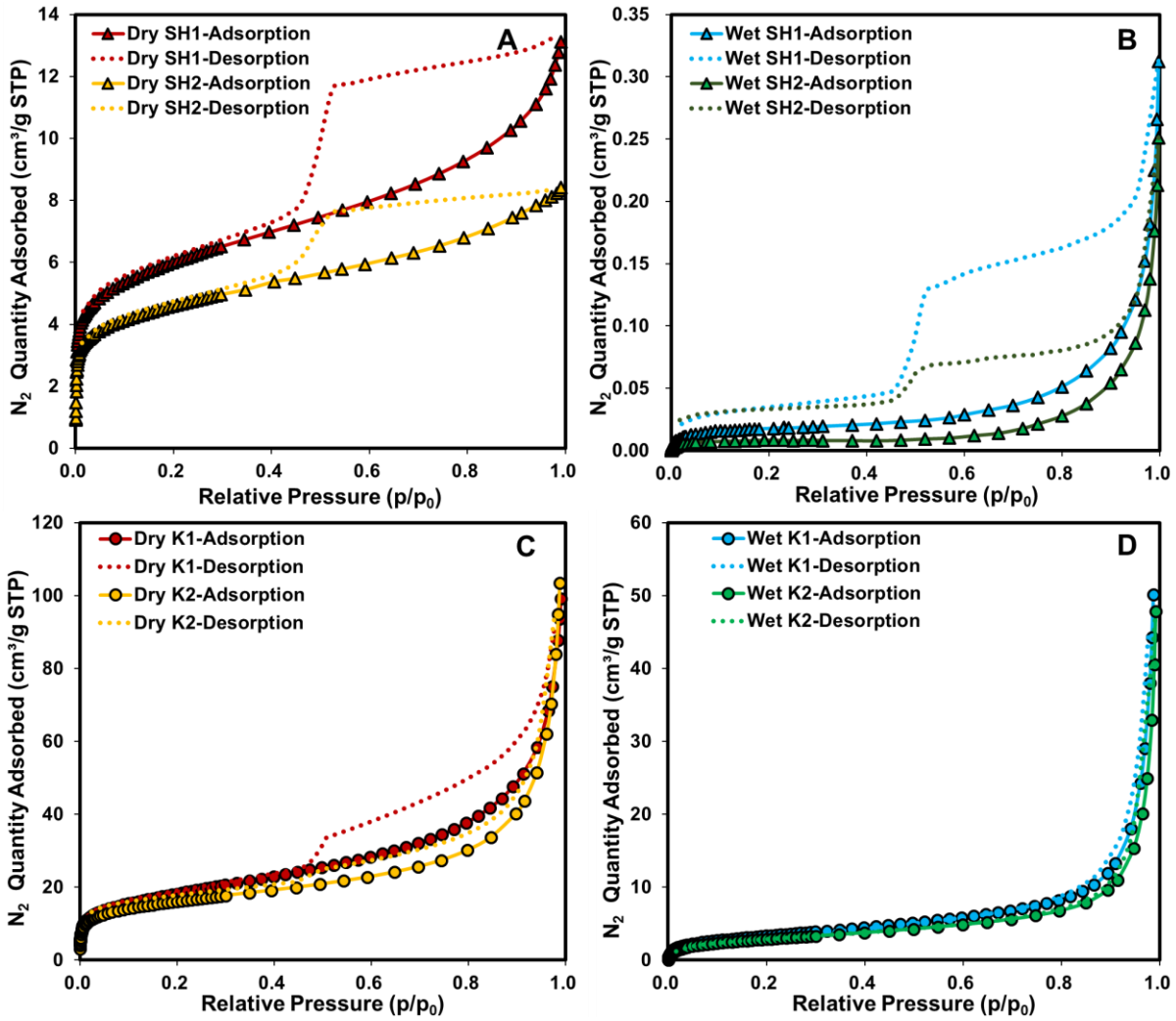

Figure 3-4. A comparison of low-pressure N_2 sorption (BET measurement) isotherms of shales and kerogen concentrates under wet and dry conditions. A) N_2 isotherms of dry shales, B) N_2 isotherms of wet shales, C) N_2 isotherms of dry kerogen concentrates, D) N_2 isotherms of wet kerogen concentrates. P/P_0, relative pressure, P is the absolute equilibrium pressure, and P_0 is the saturation pressure of N_2 at -196 °C, 1 bar.

As expected, the extents of N_2 and CO_2 adsorption are much greater for the kerogen concentrates than the corresponding shales. Table 3-3 indicates that the maximum amounts of adsorbed N_2 for the dry kerogen concentrates are 99.2 and 103.4 cm^3/g, which are 7-12 times higher than the corresponding dry shales (13.3 and 8.4 cm^3/g, respectively). SH1 and K1 have the higher SA and pore volume than SH2 and K2 as they have the higher TOC (Table 3-1). Similar differences are observed for CO_2 adsorption (Figure 3-5), the maximum adsorbed CO_2 quantities are 10.9 and 8.9 cm^3/g on the two dry kerogen concentrates, which are about 4-5 times higher than the dry shales (2.4 and 1.7 cm^3/g) (Table 3-3). The BET SAs estimated from the N_2 isotherms are quite close to those from the CO_2 isotherms of the dry samples

(Table 3-3), indicating the N_2 penetrates all the micropores that CO_2 can. Figure 3-5 indicates for the dry kerogens that K1 contains a greater micropore surface area (Table 3-3) and a greater proportion of smaller micropores than K2, consistent with the steeper methane adsorption isotherms (Figure 3-3).

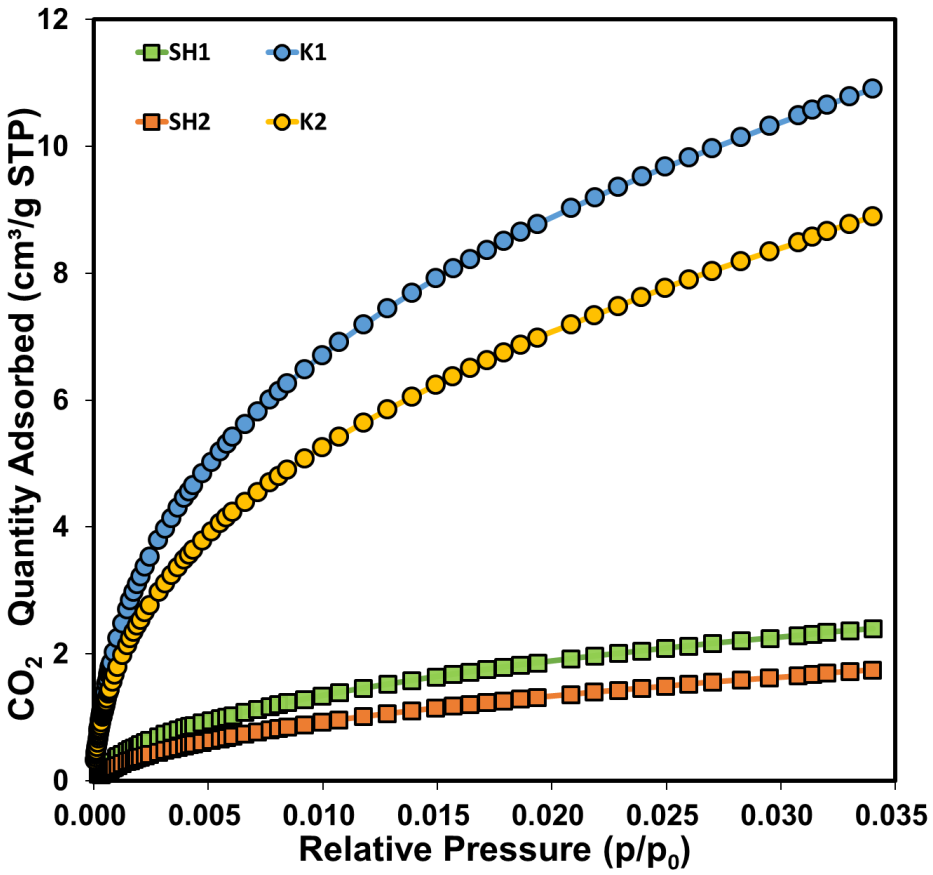

Figure 3-5. Comparison of low-pressure CO_2 adsorption (BET measurement) isotherms of dry kerogen concentrates and shales at 0 °C. P/P_0, relative pressure, P is the absolute equilibrium pressure and P_0 is the saturation pressure of CO_2 at 0 °C, 34.9 bar.

3.4.4.2 Moisture impact on pore characteristics

The SAs of dry samples obtained from N_2 and CO_2 show little difference suggesting N_2 can penetrate all ultra-micropores of both wet and dry samples. Table 3-3 reveals that more than 81% of the BET SA for the kerogen concentrates is lost, at 95% R.H., K1 and K2, reducing from 65.7-58.8 m^2/g to 12.4-10.8 m^2/g, and 48-59% total nano pore (pore <100 nm) volume is lost, reducing from 0.14-0.15 cm^3/g to 0.073-0.062 cm^3/g. The impact of moisture on the shales is even greater, with over 99% reduction in BET SA for SH1 and SH2, reducing from 21.7-16.7 m^2/g to 0.075-0.029 m^2/g, respectively, accompanied by a 98% loss in total nano pore volume.

The swelling of clay minerals in wet shale might also result in the loss of pore volume (ZHU and XIA 2013, Bertier, Schweinar et al. 2016, Feng, Li et al. 2018).

Table 3-3. Maximum adsorbed gas quantities, surface areas and pore volumes of the shales and kerogen concentrates.

Sample	N_2 $Q_{Adsorbed}$ (cm^3/g)	CO_2 $Q_{Adsorbed}$ (cm^3/g)	SA_{BET} (m^2/g)	CO_2 SA_{BET} (m^2/g)	V_{micro} (cm^3/g)	V_{meso} (cm^3/g)	V_{macro} (cm^3/g)	V_{nano} (cm^3/g)
Dry K1	99.2	10.9	65.7	68.0	0.0141	0.110	0.018	0.14
Dry K2	103.4	8.9	58.8	57.9	0.0140	0.114	0.023	0.15
Wet K1	50.1	/	12.4	/	0.0010	0.058	0.014	0.073
Wet K2	47.9	/	10.8	/	0.0011	0.044	0.017	0.062
Reduction K1 (%)	49	/	81	/	93	47	20	48
Reduction K2 (%)	54	/	82	/	92	62	24	59
Dry SH1	13.1	2.4	21.7	16.1	0.0069	0.012	0.00075	0.019
Dry SH2	8.4	1.7	16.7	12.6	0.0054	0.0067	0.00016	0.012
Wet SH1	0.31	/	0.075	/	0.0000039	0.00028	0.000063	0.00034
Wet SH2	0.25	/	0.029	/	0	0.00021	0.000056	0.00027
Reduction SH1 (%)	98	/	99.7	/	99.9	98	92	98
Reduction SH2 (%)	97	/	99.8	/	100	97	66	98

N_2 $Q_{Adsorbed}$ is the maximum adsorbed at 0.995 P/P_0; CO_2 $Q_{Adsorbed}$ is the maximum adsorbed at 3.5×10^{-2} P/P_0; SA_{BET} and CO_2 SA_{BET} are the surface areas calculated by BET theory; V_{micro}, V_{meso}, V_{macro} and V_{nano} are the micropores, mesopore, macropore and the total nano pore volume (up to 100 nm) calculated by the NLDFT model.

Moisture also changes the PSD for the kerogen concentrates and shales. For the dry samples, the cumulative SA rises rapidly in the micropore range (Figure 3-6 A, C). The two main peaks in incremental SA occur at 0.3-0.5 nm and 1-2 nm, with small peaks occurring at 2-10 nm (Figure 3-6 B, D), confirming micropores contribute most of the SA, with some contributions from small mesopores (less than 10 nm). Whereas for the wet kerogen concentrates and shales, micropores only make a small contribution to SA (Figure 3-6 E, G). Although one of the main peaks in incremental SA occurs at 1.3-2 nm, most of the other peaks occur in the range of 2-50 nm, with no obvious differences evident (Figure 3-6 F, H). Micropores less than 1.3 nm provide virtually no SA, making mesopores dominant for the wet samples (Figure 3-6 F,H), suggesting pores less than 1.3 nm are either blocked or filled with water. Micropores contribute 9 and 10% for K1 and K2 and 36 and 44% for SH1 and SH2, respectively, of the dry pore volume (Figure 3-7 A, C), since most of the maxima in the incremental pore volume occur in the mesopore range of 2-50 nm for both dry kerogen concentrates and shales. Whereas

only a few maxima exist below 2 nm for the kerogen concentrates (Figure 3-7 B), these maxima are relatively larger for the shales, indicating higher proportions of micropore volume, consistent with their steeper methane adsorption isotherms (Figure 3-3). However, micropores contribute less than 2% for the wet samples, with no pore volume below 1.3 nm (Figure 3-7 E, G), indicating most micropores especially those less than 1.3 nm are blocked by water. Therefore, methane could not adsorb on the pores with a pore size less than 1.3 nm in the wet kerogens.

Although mesopores contribute more than 55% of the total nano pore volume for both the dry or wet samples, the dry kerogen concentrates and shales have larger proportions of small mesopores (< 10 nm) volume (Figure 3-7 B, D) than their wet counterparts (Figure 3-7 F, H), since most higher peaks of incremental pore volume only exist between 10-50 nm under wet conditions, reducing the small mesopores (<10 nm) contribution (Figure 3-7 F, H). This suggests water blocking micropores can also reduce the interconnectivity to larger pores reducing the pore volume in meso and even macropores, but by a lesser and different extent (Table 3-3).

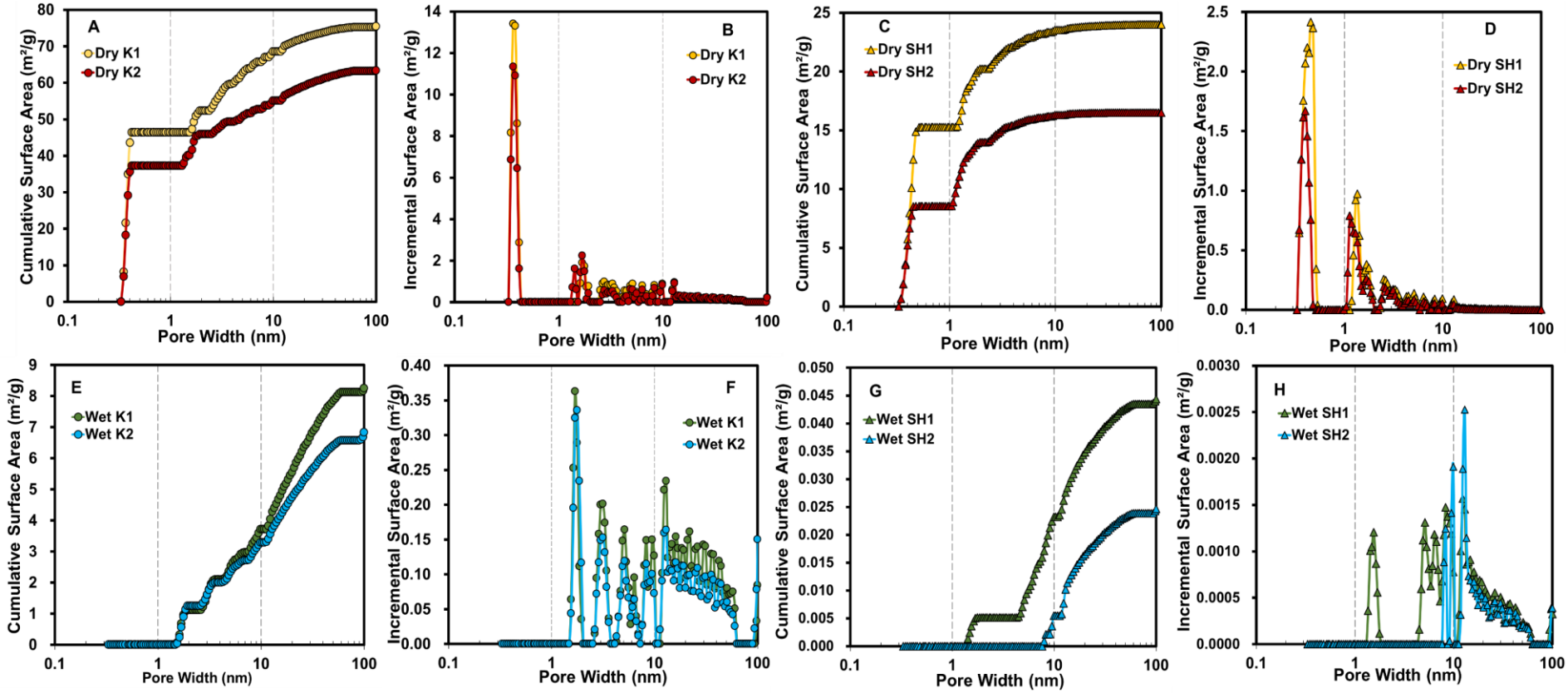

Figure 3-6. PSD and SA of dry (by N_2 and CO_2) and wet (by N_2) kerogen concentrates and shales. A) Cumulative SA and the pore width of dry kerogen concentrates, B) Incremental SA and pore width of dry kerogen concentrates, C) Cumulative SA and the pore width of dry shales, D) Incremental SA and pore width of dry shales, E) Cumulative SA and the pore width of wet kerogen concentrates, F) Incremental SA and pore width of wet kerogen concentrates, G) Cumulative SA and the pore width of wet shales, H) Incremental SA and pore width of wet shales.

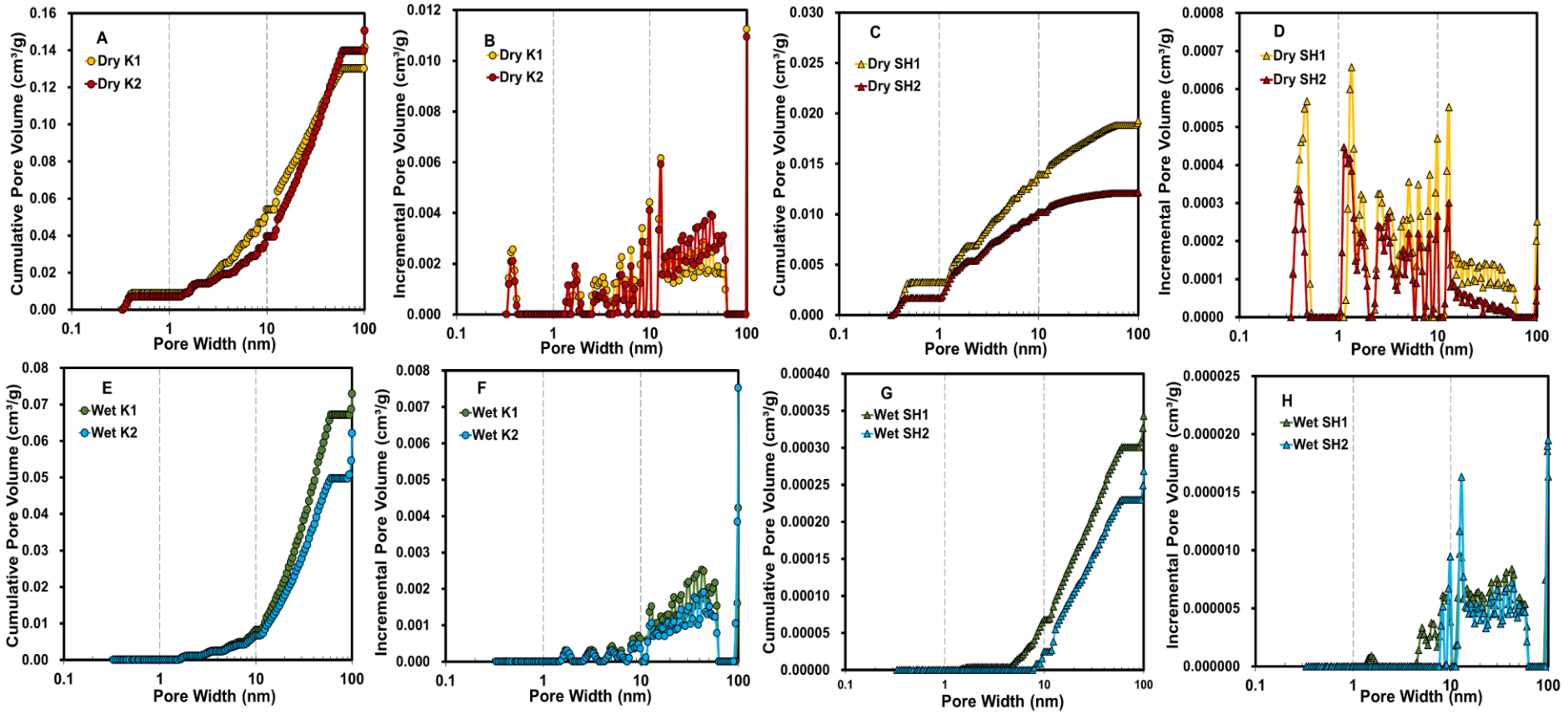

Figure 3-7. PSD and pore volume of dry (by N_2 and CO_2) and wet (by N_2) kerogen concentrates and shales. A) Cumulative pore volume and the pore width of dry kerogen concentrates, B) Incremental pore volume and pore width of dry kerogen concentrates, C) Cumulative pore volume and the pore width of dry shales, D) Incremental pore volume and pore width of dry shales, E) Cumulative pore volume and the pore width of wet kerogen concentrates, F) Incremental pore volume and pore width of wet kerogen concentrates, G) Cumulative pore volume and the pore width of wet shales, H) Incremental pore volume and pore width of wet shales.

Table 3-3 confirms that moisture has the greatest impact on micropores, followed by mesopores and macropores in both kerogen concentrates (93-92, 47-62 and 20-24% reductions for micropore, mesopore, and macropore volumes, respectively) and shales (99.9-100, 98-97 and 92-66%, respectively), which makes the extent of reduction for SA larger than that for pore volume since most of the SA is provided by micropores, whereas most of the pore volume is provided by mesopores. Also, Table 3-3 indicates that the reduction in SA and pore volume for the shales are much higher than for the kerogen concentrates. This is because the proportion of micropores in shale (36-44%) is much higher than for kerogen (9-10%). In addition, the large amount of clay minerals in some shales are responsible for these shales being most easily affected by water (Bertier, Schweinar et al. 2016, Feng, Li et al. 2018, Liming, Junli et al. 2012, ZHU and XIA 2013, Kuila, McCarty et al. 2014, Ismadji, Soetaredjo et al. 2015, Feng, Li et al. 2018).

Water molecules hinder access to the smaller micropores, as shown in Figure 3-6 and Figure 3-7, for a cylindrical/slit pore with a diameter of equal to or less than 1.3 nm. Less water is adsorbed in the larger micropores (together with mesopores) due to the reducing energy potential for adsorption (Dubinin 1966, Gregg and Sing 1982, Ruthven 1984). Also, water is adsorbed in micropores first when these can be accessed. For the pores larger than 1.3 nm, water occupies some adsorption sites and can form a cluster of molecules leading to a film (or condensate) which reduces both the accessible pore volume and SA, while other gases can still gain access if the pores are not totally blocked. It is believed that thicker water films can reduce pore volume more (Li, Li et al. 2016). The low-pressure adsorption isotherm results have indicated that the micropores, mesopores and macropores are largely connected by narrow pore necks building a complex pore system. The water volume uptake calculated by Equation 2-3 (Section 2.2.3) indicates that 33 and 40% of the pore volume for SH1 and SH2 are occupied by water, whereas more than 98% accessible pore volume of shales are reduced after sample become wet, suggesting the water reduce the pore volume by taking up the pore volume as well as by blocking the micropore pore necks connecting to larger pores. The size of the pore neck matters, when the pore necks are less than 1.3 nm, water molecule clusters can block the necks preventing other gases being transported into larger pores, but when the pore neck is larger, there is still enough space for the other gas to go into the bigger pores.

3.4.5 Depiction of the impact of moisture on methane adsorption capacity

Figure 3-8 illustrates how moisture can reduce the methane adsorption capacity for kerogens by 1) occupying adsorption surfaces. Water, as the polar molecule gives stronger interactions with the same adsorption surface (non-polar or polar) than the non-polar methane molecules, can occupy adsorption sites (Chalmers and Bustin 2007, Chalmers and Bustin 2010, Huang, Ning et al. 2018, Zhao, Li et al. 2018); 2) blocking micropore access and filing mesopores. As for the mesopores connecting with different sizes of pore necks (smaller than 1.3 nm and larger than 1.3 nm) methane can occupy most of the sorption surface in the dry samples (Figure 3-8 A). However, after samples become wet, much of the available sorption surface is taken up by water, or most pores with narrow pore necks become inaccessible since water blocks access to micropore less than 1.3 nm (Figure 3-8 B).

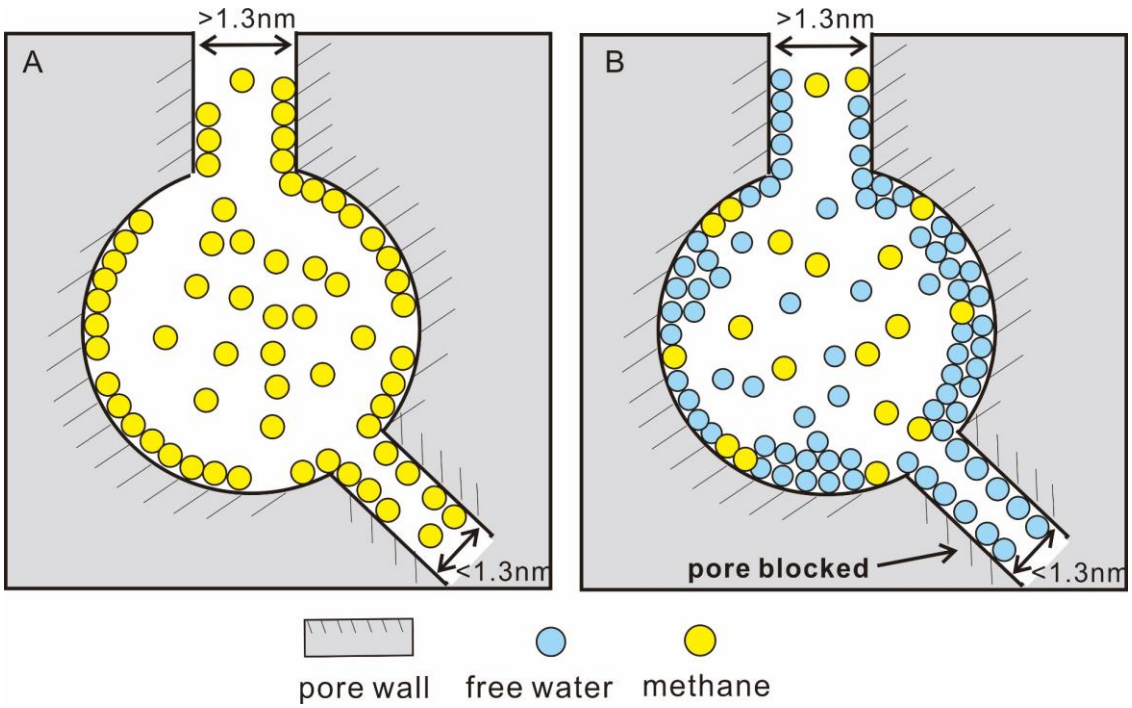

Figure 3-8. Depiction of the impact of moisture on methane adsorption in small mesopore and connecting micropores for kerogens. A) Methane adsorption in dry samples, B) Methane adsorption in wet samples, with water blocking micropore access and filling mesopores.

Moisture can affect methane adsorption differently for kerogen concentrates and shales. According to methane adsorption results, the reduction of K1 (75%) is higher than K2 (61%) since K1 has more narrow pore necks as more evident cavitation occurs in the desorption isotherms (Figure 3-4 C), and most pore necks are blocked after moisture equilibrated (Figure

3-4 D with little or no hysteresis). However, for shales, the reductions of SH1 (50%) is less than SH2 (66%) might also be due to the different pore networks (Figure 3-4 A). Furthermore, the reductions in SA and pore volume measured are higher than those for the equilibrium methane adsorption capacities. This can be explained by ice having a greater effect on blocking access to pores than water. It is because the SA and pore volume are measured at sorption experiment temperature of -196 °C for low-pressure N_2, bulk pore water or water clusters will exist as ice crystals (Pauling 1935), with a lattice of 0.45 nm width and 0.73 nm height (Bragg 1921), which could occupy more space so reducing pore SA and volume to a greater extent. Whereas water molecules are depicted with a diameter of 0.28 nm (D'Arrigo 1978, Zhang and Xu 1995) in the methane adsorption experiment temperature (25 °C). Furthermore, the pore blocking threshold of 1.3 nm summarised from the above result is obtained from low-pressure N_2 adsorption at -196 °C, which occurs with ice crystals but not necessarily water meaning the blocking effects are probably slightly exaggerated at -196 °C.

3.5 Implication for GIP

The classical GIP based on the shale gas holding capacity is estimated from the total amount of free gas and adsorbed gas content by Equation 3-3 (Tang, Ripepi et al. 2016). However, most GIP estimations use dry samples without considering the effect of moisture, and therefore could be overestimated. This research provides a realistic method for the measurement of the accessible pore volume of moisture equilibrated shales and reveals the moisture impact on the adsorbed gas content, making a more accurate GIP estimation of wet shales possible. The GIPs (the shale gas holding capacity) of dry and wet shales are listed in Table 3-4 which are calculated by Equation 3-3, the dry porosity is obtained from MIP, and wet porosity is calculated based on Equation 3-4.

$$GIP = Q_{free} + Q_a = Q_{free} + Q_e + V_a \times \rho_g = V_{tot} \times \rho_g + Q_e \quad (3\text{-}3)$$

$$Porosity_{wet} = \frac{V_{wet\ pore}}{V_{sh}} = 1 - \frac{\rho_{wet\ bulk}}{\rho_{wet\ sk}} = 1 - \frac{\rho_{dry\ bulk}}{\rho_{wet\ sk}} \times (1 + W) \quad (3\text{-}4)$$

where, Q_{free} is the free gas in the pore; Q_a is the absolute adsorption quantity; Q_e is the excess adsorption quantity; V_a is the pore volume for gas to adsorb into; ρ_g is the density of the bulk gas; V_{tot} is the total pore volume accessible to gas in shale; $Porosity_{wet}$ is the porosity of wet shale; $V_{wet\ pore}$ is the pore volume of wet shale; V_{sh} is the shale sample volume.

Table 3-4. The porosity, total pore volume and the estimated GIP of shales.

Sample	Porosity (%)	V_{tot} (m^3/t)	Q_a (kg/t)	Q_{free} (kg/t)	GIP (kg/t)
Dry SH1	10.2	0.0432	2.1	9.3	11.4
Dry SH2	4.0	0.0156	1.6	2.9	4.5
Wet SH1	6.8	0.0284	0.94	6.8	7.8
Wet SH2	2.5	0.0095	0.49	2.3	2.8

Pressure and temperature effects on the free and adsorbed gas content cannot be neglected (Luffel and Guidry 1992, Ross and Bustin 2007, Tang, Ripepi et al. 2016, Chen, Kang et al. 2018). It is estimated that the actual shale reservoir pressure and temperature of Longmaxi shale, Sichuan Basin with a depth of 4000 m are about 600 bar and more than 100 °C (Tang, Ripepi et al. 2016, Li, Zhou et al. 2018). An average reduction of 45% for adsorbed gas content from 25 °C to 100 °C is applied based on the literature (Rexer, Benham et al. 2013, Ji, Song et al. 2015, Zou, Rezaee et al. 2017, Whitelaw, Uguna et al. 2019). The total accessible pore volume (V_{tot}) of shale is calculated from the porosity, the density of methane at 600 bar and 100 °C is 241.03 kg/m^3 obtained from REFPROP version 8.0 software and the excess adsorption quantity is from the methane adsorption experiments. The estimated GIP of the shales at 600 bar and 100 °C are listed in Table 3-4, and the dominant gas is free gas for both dry and wet shales. The calculated GIP of the dry shales, SH1 and SH2 (maximum GIP) are 11.4 and 4.5 kg/t, respectively, similar to the range of 3.2-6.4 kg/t for Longmaxi shale (Tang, Ripepi et al. 2016). The GIP of the wet shales SH1 and SH2 (minimum GIP) are 7.8 and 2.8 kg/t, respectively, indicating that the estimated GIP can reduce by up to 32-38% when moisture is considered.

3.6 Conclusions

This is the first time that the impact of moisture on PSD and methane adsorption capacities of kerogens and shales have been compared and the following conclusions can be drawn.

1) Moisture has a detrimental effect on methane adsorption capacity, reductions for the kerogen concentrates and shales being 61-75% and 50-66%, respectively, at 95% R.H.. The kerogen concentrates are the most important matter in shale for methane adsorption, which account for most (83 and 59% for dry SH1 and SH2, 42 and 67% for

wet SH1 and SH2) of the equilibrium methane adsorption capacities of the shales within experimental error.

2) At lower pressures, dry shales display a steeper rise of methane adsorption than dry kerogen concentrates, suggesting that demineralisation could access larger micropores and smaller mesopores. The less steep isotherms of wet samples suggest they require higher pressure and pore energy to adsorb same amount of gas as the dry samples.
3) The kerogen concentrates have much higher average SA (62.2 m^2/g compared to 19.2 m^2/g) and average pore volume (0.15 cm^3/g compared to 0.016 cm^3/g) than corresponding shales. Moisture significantly reduces the SA (81% for kerogen, and 99% for shale) and total pore volume for kerogens concentrates (48-49%) and shales (98%), by filling or blocking micropores less than 1.3 nm, obstructing pore necks connecting to micropores and mesopores stopping gas transport, occupying adsorption sites, or swelling clays (in shale) to reduce accessible pores. These reductions are much larger than reductions observed for methane adsorption as ice in the N_2 low-pressure measurements reducing access to pores much more than liquid water for methane adsorption.
4) This research provides a realistic method for accurate GIP estimation of moisture equilibrated shales. The calculated GIP of the dry SH1 and SH2 (maximum GIP) are 11.4 and 4.5 kg/t, and the GIP of the wet shales (minimum GIP) 7.8 and 2.8 kg/t, indicating the GIP reduces by 32-38% when moisture is considered for the shales investigated. Moisture has a stronger impact on adsorbed gas, where the reduction for adsorbed gas is 55-69%, and 21-27% for free gas.

CHAPTER 4 THE EFFECT OF SOXHLET EXTRACTION ON POROSITY AND METHANE ADSORPTION FOR DRY AND MOISTURE-EQUILIBRATED SHALES

4.1 Summary

The porosity and methane adsorption capacity of shale used to estimate gas in place (GIP) are affected both by moisture and oil residing in the pore structure, as well as oil naturally present from maturation, which can include contaminant drilling mud fluids used for drilling. To demonstrate the impact of extractable oil on methane adsorption capacity for both dry and moisture-equilibrated shales, two overmature shales from China (SH1, SH2) and two lower mature shales from UK (BS3, GH4) have been investigated. The oils extracted from the overmature shales (<0.5 wt.% TOC) are in low yield and arise from oil-based drilling mud, while the much higher yields from the lower maturity UK shales (1.1-2.5 wt.% TOC) is mainly from oil generated by maturation. After extraction, minimal changes (<5%) in total nanopore volume (<100 nm) were observed for the dry over mature shales, but significant increases (95 and 176%) were observed for the dry lower maturity shales. More than 60% of the extracted oil resides in micro and mesopores, and removal could unblock the micropore necks and enlarge the accessible meso and macropore volume. Moisture contents are lower for extracted shales, with reductions of 7-37% observed. Methane equilibrium adsorption capacities increased after oil extraction for both the dry and wet shales, especially for lower maturity shales, where increases were over 200% for the wet shales. Henry's Law was used to show that there were not significant amounts of dissolved methane in oils for the dry shales. Extracting oil from shales prior to determining the porosity and methane adsorption capacity can lead to the GIP being over-estimated for moisture equilibrated shales, particularly for oil-window shales where an overestimation of 22% was obtained for the shale investigated in this chapter. These findings provide a better understanding of the combined impacts of residual oil and water on GIP and avoid its overestimation.

4.2 Literature review

Accurate shale gas reserve evaluations are valuable for gas exploration (Curtis 2002, Ross and Bustin 2007, Ross and Bustin 2009, Tang, Ripepi et al. 2016, Li, Stevens et al. 2021). Free gas is stored in the available pore volume, adsorbed gas is mainly in micropores with the greatest surface area, and some gas can dissolve in any hydrocarbon and or water (Curtis 2002, Ross and Bustin 2007, Ross and Bustin 2009, Rexer, Benham et al. 2013, Gasparik, Bertier et al. 2014). Pore networks in shale control the storage and migration of hydrocarbons (Tang, Ripepi et al. 2016, Whitelaw, Uguna et al. 2019). The accurate determination of adsorbed gas capacity and porosity is essential for estimating the shale gas in place (GIP) (Curtis 2002, Ross and Bustin 2007, Ross and Bustin 2009, Tang, Ripepi et al. 2016, Li, Stevens et al. 2021), both of which can be affected by the residual oil in target shales (Mohnhoff, Littke et al. 2016, Cao, Han et al. 2019, DiStefano, McFarlane et al. 2019, Qi, Ju et al. 2019). The impact of extracted oil has not been studied on shales at moisture-equilibrated (wet) conditions, although moisture is not a negligible factor for GIP estimation (Whitelaw, Uguna et al. 2019, Li, Stevens et al. 2021). Understanding the effect of extractable oil on porosity and gas adsorption, comparing the GIP in all conditions ((initial, extracted, dry and wet) shale can provide guidance for establishing more accurate shale gas reserve estimations.

The organic matter in shales comprises mainly the insoluble organic matter, kerogen (typically > 90%), with small amounts of extractable bitumen or oil (typically <10%) (Barker 1979) removed with common organic solvents (Eldridge 1996, DiStefano, McFarlane et al. 2019, Qi, Ju et al. 2019). Thermal maturity is the critical parameter to indicate the evolution stages of shale oil and gas generation (Bernard and Horsfield 2014, Dayal and Mani 2017). Shale can be categorized as thermally immature, oil mature, gas or high mature, and post or over-mature (Section 1.2.2.2) in terms of capability to generate hydrocarbons (Tissot and Welte 2013, Bernard and Horsfield 2014, Dayal and Mani 2017). Immature shales with vitrinite reflectance (VR) less than 0.5% Ro, may generate biogenic natural gas. Shales with VRs ranging from 0.5 to 1.2% Ro are in the 'oil window'. High maturity shales, with VR in the range 1.2-2% Ro are in the 'gas window' and will generate mainly relatively wet gas, while overmature shales (VR>2% Ro) will generate only dry gas (Chapter 1, Figure 1-1) (Tissot and Welte 2013, Bernard and Horsfield 2014, Dayal and Mani 2017).

Both initial (Guo 2013, Gasparik, Bertier et al. 2014, Rexer, Mathia et al. 2014, Wang, Zhu et al. 2016) and solvent extracted (Löhr, Baruch et al. 2015, Whitelaw, Uguna et al. 2019) shales

have been used to relate key factors, including temperature, pressure, composition, and moisture impact on the methane adsorption capacity. The difference between initial and extracted dry shales on porosity and methane adsorption capacity has been studied recently (Hu, Zhang et al. 2015, Liu, Huang et al. 2016, Mohnhoff, Littke et al. 2016, Cao, Han et al. 2019, DiStefano, McFarlane et al. 2019, Ibad and Padmanabhan 2020). Solvent extraction increases specific surface area (SA) (Guo, Jia et al. 2014, Liu, Huang et al. 2016). Methane adsorption in shales can potentially be affected by methane dissolving in any oil present (Hu, Zhang et al. 2015, Liu, Huang et al. 2016, Mohnhoff, Littke et al. 2016, Cao, Han et al. 2019, Ibad and Padmanabhan 2020). Apart from natural oil arising from maturation (Cao, Han et al. 2019, Qi, Ju et al. 2019), oil-based drilling muds, in particular, can also impact methane adsorption and gas dissolution (Berthezene, De Hemptinne et al. 1999). Oil-based drilling muds are widely used as they do not hydrate active clay minerals, and they can affect further analysis unless proper cleaning methods are applied (Eldridge 1996, Jarrett, Schinteie et al. 2013). Previous researchers have reported that the methane adsorption capacities of the dry extracted shales are larger than for the initial shales (Guo, Jia et al. 2014, Hu, Zhang et al. 2015, Liu, Huang et al. 2016, Cao, Han et al. 2019). As an example, shales were wiped with dry cloths to remove any drilling fluids before extraction (DiStefano, McFarlane et al. 2016). Different extractive solvents (acetone, tetrahydrofuran (THF), carbon disulfide (CS_2), and benzene) have different impacts on extraction yields since they have different molecular dynamic diameter, aromaticity, boiling point, and polarity, which can lead to various effects on porosity and methane adsorption. However, all these studies on the impact of solvent extraction on methane adsorption and pore characteristics of shales were carried out on dry shales (Guo, Jia et al. 2014, Hu, Zhang et al. 2015, Liu, Huang et al. 2016, Cao, Han et al. 2019). Water exists under reservoir conditions and moisture significantly reduces the methane adsorption for coals and shales (Simpson and Dearing 2000, Loucks and Ruppel 2007, Tan, Weniger et al. 2014, Li, Pang et al. 2019), making researchers focus on moisture equilibrated shales (Ross and Bustin 2007, Ji, Zhang et al. 2012, Heller and Zoback 2014, Jin and Firoozabadi 2014, Merkel, Fink et al. 2016, Zolfaghari, Dehghanpour et al. 2017, Whitelaw, Uguna et al. 2019). Water reduces gas adsorption by occupying pore volume and blocking the pore necks, and the GIP estimated for moisture-equilibrated shale is considered more accurate (Whitelaw, Uguna et al. 2019, Li, Stevens et al. 2021). Gas adsorption for wet shales before

and after solvent extraction could be different due to the combined influence of moisture and oil on the pore network. However, to date, the combined impact of moisture and residual oil on the porosity and methane adsorption capacities of shales has not been investigated. Furthermore, for dry shales, previous studies have not addressed the influence of extractable oil on GIP estimates (Mohnhoff, Littke et al. 2016, Cao, Han et al. 2019, DiStefano, McFarlane et al. 2019).

In this chapter, high-pressure methane adsorption and low-pressure gas sorption were carried out for dry and moisture-equilibrated shale before and after solvent extraction. For the first time, the impacts of solvent extraction on GIP estimations for both dry and moisture-equilibrated shales are revealed. For the shales investigated, the difference between extractable oil that arises from maturation, and that introduced as contaminants from oil-based drilling mud is emphasized. The main purpose of this chapter is to provide guidance for what kind of shale samples should be selected for the GIP estimation, since both initial and extract shales were applied.

4.3 Experiments and Methods

This chapter includes four shales, two shales (SH1 and SH2) are from China (Figure 2-1 in Section 2.1), and another two shales (BS3 and GH4) from the UK (Figure 2-2 in Section 2.1). In this chapter, the shales without extraction are called 'initial' shale to distinguish them from the 'extracted' shales. The extracted shales are obtained from the solvent extraction experiment in Section 2.2.2. The initial and solvent extracted shale samples were both dried and equilibrated at 95% relative humidity (R.H.) moisture (wet) (by method in 2.2.3) for high-pressure (2.4.2) and low-pressure gas sorption (2.4.3) experiments, and helium pycnometry (2.3.4) for the skeletal density. Dry shales are prepared for the vitrinite reflectance (2.3.5), elemental analysis (2.3.3), rock eval (2.3.1) and mercury intrusion porosimetry (MIP) (2.5.3) to obtain the maturity, TOC, and bulk density. The extracted oil is analyzed by GC-MS (by method in 2.3.6).

4.4 Results and Discussion

4.4.1 Shale characterization and geochemistry

Basic information on the shales, including their formation, burial depth, TOC, maturity, moisture content of wet samples, and the yield of extracted oil are listed in Table 4-1. The shales from different formations and depths have TOC contents ranging from 2.4 to 5.1 wt.%. Shales SH1 (2.95% Ro) and SH2 (2.58% Ro) are overmature, BS3 (1.01% Ro) is oil-window maturity and GH4 (1.95% Ro) is gas-window maturity. The moisture contents of the initial and extracted shales are in the ranges 1.22-2.72 and 1.13-2.06 wt.%, respectively, indicating the extracted shales adsorb less water with reductions of 15, 7, 37, and 25% for SH1, SH2, BS3, and GH4, respectively. The yield of extractable oil decreases with increasing maturity from 2.5 wt.% TOC for the oil-window shale, BS3 to 1.1 wt.% TOC for the gas-window shale, GH4, and 0.3-0.5 wt.% TOC for the over-mature shales, SH1 and SH2. The extracted oil volumes range from 0.13 to 0.73 μL/g, assuming the extracted oil density is 0.85 g/m^3, which is the same as light crude oil (Hanafy, Macary et al. 1997, Stasiuk and Snowdon 1997). Wufeng-longmaxi shale is dominated by Type II kerogen (Zou, Dong et al. 2010). Although the Bowland shale is a mixture of Type II/III and IV kerogens (Andrews 2013, Clarke, Turner et al. 2018), the oil has been generated predominately from the Type II kerogen present. The impact of kerogen type is limited, as all the oil in these four shales come from a similar type.

Table 4-1. Characteristics of the initial and extracted shales

Sample	Formation	Depth (m)	TOC (wt.%)	Maturity (% Ro)	Moisture (wt.%)	Oil yield (wt.% TOC)	Oil volume (V_{oil}) (μL/g)
Initial SH1	Ordovician - Lower Silurian Wufeng-Longmaxi, China	4119	5.1	2.95	1.50[a]	0.3	0.17
Ext SH1					1.27[b]		
Initial SH2	Ordovician - Lower Silurian Wufeng-Longmaxi, China	4098	2.4	2.58	1.22[a]	0.5	0.13
Ext SH2					1.13[b]		
Initial BS3	Carboniferous Bowland Becconsall, UK	2143	2.5	1.01	1.84[a]	2.5	0.73
Ext BS3					1.17[b]		
Initial GH4	Carboniferous Bowland Grange Hill, UK	3113	3.4	1.95	2.72[a]	1.1	0.44
Ext GH4					2.06[b]		

The TOC, moisture, and oil yield were the average data from triplicate determinations. Moisture[a] is the moisture content for the initial shale, and moisture[b] is that for extracted shale.

4.4.2 GC-MS characterization of the extracted oils

Figure 4-1 shows the total ion chromatograms (TIC) and m/z 71 single ion chromatograms (EIC 71) for the oils extracted from the four shales with the *n*-alkane peaks labelled. For the two over-mature shales where the extractable oil yields are low, light condensate would be expected with possibly small quantities of residual oil. The oils are relatively heavy and contain *n*-alkanes in low concentrations. However, the fact that the *n*-alkanes do not extend beyond n-C_{23} would suggest that they could arise from a small quantity of remaining oil. *n*-Hexadecane dominant in the extract from SH1 (Figure 4-1 A) is possibly drilling fluid-derived (Wenger, Davis et al. 2004). A similar phenomenon is evident for the extract from SH2 (Figure 4-1 B), where the drilling fluid is causing slightly elevated concentrations of *n*-hexadecane and *n*-octadecane over the other n-alkanes, although much less pronounced (Wenger, Davis et al. 2004). The majority of the TICs for the extracts from the two over-mature shales comprise complex mixtures extending beyond C_{30}. The common drilling mud 'oil' bases including the diesel, enhanced-mineral oil (EMO), and synthetics (olefins and esters). The oil contaminated by the diesel and EMO shows a relatively higher peak of C_{16} in GC data (Wenger, Davis et al. 2004). The evidence would suggest that EMOs account for most of the complex mixtures extracted from SH1 and SH2.

The oil from the oil-window shale, BS3, is characteristic of a paraffinic oil with *n*-alkanes prominent ranging from C_{16} to C_{33} and the pristane to phytane ratio close to 1 (Figure 4-1 C). The yield of oil extracted from the gas-window Bowland shale sample (GH4) was much lower than that for the oil-window shale (BS3) and is considerably lighter with n-alkanes from C_{12} to C_{23} (Figure 4-1 D). Furthermore, there is evidence of some non-hydrocarbon contamination from siloxane and methyl esters which are likely to rise from column bleed and the septa of the GC or the vial cap.

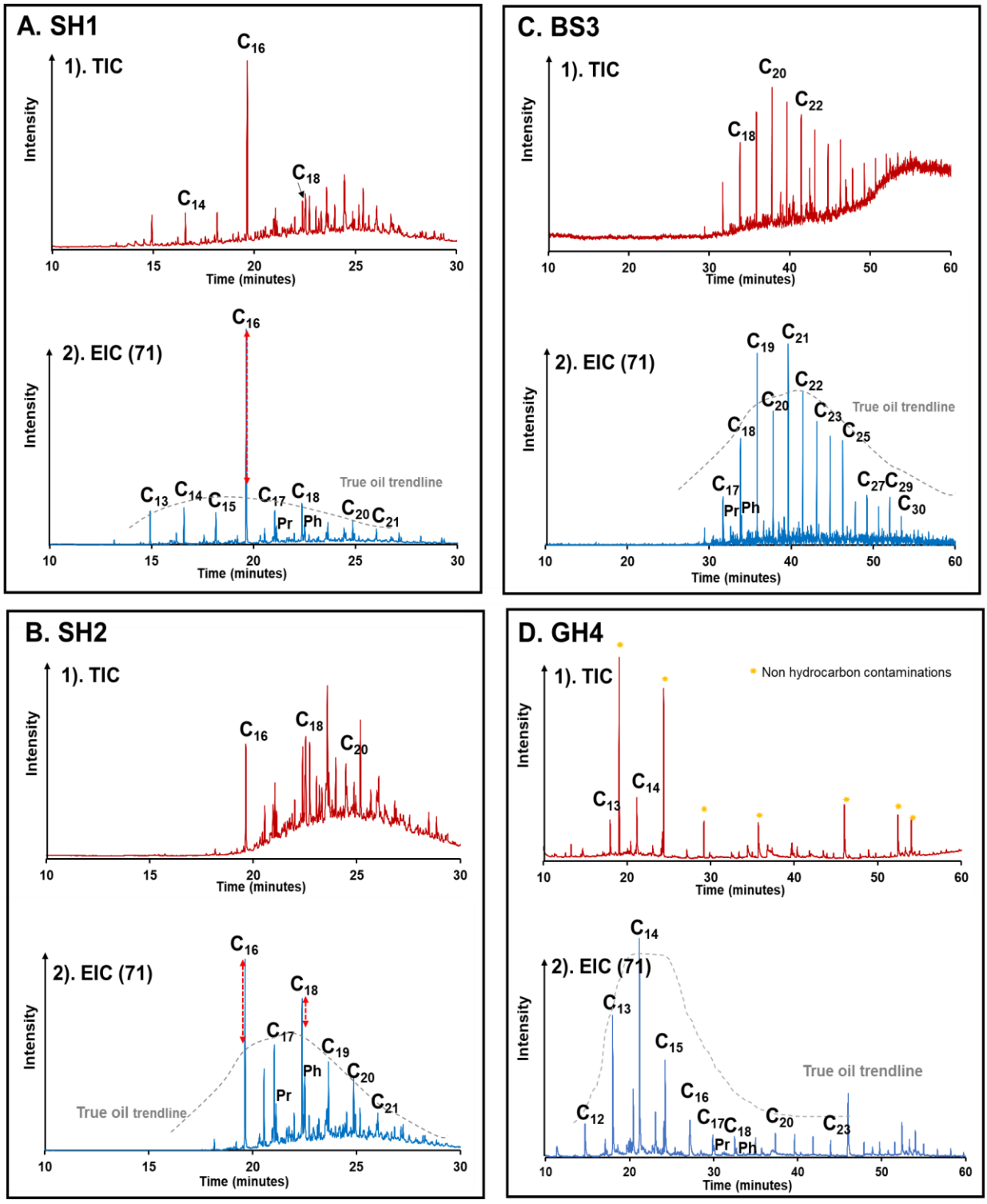

Figure 4-1. GC-MS total ion and m/z 71 single ion chromatograms for the extracted oil with the *n*-alkane peaks labelled. A, B, C, and D are the oils from SH1, SH2, BS3, and GH4.

4.4.3 Impact of solvent extraction on nanoporosity

The pore SA, micro (<2 nm), meso (2-50 nm), macro (50-100 nm), total nanopore volumes (<100 nm) (Thommes, Kaneko et al. 2015), and their changes after solvent extraction calculated from the low-pressure N_2 and CO_2 gas isotherms in this research are compared in Table 4-2. The different pore volume percentages for the dry and wet initial and extracted shales are presented in Figure 4-2. The micropore volumes of the dry shales general increase with maturity (Table 4-2), with the order being oil window (BS3), gas window (GH4), and overmature (SH1>SH2), which is also the case on a TOC basis (SH2>SH1>GH4>BS3). This implies most micropores reside with the organic matter, and high maturity shales developing more pores during hydrocarbon generation (Curtis, Cardott et al. 2012, Gasparik, Ghanizadeh et al. 2012, Hu 2014, Löhr, Baruch et al. 2015, Mastalerz, Hampton et al. 2017). Although mesopores are dominant in the dry shales (Figure 4-2), the micropores still occupy a significant fraction of the pore volume. The contributions of micropores to the total nanopore volume are much higher in the over mature shales, SH1 and SH2, than those in the gas-window shale GH4 and oil-window shale BS3 (Figure 4-2), suggesting hydrocarbon generation facilitates the development of micropores (Tissot 1984, Cao, Song et al. 2015, Mastalerz, Hampton et al. 2017).

Increases in pore volume are expected after any native oil is extracted (DiStefano, McFarlane et al. 2016, Qi, Ju et al. 2019). However, for the dry over mature shales, the changes (<20 %) in surface area and nanopore volume are small (Table 4-2) due to the low extraction yields (<0.5wt.% TOC, Table 4-1), with the extracted material being mainly drilling mud derived. Since the permeability of shales (typically less than 0.001 mD) is very low (Best and Katsube 1995, Katsube 2000, Alfi, Barrufet et al. 2019), it is difficult for the drilling muds to penetrate the shale bulk, with most being on the surface. Solvent extraction may cause additional effects, such as contributing to the swelling of clay pores by the solvent (Lee, Fischer et al. 2014) or changing the interactions with rocks if solvent is adsorbing on clay surfaces or in kerogens (DiStefano, McFarlane et al. 2016, Qi, Ju et al. 2019), which could interrupt the physical interactions between shales and adsorbed gas leading to the measured SA and pore volume decreasing after extraction.

Table 4-2. Surface area and pore volumes of dry and wet shales.

Sample name	BET SA(m^2/g)	V_{micro}(µL/g TOC)	V_{micro}(µL/g)	V_{meso}(µL/g)	V_{macro}(µL/g)	V_{nano}(µL/g)
Dry Initial SH1	21.73	135	6.9	11.7	0.75	19.3
Dry Ext SH1	19.11	112	5.7	11.8	0.87	18.4
SH1 Change*	**-12%**	**-**	**-17%**	**1%**	**15%**	**-5%**
Dry Initial SH2	16.70	224	5.37	6.7	0.16	12.2
Dry Ext SH2	16.67	226	5.42	6.5	0.14	12.1
SH2 Change*	**-0.2%**	**-**	**1%**	**-2%**	**-17%**	**-1%**
Dry Initial BS3	0.13	3.9	0.098	0.34	0.11	0.55
Dry Ext BS3	0.26	6.4	0.160	0.72	0.20	1.1
BS3 Change*	**92%**	**-**	**64%**	**110%**	**78%**	**95%**
BS3 Oil P*	**-**	**-**	**9%**	**52%**	**12%**	**73%**
Dry Initial GH4	2.19	18	0.60	1.7	0.17	2.4
Dry Ext GH4	2.62	20	0.70	5.3	0.7	6.7
GH4 Change*	**20%**	**-**	**17%**	**222%**	**273%**	**176%**
GH4 Oil p*	**-**	**-**	**23%**	**845%**	**109%**	**977%**
Wet Initial SH1	0.075	0.08	0.0039	0.28	0.063	0.34
Wet Ext SH1	0.059	0.16	0.0081	0.20	0.051	0.26
SH1 Change*	**-21%**	**-**	**105%**	**-28%**	**-19%**	**-25%**
Wet Initial SH2	0.029	0	0	0.21	0.056	0.27
Wet Ext SH2	0.036	0.14	0.0033	0.16	0.042	0.20
SH2 Change*	**25%**	**-**	**-**	**-26%**	**-25%**	**-25%**
Wet Initial BS3	0.060	0	0	0.18	0.038	0.22
Wet Ext BS3	0.108	0	0	0.32	0.07	0.40
BS3 Change*	**79%**	**-**	**-**	**80%**	**98%**	**83%**
Wet Initial GH4	0.011	0	0	0.07	0.023	0.09
Wet Ext GH4	0.045	0.04	0.0012	0.25	0.089	0.34
GH4 Change*	**310%**	**-**	**-**	**257%**	**295%**	**268%**

SA_{BET} are the surface areas calculated by BET theory; V_{micro}, V_{meso}, V_{macro}, and V_{nano} are the micropores (<2 nm), mesopore (2-50 nm), macropore (50-100 nm), and the total nanopore volume (<100 nm) calculated by the NLDFT model. Change* (in bold) is the change in pore properties resulting from solvent extraction compared with initial shales. Oil P* is the potential contribution of the increased pore volume to storing the extracted oil, which is calculated by $Oil\ P^* = 100\% \cdot (V_{Ext\ p} - V_{Ini\ p})/V_{oil}$, where $V_{Ext\ p}$ is the pore volume of shale after extraction, $V_{Ini\ p}$ is the pore volume of initial shale, and V_{oil} is the extracted oil volume (Table 4-1). Oil P* was only calculated for BS3 and GH4 since these are the only shales containing oil generated by maturation.

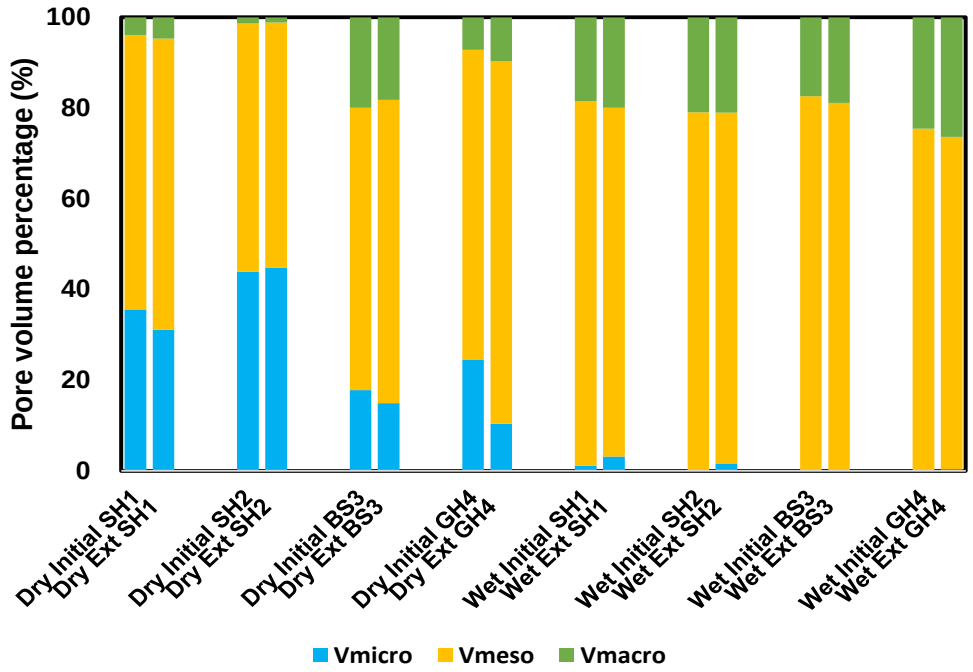

Figure 4-2. Micropore, mesopore, and macropore (<100 nm) volume percentages for the dry and wet initial and extracted shales.

The influence of solvent extraction is much larger for the two lower maturity shales. Table 4-2 indicates that the SA doubled from 0.13 to 0.26 m^2/g for dry BS3 and increased by 20% from 2.19 to 2.62 m^2/g for GH4. The total nanopore volume (up to 100 nm) also doubled for dry BS3 (from 0.55 to 1.1 µL/g) and increased by 176% for GH4 (from 2.4 to 6.7 µL/g). If the increased 64% micropore pore volume is generated solely by removing the oil, it is estimated that 9% of the extracted oil in shale BS3 is stored in the micropores (Oil p* in Table 4-2). The mesopores (from 0.34 to 0.72 µL/g) and macropores up to 100 nm (from 0.11 to 0.20 µL/g) increase by 110 and 78%, respectively, after oil extraction. This new porosity provides estimated storage space for 52 and 12%, respectively, of the extracted oil (64% in total). Similarly, for GH4, the increase of 17% micropore volume provides storage space for 23% oil, with the rest 77% oil stored in the mesopore or/and macropore, since the mesopores (from 1.7 to 5.3 µL/g) and 50-100 nm macropores volume (from 0.17 to 0.7 µL/g) increase by over 200% (Table 4-2). Clearly, for GH4, oil removal opens access to blocked meso/macropores since the increase in pore volume is considerably greater than the volume of the extracted oil. For BS3, where the increase in pore volume accounts for 73% of the extracted oil, the implication is that some of the oil resides in pores >100 nm.

The aliphatic and aromatic hydrocarbons in oils are mainly stored in micro and mesopores, but the higher molecular mass polar species and asphaltenes reside primarily in the macropores (Chen and Xiao 2014, DiStefano, McFarlane et al. 2016, Liu, Huang et al. 2016, Qi, Ju et al. 2019). The increase in macropore volume for the extracted shale is consistent with the non-hydrocarbons being removed by solvent extraction. The overall nanoporosity increases after extraction for the oil-window shale, BS3, and the gas-window shale, GH4 are larger than SH1 and SH2 since it is oil generated by maturation being extracted, as opposed to drilling fluids residing close to the surface.

As expected from our earlier studies (Whitelaw, Uguna et al. 2019, Li, Stevens et al. 2021) (Chapter 3, Section 3.4.4), most pore volume and SA are lost on wetting the shales (Table 4-2). Although mesopores are still dominant as for the dry shales, macropores replace micropores as the secondary pores in the wet shales (Figure 4-2), for both the initial and extracted samples. This arises from most of the micropores or micropore-necks being filled or/and blocked by water (Li, Stevens et al. 2021). Solvent extraction provides a more complex influence on the pore system of wet shales. For extracted wet over-mature shales, SH1 and SH2, apart from micropore volume increasing (from 0.0039 to 0.0081 μL/g for wet SH1, and from 0 to 0.0033 μL/g for wet SH2), the mesopore, macropore and nanopore pore volumes all decrease slightly, with the reduction of -28, -19 and -25% for SH1, and -26, -25, -25% for SH2 (Table 4-2). The increase of micropores indicates there is less water to fill or block micropores in the extracted shales than initial shales as oil extraction did not enlarge micropores, mesopore, or macropores as discussed above. Larger micropores in extracted wet SH1 and SH2 could be due to the solvent interacting and altering the pore surface (Job, Théry et al. 2005, DiStefano, McFarlane et al. 2016, Cao, Han et al. 2019, Qi, Ju et al. 2019), making it hard for water to condense or block micropores in solvent-extracted shales than initial shales. Additionally, the moisture contents of the extracted shales are also less than those of the initial shales (Table 4-1), with reductions of 15, 7, 37, and 25% for wet SH1, SH2, BS3, and GH4, respectively, suggesting less water is absorbed.

For the wet BS3 and GH4 shales, apart from the micropore volume of BS3 remaining close to zero, all the other pore volumes display increases after solvent extraction (Table 4-2). These increases are 80% for mesopores (from 0.18 to 0.32 μL/g), 98% for macropores (from 0.038 to 0.07 μL/g) and 83% for the total nanopores (from 0.22 to 0.40 μL/g) volumes for wet BS3.

Large proportional increases are observed for GH4, the micropores increase from 0 to 0.0012 μL/g, being 257% for mesopores (from 0.07 to 0.25 μL/g), 295% for macropores (from 0.023 to 0.089 μL/g) and 268% total nanopores (from 0.09 to 0.34 μL/g). The increases in wet shales show a similar pattern to the dry samples. The pore volume increases for the wet extracted BS3 and GH4 shales are due to a combination of oil removal enlarging the pores and the extracted shales having lower moisture contents.

Overall, the results indicate that extracted oil as well as water can have significant impact on pore characteristics. Although overmature shales have the largest pore volume, almost no oil remains, as most of the oil has migrated. The limited pore system changes of overmature shales upon solvent extraction indicates the original pore system is not changing to any significant degree, with only the interactions on the shale pore surface being modified. The oil generated by maturation mainly resides in the pores less than 50 nm (micropores and mesopores) for the early to high mature shales, and removing the oil increases the accessible pore volume for both the dry or wet shales.

4.4.4 Impact of solvent extraction on methane adsorption

The methane adsorption isotherms of the initial and solvent extracted shales are compared in Figure 4-3 and Figure 4-4, for the dry and moisture-equilibrated samples, respectively. The equilibrium methane adsorption capacities (Qm) derived from the isotherms are listed in Table 4-3. For the initial samples, the solubility of methane in oils has been estimated by Henry's Law (Section 2.4.1.3), assuming that the methane is accessible to all the extractable oil. Thus, the estimated amount of adsorbed methane after Henry's law is the difference between the total amount of methane taken up by the samples and the dissolved methane estimated by Henry's Law linear plots in Figure 4-3 and Figure 4-4. For the dry samples, the two over-mature shales, SH1 and SH2, have the higher equilibrium adsorption capacities, 77 and 127 mg/g TOC, respectively, compared to 16 and 21 mg/g TOC, respectively for the oil and gas window shales, BS3 and GH4, for the dry samples (Figure 4-3).

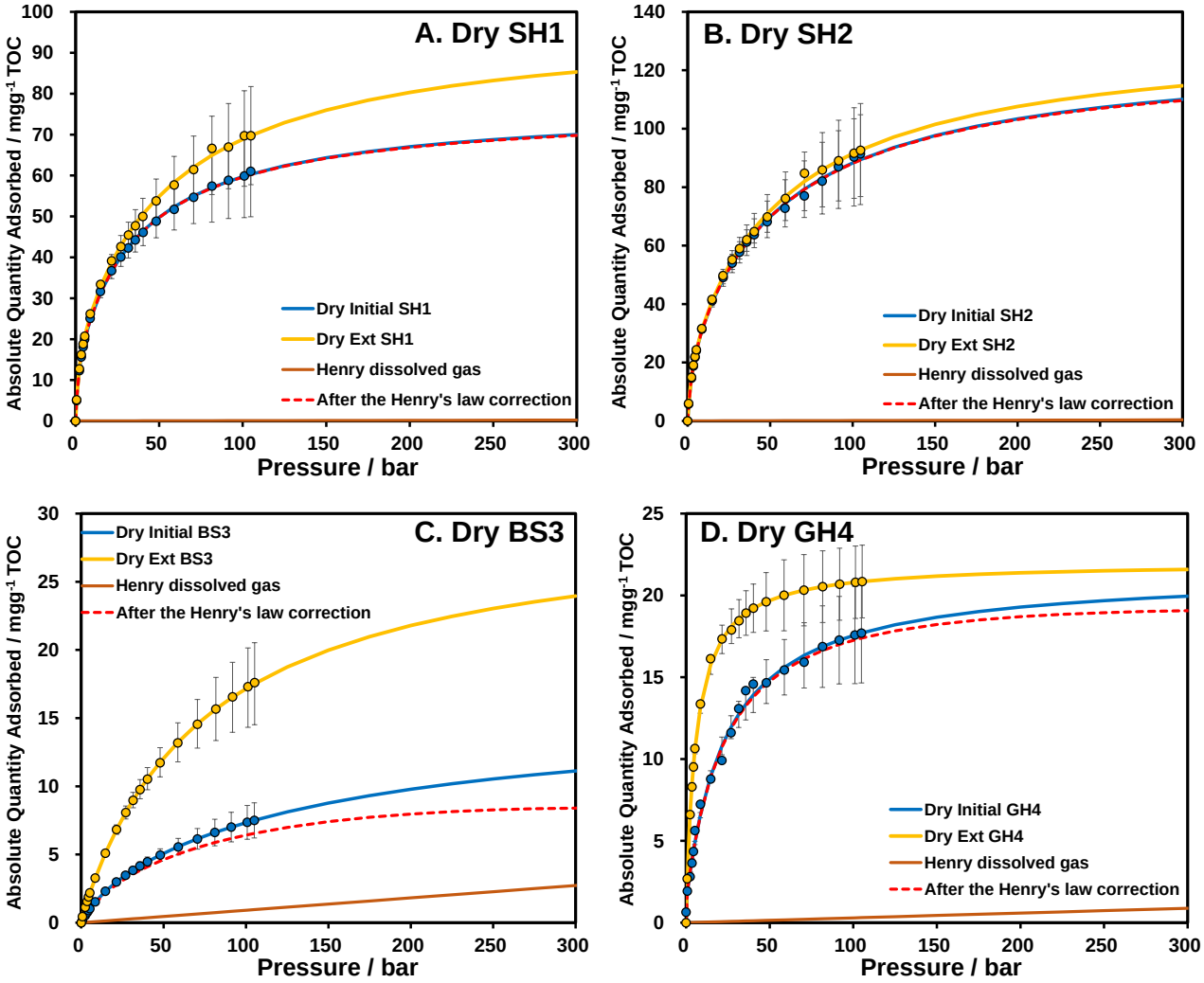

Figure 4-3. Methane adsorption isotherms of the dry initial and extracted shales, after the Henry's law correction for initial shales, and the dissolved methane uptakes calculated by Henry's Law.

Shales SH1, SH2, and BS3 have Type I(b) isotherms, with shale GH4 having a Type I(a) isotherm displaying a steeper isotherm at low pressures (Figure 4-3), arising mainly from narrow micropores (width <1 nm) (Thommes, Kaneko et al. 2015). For overmature dry shales, SH1 and SH2 (Figure 4-3 A, B), although the average methane adsorption isotherms of extracted shales are higher than the initial shales, with the Qm increasing by 27% (from 77 to 98 mg/g TOC) for SH1 and 5% (from 127 to 133 mg/g TOC) for SH2. They are still within the error range, suggesting the methane adsorption capacities of initial and extracted shales are relatively close. Thus, solvent extraction shows little impact on their methane adsorption capacities. Further, even deducting the potential contribution from dissolved methane in the low yields of extracted oil, the methane adsorption isotherms after the Henry's Law correction has very

little impact. With the methane adsorption amount at 300 bar (Q_{300bar} was used as there is no Qm for henry law) changing by only *ca*. 0.3% for SH1 (from 70.0 to 69.8 mg/g TOC) and SH2 (from 110.0 to 109.6 mg/g TOC).

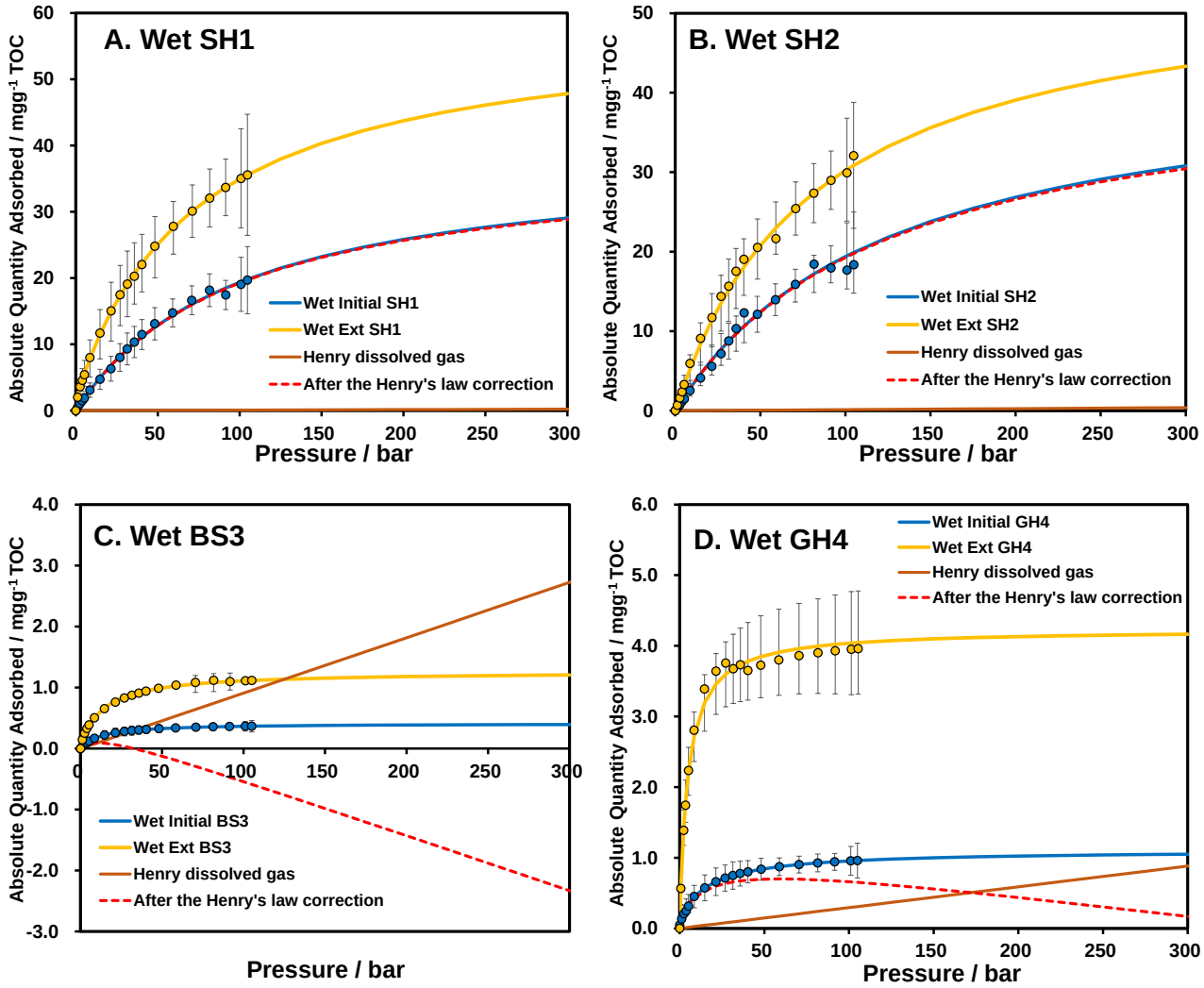

Figure 4-4. Methane adsorption isotherms of the wet initial and extracted shales, showing the Henry's Law corrections for dissolved methane in the oil present.

In contrast to the overmature shales, removing the residual oil increases the methane adsorption capacities of dry oil-window shale BS3 significantly (Qm increased by 90% from 16 to 30 mg/g TOC). A smaller increase was observed for dry gas-window shale GH4 (Qm increased by 3% from 21 to 22 mg/g TOC) consistent with the lower yield of extractable oil compared to BS3. A steeper uptake at low pressure (<50 bar) of extracted GH4 isotherm was observed (Figure 4-3 D), which indicates removing extracted GH4 oil increases narrow micropores (<1nm) (Thommes, Kaneko et al. 2015), consistent with the oil being relatively

light (Section 4.4.2). Although isotherms are less steep after the Henry's Law correction for dry shales, the isotherm type remains the same, with their shapes being similar in the low-pressure range (<50 bar, Figure 4-3). The Henry's Law corrections reduce Q_{300bar} for BS3 (from 11.1 to 8.4 mg/g TOC) (Figure 4-3 C) and GH4 (from 20.0 to 19.1 mg/g TOC) (Figure 4-3 D) by 25 and 4.4%, respectively. However, this assumes that all the oil is accessible to the methane, if this is not the case, the impact of dissolved methane will be much less.

Table 4-3. The methane adsorption amount of dry, wet, initial, and extracted shales.

Adsorption (mg/g TOC)	Initial SH1	Ext SH1	*Qm change SH1(%)*	Initial SH2	Ext SH2	*Qm change SH2 (%)*	Initial BS3	Ext BS3	*Qm change BS3 (%)*	Initial GH4	Ext GH4	*Qm change GH4 (%)*
Dry Q_{300bar}	70.0	85.3	-	110.0	114.7	-	11.1	24.0	-	20.0	21.6	-
Dry Qm	77	98	***27***	127	133	***5***	16	30	***90***	21	22	***3***
Wet Q_{300bar}	29.1	47.8	-	30.8	43.3	-	0.4	1.2	-	1.1	4.2	-
Wet Qm	39	59	***52***	44	55	***27***	0.4	1.3	***207***	1.1	4.2	***282***
Qm Reduction (%)	**50**	**40**	**-**	**66**	**58**	**-**	**97**	**96**	**-**	**95**	**81**	**-**

Qm is the equilibrium methane adsorption capacities; Q_{300bar} is the methane adsorption amount at 300 bar; Q change (%) is the methane adsorption amount changes before and after the extraction; Qm Reduction (%) is the methane adsorption reduction for wet samples compared with corresponding shales.

Methane adsorption capacities of both the initial and extracted shales are reduced after moisture equilibration due to micropores being blocked (Table 4-3) (Chapter 3, Section 3.4.4)(Li, Stevens et al. 2021). The reductions in Qm for the initial shales, SH1, SH2, BS3, and GH4 are 50, 66, 97, and 95%, respectively, which are larger than the extracted samples (40, 58, 96, and 81%, respectively), suggesting moisture has a slightly reduced impact for the extracted shales since they adsorbed less water (Table 4-1). Additionally, the methane adsorption capacities for the wet extracted shales are larger than for the initial shales (Table 4-3), even considering the experimental errors (Figure 4-4). The Qm of wet extracted SH1 increased (from 39 to 59 mg/g TOC), SH2 (from 44 to 55mg/g TOC), BS3 (from 0.4 to 1.3 mg/g TOC), and GH4 (from 1.1 to 4.2 mg/g TOC), representing increases of 52, 27, 207 and 282% compared to the wet initial shales (Table 4-3). These are consistent with the increase of accessible micropore volume for the extracted shales (Section 4.4.3).

For wet overmature shales, SH1 and SH2, the Henry's Law corrections for dissolved gas had virtually no effect on the methane sorption capacities (Figure 4-4 A, B). In contrast, the methane adsorption isotherms after the Henry's Law corrections decrease with increasing pressure and go negative for BS3 and GH4 at the pressure of ca. 40 and 300 bar, respectively

(Figure 4-4 C, D). This indicates that virtually none of the methane is accessible to the oil. This arises from water blocking the micropores or micropore necks. For both BS3 and GH4, solvent extraction significantly increases the methane adsorption capacities, by a factor of 3-4, compared to the initial moisture equilibrated shales by reducing the extent to which the pores are blocked by water.

4.5 GIP estimation

Understanding both the impact of extracted oil and moisture on porosity and gas adsorption properties is vital for an accurate evaluation of shale gas resources and the design of effective production strategies. Like moisture, the removal of oil generated by maturation can lead to an overestimation of GIP (Li, Stevens et al. 2021). The GIP can be estimated from the shale gas holding capacity which is calculated based on the free gas from porosity and adsorbed gas from high-pressure methane adsorption (Tang, Ripepi et al. 2016, Whitelaw, Uguna et al. 2019, Li, Stevens et al. 2021). Equation 3-3 (Section 3.5) has been used to calculate GIP in this study. The porosities of the dry and wet shale used for calculating the free gas are based on Equations 4-1 and 3-4 (Section 3.5). Considering the buried depths of the four samples, the reservoir pressure and temperature for the overmature shales, SH1 and SH2, are estimated as 600 bar and 100 °C, for the UK Bowland shales, BS3, 300 bar and 60 °C and GH4, 450 bar and 80 °C (Tang, Ripepi et al. 2016, Li, Zhou et al. 2018, Li, Stevens et al. 2021). The excess adsorbed gas content reduced by 45, 35, and 25 % at 100, 80, and 60 °C when compared with 25 °C (Rexer, Benham et al. 2013, Ji, Song et al. 2015, Zou, Rezaee et al. 2017).

$$Porosity_{dry} = \frac{V_{dry\ pore}}{V_{sh}} = 1 - \frac{\rho_{dry\ bulk}}{\rho_{dry\ sk}} \quad (4\text{-}1)$$

Where, $Porosity_{dry}$ is the total porosity of dry shale; $V_{dry\ pore}$ is the pore volume of dry shale; V_{sh} is the shale sample volume; $\rho_{dry\ bulk}$ is the bulk density of dry shales from mercury intrusion porosimetry (MIP) at 0.035 bar, $\rho_{dry\ sk}$ is the skeletal densities of the dry samples obtained from helium pycnometry.

The total porosity and GIPs estimated for the initial and extracted shales are compared in Table 4-4. Oil extraction increased the total porosity from 18.3 to 21.0% for the dry shales, BS3, and increases from 16.8 to 20.9% for the moisture equilibrated shale, which are much

larger increases than the other shales, as BS3 has the highest oil yield (Table 4-4). Table 4-4 indicates that the estimated GIP increases with total porosity, in the order of GH4>BS3>SH1>SH2 for the initial shales under both dry and moisture equilibrated conditions. Although SH1 and SH2 have much larger adsorbed gas (Q_a) contributions, the free gas (Q_{free}) contributions controlled by the total pore volume are smaller than for BS3 and GH4 (Table 4-3). However, in all cases, the free gas contributions dominate the GIP estimates for the initial dry shales (82, 65, 99, and 98% for SH1, SH2, BS3, and GH4, respectively, Table 4-4). As expected, the GIP estimated for the moisture equilibrated shales are lower than for dry shales, with reductions of 32, 38, 11, and 12% observed for initial SH1, SH2, BS3, and GH4, respectively, with the reductions for the extracted moisture equilibrated shales being 27, 28, 4 and 14%, respectively, when compared with the corresponding extracted dry shales (Table 4-4). The corrected GIP estimation should consider moisture on initial shales, since moisture always exists under the reservoir, and the initial shales are more representable for the geological condition. The GIP results mentioned above based on wet shales are lower than those on the dry shales (Table 4-4). This confirms that the GIP based on dry shales is significantly overestimated, as previous research (Krooss, Van Bergen et al. 2002, Chalmers and Bustin 2010, Li, Stevens et al. 2021) and Chapter 3 (Section 3.5) indicated. Moreover, moisture reduces the adsorbed gas (41-96%) more than the free gas (2-27%) for both the initial and extracted shale (Table 4-4) since the impact of moisture is mainly blocking micropores for adsorbed gas rather than the larger pores accommodating most of the free gas.

Overall, the changes arising from oil extraction are relatively small for the two overmature shales, SH1, SH2, and the gas window shale, GH4 (-3 to 6% for the dry shales and 1-12% for the moisture equilibrated shales, Table 4-4) with the largest changes being for the oil window shale, BS3. In contrast, Table 4-4 indicates that the GIP is overestimated by 16 and 22% for both dry and moisture equilibrated extracted oil window shale, BS3.

Clearly, the impact of solvent extraction on the estimated GIP is minimal for the two overmature shales investigated, especially compared to moisture (Table 4-4). In contrast, although some researchers believe removing oil in low maturity shale has little influence on methane adsorption (Liu, Huang et al. 2016), the impact of oil removal is significant for oil-window shales, with the GIP being over-estimated by 22% for the shale investigated in this

study. For such shales, a combination of moisture equilibration and not extracting oil present generated by maturation is essential to obtain reliable GIP estimates.

Table 4-4. The porosity, total pore volume, and the estimated GIP of the initial and extracted shales.

Sample name	Porosity (%)	V_{total} (m^3/t)	Q_a (kg/t)	Q_{free} (kg/t)	GIP (kg/t)	GIP change after extraction (%)
Dry Initial SH1	10.2	0.0432	2.1	9.3	11.4	6
Dry Ext SH1	10.2	0.0434	2.6	9.5	12.1	
Dry Initial SH2	4.0	0.0156	1.6	2.9	4.5	-3
Dry Ext SH2	3.8	0.0148	1.7	2.7	4.4	
Dry Initial BS3	18.3	0.0857	0.21	15.5	15.7	16
Dry Ext BS3	21.0	0.1008	0.44	18.2	18.7	
Dry Initial GH4	22.2	0.1046	0.44	22.8	23.2	3
Dry Ext GH4	22.8	0.1080	0.47	23.5	23.9	
Wet Initial SH1	6.8	0.0284	0.94	6.8	7.8	12
Wet Ext SH1	7.2	0.0304	1.5	7.3	8.8	
Wet Initial SH2	2.5	0.0095	0.49	2.3	2.8	11
Wet Ext SH2	2.7	0.0102	0.65	2.5	3.1	
Wet Initial BS3	16.8	0.0772	0.007	14.0	14.0	22
Wet Ext BS3	20.9	0.0990	0.022	17.9	18.0	
Wet Initial GH4	20.3	0.0930	0.023	20.3	20.3	1
Wet Ext GH4	20.2	0.0938	0.090	20.5	20.6	

Vtotal is the total pore volume calculated from the porosity of corresponding shales; Q_{free} is the free gas; Q_a is the absolute adsorption gas.

4.6 Conclusions

1) Solvent extraction has limited impact on the methane adsorption and pore texture for the dry overmature shales, SH1 and SH2, with the small amounts of extractable oil arising from drilling mud contamination. However, micropore volume and the methane adsorption capacities for the wet over mature shales increased after solvent extraction, possibly due to the reductions in moisture content, meaning that there is reduced pore blocking.
2) More than 60% of the extractable oil resides in micro and mesopores for the oil-window BS3. Removing the oil increased the nano, micro, meso, and macropore

volumes by nearly 300% for the dry BS3 and GH4. The increases in methane adsorption capacities are proportionally greater for the wet shales (207-282%) compared to the dry shales (90 and 3%).

3) Henry's Law estimations have indicated that the proportions of dissolved gas in the dry shale samples is very small. For wet shales, not all the residual oil is accessible if water blocks some of the micropores, which means the dissolved gas calculated by Henry's Law could be significantly overestimated.
4) Solvent extraction increases the estimated GIP by 16% for the dry oil-window shale, BS3, and moisture reduces the GIP of the initial BS3 shale by 11%. The GIP for extracted wet shale is overestimated by 22%. The impact on GIP estimates was considerably less for the over-mature shales due to their low extractable oil contents. Nevertheless, this study indicates the significant impact that natural oil arising from maturation can have on the estimated GIP for oil-window shales.

CHAPTER 5 EFFECT OF MICROPORE STRUCTURE AND FUNCTIONAL GROUPS ON METHANE ADSORPTION IN DRY KEROGENS: A COMPARISON BETWEEN MOLECULAR SIMULATION AND EXPERIMENTAL RESULTS

5.1 Summary

Understanding how thermal maturity controls methane adsorption in kerogen is crucial for predicting shale gas resources. Although porosity and chemical functionality are the main differences between kerogens, there is only a limited understanding of their impact on methane adsorption. Molecular dynamic (MD) simulations with matrix and slit pore models in conjunction with Grand Canonical Monte Carlo (GCMC) simulations and laboratory experiments of isolated Type II kerogens in a dry state are combined to demonstrate the controlling factors. The experimentally determined micropore volumes (V_{micro}) and equilibrium methane adsorption capacities (Qm) of isolated kerogens (10-75 mm^3/g TOC and 21.3-75.8 mg/g TOC, respectively) are comparable with the simulation results for over mature kerogens (19-261 mm^3/g TOC, and 36.5-148 mg/g TOC). However, the higher range of values from the simulation is due to a combination of possible larger inaccessible microporosity for methane molecules, and the largest interconnecting pore necks around 2 nm considered in the simulation being larger than the average neck size in the isolated kerogens. Both the experimental and simulation results indicate the major contributor to Type I (a) and I (b) isotherms are smaller (< 1 nm) and larger micropores (1-2 nm), respectively. The methane adsorption capacity of the kerogen matrix increases with increased maturity and micropore volume, with a positive correlation between V_{micro} and Qm observed. MD results of the relative number density and relative coordination number of methane around the functional groups at 25 and 100 °C showed that methane only has affinity with certain oxygen, sulfur, and nitrogen functional groups at very low pressure (<1.6 bar at 25 °C, <0.8 bar at 100 °C), and the affinity becomes much weaker at higher pressures with no significant differences among the functional groups considered. Moreover, the similar heats of adsorption (23.2, 23.1, 23.5, 22.8 KJ/mol) of methane with kerogens of different maturity modelled here confirm that the differences in surface functionality have a negligible effect on methane

adsorption. Therefore, micropore volume in kerogens is the key control for methane adsorption.

5.2 Literature review

Kerogen is defined as the insoluble fraction of the sedimentary organic matter present in shales (Djuricic, Murphy et al. 1971, Durand 1980, Philp 1985). The chemical and physical structure of kerogen varies enormously due to its origin and burial history (Durand 1980, Chen, Hu et al. 2013). Four kerogen types are distinguished depending on their origin (Type I: algal from a lacustrine anoxic environment, Type II: liptinitic from marine shale and continental planktons, Type III: humic originated from higher pants or terrestrial and quaternary coals, and Type IV from older sediments redeposited after erosion), leading to different elementary composition (Tissot 1984, Ganz and Kalkreuth 1987, Kelemen, Afeworki et al. 2007, Collell, Galliero et al. 2014, Tesson and Firoozabadi 2019). Type II kerogen is widely studied as the most representative for shale gas evaluation (Okiongbo, Aplin et al. 2005, Charpentier and Cook 2011, Collell, Ungerer et al. 2014, Zhao, Li et al. 2018). In addition to kerogen type, the maturity can be depicted to the Hydrogen/Carbon (H/C) and Oxygen/Carbon (O/C) elemental ratios based on the classical van Krevelen classification, which provide an overall representation of the different functional groups (Krevelen 1961, Dow 1977, Durand 1980, Tissot 1984, Behar and Vandenbroucke 1987).

The evaluation of gas in place (GIP) from adsorbed and free gas is critical for shale gas exploration (Curtis 2002, Ross and Bustin 2008, Whitelaw, Uguna et al. 2019, Li, Stevens et al. 2022). Adsorbed methane in kerogen accounts for a high proportion of the total adsorbed gas storage (Gasparik, Bertier et al. 2014, Li, Stevens et al. 2021). Laboratory experiments suggest that at least 50% of the adsorbed shale gas is adsorbed in kerogen (Fan, Tang et al. 2014, Rexer, Mathia et al. 2014), while higher contributions were observed in Chapter 3 (Section 3.4.3.2) using over mature (>2.0 %Ro) kerogens (59 and 83%), and Pang (2019) (Pang, Tian et al. 2019) with lower maturity (0.45 and 0.72 % Ro) Barnett (87%) and Eagle Ford (94.8%) kerogens. High maturity kerogens generally adsorb more methane than their lower maturity counterparts, with the physical structure and chemical surface being the main difference in these kerogens (Hu 2014, Zhao, Li et al. 2017, Huang, Ning et al. 2018). The microporosity and functional groups differences, especially sulfur and oxygen functional groups, generally are

believed to be the controls for the changes in methane adsorption capacity in kerogen with varying maturity (Zhao, Li et al. 2017, Huang, Ning et al. 2018, Wang, Li et al. 2021). A relatively strong positive correlation (R^2=0.87) between equilibrated methane adsorption capacity (Qm) and micropore volume (V_{micro}) in isolated kerogens is observed from earlier publications (Figure 5-1 A) (Rexer, Benham et al. 2013, Wang, Zhang et al. 2015, Li, Stevens et al. 2021). The positive correlation still exists (R^2=0.64) even only considering the effect of the total organic carbon content (TOC) (Figure 5-1B). The isolated kerogens from these three publications are of varying maturity (Appendix B, Table B1). Although this suggests that the micropore volume could be the main factor controlling the methane adsorption capacity of kerogen, a detailed simulation of kerogen is still needed to understand the effect of functional groups.

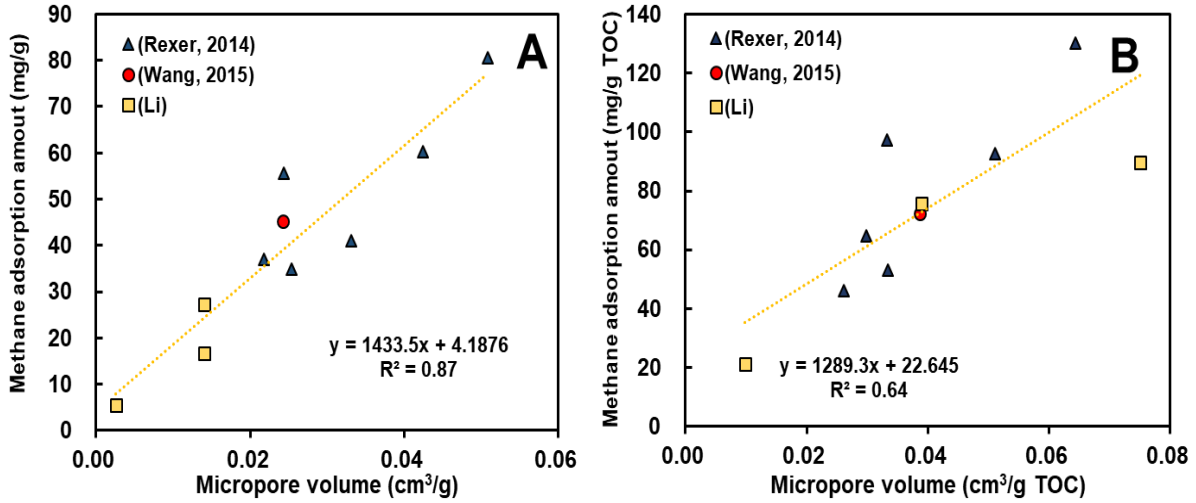

Figure 5-1. Correlation between equilibrated methane adsorption capacity (Qm) at 25 °C and micropore volume (V_{micro}). A) is the correlation with kerogen mass as the basis, B) is the correlation with TOC mass as the basis. The Qm in Rexer (2014) (Rexer, Mathia et al. 2014) and Wang (2015) (Wang, Zhang et al. 2015) are converted from 45 °C and 20 °C to 25 °C based on Rexer (2013) (Rexer, Benham et al. 2013). The micropore volume (<1.5 nm) in Rexer (2014) is measured by low-pressure CO_2 adsorption at 0 °C by the NLDFT model. The micropore volume in Wang (2015) is measured by low-pressure CO_2 adsorption at 0 °C by Dubinin-Astakhov (D-A) model. The data in (Li) is in this work (Chapter 5), the micropore volume is calculated by combined low-pressure CO_2 and N_2 adsorption at 0 °C and -196 ° C calculated by the NLDFT model (Li, Stevens et al. 2021).

Molecular simulation is a high fidelity tool that has been used to explore the local adsorption behaviour at a micro-scale, which is usually difficult to capture in experiments (Frenkel and Smit 2001, Ghanbarnezhad Moghanloo, Javadpour et al. 2013, Mosher, He et al. 2013, Collell,

Galliero et al. 2014, Li, Pang et al. 2019, Huang, Zhou et al. 2021). Significant progress was made on the simulation studies about the methane adsorption in kerogen in shale after the more realistic 3D kerogen molecules were built (Ungerer, Collell et al. 2015), based on X-ray and solid-state ^{13}C nuclear magnetic resonance (NMR) data (Kelemen, Afeworki et al. 2007). Kerogens in shales dispersed in the inorganic matrix exhibit a complex connected microporous network (Curtis, Ambrose et al. 2010). Various models are constructed to represent the kerogens in simulations. Condensed kerogen matrices used in most simulations include the small micropores (< 1 nm) due to limitations of model size (most model cell size less than 5 nm) (Zhao, Li et al. 2018, Huang, Ning et al. 2019, Wang, Li et al. 2021). Inserting dummy sphere pores (Collell, Galliero et al. 2014, Michalec and Lísal 2017, Tesson and Firoozabadi 2019) and constructing slit pores (Guo, Wang et al. 2020, Liu, Yang et al. 2022) are the main methods to introduce larger pores in kerogen models. Gas (methane/ethane/propane) adsorption on kerogen with controlled microporosity by dummy sphere pores ranging from 0.9 to 1.7 nm has been illustrated by simulation (Collell, Galliero et al. 2014, Michalec and Lísal 2017). Tesson (2019) (Tesson and Firoozabadi 2019) built a kerogen model with a 3.3 nm diameter dummy sphere pore to estimate the deformation and swelling of kerogen matrix in light hydrocarbons and carbon dioxide. Kerogen slit pore models, with pore sizes from 2 to 6 nm were constructed to state the adsorption and desorption of methane in different pores (Guo, Wang et al. 2020). Pores less than 10 nm account for most of the surface area (SA) in isolated kerogens (Li, Stevens et al. 2021), whereas the accessible volume present in micropores is regarded as the main adsorption space, which can be further distinguished as ultra-micropores (pore width <0.7 nm) and the super-micropores (pore width 0.7-2 nm) (Thommes, Kaneko et al. 2015). The realistic kerogen models that cover both ultra and super-micropores are essential to reveal the micropore impact on methane adsorption. Comparing the results from simulation with laboratory experiments is critical for verifying simulation and applying it in further research (Ungerer, Collell et al. 2015, Huang, Ning et al. 2018, Zhao, Li et al. 2018, Tesson and Firoozabadi 2019, Wang, Yao et al. 2021). A detailed comparison between simulation and experimental data for methane adsorption in micropores in kerogen has not been carried out previously (Ungerer, Collell et al. 2015, Zhao, Li et al. 2017, Chong, Sanguinito et al. 2021) due to the limited experimental data available on isolated kerogens.

The aim of this chapter combining experimental results and molecular simulations is to determine the impact of micropores and functional groups on methane adsorption in kerogen of varying maturity and to reveal the predominant controlling factor. Moreover, the detailed comparison between the experimental results and molecular simulations through Grand Canonical Monte Carlo (GCMC) and molecular dynamic (MD) simulations of kerogen matrices and pore slit models, can provide a solid foundation for further simulation work, for example, to understand the impact of moisture and to estimate GIP through simulation.

5.3 Experiments and Methods

The three kerogen concentrates (K1, K2, GHK3) were isolated by demineralization from two China shales (SH1 and SH2) and one UK shale (GH4) as previously described (Section 2.2.1). The two China shales (Ordovician-Lower Silurian, Sichuan Basin) investigated are dominated by Type II kerogen (Zou, Dong et al. 2010, Li, Stevens et al. 2022). The UK shale (Carboniferous, Bowland basin) is a mixture of Type II, III, and IV kerogens, with Type II/Type III interpreted as the majority (Andrews 2013, Clarke, Turner et al. 2018). The maturity (vitrinite reflectance) and total organic carbon content (TOC) are measured by LEICA DM4500P microscope and Leco CHN628 instruments as described in Sections 2.3.5 and 2.3.3. Low-pressure gas (CO_2, N_2) sorption at 0 and -196 °C (2.4.3), Mercury intrusion porosimetry (2.5.3), and Helium pycnometry (2.3.4) have been used to obtain the pore characteristics, porosity, bulk, and skeletal density. High-pressure methane adsorption experiments (2.4.2) were carried out on isolated kerogen at 25 °C in laboratory conditions by the High-Pressure Volumetric Analyzer (HPVA-100). Field Emission Scanning Electron Microscopy (FE-SEM) (2.5.1.2) and Transmission Electron Microscope (TEM) (2.5.1.3) are used for getting the images of kerogen in shale.

The simulation methods are detailed described in Section 2.6.2. Dry kerogen simulated models (matrix, 0.5 nm, 1.0 nm, 1.5 nm and 2.0 nm slits) are applied in this chapter, with the detail simulation setup in Section 2.6.2.1, model construction in Section 2.6.2.2, the methane adsorption capacity measured by GCMC method in Section 2.6.2.3, the microporosity measurement from simulation in Section 2.6.2.4, and the parameters of relative number density ($g(r)$) and relative coordination number (C_r) from MD simulation in Section 2.6.2.5. The simulated models constructed in Chapters 5 and 6 are representative for the pure dry

kerogen (Chapter 5) and kerogen with moisture (Chapter 6) with micropores (<2 nm) ranges, from immature (KIIA), early mature (KIIB), late mature (KIIC), to the overmature stage (KIID). All kerogen models are constructed with the periodic boundary condition at 600 bar and 100°C, as stated in Chapter 2, Section 2.6.2. The kerogen with pores larger than 2 nm and with mixed maturities are not considered in this thesis.

5.4 Results and discussion

5.4.1 Model verification

Comparing the density of the kerogen matrix with other simulation studies is an effective method for model verification (Ungerer, Collell et al. 2015, Huang, Ning et al. 2018). Table 5-1 lists the basic parameters of the simulated matrix. As expected, the matrix cell size of kerogen ranged from 3.52 to 3.85 nm, which is bigger than twice of cut-off distance, 3.1 nm. The average density of KIIA, KIIB, KIIC, and KIID from the triplicate matrix models increases with the maturity, from 1.11, 1.12, and 1.16 to 1.20 g/cm^3. The density is in good agreement with previous simulations, where, 1.0-1.15 g/cm^3 for KIIA (Ungerer, Collell et al. 2015, Huang, Ning et al. 2018, Huang, Ning et al. 2018, Tesson and Firoozabadi 2019), 1.16 and 1.18 g/cm^3 for KIIB and KIIC (Huang, Ning et al. 2018), and 1.18-1.28 for KIID (Ungerer, Collell et al. 2015, Perez and Devegowda 2017, Huang, Ning et al. 2018) are observed. The different simulated parameters for model construction, including temperature, pressure, kerogen molecule number, result in the slight difference of density in these studies.

Table 5-2 list the basic parameters of the isolated kerogen measured by experiment. Kerogens K1 and K2 are in the overmature stage with the VRs of 2.95 and 2.58 %Ro, GHK3 with the VR of 1.95 %Ro, is in the gas window stage, all of which can be compared with the KIID simulated model. Densities between 1.15 and 1.65 g/cm^3 have been previously reported for immature isolated kerogen (Hartgers, Damsté et al. 1995), and the density within the range of 1.10-1.40 g/cm^3 for the Type II kerogen with different maturity are also reported from experiments (Okiongbo, Aplin et al. 2005, Rexer, Mathia et al. 2014, Stankiewicz*, Bennett et al. 2015). The density varies due to the purity of isolated kerogen, most of which includes denser shale minerals. The matrix density from the simulation is comparable with the density measured from experiments, although results from experiments are relatively larger.

The bulk density measured from MIP is in the range of 0.21-0.59 g/cm^3, much lower than the skeleton densities (1.17-1.83 g/cm^3), due to the high porosities (75-89 %) of the isolated kerogens (Table 5-2). The pores in 'real' kerogen of shale contain meso, macropores (>2 nm) (Figure 5-2 A), and micropores (<2 nm) (Figure 5-2 B, C), where the kerogen matrix model can represent the kerogen matrix in shale, with most micropores less than 1 nm (Figure 5-2 B). Larger micropores exist in the kerogen matrix (Figure 5-2 C), indicating the kerogen slit models are necessary. The kerogen matrix and slit models built in this research are representable to cover the entire range of micropores to reveal the methane adsorption in micropores of kerogen.

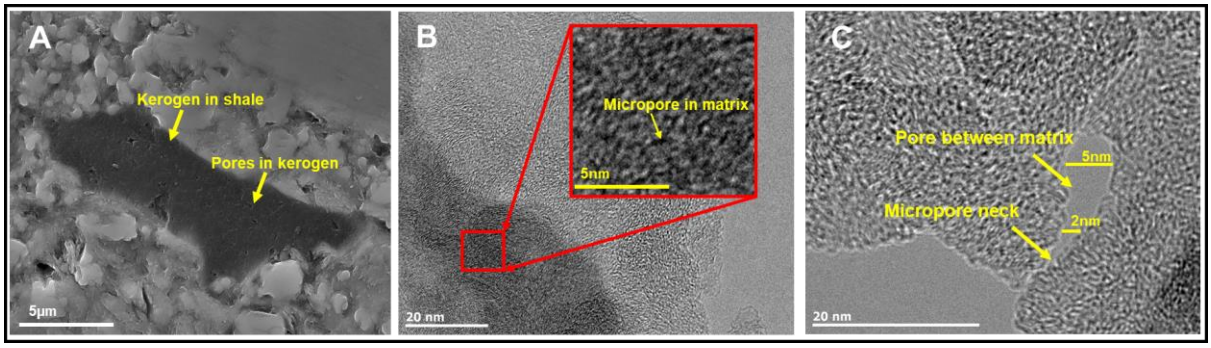

Figure 5-2. The SEM and TEM images of shale and isolated kerogen. A) The SEM image of meso-macropores of kerogen (K2) in shale, B) The TEM image of micropore in isolated kerogen matrix (K1), C) The TEM image of micropore neck between kerogen matrices (K2).

Table 5-1. The basic parameters for the kerogen units and matrix models.

Kerogen unit				Kerogen condensed matrix		
Name	Unit formula	Maturity*	TOC (wt.%)	Input kerogen unit number	Skeleton density(g/cm^3)	Cell size(nm) a= b=c
KIIA	C_{252} H_{294} N_6 O_{24} S_3	immature	78	10	1.11±0.009	3.85±0.004
KIIB	C_{234} H_{263} N_5 O_{14} S_2	beginning of the oil window	82	10	1.12±0.003	3.70±0.008
KIIC	C_{242} H_{219} N_5 O_{13} S_2	middle of the oil window	84	10	1.16±0.003	3.68±0.004
KIID	C_{175} H_{102} N_4 O_9 S_2	overmature, gas window	85	13	1.20±0.046	3.52±0.050

The maturity* description of each kerogen molecule is from (Ungerer, Collell et al. 2015). The mean of skeleton density and cell size are from triplicate models, and the errors represent the dispersion of a dataset relative to its mean.

Table 5-2. Basic parameters for the isolated kerogens from experimental data used this chapter.

Kerogen name	VR (% Ro)	TOC (wt.%)	Porosity (%)	Skeleton Density (cm^3/g)	Bulk Density (cm^3/g)	V_{ultra} (mm^3/g TOC)	V_{micro} (mm^3/g TOC)	Qm (mg/g TOC)
K1	2.95	36.0	89	1.17	0.21	24	39	75.8±4
K2	2.58	18.7	85	1.83	0.43	37	75	89.6±5
GHK3	1.95	26.0	75	1.44	0.59	9.8	10	21.3±2

Porosity is the ratio of the total pore space divided by the total sample volume, V_{ultra} is the ultra-micropore volume (<0.7 nm), V_{micro} is the total micropore volume (<2 nm). Qm is the mean from triplicate experiments, and the errors represent the dispersion of a dataset relative to its mean.

5.4.2 Comparison of simulation and experiment for pore volume

As Table 5-3 indicates, the pore volume of kerogen matrices and slits measured by different dummy probes (Figure 5-3 A, B) decreases with increasing probe size since the larger probes cannot detect all the pores (Figure 5-3 C). The pore volume measured by the smallest probe (probe d=0.10 nm) by simulation closed to pore volume covered by van der Waals surface (Figure 2-21 C), contains a high proportion of inaccessible pore volumes for any existing gas molecule, even for He, the smallest gas molecule, with a diameter of 0.26 nm (Figure 5-3 C). The micropore pore volume (probe d=0.10 nm) of the kerogen matrix increases with the maturity from 108, 113, 122 to 156 mm3/g TOC for KIIA to KIID (Table 5-3). This positive correlation between maturity and measured pore volume still exists until the probe diameter reaches 0.33 nm, where the measured micropore volumes are 0.93, 2.2, 2.3, and 19 mm3/g TOC for KIIA, KIIB, KIIC, and KIID. Although the 0.33 nm (CO_2) diameter probe could be too big to access all the pores in kerogen models (Figure 5-3 C), the pore volumes measured by 0.33 nm (CO_2) diameter probe (Figure 5-3 B) is considered as the 'CO_2 accessible' micropore volume used to compare with the pore volume of isolated kerogens measured by low-pressure gas (CO_2 and N_2) sorption experiment.

Table 5-3. Micropore volume of kerogen (KIIA, KIIB, KIIC, and KIID) matrix and KIID slits measured by different probes (probe diameter from 0.10 to 0.38nm) from simulation.

Probe diameter (nm)	Matrix V_{micro} (mm^3/g TOC)				KIID Slit V_{micro} (mm^3/g TOC)			
	KIIA	KIIB	KIIC	KIID	0.5 nm slit	1.0 nm slit	1.5 nm slit	2.0 nm slit
0.10[a]	**108**	**113**	**122**	**156**	**241**	**296**	**369**	**437**
0.15	44	51	60	98	172	227	303	371
0.20	16	22	27	61	124	180	258	326
0.25	5.6	9.1	11	39	91	146	226	295
0.30	1.8	3.9	4.2	25	66	121	203	272
0.33[b]	**0.93**	**2.2**	**2.3**	**19**	**54**	**109**	**191**	**261**
0.35	0.60	1.7	1.3	16	47	102	184	254
0.36[c]	**0.48**	**1.5**	**1.0**	**15**	**44**	**99**	**181**	**251**
0.38[d]	**0.32**	**1.0**	**0.58**	**13**	**38**	**93**	**175**	**245**

0.10[a], 0.10 nm diameter probe is the smallest probe in this simulation; 0.33[b], 0.33 nm diameter probe has the same diameter as a CO_2 molecule; 0.36[c], 0.36 nm diameter probe has the same diameter as a N_2 molecule; 0.38[d], 0.38 nm diameter probe has the same diameter as a CH_4 molecule.

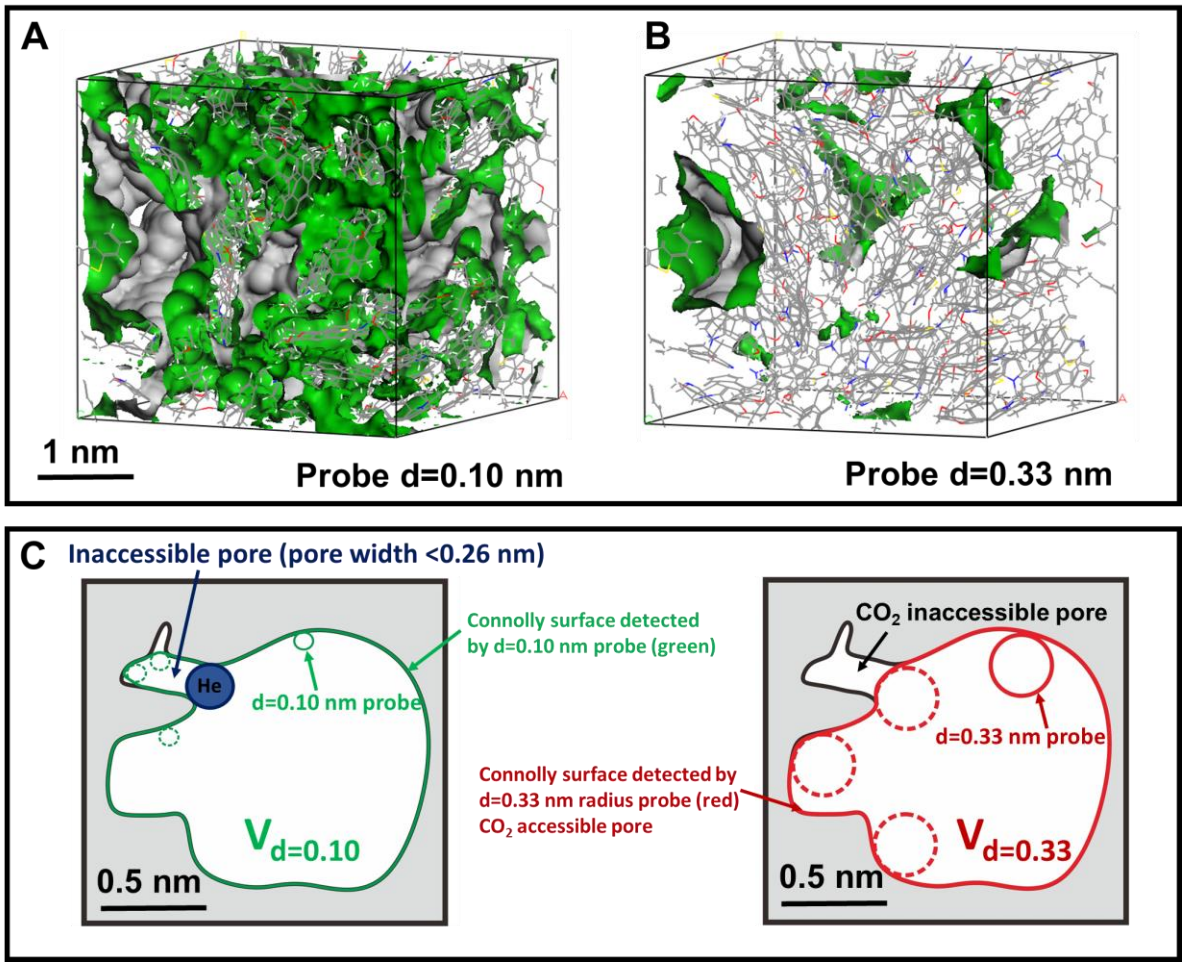

Figure 5-3. The pore volume of KIID matrix wrapped by Connolly surface (detected pores are inside of grey surface) measured by 0.10 nm (A) and 0.33 nm diameter probes (B), and a schematic representation of the difference between inaccessible and CO_2 accessible pore in the pore volumes measured by 0.10 nm, and 0.33 nm probe (C).

Figure 5-4 presents the micropore size distribution (MPSD) of isolated kerogen, simulated kerogen matrix, and kerogen slits. The micropore volume of the isolated kerogen is on a TOC basis to eliminate the impact of residue minerals. Two prominent peaks are observed (Figure 6A), the first (P_{ul}) is ultra-micropore (<0.7 nm) peak, in the range of 0.3 to 0.5 nm (K1, K2, and GHK3), and the second (P_{su}) is super-micropore (0.7-2.0 nm) peak, in the range of 1.2 to 2.0 nm (K1 and K2), which is smaller for GHK3. The total micropore volumes of K1, K2, and GHK3 are 39, 75, and 10 mm^3/g TOC, respectively, with more than 50% (62, 50, and 98%), contributed by ultra-micropores (< 0.7 nm), accounting for 24, 37, and 9.8 mm^3/g TOC for K1, K2, and GHK3, respectively (Table 5-2).

The major peak (P_{in}, peak value <300 mm^3/g TOC) is contributed by the inaccessible pore (pore width < 0.26 nm) in simulation for all the kerogen models (Figure 5-4 B, C), which is not comparable with the 0.3 to 0.5 nm ultra-micropore (< 0.7 nm) peak (P_{ul}) found in isolated kerogen (Figure 5-4 A), since pores less than 0.26 nm are not measured experimentally. However, another peak (P_{ul}, peak value <6 mm^3/g TOC) within 0.3 to 0.5 nm is observed in the enlarged MPSD of the kerogen matrix models (Figure 5-4 D) and the MPSD of kerogen slits model (Figure 5-4 C), which matches very well with the ultra-micropore (< 0.7 nm) peaks (P_{ul}, peak value is 3-12 mm^3/g TOC) for the isolated kerogen (Figure 5-4 A), even considering the incremental micropore value at peaks. A third peak (P_{su}, peak value < 30 mm^3/g TOC) in the kerogen slit models is observed ranging from 0.8 to 2.0 nm depending on the size of the slit (Figure 5-4 C), which matches the super-micropore (0.7-2.0 nm) peak (P_{su}, peak value < 12 mm^3/g TOC) in isolated kerogen in Figure 5-4 A very well.

The micropores in the KIID matrix and KIID 0.5 nm slit models are dominated by ultra-micropores (Figure 5-4 B, C), matching the MPSD of isolated kerogen GHK3 well (Figure 5-4 A). While, simulated kerogen 1.0, 1.5, and 2.0 slits models provide good MPSD representations for K1 and K2 isolated kerogens since they include both ultra as well as super micropores (Figure 5-4). However, the micropore volumes of simulated kerogens are relatively higher than those of corresponding isolated kerogens they represented. The micropore volumes (CO_2, d=0.33 nm) for KIID matrix and 0.5 nm slit are 19 and 54 mm^3/g TOC, with an average of 36.5 mm^3/g TOC, being about 3 times larger than that of GHK3 (10 mm^3/g TOC). For KIID 1.0, 1.5, and 2.0 nm slits models, the micropore volumes (CO_2, d=0.33 nm) are 109, 191, and 261 mm^3/g TOC, respectively, the average of which (187 mm^3/g TOC) is around 2-4 times higher than those of isolated kerogens K1 and K2 (39 and 75 mm^3/g TOC). Higher pore volumes are observed in simulation as all the pores, even closed pores and larger pores interconnected with narrow or complex pore necks (<0.33 nm), are measurable as long as they are larger than the probe size, which is 0.33 nm diameter probes here. In actual kerogens, closed pores and the larger pores interconnected with narrow or complex pore necks (<0.33 nm) are inaccessible to CO_2.

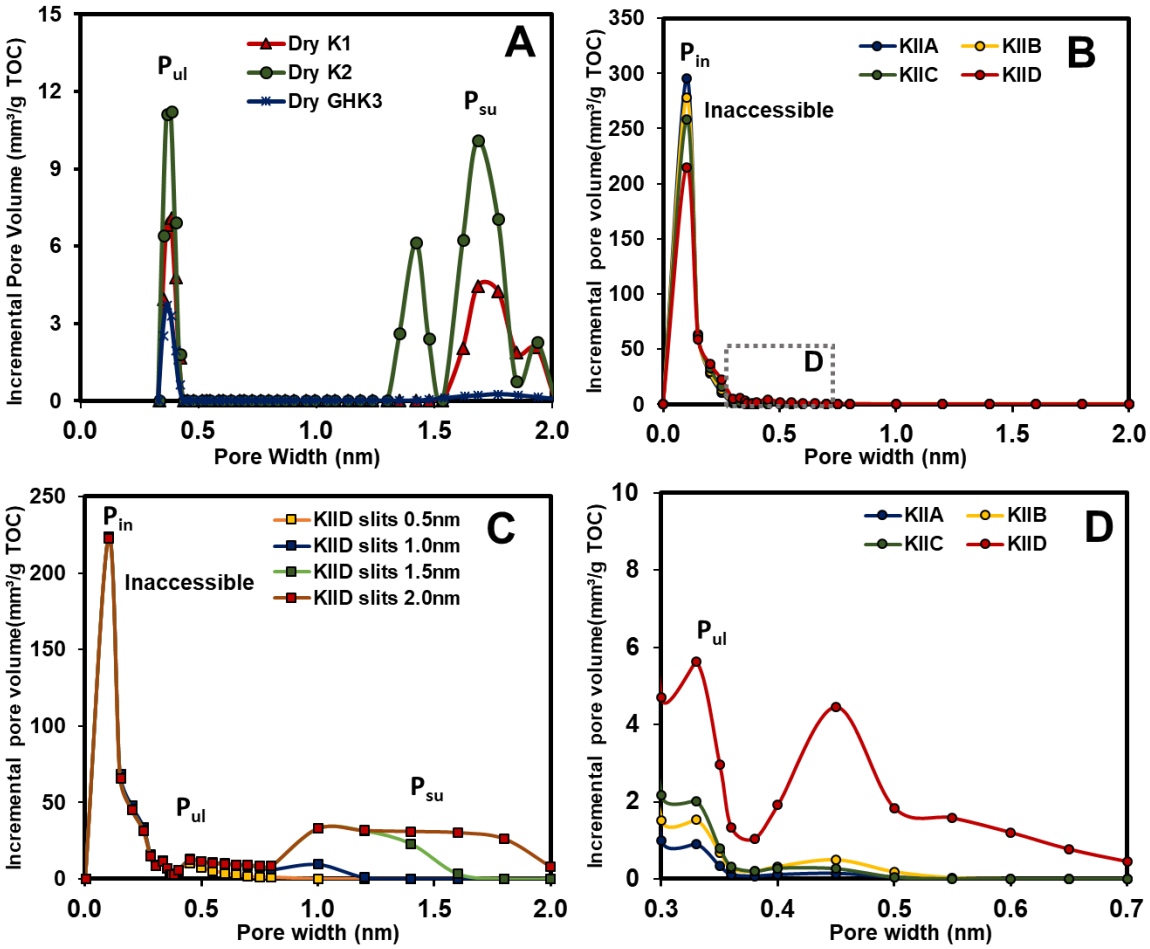

Figure 5-4. The micropore size distributions (MPSD) of A) the isolated kerogens (K1, K2, and GHK3) from experiment, B) kerogen matrices ((KIIA, KIIB, KIIC, and KIID) from simulation, C) KIID kerogen slits from simulation, D) kerogen matrices ((KIIA, KIIB, KIIC, and KIID) from simulation (pore size range 0.3 to 0.7 nm).

5.4.3 Methane adsorption capacities by simulation

The methane adsorption isotherms at 25 and 100 °C of the kerogen matrices with varying maturity (KIIA, KIIB, KIIC, and KIID) from simulation are compared in Figure 5-5. All kerogen matrices have Type I (a) isotherms displaying a steep isotherm at a low-pressure range (Thommes, Kaneko et al. 2015). The methane adsorption capacity, Qm increases with maturity, from 15.9 to 45.9 mg/g TOC at 25 °C (Figure 5-5 A), and from 12.5 to 36.5 mg/g TOC at 100 °C (Figure 5-5 B) (Table 5-4). The weaker methane adsorption capacity is observed at a higher temperature, in common with experimental researches studies (Rexer, Benham et al. 2013, Hu 2014, Zou, Rezaee et al. 2017), where the Qm reduced less than 40 % (from 25 °C to 100 °C) for overmature shale (Rexer, Benham et al. 2013), 23.1-41.1 % (from 25 °C to 80 °C)

for oil window shales (Zou, Rezaee et al. 2017), and 10-18 % (from 35 °C to 75 °C) for low-overmature kerogen (Hu 2014). The Qm of KIIA, KIIB, KIIC, and KIID matrix decrease 21, 18, 25, and 20 %, with an average of 21 %, as the temperature increases from 25 °C to 100 °C (Table 5-4), which is relatively less than above reductions (around 30%) observed from experiments considering same temperature increase. This could be because kerogen matrices from simulations dominated by ultramicropores have higher adsorption potential than the real kerogen in shales containing both ultra- and super micropores pores (Polanyi 1963, Thommes, Kaneko et al. 2015), resulting in more methane molecules adsorbed on matrices in simulation at same temperature.

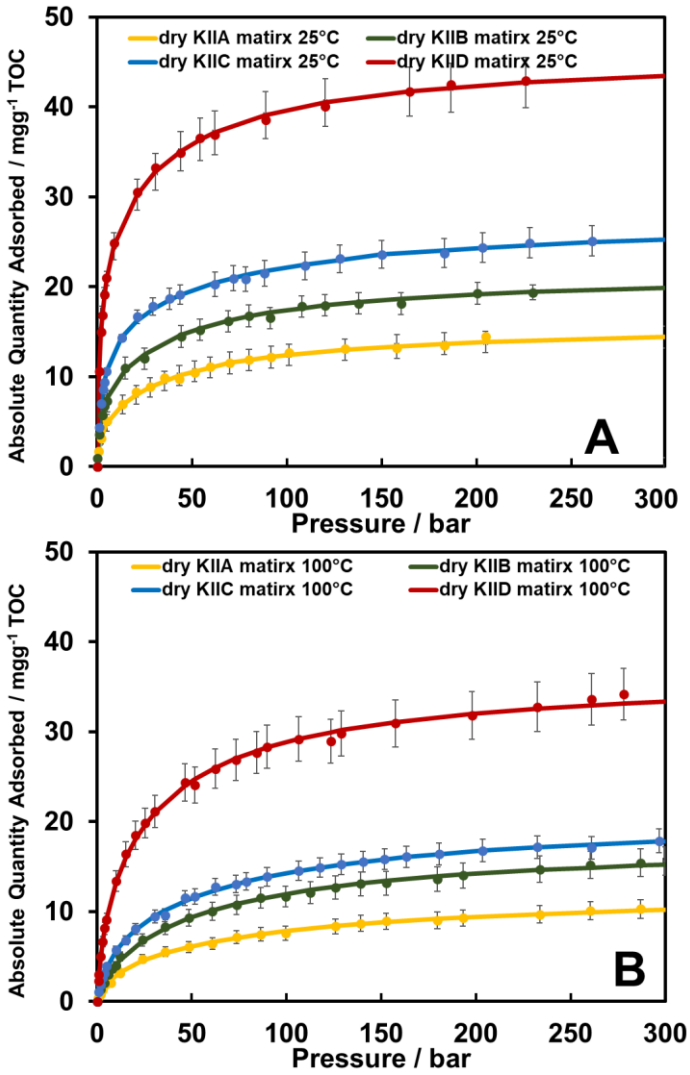

Figure 5-5. The methane adsorption isotherms of the kerogen matrices at 25 °C (A) and 100 °C (B) from simulation. The points on each isotherm are the absolute methane adoption amount from simulation, and the solid lines are the data predicated by the dual-site Langmuir model (Section 2.4.1.3, Equation 2-15).

Table 5-4. The Qm of the kerogen matrices and slit models from simulation.

Kerogen matrix	Qm (mg/g TOC) at 25 °C	Qm (mg/g TOC) at 100 °C	Kerogen slits	Qm (mg/g TOC) at 25 °C	Qm in slit pores contribution (%)
KIIA	15.9±1.2	12.5±1.3	KIID 0.5nm	74.7±6.3	39
KIIB	21.7±1.4	17.9±1.8	KIID 1.0nm	96.1±8.0	52
KIIC	27.8±1.9	20.9±1.5	KIID 1.5nm	122±10	62
KIID	45.9±2.8	36.5±3.1	KIID 2.0nm	148±12	69

The mean of Qm is from triplicate experiments, and the errors represent the dispersion of a dataset relative to its mean.

The methane adsorption capacity of the kerogen matrix increases in the order of KIIA<KIIB<KIIC<KIID (Table 5-4), consistent with their increase micropore volumes with maturity (Table 5-3). The correlations of Qm and micropore volume measured by different probes of the twelve-matrix models using the triplicate matrix models and simulations are plotted in Figure 5-6. Positive linear correlations of Qm with micropore volume are observed, especially for the micropore volume measured by the probes with diameters smaller than 0.2 nm (0.10, 0.15, and 0.2 nm), and so this includes inaccessible pores (<0.26 nm) (Figure 5-6 A, B, C), with R^2>0.96. Slightly weaker correlations are observed when the probe size increases from 0.25 to 0.38 nm (Figure 5-6 D-I), with R^2 in the range of 0.82-0.93. This could arise from the differences in shape between dummy probes (sphere) and the methane molecule (face configuration), making some pores accessible to methane but not by dummy probes. The positive correlations confirm that the micropore volume impacts the methane adsorption capacity of kerogen significantly. Wang (2021) (Wang, Li et al. 2021) states that pores closer to methane's diameter are responsible for about 20% of the adsorption inside the sample, and it is these small pores that dictate the largest adsorption capacity inside kerogen.

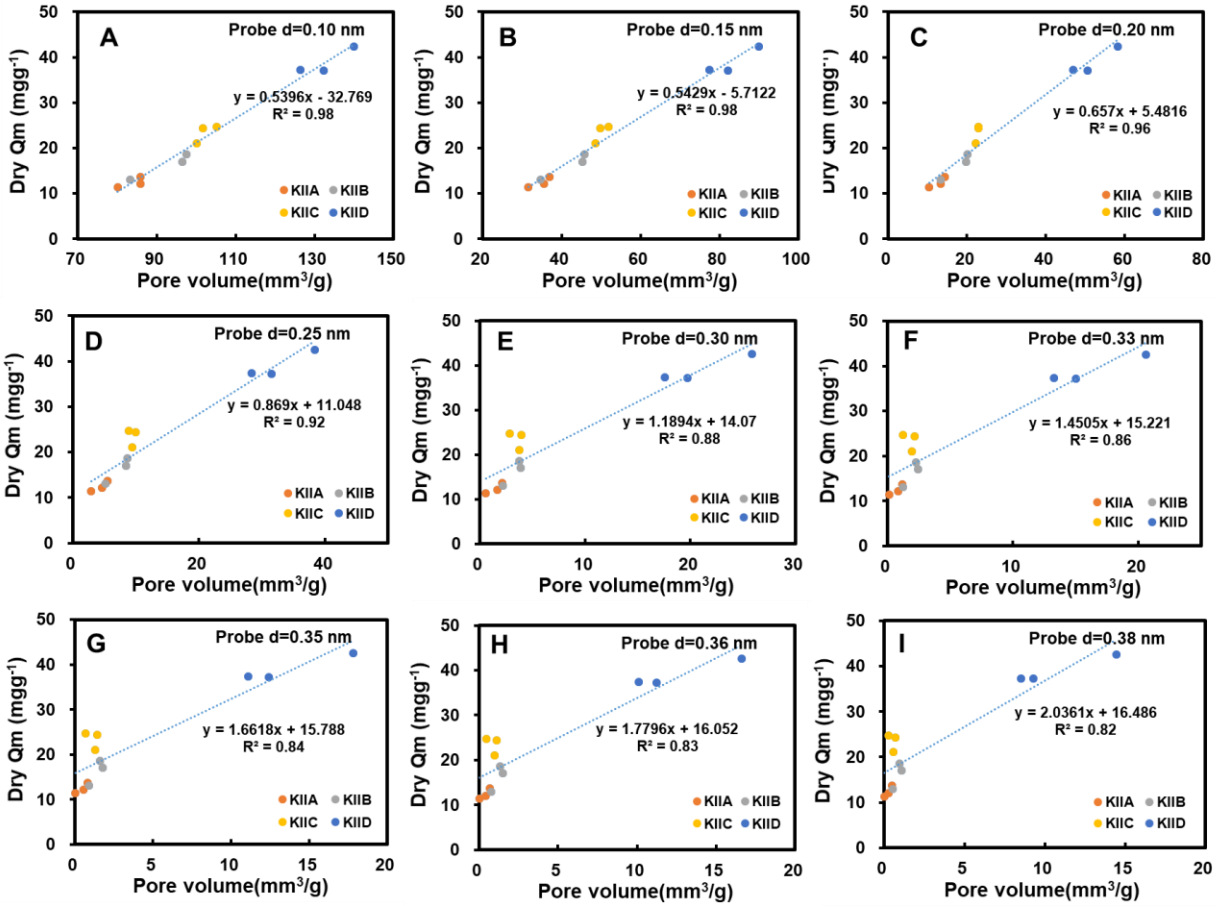

Figure 5-6. The correlations of Qm and micropore volume measured by different probes for the twelve kerogen matrix models (KIIA, KIIB, KIIC, KIID) at 25 °C. The three points with the same colour for each kerogen indicate the simulation results from its triplicate matrix models.

5.4.4 Comparison of simulation and experiment for methane adsorption capacities

The methane adsorption isotherms of the KIID matrix, slits (from simulation), and isolated kerogens (from experiment) at 25 °C are compared in Figure 5-7. The pore characteristics control the methane adsorption isotherm shapes, both in simulation and experiment. GHK3, KIID matrix, KIID slit 0.5 nm have typical Type I (a) isotherms (Figure 5-7 A), arising from the small micropores (<1.0 nm) (Thommes, Kaneko et al. 2015), since mainly ultra-micropores (<0.7 nm) present in these three samples (Figure 5-7). The Type I (a) isotherms display a steep uptake at low pressure due to the enhanced interactions between methane and kerogen in the ultra-micropores, resulting in micropore filling (Thommes, Kaneko et al. 2015). Larger micropores (>1.0 nm) predominate in Type I (b) isotherms (Thommes, Kaneko et al. 2015), which are found in the isolated kerogens K1, K2, simulated KIID 1.5 nm and 2.0 nm slit models

(Figure 5-7 A), as they include both ultra- (<0.7 nm) and super-micropores (0.7-2.0 nm) (Section 5.4.2, Figure 5-4). As expected, the isotherm for the KIID slit 1.0 nm model is intermediate between Type I (a) and (b) isotherms, due to the existence of small proportions of super-micropores from 0.7 to 1.0 nm.

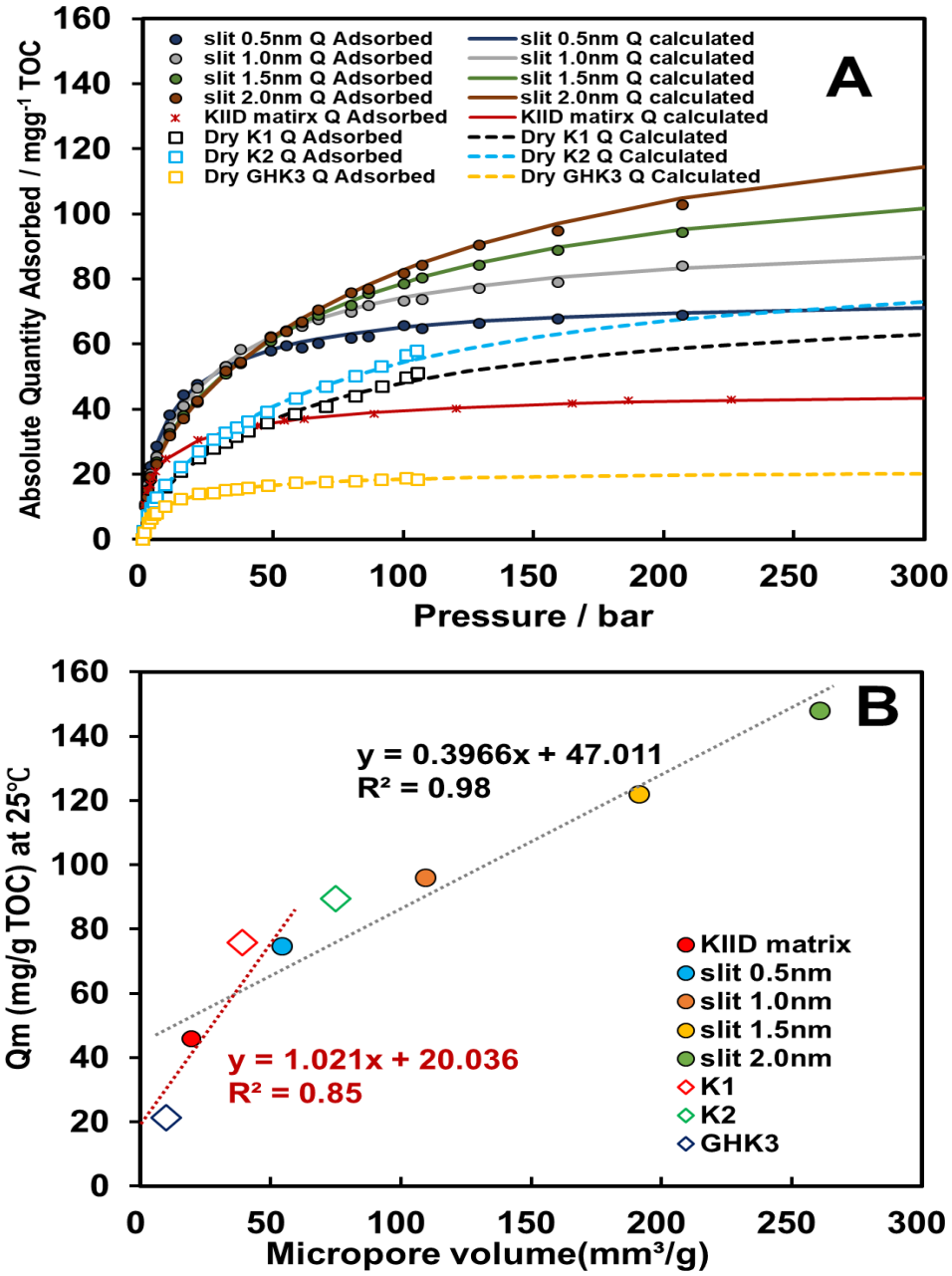

Figure 5-7. A) The methane adsorption isotherms of KIID matrix, slits (from simulation), and isolated kerogen (from laboratory experiment), B) The correlations of Qm and micropore volume of the KIID models from simulation and isolated kerogens from the experiment. The micropore volume in simulation is measured by a 0.33 nm diameter probe (same diameter as CO_2) to compare with the experimental data (measured by N_2 and CO_2).

For the same type of kerogen (KIID/overmature), the methane adsorption capacity increases as the micropore volume increases in both simulation and experiment (Figure 5-7 B). The Qm of the simulated KIID matrix, slits of 0.5 nm, 1.0 nm, 1.5 nm, and 2.0 nm are 45.9, 74.7, 96.1, 122, and 148 mg/g TOC, respectively (Table 5-4), which correlates well (R^2 is 0.98) with the micropore volume (probe d=0.33 nm) (Figure 5-7 B). The Qm in slit pores can contribute 39, 52, 62, and 69% to the total Qm for simulated kerogens with slits of 0.5 nm, 1.0 nm, 1.5 nm, and 2.0 nm, respectively (Table 5-4), assuming the kerogen matrix layer in the slit models adsorbed the same amount of methane as kerogen matrix alone. Thus, more super-micropores can provide more sites for methane adsorption. Similar positive correlation results between Qm and micropore volume are found for isolated kerogens, K1 and K2, with the higher micropore volumes giving a higher Qm (75.8 and 89.6 mg/g TOC) than GHK3 (21.3 mg/g TOC) (Table 5-2). However, the correlation (R^2 is 0.85) is less than simulation. Overall, these results indicate that for the same type of kerogen (overmature) with a similar chemical surface (functional groups), micropore volume is the critical control for methane adsorption capacity.

The experimental results match well with the simulation results considering the methane adsorption isotherm shapes. Isolated kerogen GHK3 matches well with the KIID matrix and KIID 0.5 nm slit models, reflecting Type I (a) isotherms, and the isolated K1 and K2 kerogens display Type I (b) isotherms, comparable with the KIID 1.5 nm slit model, slightly out of range compared to KIID 1.0, and 2.0 nm slit isotherms (Figure 5-7 A). Consistent with the higher pore volumes obtained from simulation, the methane adsorption capacities (Qm) from simulation are also generally higher than those from experiment. The average Qm (60.3 mg/g TOC) of the KIID matrix (45.9 mg/g TOC) and 0.5 nm slit (74.7 mg/g TOC) models are about 2 times larger than that for GHK3 (21.3 mg/g TOC). Further, the Qm of KIID 1.5 nm slit model (122 mg/g TOC), as well as the average Qm (122 mg/g TOC) of KIID 1.0, 1.5, and 2.0 nm slit models (96.1, 122, and 148 mg/g TOC) are 1.1-2.0 times as large as those for K1 and K2 (75.8 and 89.6 mg/g TOC).

Generally, the larger Qm values from simulation arise from the much higher accessible pore volumes in the simulated kerogens (Table 5-2 and Table 5-3). The GCMC method utilised to simulate the methane adsorption amount in simulation is based on the random insertion of gas molecules based on massive probability statistics (Nicholson 1982, Frenkel and Smit 2001,

Ho, Criscenti et al. 2016), where all the pores should be accessible as long as pores are large enough for methane molecules inserting. Thus, the effects of closed pores and the complexed pore interconnectivity are neglected in GCMC simulation. Although there are plenty of closed pores and complex pore networks in isolated kerogens (Li, Stevens et al. 2021, Wang, Tian et al. 2021), resulting in inaccessible pores or limiting the migration for methane molecules under experimental conditions. In addition, the closer Qm difference between KIID 1.5 nm slit and isolated kerogens (K1 and K2), than the Qm difference between KIID matrix, 0.5 nm slit, and GHK3 isolated kerogen, suggests that GHK3 has a higher proportion of methane inaccessible pores, and the pores interconnectivity considered in slits models, especially 1.5 nm slit, is more representative to the K1 and K2, where the pores <1.5 nm should mostly be connected. The slightly steeper isotherm and much larger Qm for the 2.0 nm slit model compared to the isolated kerogens, K1 and K2, indicate that the average neck size in the isolated kerogens investigated are smaller than the largest interconnecting pore necks (2.0 nm) used in the models, where lots of pore necks less than 1.3 nm exist in isolated keroegns (Chapter 3, Section 3.4.4).

5.4.5 The impact of functional groups on methane adsorption capacity by simulation

The C, O, N, and S functional groups used are listed in Table 5-5, which reflects the major compositional differences between the kerogens. KIIA, as the most immature kerogen, contains all the functional groups considered (Figure 5-8), and, clearly, the concentrations of the O, N, S, and aliphatic C functional groups decrease with increased maturity (Table 5-5). The MD analysis discussed in this section is based on KIIA and KIID, and the data of KIIB and KIIC is in the supplemental information (Appendix B, Figure B1).

Table 5-5. The number of carbons associated with the functional groups in each kerogen molecule presented in Figure 2-20.

Element	Functional groups ID	KIIA No. of C / kerogen molecule	KIIB No. of C/ kerogen molecule	KIIC No. of C/ kerogen molecule	KIID No. of C/ kerogen molecule
O	COOH	2	1	1	0
	C=O	7	0	2	0
	C-OH	4	1	0	0
	C-O-C	18	22	18	18
N	C-NH-C	8	8	6	6
	C-N=C	2	2	4	2
	NC3	3	0	0	0
S	C-S-C ring	4	2	2	4
	C-S-C chain	2	2	2	0
C	C sp2	85	91	126	120
	C sp3 CH2	93	73	64	14
	C sp3 CC3	24	32	17	11

Each functional group amount is presented in terms of the number of associated carbons (C) atoms. The chemical formulas for KIIA, KIIB, KIIC, and KIID are $C_{252}H_{294}O_{24}N_6S_3$, $C_{234}H_{263}O_{14}N_5S_2$, $C_{242}H_{219}O_{13}N_5S_2$, and $C_{175}H_{102}O_9N_4S_2$. The functional groups (Figure 5-8) include carboxyl (COOH) (Figure 5-8A), carbonyl (C=O) in aldehyde and ketone (Figure 5-8B), hydroxy (C-OH) in alcohol and phenol (Figure 5-8C), ether bond (C-O-C) in tetrahydrofuran, aliphatic and linked with aromatic compounds (Figure 5-8D), C-NH-C in pyrrole (C-NH-C) (Figure 5-8E), C-N=C in pyridine (C-N=C) (Figure 5-8F), NC3 in n-alkyl 2-pyrroline (NC3) (Figure 5-8G), C-S-C in thiophene (C-S-C ring) (Figure 5-8H), sulfide in the aliphatic chain (C-S-C chain) (Figure 5-8I), aromatic carbon (C sp2) (Figure 5-8J), the aliphatic carbons, sp3 hybridised, linked with two or three hydrogen bonded atoms, the secondary or the primary carbon atom, (C sp3 CH2) (Figure 5-8K), and the quaternary aliphatic (C sp3 CC3).

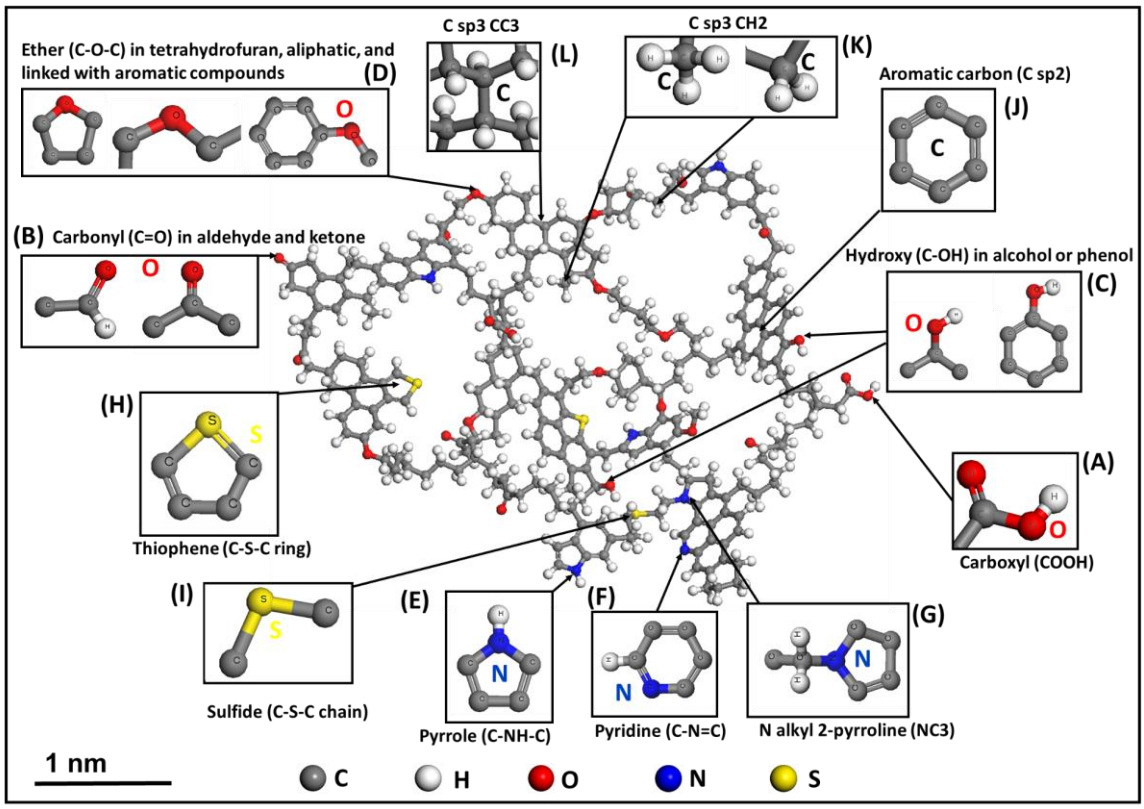

Figure 5-8. Examples of the functional group types in Table 5-5, considered in the KIIA molecule.

Figure 5-9 presents the relative methane number density (g(r)) of the different functional groups in KIIA at 25 °C. The higher peaks of g(r) around selected functional groups (C-O-C, NC3, C-S-C chain) are only apparent when methane is at very low number amount (<25 CH_4), which is also the low density and pressure (<0.001 g/cm^3, <1.6 bar 25 °C) (Figure 5-9 A-C). The impact of each functional group is limited by the distance (r) from methane, as all the peaks observed end at 1.4 nm, with most ending before 0.6 nm, confirming the affinity between methane and the functional group become weaker with the distance increase, since the affinity is mainly controlled by the van der Waals (vdW) force with a cut-off distance of 1.55 nm. Moreover, the g(r) peaks start to level off when the methane pressure increases from 3.2 to 18.5 bar at 25 °C (methane amount increase from 50 to 300) (Figure 5-9 D-H, Figure 2-22 in Section 2.6.2.5), suggesting the methane affinity will not be affected by the functional group difference when the pressure is higher than 3.2 bar at 25 °C (methane amount larger than 50, Figure 5-9 D-H).

Similar results are found in the relative coordination number (C_r) of methane around each functional group. For example, KIIA, the C_r of these functional groups only have apparent differences ranging from 0.002 to 0.008, when methane is in low amount (<25), with the corresponding low pressure of 1.6 bar at 25 °C (Figure 5-10 A). In contrast, as soon as the pressure increases (>1.6 bar), the C_r of these functional groups decrease and become very close, all being less than 0.0015 (Figure 5-10 A), which indicates the affinity between methane and these functional groups become much weaker at higher pressures with no significant differences among the functional groups considered. The effect of functional groups on methane adsorption is even weaker at 100 °C (Figure 5-10 B), with all the average C_rs are lower than those at 25 °C. Values of C_r above 0.006 only for a few function groups (C-S-C chain and NC3) is observed when the methane amount is less than 10, with the corresponding pressure lower than 0.8 bar at 100 °C (Figure 5-10 B). The same effects of pressure and temperature on C_r are observed for KIIB, KIIC (Appendix B, Figure B1), and KIID (Figure 5-10 C, D), and the selected functional groups at low pressure are varied with different kerogen and temperature. These results further indicate the selectivity of methane on these functional groups makes little difference when the pressure is at a low range and almost no difference when the pressure increases since all the C_rs are very close, suggesting no preferred sorption sites around these functional groups exist for methane at reservoir conditions (high pressure and high temperature).

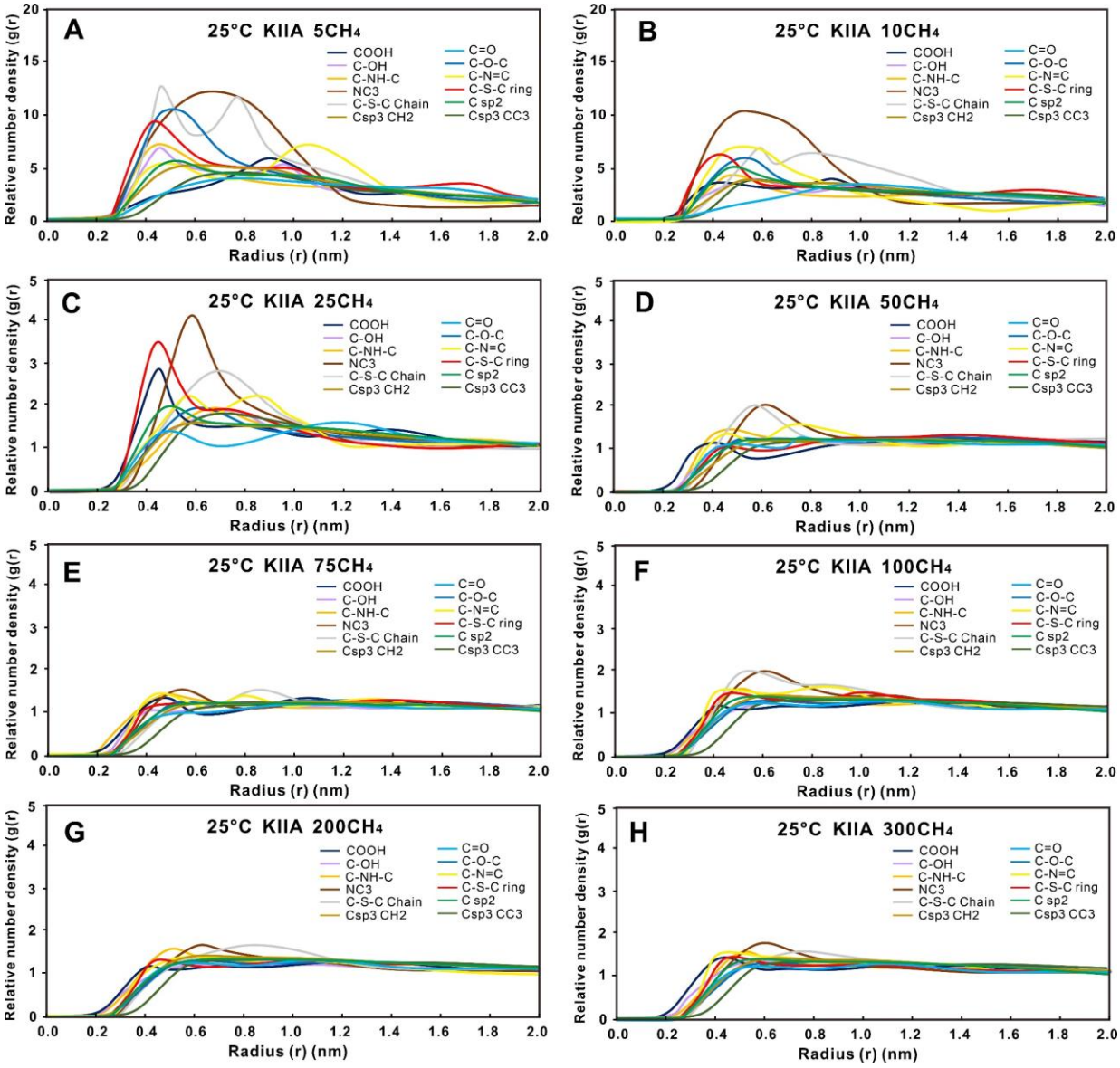

Figure 5-9. The relative number density (g(r)) of methane (CH_4) around functional groups in the KIIA relaxed kerogen matrix model at 25 °C. A to H is the loaded methane from low to high number amount (5-300), whose corresponding density and pressure range from (0.0002 to 0.0124 g/cm^3, and 0.3-18.5 bar as presented in (Figure 2-22, in Section 2.6.2.5).

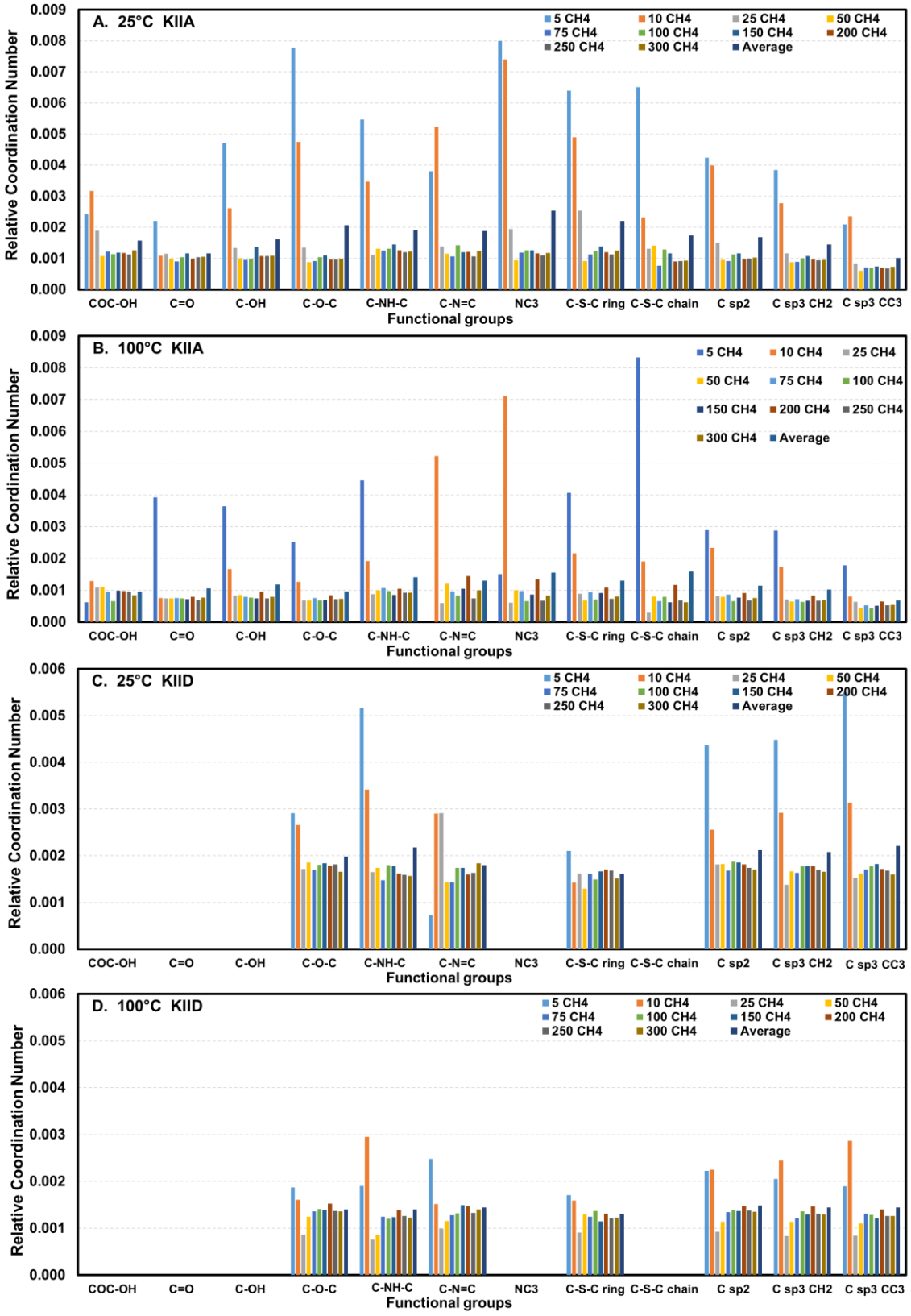

Figure 5-10. The relative coordination number (C_r) for methane around functional groups in kerogens KIIA and KIID at 25 and 100 °C. 'Average' is the average C_r of methane from 5 to 300 methane molecules. A) KIIA at 25 °C, B) KIIA at 100 °C, C) KIID at 25 °C, D) KIID at 100 °C.

Moreover, the adsorption heat of methane adsorption for kerogen matrix showed no significant variation with maturity at 25 °C, which is very close to 23 KJ/mol, varies from 23.2, 23.1, 23.5, and 22.8 KJ/mol for KIIA, KIIB, KIIC, and KIID matrix. The simulation adsorption heat results are close to the calculated adsorption heat range from 20.77 to 24.05 kJ/mol for the isolated kerogen samples (Li, Zhou et al. 2018). The similar adsorption heats with the kerogen matrix suggest the affinities between methane and kerogens of varying maturity (and functional groups) are very close, with no selected sorption sites existing for methane. This confirms that microporosity is the critical control for the methane adsorption capacity in kerogen rather than any functional group differences.

The data (V_{micro} and Qm) from the simulation are larger than those from experiments due to the measurement method and models constructed in the simulation being different to the experimental method and the isolated kerogen. For the V_{micro}, probe measurement (Section 2.6.2.4) is applied in simulation, where all the pores with a pore size larger than the CO_2 dummy probe (0.33 nm) are accessible for the probe, even for the dead pores and the pores blocked by narrow pores necks (<0.33 nm). For the real isolated kerogens, a low-pressure gas sorption experiment (Section 2.4.3) is carried out. These dead pores and pores blocked by narrow pore necks are not measurable since they are not accessible to CO_2 molecules, indicating these pores could not be measured in this experiment. The V_{micro} from the simulation is all the micropores bigger than 0.33 nm, while the V_{micro} from the experiment indicates all the accessible pores for the CO_2 molecules.

The difference can be calibrated once the proportion of the dead pores and pores blocked by narrow pore necks is known. Similar to the measurement of methane adsorption capacity (Qm), the Qm from the simulation is larger than that from the experiment due to the GCMC method (Section 2.6.2.3), which allows methane to adsorb in any place that can fit methane molecule, while in the high-pressure methane adsorption (Section 2.4.2), the methane adsorption is limited by the pore connectivity and experimental conditions. The difference between the simulation and experiment exists, like any other results difference between different experiments, which will not be a problem. The results from the simulation represent the ideal condition revealing the phenomena in theory, and the results from the laboratory represent the experiment conditions limited by the equipment, experiment conditions, and the samples.

5.5 Conclusions

1) The measured micropore volume (by either CO_2 or/and N_2 from experiment or the 0.33 nm diameter probe from simulation) is much smaller than the micropore volume covered by van der Waals surface. Although the micropore volume measured by 0.33 nm diameter probes is smaller than that from 0.10 nm diameter probes, it is comparable to the experimental results measured from CO_2 molecules, with all these micropore volume increasing with maturity. The MPSD of the KIID 0.5 nm slit (V_{micro}=54 mm^3/g TOC), and KIID 1.0, 1.5 and 2.0 nm slits (V_{micro} from 109 to 261 mm^3/g TOC) are comparable with the MPSD of GHK3 (V_{micro}=10 mm^3/g TOC), and K1 and K2 (V_{micro}=39 and 75 mm^3/g TOC), although the micropore volumes from the simulation are higher.
2) The methane adsorption isotherms and capacities from the simulation and experiment are comparable. Both simulation and experimental results indicate that the Type I (a) and Type I (b) isotherms are contributed to by the smaller micropores (<1 nm), and larger micropores (>1 nm), respectively. The Qm from simulations (45.9, 74.7, 96.1, 122, and 148mg/g TOC for KIID matrix, 0.5, 1.0, 1.5, and 2.0 nm slits) is higher than the corresponding Qm from experiments (21.3, 75.8, and 89.6 mg/g TOC for GHK3, K1, and K2), due to the effects of narrow pore neck blocking and the closed pores are neglected in simulated models.
3) Higher methane adsorption capacities are observed in high maturity kerogens, which have larger micropore volumes, with positive correlations between Qm and micropore volume are observed in both simulation and experimental results.
4) The affinities between methane molecules and different functional groups are affected by pressure. Methane has noticeable different affinities with few functional groups (C-O-C, NC3, C-S-C chain) at lower pressure (<1.6 bar at 25 °C), whereas all the affinities become similar and weaker at higher pressure (>3.2 bar at 25 °C). The interactions between the kerogen matrix and methane have little difference as the heat of absorption only varies from and 22.8 to 23.5 KJ/mol at 25 °C. Therefore, methane has no selectivity on preferred adsorption sites in kerogens, making micropore volume the key control with varying maturity.

CHAPTER 6 COMBINING MOLECULAR SIMULATION AND EXPERIMENT TO UNDERSTAND THE EFFECT OF MOISTURE ON METHANE ADSORPTION IN KEROGEN

6.1 Summary

There is still a limited understanding of the critical impact moisture has on shale gas resources estimation by affecting gas adsorption capacity and pore structure. Laboratory experiments on dry and 95 % relative humidity (R.H.) (wet) isolated kerogens are combined with Grand Canonical Monte Carlo (GCMC) and Molecular Dynamic (MD) simulations on kerogen models, including matrix and slits (0.5, 1.0, 1.5, and 2.0 nm) with a range of moisture contents (0-42 wt.% TOC) to better understand how moisture impacts methane adsorption. Higher methane adsorption capacity (Qm) and micropore volume (V_{micro}) are observed for simulated kerogens since all the pores in GCMC are accessible. Moisture has a negative effect on Qm, presenting as 'rapid', 'gentle', and 'slow' stages with increased moisture content in simulation. The slope and knee point of the reduction stages are less evident for kerogens with larger pores. Large reductions in Qm (61-75%) and V_{micro} (88-93%) are obtained for isolated kerogens containing moisture contents in the range of 38-70 wt. % TOC for overmature kerogens with up to 56% of the moisture in micropores. As same Qm and V_{micro} reductions can be reached for simulated kerogens with moisture contents of 4-24 wt. % TOC for matrix and slits. The relative coordination number (C_r) from MD simulation indicates water has a stronger affinity than methane for the same functional groups where the preferred sorption sites like carboxyl (COOH) (if available) under reservoir conditions. The selected functional groups provide primary sorption sites for water, and the microporosity controls the condensed water cluster size. Water adsorbed in ultra-micropores (<0.7 nm) leads to 'rapid' reduction for Qm, the 'gentle' Qm reduction stage arises from water condensing, and filling of the remaining pores at the highest moisture is related to the 'slow' Qm reduction stage. Therefore, water reduces the methane adsorption capacity of kerogen by taking up and blocking the adsorption pore volume rather than competing directly for sorption sites with methane.

6.2 Literature review

The previous Chapters have indicated that kerogen, as the primary insoluble organic matter in shale, plays a crucial role in shale gas evaluation and production (Gasparik, Bertier et al. 2014, Rexer, Mathia et al. 2014, Collell, Galliero et al. 2015, Li, Stevens et al. 2021). More than 50% adsorbed gas in shale is contributed by isolated kerogens at dry (Fan, Tang et al. 2014, Rexer, Mathia et al. 2014, Li, Stevens et al. 2021), and 95 % relative humidity (R.H.) moisture-equilibrated (wet) condition (Li, Stevens et al. 2021), due to their well-developed microporosity.

Laboratory experimental results indicate moisture has a negative impact on methane adsorption capacity, which together with occupying some of the pore volume, results in gas in place being over-estimated (Gasparik, Bertier et al. 2014, Li, Pang et al. 2019, Whitelaw, Uguna et al. 2019, Li, Stevens et al. 2021, Li, Stevens et al. 2022). Reductions of 20-85% in methane adsorption capacities at 97% relative humidity (R.H.) for moisture-equilibrated shales have been reported (Gasparik, Bertier et al. 2014, Merkel, Fink et al. 2016, Whitelaw, Uguna et al. 2019, Wang and Zhang 2020). It was believed that this is mainly due to moisture blocking the available adsorption sites/pores for methane in clay directly and in organic matter indirectly (Li, Li et al. 2016, Zou, Rezaee et al. 2018), since hydrophilic clay minerals are the main component to adsorb water in shale (Heller and Zoback 2014, Tang, Ripepi et al. 2017, Zolfaghari, Dehghanpour et al. 2017, Luo, Zhong et al. 2019).

Whereas, recent experiments reveal that the amount of water absorbed in shale is positively related to the content of organic matter, possibly because of their oxygen-containing functional groups and the larger specific surface area (Sang, Liu et al. 2019, Bai, Kang et al. 2020, Wang and Zhang 2020), which indicates water exist in organic matter of shale being significant and could affect methane adsorption in the organic matter directly. The negative effects of moisture on methane adsorption capacity of isolated kerogens are ravelled by high-pressure methane adsorption experiments in Chapter 3 (Section 3.4.3.1), which states that more than 50% of methane adsorption capacities are lost for 95% R.H. moisture-equilibrated (wet) isolated kerogen since the pores or/and pore necks less than 1.3 nm are blocked by moisture, leaving the dynamic distribution characteristic and the mechanism of moisture impact on methane adsorption of kerogen in this Chapter combining molecular simulations and laboratory experiments.

In contrast to the limited laboratory research on wet isolated kerogens (Li, Stevens et al. 2021), the negative effects of moisture on methane adsorption capacity of simulated kerogen have been revealed by GCMC and MD simulations (Huang, Ning et al. 2018, Zhou, Mao et al. 2019) (Zhao, Li et al. 2017, Huang, Ning et al. 2018). Significantly decreased methane adsorption was observed for the moist kerogen matrix models with moisture content from 0.6 to 2.4 wt % (Zhao, Li et al. 2017, Huang, Ning et al. 2018, Gong, Shi et al. 2020), and from 0.6 to 3.0 wt% (Zhao, Li et al. 2018). Molecular simulations have also been carried out on kerogen matrix under a wider range of moisture contents from 0.5 to 6.0 wt % to illustrate the moisture and salinity effects on methane adsorption, and the results indicate 42.5% methane adsorption capacity is reduced for gas window kerogen with the moisture content of 6.0 wt.% at 65°C (Zhou, Mao et al. 2019).

The reduced methane adsorption capacity in wet kerogen matrices could result from the limited pore volume and/or water could compete with the sorption sites for methane (Zhao, Li et al. 2017, Huang, Ning et al. 2019, Gong, Shi et al. 2020), as water has a higher affinity with kerogen than methane (Chong, Sanguinito et al. 2021). However, much more detailed research on how water affects methane adsorption in kerogen, considering the difference of physical micropore structure and chemical components, is still needed. Moreover, the limited moisture content up to 3wt.% for kerogen in most simulations which was taken from studies on coal (Fry, Day et al. 2009, Zhang, Clennell et al. 2014) or shales (Gasparik, Ghanizadeh et al. 2013), is much less than the moisture content in isolated kerogen from the experiment (about 15 wt.% at 95%R.H., Chapter 3, Table 3-1)(Li, Stevens et al. 2021). The molecular simulation work to date has only involved making simple comparisons of the predicted methane adsorption isotherms to experimental data for coals, shales, and dry isolated kerogens (Zhao, Li et al. 2017, Huang, Ning et al. 2019, Gong, Shi et al. 2020) due to the limited experimental results on wet kerogens. In addition, the moist models applied in simulations to date are mainly on the kerogen matrix, covering pores less than 1nm. However, the larger micropores (1-2 nm) are essential for methane adsorption (Thommes, Kaneko et al. 2015), and moisture can block the pore or/and pore neck less than 1.3 nm and impact the pore connectivity of kerogens (Chapter 3, Section 3.4.5)(Li, Stevens et al. 2021).

Therefore, this study is the first to combine experiment and molecular simulation on wet kerogens to reveal the behaviour and mechanism of moisture impact on methane adsorption.

Dry and moist kerogen models (matrix, 0.5, 1.0, 1.5, and 2.0 nm slits) covering the ultra (<0.7 nm) and super-micropores (0.7-2.0 nm) are constructed for the molecular dynamic (MD) and the Grand Canonical Monte Carlo (GCMC) simulation. The consistency of moisture content, microporosity, and methane adsorption capacity between experiment and simulation results are compared. The findings in this study can provide a new perspective on understanding methane adsorption in wet kerogen and pave the way for shale gas recovery.

6.3 Experiments and Methods

The sample preparation and the corresponding experiments of the three dry kerogen isolated concentrates (K1, K2, and GHK3) are same as in Chapter 5 (Section 5.3). Moisture-Equilibrated kerogens preparation with different relative humidity (10, 30, 50, 70, and 95 % R.H.) are described in Section (2.2.3). Low-pressure gas (CO_2, N_2) sorption at 0 and -196 °C (2.4.3) and High-pressure methane adsorption experiments (2.4.2) were carried out on isolated kerogen at 25 °C both dry and wet (95%R.H.).

The simulation methods are detailed described in Chapter 2 (Section 2.6.2). Dry and Moist (with the moisture content of 0, 0.6, 1.2, 2.4, 3.6, 6, 9, 12, 15, 18, 21, 24, 27, 30, 36, and 42wt.%TOC) simulated kerogen models (matrix, 0.5 nm, 1.0 nm, 1.5 nm, and 2.0 nm slits) are applied in this Chapter for the molecular simulation, with the detailed simulation setup in Section 2.6.2.1, model construction in Section 2.6.2.2, the methane adsorption capacity measured by GCMC method in Section 2.6.2.3, the microporosity measurement from simulation in Section 2.6.2.4, and the parameters of relative number density ($g(r)$) and relative coordination number (C_r) from MD simulation in Section 2.6.2.5. The model validation is presented in Chapter 5 (Section 5.4.1).

6.4 Results and Discussion

6.4.1 Impact of moisture on methane adsorption by simulation

The impact of moisture on methane adsorption capacity for the KIIA, B, C, and D matrices with varying maturity at 25 and 100°C is illustrated in Figure 6-1. The equilibrium methane adsorption capacity (Qm) of the dry kerogen matrices increases with maturity and decreases with the temperature, as the Qm for the dry KII A, B, C, D matrices are 16, 20, 28, and 46 mg/g TOC, respectively at 25°C, compared to the lower Qm of 13, 18, 21, and 36 mg/g TOC, respectively, at 100°C (Figure 6-1 A, B). The same effects of maturity and temperature on methane adsorption capacity also exist for the moist kerogens (Figure 6-1 A, B). Moisture has the expected negative impact on the methane adsorption capacities of the kerogen matrices, the isotherms of which are presented in (Appendix C, Figure C1). The negative effect increases with moisture content until the moisture contents reach 9, 12, 12, and 18wt.% TOC for KII A, B, C, D matrix, respectively, where all the methane adsorption capacity is lost (Figure 6-1 C, D).

The correlations between Qm reductions and moisture contents for the kerogen matrices can be divided into three 'rapid', 'gentle' and 'slow' stages as the increase of moisture content (Figure 6-1 C, D), with different slopes and knee points observed for the kerogens of varying maturity (Figure 6-1 C, D). The impact of a given moisture content increases with decreasing maturity going from KIID to KIIA. Although the moisture content ranges for corresponding stages can differ slightly depending upon maturity and temperature, they are approximately within 0-4 wt.% TOC, 4-8 wt.% TOC, and >8 wt.% TOC for 'rapid', 'gentle', and 'slow' stages (Figure 6-1 C, D). Over 50% reductions in the Qm of KII A, B, C, D matrices occur when the moisture reaches *ca*. 4wt.% TOC. Moisture has the greatest effect on the low maturity kerogen KIIA, since more moisture content is needed to occupy the larger micropores in the more mature kerogens.

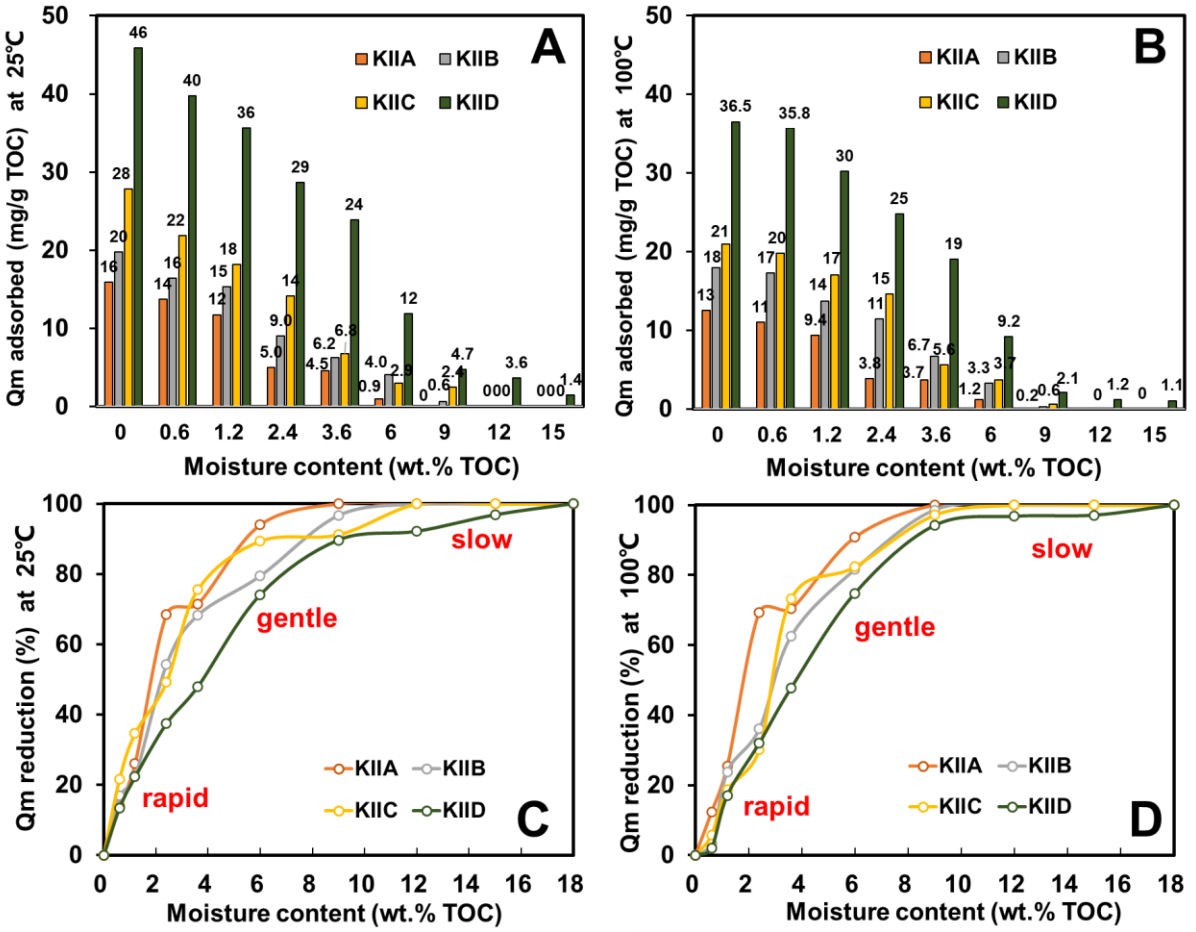

Figure 6-1. The equilibrium methane adsorption capacities (Qm) of the KII A, B, C, D matrices with different moisture contents at A) 25°C and B) 100°C, and the corresponding percentage Qm reductions at C) 25°C and D) 100°C.

6.4.2 Comparison between experiment and simulation for the impact of moisture on methane adsorption

The methane adsorption capacities of overmature kerogens from simulation and experiment at 25°C are compared in Figures 6-2 and 6-3. For dry kerogens, the methane adsorption isotherms of the KIID matrix and 0.5nm slit models are comparable with GHK3 kerogen, and the isotherms of K1 and K2 kerogens are comparable with that of the KIID 1.5 nm slit model, slightly out of range compared to KIID 1.0, and 2.0 nm slit isotherms (Figure 6-2 A). The Qm of dry KIID matrix, 0.5, 1.0. 1.5 and 2.0 nm slit models increases with pore size, from 46, 75, 95, 122, to 148 mg/g TOC (Figure 6-2 B), which are roughly twice as high as the Qm of the dry K1, K2, and GHK3 (75.8, 89.6, and 21.25 mg/g TOC, Table 6-1) kerogens from the experiment due to all the pores are accessible for the GCMC method as stated in Chapter 5 (Section 5.4.4).

Moisture reduces the Qm by 75, 61, and 71% for K1, K2, and GHK3, respectively (the Qm for wet isolated kerogens being 19.3, 35.1, and 6.1mg/g TOC, respectively (Table 6-1). The Qm of the KIID models with different moisture contents (0-42wt.% TOC) obtained by GCMC simulation at 25°C is presented in Figure 6-2 B. The moist kerogen structures lose all the methane adsorption capacity when the moisture contents are 18, 27, 30, 36, to 42 wt.% TOC for KIID matrix, 0.5, 1.0, 1.5, and 2.0 nm slits, indicating higher moisture content is needed for kerogen models with a larger pore size (Figure 6-2 B).

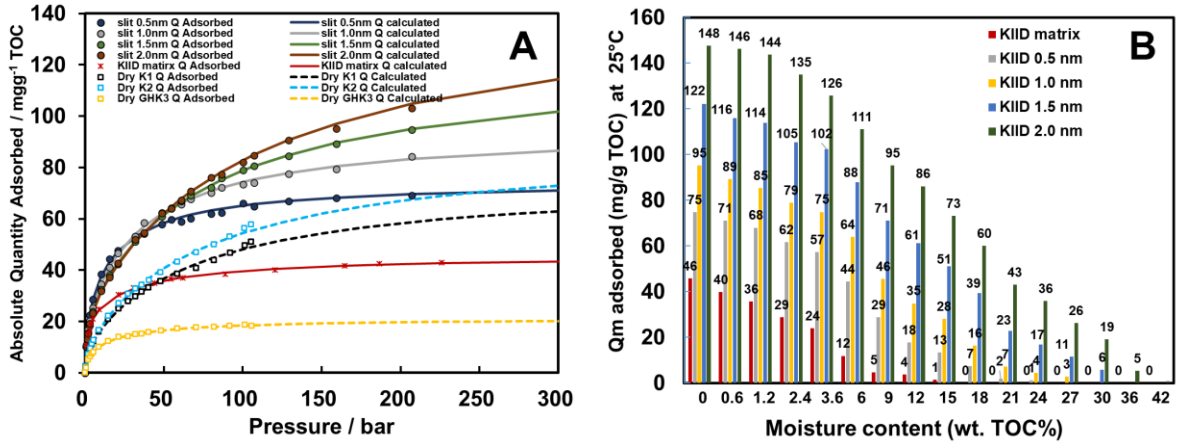

Figure 6-2. A) Methane adsorption isotherms of the dry isolated kerogens and KIID models at 25°C, B) The equilibrium methane adsorption quantity (Qm) of KIID models with different moisture contents at 25°C.

Table 6-1. Basic parameters for the isolated kerogens from experimental data used in this study.

Kerogen name	Porosity (%)	Skeleton Density (cm^3/g)	Bulk Density (cm^3/g)	Dry V_{ultra} (mm^3/g TOC)	Dry V_{micro} (mm^3/g TOC)	Dry Qm (mg/g TOC)	Wet V_{ultra} (mm^3/g TOC)	Wet V_{micro} (mm^3/g TOC)	Wet Qm (mg/g TOC)	Qm reduction
K1	89	1.17	0.21	24	39	75.8±3.96	0	2.7	19.3	75%
K2	85	1.83	0.43	37	75	89.6±5.01	0	5.9	35.1	61%
GHK3	75	1.44	0.59	9.8	10	21.25±1.54	0	1.2	6.1	71%

Porosity is the ratio of the total pore space divided by the total sample volume, V_{ultra} is the ultra-micropore (<0.7 nm) volume, V_{micro} is the total micropore (<2 nm) volume. Qm is the maximum equilibrium methane adsorption quantity, the mean of Qm is from triplicate experiments, and the errors represent the dispersion of a dataset relative to its average. The 'wet' in this table means the 95 % R.H. moisture equilibrium isolated kerogens.

The Qm reduction for the kerogen slit models (Figure 6-3 A) can also be divided into 'rapid', 'gentle', and 'slow' stages as for kerogen matrices (Figure 6-1), with the changes from 'rapid' to 'gentle' stages are less evident for larger size slits (Figure 6-3 A). Experimental results reveal similar effects of moisture on methane adsorption of shale, with that the Qm versus moisture

content exhibits a linear decreasing stage, a flat stage, and a convex decreasing stage (Fan, Li et al. 2018). The same Qm reductions (61-75%) as for 95% R.H wet isolated kerogens are reached for the moist KIID kerogen matrix, 0.5, 1.0, 1.5, and 2.0 nm slit models (only containing micropores) with the moisture content ranging from 4 to 24 wt.% TOC (Figure 6-3 A). Whereas, the moisture contents of 4 to 24 wt.% TOC from the simulation are less than the moisture contents (70, 43, and 38 wt.% TOC for K1, K2, and GHK3) for wet (95 %R.H.) isolated kerogens, suggesting not all the moisture is in the micropores.

The methane adsorption isotherms of moist KIID matrix, 0.5, 1.0, 1.5, and 2.0 nm slit models with moisture contents of 6, 12, 15, 18, and 21 wt.% TOC, respectively, are selected to compare with the experimental results (Figure 6-3 B), since the Qm reductions for moist KIID matrix and 0.5 nm slit models at 6 and 12 wt.% TOC are close to the Qm reduction for wet GHK3. Similarly, the Qm reductions for moist KIID 1.0, 1.5, and 2.0 nm slit models at 15, 18, and 21 wt.% TOC are close to the average Qm reduction for wet K1 and K2 (Figure 6-3 A).

Similar to the dry kerogens (Figure 6-2 A), the Qm of moist kerogens from the simulation are higher than those of the compared wet kerogens from the experiment (Figure 6-3 B). The methane adsorption isotherms of the moist KIID matrix (6 wt.% TOC) and 0.5 nm slit (12wt.%TOC) models are comparable to those for wet GHK3, all Type I (a). In contrast, the isotherms for wet K1 and K2 are Type I (b), similar to those of the moist KIID 1.0 nm (15wt.%TOC), 1.5 nm (18wt.%TOC), and 2.0 nm (21wt.%TOC) slit models (Figure 6-3 B). However, how moisture affects the methane adsorption capacity of kerogens in simulation is slightly different from the experiment. For isolated kerogens, moisture reduces the methane adsorption capacity by occupying pore volume or/and blocking the narrow pore necks (<1.3 nm) as experimental results indicated (Chapter 3, Section 3.4.5) (Li, Stevens et al. 2021), while for the simulated kerogens, moisture can only reduce the available pore volume for methane adsorption without considering blocking the pores' interconnectivity. Therefore, the same amount of moisture should have a greater effect on the isolated kerogens than the simulated kerogens. Thus, at most, 24wt.% TOC moisture is in the wet (95% R.H.) isolated kerogen micropores, with the rest in larger pores.

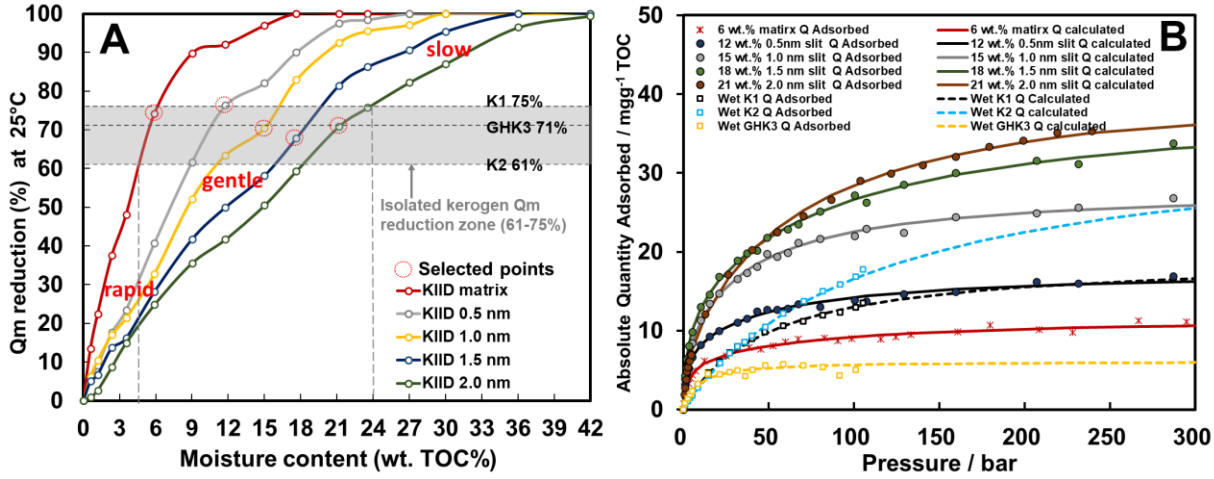

Figure 6-3. A) The Qm reduction of the KIID matrix, 0.5, 1.0, 1.5, and 2.0 nm slit models with the different moisture contents at 25°C, B) Methane adsorption isotherms of wet isolated kerogen and moist KIID models at 25°C.

6.4.3 Comparison of experiment and simulation for the impact of moisture on microporosity

The micropore characteristics for overmature kerogens from the simulation are measured by d=0.33 nm (same as CO_2 for dry samples) and d=0.36 nm (same as N_2 for wet samples) probes (Appendix C, Table C1), in order to compare with the results for isolated kerogens from low-pressure gas (N_2, and CO_2) sorption experiment. The experimental results indicate that reductions in micropore volume of 93, 92, and 88% occur for the wet (95 %R.H.) K1, K2, and GHK3 kerogens, from 39, 75, 10 mm_3/g TOC to 27, 5.9, and 1.2 mm^3/g TOC, respectively (Table 6-1). The negative impact of moisture on micropores is also found in simulation, with the micropore volume decreasing with increasing moisture content (Figure 6-4), where the micropore volume decreases fast first and then becomes stable with increasing moisture content. The same moisture content has a greater impact on kerogen models with smaller pores since smaller pores are more easily blocked by water. All micropores (d=0.36 nm) are lost when the moisture contents are 6, 9, 12, 15, 24, 30, 33, and 36 wt. % TOC for KIIA matrix, KIIB matrix, KIIC matrix, KIID matrix, KIID matrix, KIID 0.5nm slit, KIID 1.0 nm slit, KIID 1.5 nm slit, KIID 2.0 nm slit models, respectively (Figure 6-4).

As stated in Section 6.4.2, when the moisture content is in the range of 4-24 wt.% TOC for the kerogen models, the same Qm reduction (61-75%) is obtained as for 95 %R.H. wet isolated kerogens (Figure 6-3), with the micropore reduction being around 85% (Figure 6-4), slightly

lower than the micropore reductions (88-93%) for wet (95% R.H.) isolated kerogens. The relatively close reduction of methane adsorption capacity (61-75%) and microporosity (85%) at the same moisture content suggests that the accessible micropore volume is the main control factor for methane adsorption capacity. More moisture (4-27wt.% TOC, cf. 4-24 wt.% TOC) is needed for the kerogen models to reach the same micropore reduction (88-93%) as for the wet (95 %R.H.) isolated kerogen (Figure 6-4). However, the micropore volume for wet isolated kerogens is measured at -196°C by N_2, where water becomes ice and can potentially block more micropores (Chapter 3, Section 3.4.5) (Li, Stevens et al. 2021). The results further indicate the moisture in wet isolated kerogens (38-70 wt.% TOC) is distributed in micropores as well as larger pores, with at most 56% moisture (24 wt.% TOC in micropores for K1 and K2, and 12 wt.% TOC in micropores of GHK3) in micropores.

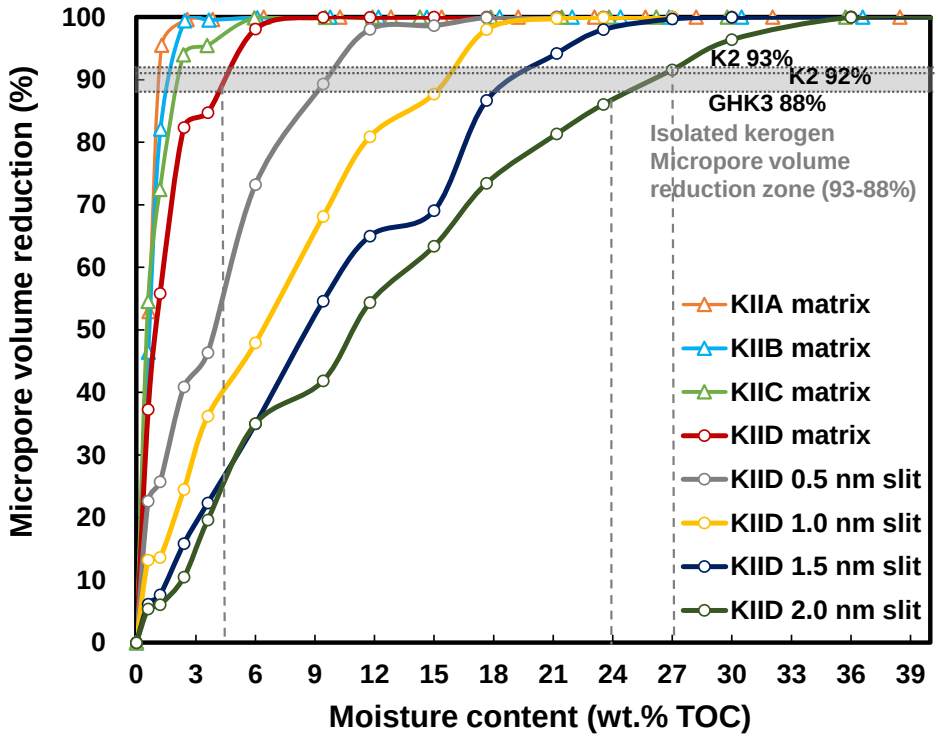

Figure 6-4. Reductions in micropore volume for the kerogen (KIIA, B, C, and D) matrix and KIID 0.5, 1.0, 1.5, and 2.0 nm slit models with increasing moisture content.

Figure 6-5 shows the MPSD results for wet/moist kerogens from the experiment and simulation. All ultra-micropores (<0.7 nm), as well as the super-micropores (0.7-2.0 nm) less than 1.3nm, are lost for wet isolated kerogen in experiment (Li, Stevens et al. 2021), leaving one major micropore peak ranging from 1.3 to 2.0 nm (Figure 6-5 A). Unlike the results from experiments, not all the pores less than 1.3 nm are lost when the moisture is in the range 4-

24 wt.% TOC for KIID matrix and slit models (Figure 6-5). As for the dry simulated kerogens, there are two peaks (P_{in} and P_{ul}) for the moist kerogen matrix and 0.5 nm slit model (Figure 6-5 B, C), including the inaccessible and ultra-micropore (<0.7 nm), and three peaks (P_{in}, P_{ul}, and P_{su}) observed for moist kerogen 1.0, 1.5, and 2.0 nm slits (Figure 6-5 D, E, and F), covering the inaccessible, ultra (<0.7 nm) and super-micropores (0.7-2.0 nm). Although all the MPSD for moist kerogen from the simulation shows a prominent high peak for inaccessible pores (<0.26 nm), these are not accessible by any gas as stated in Chapter 5 (Section 5.4.2). Both ultra-(<0.7 nm) and super-micropores (0.7-2.0 nm) exist for moist KIID slit models, and the increasing moisture content reduces the peak of P_{ul} and P_{su} at the same time (Figure 6-5 D-F), suggesting moisture reduces the ultra-(<0.7 nm) as well as super-micropore (0.7-2.0 nm) volume simultaneously.

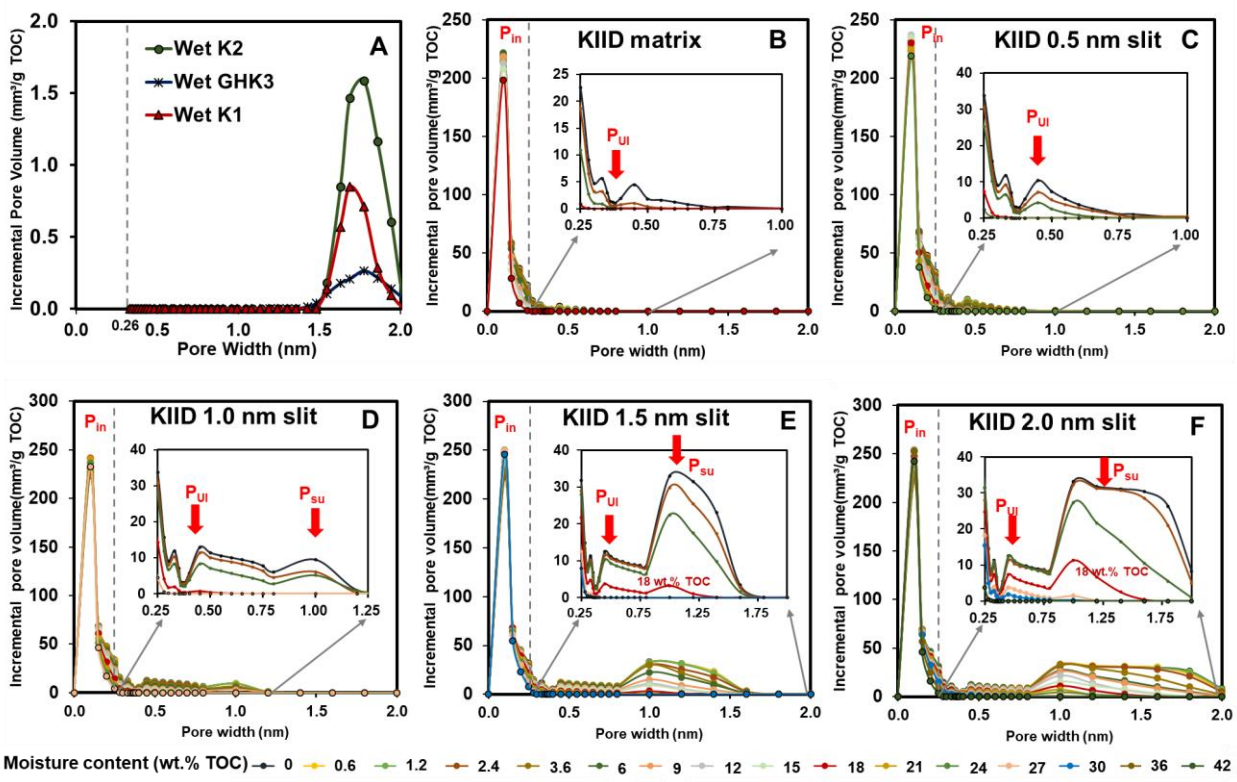

Figure 6-5. The MPSD of wet (95 % R.H.) isolated kerogen (A) and the MPSD of moist KIID kerogen matrix (B), 0.5 nm (C), 1.0 nm (D), 1.5 nm (E), and 2.0 nm (F) slit models with different moisture contents (wt.% TOC). The enlarged MPSD in figure B-F includes the selected moisture content from 0, 2.4, 6, 18, 24, 27, 30, and 42 wt.% TOC to make the MPSD clear.

6.4.4 Mechanistic description of the impact of moisture

6.4.4.1 Microporosity

The moisture contents of the isolated kerogens at different relative humidities (10, 30, 70, and 95 % R.H.) are presented in Figure 6-6, which shows the gentle increase in the lower humidity range (<30 %R.H.) for K1, K2, and GHK3 (stage 1), followed by a rapid increase in the higher humidity range for K2 and GHK3 (stage 2), with K1 reaching a plateau at the highest humidity. The maximum moisture contents of K1, K2, and GHK3 are 15.5, 13, and 9.9 wt.%, which correspond to 43, 70, and 38 wt.% TOC, respectively at 95% R.H. (Figure 6-6). At 30 %R.H., the isolated kerogen moisture contents are in the range 7.5-15.3%, close to the estimated moisture contents in the micropores of kerogen simulated models (4-24wt.% TOC) (6.4.3). Therefore, stage 1 could be due to water adsorbing/condensing in micropores first. The stage 2 at higher relative humidity could be due to water starting to fill the larger pores and form water condensation. Similar moisture uptake stages have been reported (Bai, Kang et al. 2020), which believe the gentle increase stage could be related to the monolayer adsorbed water, and the rapid increase could associate with the multiple layer and condensation of water. Fisher (1979), Fan (2018), and Wang (2018) (Fisher and Israelachvili 1979, Fan, Li et al. 2018, Wang, Su et al. 2018) state that water condensation may occur in the larger pores after adsorption in the smaller pores, as water fills the micropore first.

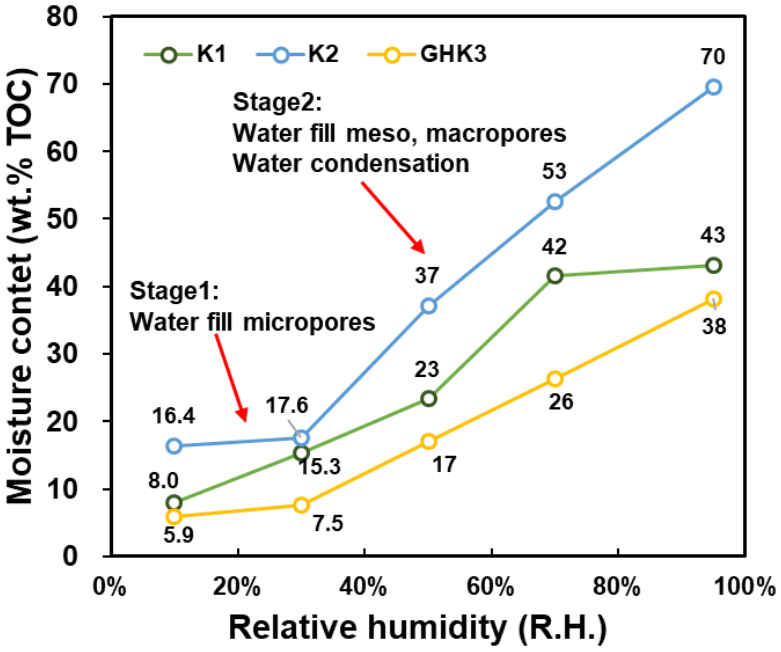

Figure 6-6. The moisture contents of isolated kerogens (K1, K2, and GHK3) at different relative humidities.

Figure 6-7 provides snapshots of the distribution of water in kerogen 2.0 nm slit models at different moisture contents from MD simulation. First, water adsorbs in the ultra-micropores (< 0.7 nm) (Figure 6-7 A), and then water starts adsorbing on the surface of super-micropores (0.7-2.0 nm) and filling the ultra-micropore (<0.7 nm) simultaneously (Figure 6-7 B, C). Next, water condenses in all the micropores and finally blocks the pore connectivity (Figure 6-7D, E). The same results can also be obtained from the MPSD of KIID models (Figure 6-5), where all the ultra-micropores (<0.7 nm) in the KIID matrix model can be filled when the moisture content is 18 wt.% TOC (Figure 6-5B), but not all the ultra-micropore (< 0.7 nm) in KIID slits are occupied by water (Figure 6-5 E, F). This indicates that although water primarily adsorbs on ultra-micropores (< 0.7 nm) first, water would fill the ultra-micropores (< 0.7 nm) and start adsorbing and condensing in the super-micropore (0.7-2.0 nm) simultaneously as the moisture content increases, as opposed to filling all ultra-micropores (<0.7 nm) before adsorbing/filling the super-micropores (0.7-2.0 nm).

Moreover, the reduction in super-micropore (0.7-2.0 nm) volume is larger than that for ultra-micropores (< 0.7 nm) at 18 wt.% TOC moisture for the KIID models with larger pores (1.5 and 2.0 nm slits, Figure 6-5 E, F). This suggests water preferentially condensing in super-micropores (0.7-2.0 nm) rather than continuing to fill the remaining ultra-micropores (<0.7 nm) at higher moisture contents, possibly related to the strong H-bonds between water molecules. Figure 6-7 G illustrates that the pore connectivity is the main difference between simulation and experiment, where the blocked pores are inaccessible for methane but accessible in the GCMC simulation.

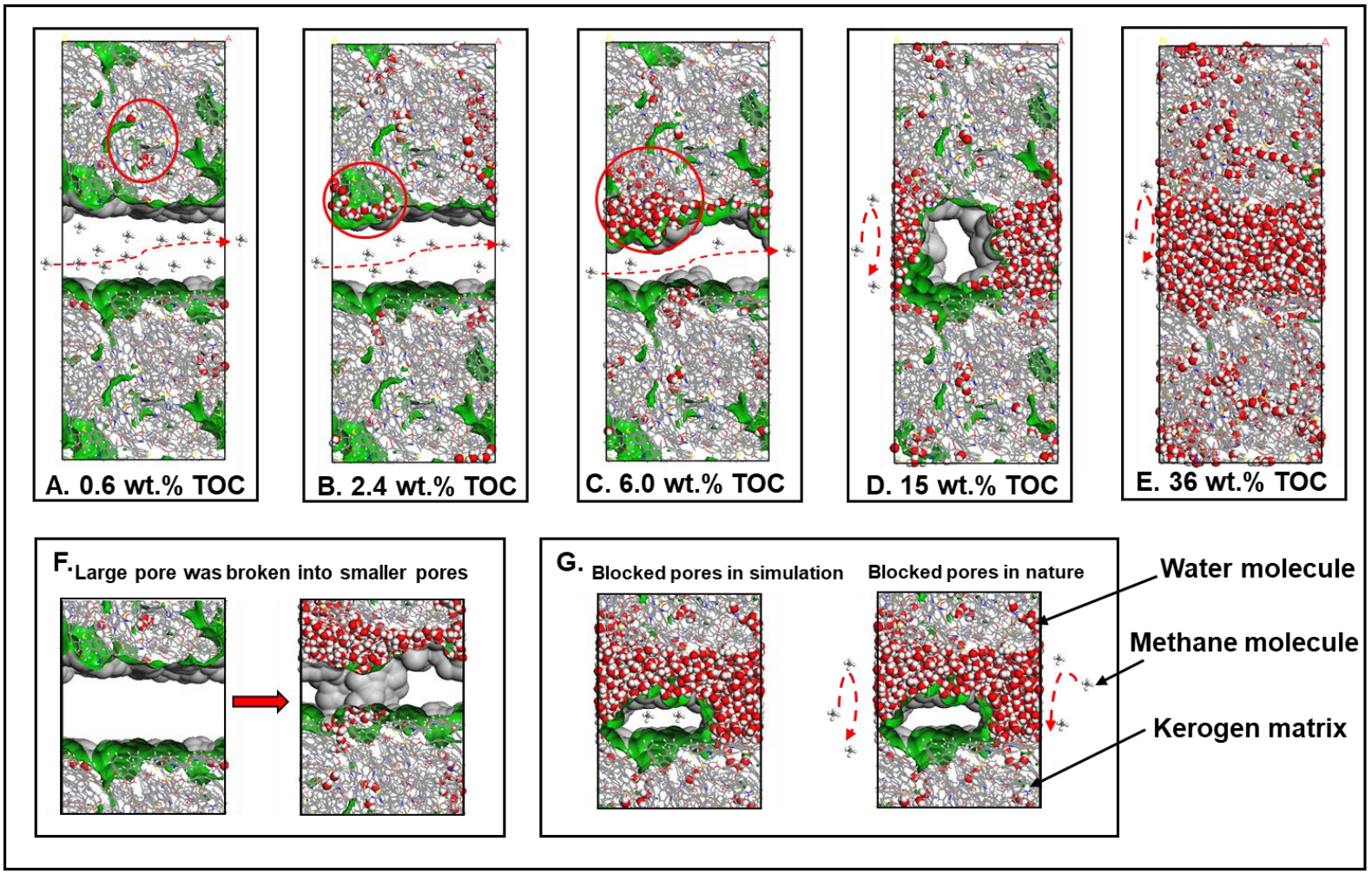

Figure 6-7. Depiction of how water reduces methane adsorption capacity by filling the microporosity in the 2.0 nm slits for the KIID kerogen model.

6.4.4.2 The impact of functional groups for moist kerogen

As Chapter 5 (Section 5.4.5) indicates, with the increase of maturity, kerogen lost most of C, O, N, S, and aliphatic C functional groups due to the generation of hydrocarbon (Table 5-5). KIIA, as the immature kerogen, includes all kinds of functional groups (Figure 5-8).

The affinities between water/methane molecules and functional groups are represented by the relative coordination number (C_r) from MD simulation, with the least mature kerogen, KIIA covering all functional groups, and overmature KIID selected as the representation (Figure 5-10 for methane, and Figure 6-8 for water). The results of C_r of water for other models (KIIB and KIIC) are in Appendix C (Figure C2). The affinity of methane is related to pressure and temperature as stated in Chapter 5 (Section 5.4.5). At 25°C, the C_r of methane for most functional groups are in the range of 0.002-0.008 at low methane amount/pressure (<25 CH_4, <1.6bar, at 25°C) conditions (Figure 5-10). As the amount of methane and pressure increase (>25 CH_4, >1.6bar, at 25°C), the lower C_r are observed (Figures 5-10 A and C), all less than 0.0015, which indicates that the affinity of methane with these functional groups is weaker and shows no significant differences at higher pressures. The higher temperature leads to lower C_r (Figures 5-10 B and D). Furthermore, the average C_r of methane with different functional groups for KIIA, KIIB, KIIC, and KIID are combined further to present the selectivity of methane (Figure 6-9). The average C_r of methane for the different functional groups are very close (Figure 6-9), as expected, confirming preferred sorption sites exist.

In contrast, the average C_r of water for most functional groups (except COOH for KIIA) is close to 0.005 at 25°C, and 0.003 at 100°C, for both KIIA and KIID (Figure 6-8), much higher than those for methane (<0.0015) (Figure 5-10), confirming that water, being a polar molecule, has a stronger affinity than methane (nonpolar) with all the functional groups in kerogen due to the higher Van der Waals or/and the H-bonds. Further, the changes in water content have different impacts on affinity compared to methane. At low moisture content (<10H_2O, <0.7wt.TOC) in KIIA (Figure 6-8 A, B), the C_r of water for specific functional groups like COOH and C-S-C ring is higher, the C_r of water for other functional groups (C=O, C-OH, C-O-C, C-NH-C, C-N=C, NC3, C-S-C chain) is even lower, with the C_r of water for the remaining functional groups (C sp2, C sp3 CH2, and C sp3 CC2) showing only minor variations. This is because water is clearly selective towards certain functional groups (like COOH and C-S-C rings) at low

moisture contents in KIIA, which contains all the possible functional groups. Whereas, with increasing moisture content, water starts condensing to form clusters (Figure 2-22), the C_r is not only controlled by the interaction between water and functional group but also is impacted by the H-bond interactions between water molecules. For the overmature kerogen (KIID), the C_r of water for some N-containing functional groups like C-NH-C and C-N=C at low moisture content (<10H_2O, <0.7wt.TOC) is slightly higher than those at higher moisture content, which are all higher than the C_r of water for C-containing functional groups (Figure 6-8 C, D). This suggests in the overmature kerogen, the lacking of O and S- containing functional groups results in the N- containing functional groups being the preferred sorption sites than C- containing functional groups at low moisture content. However, the C_r of water for all functional groups in KIID is very closed (C_r close to 0.005 at 25°C, and close to 0.003 at 100°C) at higher moisture content due to the forming of water cluster, suggesting the preferred sorption sites in N-containing functional groups for overmature kerogen make little difference for water adsorption.

The average C_r of water for all functional groups in KIIA, KIIB, KIIC, and KIID at 25°C and 100°C (Figure 6-9) shows that C_r of water for COOH is obviously highest, followed by the S-containing functional groups, especially C-S-C ring, and N-containing functional group, indicating water has the strongest affinity with COOH than others. Although the average C_r at 100°C is lower than that at 25°C, the strongest affinity of water is still with COOH (Figure 6-9). This suggests water selectivity for COOH does not change with temperature and kerogen type, with the increase in temperature only leading to weaker affinity. The other preferred S and N-containing functional groups vary with kerogen maturity (Appendix C, Figure C2), due to the availability of these functional groups.

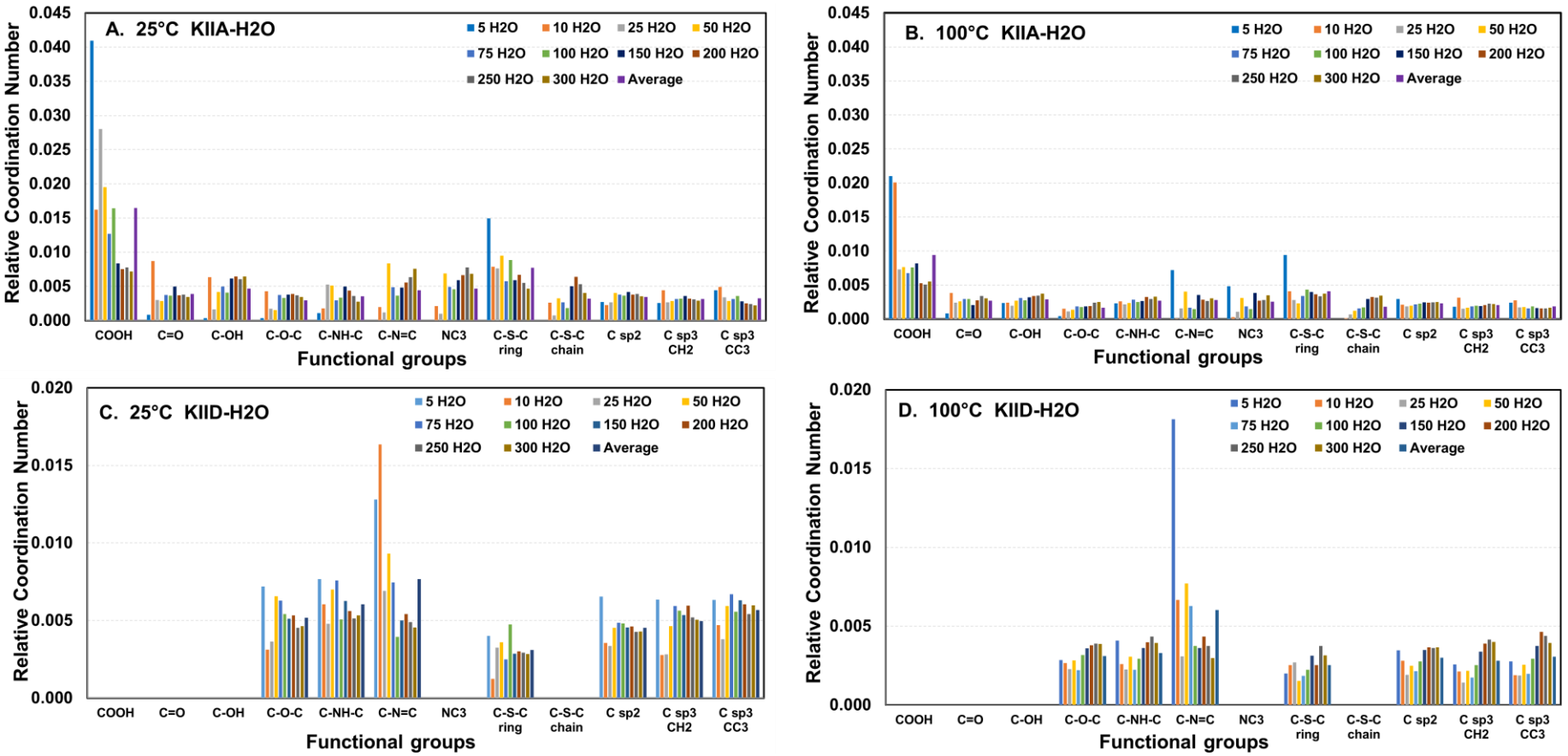

Figure 6-8. The relative coordination number (C_r) of water (H2O) for the different functional groups in kerogen (KIIA and KIID) at 25°C and 100°C. 'Average' is the average C_r of methane going from 5 to 300 methane molecules. A) KIIA at 25 °C, B) KIIA at 100 °C, C) KIID at 25 °C, D) KIID at 100 °C.

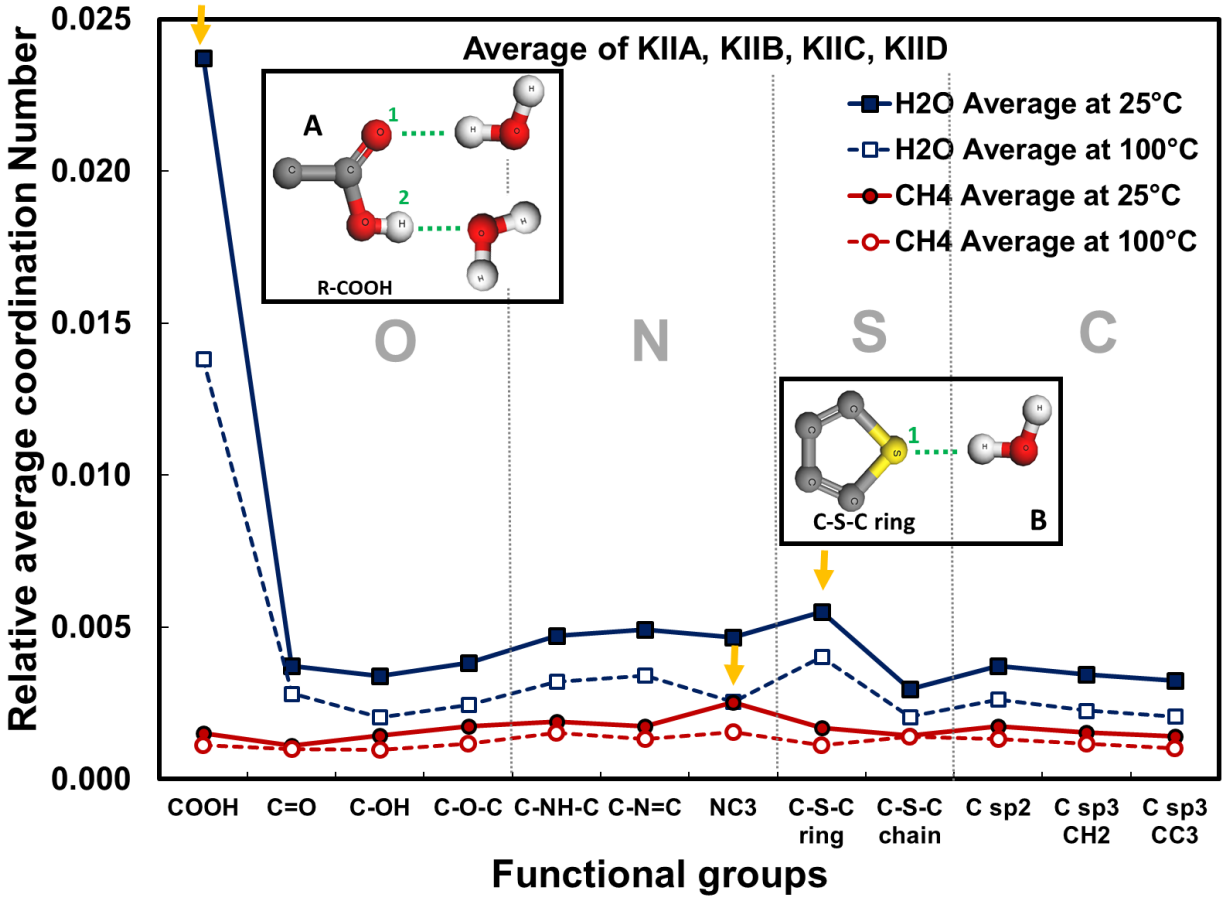

Figure 6-9. The relative average coordination numbers of methane and water for the KIIA, KIIB, KIIC, and KIID kerogens with between 5 and 300 molecules.

6.4.4.3 Combination of microporosity and functional groups

A smaller pore size would enhance water adsorption for a given adsorption site, due to its higher adsorption potential, according to the potential theory of Polany (Polanyi 1963). The adsorption of water can be divided into primary and secondary sorption. Water adsorbed on kerogen directly is the primary adsorption (monolayer), which is directly related to the ultra-micropores (<0.7 nm), number and type of the preferred functional groups. Secondary sorption is multi-layger adsorption and condensation of water. The increase of moisture content will not affect the primary adsorption once all these primary sites are adsorbed by water, which mainly occurs at extremely low moisture contents (Figures 6-7 A and B). In comparison, the adsorption on secondary sites is directly related to the pre-adsorbed water. The adsorption and condensation of water on secondary sites is limited by the available pore

space (Figure 6-7 C, D, and E) rather than the preferred functional groups. Water adsorption on the secondary sites would increase with moisture content until all the pores are filled. The higher maturity samples potentially contain a more restricted distribution of functional groups and more micropores. The larger equilibrium moisture content in the over mature kerogen (Figure 6-1) proves that microporosity has a stronger effect than the functional groups on water adsorption.

The dynamic behaviour of water in kerogens with increasing moisture content can be divided into four stages, considering the combined effects of microporosity and functional groups. The effect of each stage on methane adsorption related to the Qm 'rapid', 'gentle' and 'slow' reduction is explained.

Stage (a) water molecules adsorb on the primary sites of preferred functional groups in ultra-micropores (<0.7 nm) or adsorbed on the ultra-micropore (<0.7 nm) if no preferred functional groups are found, correlated to the monolayer water adsorption in ultra-micropores (<0.7 nm) (Figure 6-7 A).

Stage (b) water starts to adsorb on the primary sorption sites of the super-micropores (0.7-2.0 nm) or adsorbs on the secondary sites (pre-absorbed water) in ultra-micropores (<0.7 nm), reducing both ultra and super-micropore (Figure 6-7 B), correlated to the monolayer adsorption in super-micropores (0.7-2.0 nm), and multi-layer water adsorption/condensation in ultra-micropores (<0.7 nm) (Figure 6-7 B). During stage (a) and (b), water occupying (adsorbing and condensing) in ultra-micropores (<0.7 nm) and starting adsorping in super-micropores (0.7-2.0 nm), reducing methane adsorption space directly, which lead to the 'rapid' Qm reduction in Figure 6-1 C, D, and Figure 6-3 A at low moisture contents stage;

Stage (c), water keeps adsorbing on all the secondary sites by H-bonds (Figure 6-7 C, D), multi-layer adsorption forming water clusters, in all the micropores. As a result, the water clusters in stage (c) reduce the methane adsorption space (for simulated and isolated kerogens) and affects their migration (for isolated kerogens), which is related to the 'gentle' Qm reduction stage.

Stage (d) water keeps condensing as larger clusters until all the available pores are filled (Figure 6-7 E). In this stage, the constantly increasing water can fill the remainder of the less accessible pores for methane, having little impact on the methane adsorption, which correlates to the 'slow' Qm reduction in Figures 6-1 C and D, and Figure 6-3 A.

For isolated kerogens, the effects of water clusters blocking pore necks can lead to a larger Qm reduction than for simulated kerogens, which could be even more evident than the 'gentle' Qm reduction stage. In addition, the pore volume occupied by water is hard for methane to access, as the water adsorbed on the primary or secondary sites controlled by H-bonds which is stronger than the van der Waals interactions for methane molecules.

In earlier work, water was believed to reduce methane adsorption by affecting the microporosity as well as reducing the number of potential adsorption sites for methane or by directly occupying polar adsorption sites that would otherwise be available for methane (Krooss, Van Bergen et al. 2002, Chalmers and Bustin 2007, Fan, Li et al. 2018, Luo, Zhong et al. 2019, Bai, Kang et al. 2020). These studies assumed that there were preferred sorption sites for methane. However, the results from this research indicate that there are only preferred sorption sites for water but not for methane. Water can only affect methane adsorption by occupying or blocking the available microporosity for methane rather than just occupying the sorption sites available for methane.

6.5 Implications and Conclusions

Studying the impact and mechanism of moisture impact on methane adsorption and porosity has significant implications for the industry, particularly in the estimation and production of the shale gas resource. Accurate estimation for the shale gas resource is the foundation for production, and considering the moisture in shale can avoid overestimation. The GIP reductions or/and the methane adsorption capacity reductions obtained in this study can be applied as a correction for the GIP estimated from dry samples, which is already used in Li M., et al (2022). Moreover, the mechanism of moisture affects the methane adsorption by occupying pore volume rather than competing adsorption sites with methane can provide guidance for shale gas production as hydraulic fracturing is the most popular method, where the pore volume should be more critical compared to the various maturities in shales considering these factors impact on the intrusion of water.

1) Moisture has negative effects on the methane adsorption capacity and the microporosity of the simulated kerogen matrices. The negative impact of water on methane adsorption capacity can be divided into 'rapid', 'gentle' and 'slow' three stages as the increase of moisture content. A range of 4-24 wt.%TOC moisture content

is needed for KIID matrix and slit models to reach the same reduction of Qm (61-75%) and V_{micro} (88-93%) as 95%R.H. (wet) isolated kerogens. At most, 56% moisture in wet isolated kerogen is stored in micropores. The relatively close reduction (with a reduction difference of 18-27%) of methane adsorption capacity and microporosity at the same moisture content suggests accessible microporosity volume is the main controlling factor for methane adsorption.

2) Ultra-micropores (<0.7 nm) are primarily pores responsible for water adsorption at low moisture contents. Water then fills the ultra-(<0.7 nm) and super-micropore (0.7-2.0 nm) simultaneously as moisture content increases.
3) Water has a much stronger affinity with functional groups than methane. Preferred sorption sites for key functional groups (like carboxyl (COOH)) exist for water but not for methane at reservoir conditions. Thus, the preferred sorption sites (primary site) directly control water monolayer adsorption at the low moisture contents, while micropore volume limits the water adsorption (multiple-layer or condensation).
4) Water occupying ultra-micropores (<0.7 nm) reduces methane adsorption space directly, leading to the 'rapid' Qm reduction stage at extremely low moisture Contents. The condensed water clusters in most super-micropores (0.7-2.0 nm) and some ultra-micropores (<0.7 nm) can relate to the 'gentle' Qm reduction stage. Water can then fill the remaining inaccessible pores for methane at higher moisture content, with little impact on the methane adsorption, which correlates to the 'slow' Qm reduction stage. Therefore, water affects methane adsorption by occupying or blocking the available microporosity for methane rather than occupying the preferred sorption sites available for methane.

CHAPTER 7 CONCLUSIONS AND FUTURE WORK

7.1 Main conclusions

1) Kerogen is more important than mineral in shales for methane adsorption, which account for the most adsorbed gas. As a result, the isolated kerogens have much higher methane adsorption capacities, SA, and average pore volumes than corresponding shales. After demineralisation, larger micropores and smaller mesopores are accessed for the isolated kerogens, resulting in more methane being adsorbed.
2) Moisture has a detrimental effect on methane adsorption capacities and pore volumes, for both kerogens and shales. According to the low-pressure gas sorption results, moisture significantly reduces the SA (81% for kerogen, and 99% for shale) and total pore volume for kerogens (48-49%) and shales (98%), by filling or blocking micropores less than 1.3 nm, obstructing pore necks connecting to micropores and mesopores stopping gas transport, occupying adsorption sites, or swelling clays (in shale) to reduce accessible pores.
3) Solvent extraction has limited impact on the methane adsorption and pore texture for the dry overmature shales, with the small amounts of extractable oil arising from drilling mud contamination. In contrast, removing the residual oil increases the methane adsorption capacities of dry oil-window shale (BS3) significantly (Qm increased by 90%). A smaller increase was observed for dry gas-window shale GH4 (Qm increased by 3%), consistent with the lower yield of extractable oil compared to BS3. Removing the oil increased the pore volumes by nearly 300% for the dry BS3 and GH4.
4) Micropore volume and the methane adsorption capacities for the wet over mature shales (SH1 and SH2) increased after solvent extraction, possibly due to the reductions in moisture content reducing pore blocking. Moreover, the increases in methane adsorption capacities for oil-window (BS3) and gas-window (GH4) shales are proportionally greater for the wet shales (207-282%) compared to the dry shales (90 and 3%).
5) The calculated GIP reduces by 32-38% when moisture is considered for the shales investigated. Natural oil arising from maturation can have significant impact on the estimated GIP for oil-window shales. Here, the GIP for extracted wet oil-window shale (BS3) is overestimated by 22%. The impact of solvent extraction on GIP estimates was considerably less for the over-mature shales due to their low extractable oil contents.

6) The measured micropore volume (by either CO_2 or/and N_2 from experiment or the 0.33 nm diameter probe from simulation) is smaller than the micropore volume covered by van der Waals surface. The micropore volume and the methane adsorption capacities from simulation are relatively higher than those from experimental results, due to the effects of narrow pore neck blocking and the closed pores are neglected in simulated models. Higher methane adsorption capacities are observed in high maturity kerogens with larger micropore volumes. The positive correlations between Qm and micropore volume are observed in both simulation and experimental results.
7) Moisture negatively impacts the methane adsorption capacity and the microporosity of the simulated kerogens, the effect of which can be divided into 'rapid', 'gentle' and 'slow' three stages as the increase of moisture. A range of 4-24 wt.%TOC moisture content is needed for KIID matrix and slit models to reach the same reduction of Qm (61-75%) and V_{micro} (88-93%) as 95%R.H. (wet) isolated kerogens. At most 56% moisture in wet isolated kerogen is stored in micropores. The relatively close reduction of methane adsorption capacity and microporosity at the same moisture content suggests accessible microporosity volume is the main controlling factor for methane adsorption.
8) Water has a much stronger affinity with functional groups than methane. Preferred sorption sites for key functional groups (like carboxyl (COOH)) exist for water but not for methane at reservoir conditions. The preferred sorption sites (primary site) directly control water monolayer adsorption at the low moisture contents, while micropore volume limits the water adsorption (multiple-layer or condensation).
9) Water occupying ultra-micropores (<0.7 nm), the main pores for water adsorption, reduces methane adsorption space directly, leading to the 'rapid' Qm reduction stage at extremely low moisture contents. The condensed water clusters in most super-micropores (0.7-2.0 nm) and some ultra-micropores (<0.7 nm) simultaneously as moisture content increases are related to the 'gentle' Qm reduction stage. Water then fills the remaining inaccessible pores for methane at higher moisture content, with little impact on the methane adsorption, which correlates to the 'slow' Qm reduction stage. Therefore, water affects methane adsorption by occupying or blocking the available microporosity for methane rather than occupying the preferred sorption sites available for methane.

7.2 Future work

1) Type II kerogen has been used for comparing the simulated kerogens with the isolated kerogens from experiments. If possible, further simulations on other types of kerogens, including Type I, Type III, and Type IV, and the mixed types kerogens are recommended considering some kerogens contain various types of kerogen in realistic.
2) A comprehensive GIP model that combines both experiment and simulation is recommended to build, as it can benefit the research and industry. The shale gas holding capacity (or GIP) estimation model from the experiment will be useful for the measured shales with sufficient laboratory data. In comparison, the model based on simulation through kerogens has a much broader application once the kerogen type, maturity, and content in shale are tested, making the estimation of shale gas reserves efficient and economical. The carbon capture, utilisation and storage (CCUS) in shale by modelling will be considered.
3) The artificial maturation by high-pressure water pyrolysis of pre-gas window shales is recommended so that the generated gas can be used to compare with the GIP calculated in this study.

REFERENCES

Abràmoff, M. D., P. J. Magalhães and S. J. Ram (2004). "Image processing with ImageJ." Biophotonics international **11**(7): 36-42.

Adesida, A. G., I. Akkutlu, D. E. Resasco and C. S. Rai (2011). Characterization of barnett shale kerogen pore size distribution using DFT analysis and grand canonical monte carlo simulations. SPE annual technical conference and exhibition, Society of Petroleum Engineers.

Aguilar-Armenta, G., M. E. Patiño-Iglesias and R. Leyva-Ramos (2003). "Adsorption kinetic behaviour of pure CO2, N2 and CH4 in natural clinoptilolite at different temperatures." Adsorption Science & Technology **21**(1): 81-91.

Aitkenhead, N. (2002). British Regional Geology: the Pennines and adjacent areas, British Geological Survey.

Akhtar, K., S. A. Khan, S. B. Khan and A. M. Asiri (2018). Scanning electron microscopy: Principle and applications in nanomaterials characterization. Handbook of materials characterization, Springer**:** 113-145.

Alfi, M., M. Barrufet and J. Killough (2019). "Effect of pore sizes on composition distribution and enhance recovery from liquid shale—Molecular sieving in low permeability reservoirs." Fuel **235**: 1555-1564.

Ambrose, R. J., R. C. Hartman, M. Diaz-Campos, I. Y. Akkutlu and C. H. Sondergeld (2012). "Shale gas-in-place calculations part I: new pore-scale considerations." Spe Journal **17**(01): 219-229.

Ambrose, R. J., R. C. Hartman, M. Diaz Campos, I. Y. Akkutlu and C. Sondergeld (2010). New pore-scale considerations for shale gas in place calculations. SPE Unconventional Gas Conference, Society of Petroleum Engineers.

Andrews, I. J. (2013). "The Carboniferous Bowland Shale gas study: geology and resource estimation."

Arif, M., M. Mahmoud, Y. Zhang and S. Iglauer (2020). "X-ray tomography imaging of shale microstructures: A review in the context of multiscale correlative imaging." International Journal of Coal Geology: 103641.

Bai, J., Y. Kang, M. Chen, Z. Chen, L. You, X. Li and G. Chen (2020). "Impact of surface chemistry and pore structure on water vapor adsorption behavior in gas shale." Chemical Engineering Journal **402**: 126238.

Barker, C. E. and M. Pawlewicz (1986). The correlation of vitrinite reflectance with maximum temperature in humic organic matter. Paleogeothermics, Springer**:** 79-93.

Barker, F. (1979). Trondhjemite: definition, environment and hypotheses of origin. Developments in petrology, Elsevier. **6:** 1-12.

Barrett, E. P., L. G. Joyner and P. P. Halenda (1951). "The determination of pore volume and area distributions in porous substances. I. Computations from nitrogen isotherms." Journal of the American Chemical society **73**(1): 373-380.

Baur, F. U., B. J. Katz and G. Gaus (2020). "Gas sorption in source rocks–A short discussion." International Journal of Coal Geology **219**: 103372.

Behar, F. and M. Vandenbroucke (1987). "Chemical modelling of kerogens." Organic Geochemistry **11**(1): 15-24.

Bernard, S. and B. Horsfield (2014). "Thermal maturation of gas shale systems." Annual Review of Earth and Planetary Sciences **42**: 635-651.

Berthezene, N., J.-C. De Hemptinne, A. Audibert and J.-F. Argillier (1999). "Methane solubility in synthetic oil-based drilling muds." Journal of Petroleum Science and Engineering **23**(2): 71-81.
Bertier, P., K. Schweinar, H. Stanjek, A. Ghanizadeh, C. R. Clarkson, A. Busch, N. Kampman, D. Prinz, A. Amann-Hildenbrand and B. M. Krooss (2016). On the use and abuse of N2 physisorption for the characterization of the pore structure of shales. The clay minerals society workshop lectures series.
Best, M. and T. Katsube (1995). "Shale permeability and its significance in hydrocarbon exploration." The Leading Edge **14**(3): 165-170.
Bragg, W. (1921). "The crystal structure of ice." Proceedings of the Physical Society of London **34**(1): 98.
Brandani, S., E. Mangano and L. Sarkisov (2016). "Net, excess and absolute adsorption and adsorption of helium." Adsorption **22**(2): 261-276.
Bruch, L. (1983). "Theory of physisorption interactions." Surface Science **125**(1): 194-217.
Brunauer, S., P. H. Emmett and E. Teller (1938). "Adsorption of gases in multimolecular layers." Journal of the American chemical society **60**(2): 309-319.
Builes, S., S. I. Sandler and R. Xiong (2013). "Isosteric heats of gas and liquid adsorption." Langmuir **29**(33): 10416-10422.
Caineng, Z., D. Dazhong, W. Yuman, L. Xinjing, J. HUANG, W. Shufang, G. Quanzhong, C. ZHANG, W. Hongyan and L. Honglin (2016). "Shale gas in China: Characteristics, challenges and prospects (II)." Petroleum Exploration and Development **43**(2): 182-196.
Caineng, Z., Z. Guosheng, Y. Zhi, T. Shizhen, H. Lianhua, Z. Rukai, Y. Xuanjun, R. Qiquan, L. Denghua and W. Zhiping (2013). "Geological concepts, characteristics, resource potential and key techniques of unconventional hydrocarbon: On unconventional petroleum geology." Petroleum Exploration and Development **40**(4): 385-399.
Caineng, Z., Z. Rukai, B. Bin, Y. Zhi, W. Songtao, S. Ling, D. Dazhong and L. XingJing (2011). "First discovery of nano-pore throat in oil and gas reservoir in China and its scientific value." Acta Petrologica Sinica **27**(6): 1857-1864.
Cao, T., Z. Song, S. Wang and J. Xia (2015). "A comparative study of the specific surface area and pore structure of different shales and their kerogens." Science China Earth Sciences **58**(4): 510-522.
Cao, Y., H. Han, H.-w. Liu, J.-c. Jia, W. Zhang, P.-w. Liu, Z.-g. Ding, S.-j. Chen, J.-g. Lu and Y. Gao (2019). "Influence of solvents on pore structure and methane adsorption capacity of lacustrine shales: An example from a Chang 7 shale sample in the Ordos Basin, China." Journal of Petroleum Science and Engineering **178**: 419-428.
Carr, A. (1999). "A vitrinite reflectance kinetic model incorporating overpressure retardation." Marine and Petroleum Geology **16**(4): 355-377.
Chalmers, G. R. and M. R. Bustin (2010). "PS The Effects and Distribution of Moisture in Gas Shale Reservoir Systems." AAPG Annual Convention and Exhibition.
Chalmers, G. R. and R. M. Bustin (2007). "The organic matter distribution and methane capacity of the Lower Cretaceous strata of Northeastern British Columbia, Canada." International Journal of Coal Geology **70**(1-3): 223-239.
Chalmers, G. R., R. M. Bustin and I. M. Power (2012). "Characterization of gas shale pore systems by porosimetry, pycnometry, surface area, and field emission scanning electron microscopy/transmission electron microscopy image analyses: Examples from the Barnett, Woodford, Haynesville, Marcellus, and Doig unitsCharacterization of Gas Shale Pore Systems." AAPG bulletin **96**(6): 1099-1119.
Charpentier, R. R. and T. A. Cook (2011). "USGS methodology for assessing continuous petroleum resources."

Chen, C., D. Hu, D. Westacott and D. Loveless (2013). "Nanometer - scale characterization of microscopic pores in shale kerogen by image analysis and pore - scale modeling." Geochemistry, Geophysics, Geosystems **14**(10): 4066-4075.
Chen, J. and X. Xiao (2014). "Evolution of nanoporosity in organic-rich shales during thermal maturation." Fuel **129**: 173-181.
Chen, M., Y. Kang, T. Zhang, X. Li, K. Wu and Z. Chen (2018). "Methane adsorption behavior on shale matrix at in-situ pressure and temperature conditions: Measurement and modeling." Fuel **228**: 39-49.
Chen, M., Y. Kang, T. Zhang, L. You, X. Li, Z. Chen, K. Wu and B. Yang (2018). "Methane diffusion in shales with multiple pore sizes at supercritical conditions." Chemical Engineering Journal **334**: 1455-1465.
Chen, Y., S. Jiang, D. Zhang and C. Liu (2017). "An adsorbed gas estimation model for shale gas reservoirs via statistical learning." Applied energy **197**: 327-341.
Cheng, P., H. Tian, X. Xiao, H. Gai, T. Li and X. Wang (2017). "Water distribution in overmature organic-rich shales: implications from water adsorption experiments." Energy & Fuels **31**(12): 13120-13132.
Chong, L., S. Sanguinito, A. L. Goodman and E. M. Myshakin (2021). "Molecular characterization of carbon dioxide, methane, and water adsorption in micropore space of kerogen matrix." Fuel **283**: 119254.
Church, K. D. and R. L. Gawthorpe (1994). "High resolution sequence stratigraphy of the late Namurian in the Widmerpool Gulf (East Midlands, UK)." Marine and Petroleum Geology **11**(5): 528-544.
Clarke, H., P. Turner, R. M. Bustin, N. Riley and B. Besly (2018). "Shale gas resources of the Bowland Basin, NW England: a holistic study." Petroleum Geoscience **24**(3): 287-322.
Clarkson, C. R., N. Solano, R. M. Bustin, A. Bustin, G. Chalmers, L. He, Y. B. Melnichenko, A. Radliński and T. P. Blach (2013). "Pore structure characterization of North American shale gas reservoirs using USANS/SANS, gas adsorption, and mercury intrusion." Fuel **103**: 606-616.
Collell, J., G. Galliero, F. Gouth, F. Montel, M. Pujol, P. Ungerer and M. Yiannourakou (2014). "Molecular simulation and modelisation of methane/ethane mixtures adsorption onto a microporous molecular model of kerogen under typical reservoir conditions." Microporous and Mesoporous Materials **197**: 194-203.
Collell, J., G. Galliero, R. Vermorel, P. Ungerer, M. Yiannourakou, F. Montel and M. Pujol (2015). "Transport of multicomponent hydrocarbon mixtures in shale organic matter by molecular simulations." The Journal of Physical Chemistry C **119**(39): 22587-22595.
Collell, J., P. Ungerer, G. Galliero, M. Yiannourakou, F. o. Montel and M. Pujol (2014). "Molecular simulation of bulk organic matter in type II shales in the middle of the oil formation window." Energy & Fuels **28**(12): 7457-7466.
Colletta, B., J. Letouzey, R. Pinedo, J. F. Ballard and P. Balé (1991). "Computerized X-ray tomography analysis of sandbox models: Examples of thin-skinned thrust systems." Geology **19**(11): 1063-1067.
Connolly, M. L. (1983). "Solvent-accessible surfaces of proteins and nucleic acids." Science **221**(4612): 709-713.
Cristancho-Albarracin, D., I. Y. Akkutlu, L. J. Criscenti and Y. Wang (2017). "Shale gas storage in kerogen nanopores with surface heterogeneities." Applied geochemistry **84**: 1-10.
Curtis, J. B. (2002). "Fractured shale-gas systems." AAPG bulletin **86**(11): 1921-1938.
Curtis, M. E., R. J. Ambrose and C. H. Sondergeld (2010). Structural characterization of gas shales on the micro-and nano-scales. Canadian unconventional resources and international petroleum conference, Society of Petroleum Engineers.

Curtis, M. E., B. J. Cardott, C. H. Sondergeld and C. S. Rai (2012). "Development of organic porosity in the Woodford Shale with increasing thermal maturity." International Journal of Coal Geology **103**: 26-31.
D'Arrigo, J. S. (1978). "Screening of membrane surface charges by divalent cations: an atomic representation." American Journal of Physiology-Cell Physiology **235**(3): C109-C117.
Dai, J., C. Zou, S. Liao, D. Dong, Y. Ni, J. Huang, W. Wu, D. Gong, S. Huang and G. Hu (2014). "Geochemistry of the extremely high thermal maturity Longmaxi shale gas, southern Sichuan Basin." Organic Geochemistry **74**: 3-12.
Dauber‐Osguthorpe, P., V. A. Roberts, D. J. Osguthorpe, J. Wolff, M. Genest and A. T. Hagler (1988). "Structure and energetics of ligand binding to proteins: Escherichia coli dihydrofolate reductase‐trimethoprim, a drug‐receptor system." Proteins: Structure, Function, and Bioinformatics **4**(1): 31-47.
Day, S., R. Sakurovs and S. Weir (2008). "Supercritical gas sorption on moist coals." International Journal of Coal Geology **74**(3-4): 203-214.
Dayal, A. M. and D. Mani (2017). Shale gas: Exploration and environmental and economic impacts, Elsevier.
DiStefano, V. H., J. McFarlane, L. M. Anovitz, A. G. Stack, A. D. Gordon, K. C. Littrell, S. J. Chipera, R. D. Hunt, S. A. Lewis Sr and R. E. Hale (2016). "Extraction of organic compounds from representative shales and the effect on porosity." Journal of Natural Gas Science and Engineering **35**: 646-660.
DiStefano, V. H., J. McFarlane, A. G. Stack, E. Perfect, D. F. Mildner, M. Bleuel, S. J. Chipera, K. C. Littrell, M. C. Cheshire and K. E. Manz (2019). "Solvent-pore interactions in the Eagle Ford shale formation." Fuel **238**: 298-311.
Djuricic, M., R. Murphy, D. Vitorovic and K. Biemann (1971). "Organic acids obtained by alkaline permanganate oxidation of kerogen from the Green River (Colorado) shale." Geochimica et Cosmochimica Acta **35**(12): 1201-1207.
Donaldson, E. C., G. V. Chilingarian and T. F. Yen (1985). Enhanced oil recovery, I: fundamentals and analyses, Elsevier.
Dong, D., Z. Shi, Q. Guan, S. Jiang, M. Zhang, C. Zhang, S. Wang, S. Sun, R. Yu and D. Liu (2018). "Progress, challenges and prospects of shale gas exploration in the Wufeng–Longmaxi reservoirs in the Sichuan Basin." Natural Gas Industry B **5**(5): 415-424.
Dow, W. G. (1977). "Kerogen studies and geological interpretations." Journal of geochemical exploration **7**: 79-99.
Dubbeldam, D., A. Torres-Knoop and K. Walton (2013). "On the inner workings of Monte Carlo codes." Molecular Simulation **39**(14-15): 1253-1292.
Dubinin, M. (1966). "Chemistry and physics of carbon." M. Dekker, New York: 51-120.
Durand, B. (1980). Kerogen: Insoluble organic matter from sedimentary rocks, Editions technip.
Dzyaloshinskii, I. E., E. M. Lifshitz and L. P. Pitaevskii (1961). "The general theory of van der Waals forces." Advances in Physics **10**(38): 165-209.
Earnest, C. M. (1988). Compositional analysis by thermogravimetry, ASTM International.
Eldridge, R. B. (1996). "Oil contaminant removal from drill cuttings by supercritical extraction." Industrial & engineering chemistry research **35**(6): 1901-1905.
Emsley, J. (1980). "Very strong hydrogen bonding." Chemical Society Reviews **9**(1): 91-124.
Fan, E., S. Tang, C. Zhang, Q. Guo and C. Sun (2014). "Methane sorption capacity of organics and clays in high-over matured shale-gas systems." Energy Exploration and Exploitation **32**(6): 927-942.
Fan, K., Y. Li, D. Elsworth, M. Dong, C. Yin, Y. Li and Z. Chen (2018). "Three stages of methane adsorption capacity affected by moisture content." Fuel **231**: 352-360.

Feng, D., X. Li, X. Wang, J. Li, F. Sun, Z. Sun, T. Zhang, P. Li, Y. Chen and X. Zhang (2018). "Water adsorption and its impact on the pore structure characteristics of shale clay." Applied Clay Science **155**: 126-138.
Fisher, L. and J. Israelachvili (1979). "Direct experimental verification of the Kelvin equation for capillary condensation." Nature **277**(5697): 548-549.
Frank, J. (2013). Electron tomography: three-dimensional imaging with the transmission electron microscope, Springer Science & Business Media.
Fraser, A. J. and R. L. Gawthorpe (2003). An atlas of Carboniferous basin evolution in northern England, Geological Society.
Frenkel, D. and B. Smit (2001). Understanding molecular simulation: from algorithms to applications, Elsevier.
Fry, R., S. Day and R. Sakurovs (2009). "Moisture-induced swelling of coal." International Journal of Coal Preparation and Utilization **29**(6): 298-316.
Gaedt, K. and H. D. Höltje (1998). "Consistent valence force‐field parameterization of bond lengths and angles with quantum chemical ab initio methods applied to some heterocyclic dopamine D3‐receptor agonists." Journal of computational chemistry **19**(8): 935-946.
Ganz, H. and W. Kalkreuth (1987). "Application of infrared spectroscopy to the classification of kerogentypes and the evaluation of source rock and oil shale potentials." Fuel **66**(5): 708-711.
Gasparik, M., P. Bertier, Y. Gensterblum, A. Ghanizadeh, B. M. Krooss and R. Littke (2014). "Geological controls on the methane storage capacity in organic-rich shales." International Journal of Coal Geology **123**: 34-51.
Gasparik, M., A. Ghanizadeh, P. Bertier, Y. Gensterblum, S. Bouw and B. M. Krooss (2012). "High-pressure methane sorption isotherms of black shales from the Netherlands." Energy & fuels **26**(8): 4995-5004.
Gasparik, M., A. Ghanizadeh, Y. Gensterblum and B. M. Krooss (2013). "“Multi-temperature” method for high-pressure sorption measurements on moist shales." Review of Scientific Instruments **84**(8): 085116.
Gawthorpe, R. L. (1987). "Burial dolomitization and porosity development in a mixed carbonate‐clastic sequence: an example from the Bowland Basin, northern England." Sedimentology **34**(4): 533-558.
Gawthorpe, R. L. (1987). "Tectono-sedimentary evolution of the Bowland Basin, N England, during the Dinantian." Journal of the Geological Society **144**(1): 59-71.
Ghanbarnezhad Moghanloo, R., F. Javadpour and D. Davudov (2013). Contribution of methane molecular diffusion in kerogen to gas-in-place and production. SPE Western Regional & AAPG Pacific Section Meeting 2013 Joint Technical Conference, Society of Petroleum Engineers.
Giesche, H. (2006). "Mercury porosimetry: a general (practical) overview." Particle & particle systems characterization **23**(1): 9-19.
Gong, L., J.-H. Shi, B. Ding, Z.-Q. Huang, S.-Y. Sun and J. Yao (2020). "Molecular insight on competitive adsorption and diffusion characteristics of shale gas in water-bearing channels." Fuel **278**: 118406.
Gorshkov, A. and I. Khomyakov (2019). Thermal treatment of reservoir as one of the powerful method of shale formation development in Russia. IOP conference series: Earth and environmental science, IOP Publishing.
Gregg, S. and K. Sing (1982). "W. Adsorption, surface area and porosity." London: Academic Press: 195-197.
Guo, F., S. Wang, Q. Feng, X. Yao, Q. Xue and X. Li (2020). "Adsorption and absorption of supercritical methane within shale kerogen slit." Journal of Molecular Liquids **320**: 114364.

Guo, H., W. Jia, Y. Lei, X. Luo, M. Cheng, X. Wang, L. Zhang and C. Jiang (2014). "The composition and its impact on the methane sorption of lacustrine shales from the Upper Triassic Yanchang Formation, Ordos Basin, China." Marine and Petroleum Geology **57**: 509-520.
Guo, S. (2013). "Experimental study on isothermal adsorption of methane gas on three shale samples from Upper Paleozoic strata of the Ordos Basin." Journal of Petroleum Science and Engineering **110**: 132-138.
Guthrie, J. M. and L. M. Pratt (1994). "Geochemical indicators of depositional environment and source-rock potential for the Upper Ordovician Maquoketa Group, Illinois Basin." AAPG bulletin **78**(5): 744-757.
Hanafy, H., S. Macary, Y. ElNady, A. Bayomi and M. El Batanony (1997). A new approach for predicting the crude oil properties. SPE Production Operations Symposium, Society of Petroleum Engineers.
Hartgers, W. A., J. S. S. Damsté, J. W. De Leeuw, Y. Ling and J. C. Crelling (1995). "The influence of mineral matter on the separation of amorphous marine kerogens using density gradient centrifugation." Organic geochemistry **23**(8): 777-784.
Heller, R. and M. Zoback (2014). "Adsorption of methane and carbon dioxide on gas shale and pure mineral samples." Journal of Unconventional Oil and Gas Resources **8**: 14-24.
Henry, W. (1803). "III. Experiments on the quantity of gases absorbed by water, at different temperatures, and under different pressures." Philosophical Transactions of the Royal Society of London(93): 29-274.
Ho, T. A., L. J. Criscenti and Y. Wang (2016). "Nanostructural control of methane release in kerogen and its implications to wellbore production decline." Scientific reports **6**(1): 1-9.
Hoover, W. G. (1986). "Constant-pressure equations of motion." Physical Review A **34**(3): 2499.
Horváth, G. and K. Kawazoe (1983). "Method for the calculation of effective pore size distribution in molecular sieve carbon." Journal of Chemical Engineering of Japan **16**(6): 470-475.
Hounsfield, G. N. (1973). "Computerized transverse axial scanning (tomography): Part 1. Description of system." The British journal of radiology **46**(552): 1016-1022.
Hu, H. (2014). "Methane adsorption comparison of different thermal maturity kerogens in shale gas system." Chinese Journal of Geochemistry **33**(4): 425-430.
Hu, H., T. Zhang, J. D. Wiggins-Camacho, G. S. Ellis, M. D. Lewan and X. Zhang (2015). "Experimental investigation of changes in methane adsorption of bitumen-free Woodford Shale with thermal maturation induced by hydrous pyrolysis." Marine and Petroleum Geology **59**: 114-128.
Huang, L., Z. Ning, Q. Wang, R. Qi, Z. Cheng, X. Wu, W. Zhang and H. Qin (2019). "Molecular insights into kerogen deformation induced by CO2/CH4 sorption: effect of maturity and moisture." Energy & Fuels **33**(6): 4792-4805.
Huang, L., Z. Ning, Q. Wang, R. Qi, Y. Zeng, H. Qin, H. Ye and W. Zhang (2018). "Molecular simulation of adsorption behaviors of methane, carbon dioxide and their mixtures on kerogen: effect of kerogen maturity and moisture content." Fuel **211**: 159-172.
Huang, L., Z. Ning, Q. Wang, W. Zhang, Z. Cheng, X. Wu and H. Qin (2018). "Effect of organic type and moisture on CO 2/CH 4 competitive adsorption in kerogen with implications for CO 2 sequestration and enhanced CH 4 recovery." Applied Energy **210**: 28-43.
Huang, L., W. Zhou, H. Xu, L. Wang, J. Zou and Q. Zhou (2021). "Dynamic fluid states in organic-inorganic nanocomposite: Implications for shale gas recovery and CO2 sequestration." Chemical Engineering Journal **411**: 128423.
Hübschmann, H.-J. (2015). Handbook of GC-MS: fundamentals and applications, John Wiley & Sons.

Hunt, J. (1979). "Petroleum geochemistry and geology, San Francisco, California."
Ibad, S. M. and E. Padmanabhan (2020). "Methane sorption capacities and geochemical characterization of Paleozoic shale Formations from Western Peninsula Malaysia: Implication of shale gas potential." International Journal of Coal Geology: 103480.
Ismadji, S., F. E. Soetaredjo and A. Ayucitra (2015). The Characterization of Clay Minerals and Adsorption Mechanism onto Clays. Clay Materials for Environmental Remediation, Springer**:** 93-112.
Ismail, A. F., K. C. Khulbe and T. Matsuura (2015). "Gas separation membranes." Switz. Springer **10**: 978-973.
Jarrett, A. J., R. Schinteie, J. M. Hope and J. J. Brocks (2013). "Micro-ablation, a new technique to remove drilling fluids and other contaminants from fragmented and fissile rock material." Organic geochemistry **61**: 57-65.
Jarvie, D. M., R. J. Hill, T. E. Ruble and R. M. Pollastro (2007). "Unconventional shale-gas systems: The Mississippian Barnett Shale of north-central Texas as one model for thermogenic shale-gas assessment." AAPG bulletin **91**(4): 475-499.
Javadpour, F. (2009). "Nanopores and apparent permeability of gas flow in mudrocks (shales and siltstone)." Journal of Canadian Petroleum Technology **48**(08): 16-21.
Ji, L., T. Zhang, K. L. Milliken, J. Qu and X. Zhang (2012). "Experimental investigation of main controls to methane adsorption in clay-rich rocks." Applied Geochemistry **27**(12): 2533-2545.
Ji, W., Y. Song, Z. Jiang, L. Chen, Z. Li, X. Yang and M. Meng (2015). "Estimation of marine shale methane adsorption capacity based on experimental investigations of Lower Silurian Longmaxi formation in the Upper Yangtze Platform, south China." Marine and Petroleum Geology **68**: 94-106.
Ji, W., Y. Song, Z. Rui, M. Meng and H. Huang (2017). "Pore characterization of isolated organic matter from high matured gas shale reservoir." International Journal of Coal Geology **174**: 31-40.
Jin, Z. and A. Firoozabadi (2014). "Effect of water on methane and carbon dioxide sorption in clay minerals by Monte Carlo simulations." Fluid Phase Equilibria **382**: 10-20.
Job, N., A. Théry, R. Pirard, J. Marien, L. Kocon, J.-N. Rouzaud, F. Béguin and J.-P. Pirard (2005). "Carbon aerogels, cryogels and xerogels: Influence of the drying method on the textural properties of porous carbon materials." Carbon **43**(12): 2481-2494.
Jones, T., T. Hughes and P. Tomkins (1989). "The ion content and mineralogy of a North Sea Cretaceous shale formation." Clay minerals **24**(2): 393-410.
Joubert, J. I., C. T. Grein and D. Bienstock (1973). "Sorption of methane in moist coal." Fuel **52**(3): 181-185.
Kannan, M. (2018). "Scanning Electron Microscopy: Principle, Components and Applications." A textbook on Fundamentals and Applications of Nanotechnology: 81-92.
Kannan, M. (2018). "Transmission Electron Microscope–Principle, Components and Applications." A Textbook on Fundamentals and Applications of Nanotechnology: 93-102.
Katsube, T. (2000). Shale permeability and pore-structure evolution characteristics, Natural Resources Canada, Geological Survey of Canada.
Kelemen, S., M. Afeworki, M. Gorbaty, M. Sansone, P. Kwiatek, C. Walters, H. Freund, M. Siskin, A. Bence and D. Curry (2007). "Direct characterization of kerogen by X-ray and solid-state 13C nuclear magnetic resonance methods." Energy & Fuels **21**(3): 1548-1561.
Kibria, M. G., S. Das, Q.-H. Hu, A. R. Basu, W.-X. Hu and S. Mandal (2020). "Thermal maturity evaluation using Raman spectroscopy for oil shale samples of USA: comparisons with vitrinite reflectance and pyrolysis methods." Petroleum Science **17**(3): 567-581.

Kirkwood, J. G. and F. P. Buff (1949). "The statistical mechanical theory of surface tension." The Journal of Chemical Physics **17**(3): 338-343.
Klaver, J., S. Hemes, M. Houben, G. Desbois, Z. Radi and J. Urai (2015). "The connectivity of pore space in mudstones: insights from high ‐ pressure Wood's metal injection, BIB ‐ SEM imaging, and mercury intrusion porosimetry." Geofluids **15**(4): 577-591.
Krevelen, D. v. (1961). "Coal: Typology, Chemistry, Physics." Constitution **3**.
Krooss, B. v., F. Van Bergen, Y. Gensterblum, N. Siemons, H. Pagnier and P. David (2002). "High-pressure methane and carbon dioxide adsorption on dry and moisture-equilibrated Pennsylvanian coals." International Journal of Coal Geology **51**(2): 69-92.
Kuila, U., D. K. McCarty, A. Derkowski, T. B. Fischer, T. Topór and M. Prasad (2014). "Nano-scale texture and porosity of organic matter and clay minerals in organic-rich mudrocks." Fuel **135**: 359-373.
Labani, M. M., R. Rezaee, A. Saeedi and A. Al Hinai (2013). "Evaluation of pore size spectrum of gas shale reservoirs using low pressure nitrogen adsorption, gas expansion and mercury porosimetry: A case study from the Perth and Canning Basins, Western Australia." Journal of Petroleum Science and Engineering **112**: 7-16.
Labinger, J. A. and J. E. Bercaw (2002). "Understanding and exploiting C–H bond activation." Nature **417**(6888): 507-514.
Lafargue, E., F. Marquis and D. Pillot (1998). "Rock-Eval 6 applications in hydrocarbon exploration, production, and soil contamination studies." Revue de l'institut français du pétrole **53**(4): 421-437.
Landers, J., G. Y. Gor and A. V. Neimark (2013). "Density functional theory methods for characterization of porous materials." Colloids and Surfaces A: Physicochemical and Engineering Aspects **437**: 3-32.
Landis, E. N. and D. T. Keane (2010). "X-ray microtomography." Materials characterization **61**(12): 1305-1316.
Langmuir, I. (1918). "The adsorption of gases on plane surfaces of glass, mica and platinum." Journal of the American Chemical society **40**(9): 1361-1403.
Larson, J. and T. McMahon (1984). "Gas-phase bihalide and pseudobihalide ions. An ion cyclotron resonance determination of hydrogen bond energies in XHY-species (X, Y= F, Cl, Br, CN)." Inorganic Chemistry **23**(14): 2029-2033.
Lee, S., T. B. Fischer, M. R. Stokes, R. J. Klingler, J. Ilavsky, D. K. McCarty, M. O. Wigand, A. Derkowski and R. E. Winans (2014). "Dehydration effect on the pore size, porosity, and fractal parameters of shale rocks: Ultrasmall-angle X-ray scattering study." Energy & fuels **28**(11): 6772-6779.
Levine, J. R. and A. Davis (1984). "Optical anisotropy of coals as an indicator of tectonic deformation, Broad Top Coal Field, Pennsylvania." Geological Society of America Bulletin **95**(1): 100-108.
Levy, D. H. (2007). "Van der Waals molecules." Advances in Chemical Physics (Wiley, 2007): 323.
Li, J., X. Li, X. Wang, Y. Li, K. Wu, J. Shi, L. Yang, D. Feng, T. Zhang and P. Yu (2016). "Water distribution characteristic and effect on methane adsorption capacity in shale clay." International Journal of Coal Geology **159**: 135-154.
Li, J., S. Zhou, G. Gaus, Y. Li, Y. Ma, K. Chen and Y. Zhang (2018). "Characterization of methane adsorption on shale and isolated kerogen from the Sichuan Basin under pressure up to 60 MPa: Experimental results and geological implications." International Journal of Coal Geology **189**: 83-93.
Li, M., X. Pang, L. Xiong, T. Hu, D. Chen, Z. Zhao, S. Hui, Y. Liu and S. Zhang (2022). "The main controlling factors on shale gas occurrence characteristics in deep and high-over mature

shales: A case study of Silurian Longmaxi Formation in the Sichuan Basin, southern China." Energy Reports 8: 6901-6913.
Li, W., X. Pang, C. Snape, B. Zhang, D. Zheng and X. Zhang (2019). "Molecular Simulation Study on Methane Adsorption Capacity and Mechanism in Clay Minerals: Effect of Clay Type, Pressure, and Water Saturation in Shales." Energy & Fuels **33**(2): 765-778.
Li, W., L. A. Stevens, W. Meredith, C. N. Uguna, C. H. Vane, B. Zhang, A. D. Carr, D. Zheng and C. E. Snape (2022). "The effect of oil extraction on porosity and methane adsorption for dry and moisture-equilibrated shales." Fuel **316**: 123304.
Li, W., L. A. Stevens, C. N. Uguna, C. H. Vane, W. Meredith, L. Tang, Q. Li and C. E. Snape (2021). "Comparison of the impact of moisture on methane adsorption and nanoporosity for over mature shales and their kerogens." International Journal of Coal Geology: 103705.
Lille, Ü. (2004). "BEHAVIOR OF ESTONIAN KUKERSITE KEROGEN IN MOLECULAR MECHANICAL FORCE FIELD." Oil Shale **21**(2).
Liming, J., Q. Junli and Z. Tongwei (2012). "Experiments on methane adsorption of common clay minerals in shale." Earth Science: Journal of China University of Geosciences **37**(5): 1043-1050.
Liming, J., Q. Junli, X. Yanqing and Z. Tongwei (2012). "Micro-pore characteristics and methane adsorption properties of common clay minerals by electron microscope scanning." Acta Petrolei Sinica **33**(2): 249-256.
Liu, G., Z. Huang, Z. Jiang, J. Chen, F. Chen and J. Xing (2016). "Gas adsorption capacity calculation limitation due to methane adsorption in low thermal maturity shale: A case study from the Yanchang Formation, Ordos Basin." Journal of Natural Gas Science and Engineering **30**: 106-118.
Liu, J., N. Sun, C. Sun, H. Liu, C. Snape, K. Li, W. Wei and Y. Sun (2015). "Spherical potassium intercalated activated carbon beads for pulverised fuel CO2 post-combustion capture." Carbon **94**: 243-255.
Liu, J., Y. Yang, S. Sun, J. Yao and J. Kou (2022). "Flow Behaviors of Shale Oil in Kerogen Slit by Molecular Dynamics Simulation." Chemical Engineering Journal: 134682.
Liu, Y. and J. Wilcox (2010). "CO2 adsorption on carbon models of organic constituents of gas shale and coal." Environmental science & technology **45**(2): 809-814.
Löhr, S., E. Baruch, P. Hall and M. Kennedy (2015). "Is organic pore development in gas shales influenced by the primary porosity and structure of thermally immature organic matter?" Organic Geochemistry **87**: 119-132.
Loucks, R. G., R. M. Reed, S. C. Ruppel and U. Hammes (2010). "Preliminary classification of matrix pores in mudrocks."
Loucks, R. G., R. M. Reed, S. C. Ruppel and U. Hammes (2012). "Spectrum of pore types and networks in mudrocks and a descriptive classification for matrix-related mudrock pores." AAPG bulletin **96**(6): 1071-1098.
Loucks, R. G., R. M. Reed, S. C. Ruppel and D. M. Jarvie (2009). "Morphology, genesis, and distribution of nanometer-scale pores in siliceous mudstones of the Mississippian Barnett Shale." Journal of sedimentary research **79**(12): 848-861.
Loucks, R. G. and S. C. Ruppel (2007). "Mississippian Barnett Shale: Lithofacies and depositional setting of a deep-water shale-gas succession in the Fort Worth Basin, Texas." AAPG bull **91**(4): 579-601.
Luffel, D. and F. Guidry (1992). "New core analysis methods for measuring reservoir rock properties of Devonian shale." Journal of Petroleum Technology **44**(11): 1,184-181,190.
Luo, P., N. Zhong, I. Khan, X. Wang, H. Wang, Q. Luo and Z. Guo (2019). "Effects of pore structure and wettability on methane adsorption capacity of mud rock: Insights from mixture of organic matter and clay minerals." Fuel **251**: 551-561.

Ma, L., A.-L. Fauchille, P. J. Dowey, F. F. Pilz, L. Courtois, K. G. Taylor and P. D. Lee (2017). "Correlative multi-scale imaging of shales: a review and future perspectives." Geological Society, London, Special Publications **454**(1): 175-199.
Ma, P.-s., C. Hua and S.-q. Xia (2002). "Study of the solubility of methane in alkanes." Journal of Chemical Engineering of Chinese Universities **16**(6): 680-685.
Malik, S., L. Smith, J. Sharman, E. M. Holt and S. P. Rigby (2016). "Pore structural characterization of fuel cell layers using integrated mercury porosimetry and computerized X-ray tomography." Industrial & Engineering Chemistry Research **55**(41): 10850-10859.
Martin, T. and Z. S. Derewenda (1999). "The name is bond—H bond." nature structural biology **6**(5): 403-406.
Mastalerz, M., L. Hampton, A. Drobniak and H. Loope (2017). "Significance of analytical particle size in low-pressure N2 and CO2 adsorption of coal and shale." International Journal of Coal Geology **178**: 122-131.
Mathias, P. M. and T. W. Copeman (1983). "Extension of the Peng-Robinson equation of state to complex mixtures: evaluation of the various forms of the local composition concept." Fluid phase equilibria **13**: 91-108.
Mayo, S. L., B. D. Olafson and W. A. Goddard (1990). "DREIDING: a generic force field for molecular simulations." Journal of Physical chemistry **94**(26): 8897-8909.
McCarthy, K., K. Rojas, M. Niemann, D. Palmowski, K. Peters and A. Stankiewicz (2011). "Basic petroleum geochemistry for source rock evaluation." Oilfield Review **23**(2): 32-43.
McMillan, W. and E. Teller (1951). "The assumptions of the BET theory." The Journal of Physical Chemistry **55**(1): 17-20.
Merkel, A., R. Fink and R. Littke (2015). "The role of pre-adsorbed water on methane sorption capacity of Bossier and Haynesville shales." International Journal of Coal Geology **147**: 1-8.
Merkel, A., R. Fink and R. Littke (2016). "High pressure methane sorption characteristics of lacustrine shales from the Midland Valley Basin, Scotland." Fuel **182**: 361-372.
Michalec, L. and M. Lísal (2017). "Molecular simulation of shale gas adsorption onto overmature type II model kerogen with control microporosity." Molecular Physics **115**(9-12): 1086-1103.
Milliken, K. L., M. Rudnicki, D. N. Awwiller and T. Zhang (2013). "Organic matter–hosted pore system, Marcellus formation (Devonian), Pennsylvania." AAPG bulletin **97**(2): 177-200.
Milner, M., R. McLin and J. Petriello (2010). Imaging texture and porosity in mudstones and shales: Comparison of secondary and ion-milled backscatter SEM methods. Canadian unconventional resources and international petroleum conference, Society of Petroleum Engineers.
Mohnhoff, D., R. Littke, B. M. Krooss and P. Weniger (2016). "Flow-through extraction of oil and gas shales under controlled stress using organic solvents: Implications for organic matter-related porosity and permeability changes with thermal maturity." International Journal of Coal Geology **157**: 84-99.
Moses, P. (1961). Geothermal gradients. Drilling and production practice, OnePetro.
Mosher, K., J. He, Y. Liu, E. Rupp and J. Wilcox (2013). "Molecular simulation of methane adsorption in micro-and mesoporous carbons with applications to coal and gas shale systems." International Journal of Coal Geology **109**: 36-44.
Mukhopadhyay, P. K. (1994). "Vitrinite reflectance as maturity parameter: petrographic and molecular characterization and its applications to basin modeling."
Nair, H. and W. Clarke (2016). Mass spectrometry for the clinical laboratory, Academic Press.
Nelson, P. H. (2009). "Pore-throat sizes in sandstones, tight sandstones, and shales." AAPG bulletin **93**(3): 329-340.

Nicholson, A. J. and D. Swingler (1980). "Ion formation in the flame ionization detector." Combustion and Flame **39**(1): 43-52.
Nicholson, D. (1982). Computer simulation and the statistical mechanics of adsorption, Academic Press.
Nosé, S. (1984). "A molecular dynamics method for simulations in the canonical ensemble." Molecular physics **52**(2): 255-268.
Nosé, S. (1984). "A unified formulation of the constant temperature molecular dynamics methods." The Journal of chemical physics **81**(1): 511-519.
Nosé, S. and M. L. Klein (1983). "A study of solid and liquid carbon tetrafluoride using the constant pressure molecular dynamics technique." The Journal of Chemical Physics **78**(11): 6928-6939.
Okiongbo, K. S., A. C. Aplin and S. R. Larter (2005). "Changes in type II kerogen density as a function of maturity: Evidence from the Kimmeridge Clay Formation." Energy & fuels **19**(6): 2495-2499.
Otsu, N. (1979). "A threshold selection method from gray-level histograms." IEEE transactions on systems, man, and cybernetics **9**(1): 62-66.
Pan, H., J. A. Ritter and P. B. Balbuena (1998). "Examination of the approximations used in determining the isosteric heat of adsorption from the Clausius-Clapeyron equation." Langmuir **14**(21): 6323-6327.
Pang, Y., Y. Tian, M. Y. Soliman and Y. Shen (2019). "Experimental measurement and analytical estimation of methane absorption in shale kerogen." Fuel **240**: 192-205.
Parsegian, V. A. (2005). Van der Waals forces: a handbook for biologists, chemists, engineers, and physicists, Cambridge University Press.
Passey, Q. R., K. Bohacs, W. L. Esch, R. Klimentidis and S. Sinha (2010). From oil-prone source rock to gas-producing shale reservoir-geologic and petrophysical characterization of unconventional shale gas reservoirs. International oil and gas conference and exhibition in China, Society of Petroleum Engineers.
Pauling, L. (1935). "The structure and entropy of ice and of other crystals with some randomness of atomic arrangement." Journal of the American Chemical Society **57**(12): 2680-2684.
Peng, J., K. Milliken, Q. Fu, X. Janson and S. Hamlin (2020). Grain assemblages and diagenesis in organic-rich mudrocks, Late Pennsylvanian Cline Shale (Wolfcamp D), Midland Basin, Texas. 2019 AAPG Annual Convention and Exhibition.
Peng, J., K. L. Milliken and Q. Fu (2019). "Quartz types in the Upper Pennsylvanian organic-rich Cline Shale (Wolfcamp D), Midland Basin, Texas: Implications for silica diagenesis, porosity evolution and rock mechanical properties." Sedimentology.
Perez, F. and D. Devegowda (2017). "Estimation of adsorbed-phase density of methane in realistic overmature kerogen models using molecular simulations for accurate gas in place calculations." Journal of Natural Gas Science and Engineering **46**: 865-872.
Peters, K. E. (1986). "Guidelines for evaluating petroleum source rock using programmed pyrolysis." AAPG bulletin **70**(3): 318-329.
Peters, K. E. and M. R. Cassa (1994). "Applied source rock geochemistry: Chapter 5: Part II. Essential elements."
Philp, R. (1985). "Petroleum formation and occurrence." Eos, Transactions American Geophysical Union **66**(37): 643-644.
Piazzesi, G. (1973). "Photogrammetry with the scanning electron microscope." Journal of Physics E: Scientific Instruments **6**(4): 392.
Polanyi, M. (1963). "The potential theory of adsorption." Science **141**(3585): 1010-1013.

Qi, L., X. Tang, Z. Wang and X. Peng (2017). "Pore characterization of different types of coal from coal and gas outburst disaster sites using low temperature nitrogen adsorption approach." International Journal of Mining Science and Technology **27**(2): 371-377.
Qi, Y., Y. Ju, J. Cai, Y. Gao, H. Zhu, C. Hunag, J. Wu, S. Meng and W. Chen (2019). "The effects of solvent extraction on nanoporosity of marine-continental coal and mudstone." Fuel **235**: 72-84.
Rappé, A. K., C. J. Casewit, K. Colwell, W. A. Goddard III and W. M. Skiff (1992). "UFF, a full periodic table force field for molecular mechanics and molecular dynamics simulations." Journal of the American chemical society **114**(25): 10024-10035.
Rexer, T. F., M. J. Benham, A. C. Aplin and K. M. Thomas (2013). "Methane adsorption on shale under simulated geological temperature and pressure conditions." Energy & Fuels **27**(6): 3099-3109.
Rexer, T. F., E. J. Mathia, A. C. Aplin and K. M. Thomas (2014). "High-pressure methane adsorption and characterization of pores in Posidonia shales and isolated kerogens." Energy & Fuels **28**(5): 2886-2901.
Rexer, T. F., E. J. Mathia, A. C. Aplin and K. M. Thomas (2020). "Supercritical methane adsorption and storage in pores in shales and isolated kerogens." SN Applied Sciences **2**: 1-17.
Rigby, S. P. (2018). "Recent developments in the structural characterisation of disordered, mesoporous solids." Johnson Matthey Technology Review **62**(3): 296-312.
Rigby, S. P. and K. J. Edler (2002). "The influence of mercury contact angle, surface tension, and retraction mechanism on the interpretation of mercury porosimetry data." Journal of colloid and interface science **250**(1): 175-190.
Rigby, S. P., H. Jahan, L. Stevens, C. Uguna, C. Snape, B. Macnaughton, D. J. Large and R. S. Fletcher (2020). "Pore structural evolution of shale following thermochemical treatment." Marine and Petroleum Geology **112**: 104058.
Ross, D. J. and R. M. Bustin (2007). "Shale gas potential of the lower Jurassic Gordondale member, northeastern British Columbia, Canada." Bulletin of Canadian Petroleum Geology **55**(1): 51-75.
Ross, D. J. and R. M. Bustin (2008). "Characterizing the shale gas resource potential of Devonian–Mississippian strata in the Western Canada sedimentary basin: Application of an integrated formation evaluation." AAPG bulletin **92**(1): 87-125.
Ross, D. J. and R. M. Bustin (2009). "The importance of shale composition and pore structure upon gas storage potential of shale gas reservoirs." Marine and petroleum Geology **26**(6): 916-927.
Rouquerol, J., P. Llewellyn and F. Rouquerol (2007). "Is the BET equation applicable to microporous adsorbents." Stud. Surf. Sci. Catal **160**(07): 49-56.
Rouquerol, J., F. Rouquerol, P. Llewellyn, G. Maurin and K. S. Sing (2013). Adsorption by powders and porous solids: principles, methodology and applications, Academic press.
Ruthven, D. M. (1984). Principles of adsorption and adsorption processes, John Wiley & Sons.
Sadus, R. (2002). Molecular simulation of fluids, Elsevier.
Sander, R. (2014). "Compilation of Henry's law constants, version 3.99." Atmos. Chem. Phys. Discuss **14**(21): 29615-30521.
Sang, G., S. Liu and D. Elsworth (2019). "Water vapor sorption properties of Illinois shales under dynamic water vapor conditions: experimentation and modeling." Water Resources Research **55**(8): 7212-7228.
Schoenherr, J., R. Littke, J. L. Urai, P. A. Kukla and Z. Rawahi (2007). "Polyphase thermal evolution in the Infra-Cambrian Ara Group (South Oman Salt Basin) as deduced by maturity of solid reservoir bitumen." Organic Geochemistry **38**(8): 1293-1318.

Schön, J. (2011). Physical properties of rocks-a workbook. Handbook of Petroleum Exploration and Production, Elsevier Amsterdam.
Seaton, N. and J. Walton (1989). "A new analysis method for the determination of the pore size distribution of porous carbons from nitrogen adsorption measurements." Carbon **27**(6): 853-861.
Sharma, A., S. Namsani and J. K. Singh (2015). "Molecular simulation of shale gas adsorption and diffusion in inorganic nanopores." Molecular Simulation **41**(5-6): 414-422.
Simpson, J. and H. Dearing (2000). Diffusion Osmosis-An unrecognized cause of shale instability. IADC/SPE Drilling Conference, Society of Petroleum Engineers.
Sing, K. S. (1985). "Reporting physisorption data for gas/solid systems with special reference to the determination of surface area and porosity (Recommendations 1984)." Pure and applied chemistry **57**(4): 603-619.
Sircar, S. (1999). "Gibbsian surface excess for gas adsorption revisited." Industrial & engineering chemistry research **38**(10): 3670-3682.
Slatt, R. M. and N. R. O'Brien (2011). "Pore types in the Barnett and Woodford gas shales: Contribution to understanding gas storage and migration pathways in fine-grained rocks." AAPG bulletin **95**(12): 2017-2030.
Sondergeld, C. H., R. J. Ambrose, C. S. Rai and J. Moncrieff (2010). Micro-structural studies of gas shales. SPE unconventional gas conference, Society of Petroleum Engineers.
Song, J., R. Littke and P. Weniger (2017). "Organic geochemistry of the lower Toarcian Posidonia shale in NW Europe." Organic Geochemistry **106**: 76-92.
Sparkman, O. D., Z. Penton and F. G. Kitson (2011). Gas chromatography and mass spectrometry: a practical guide, Academic press.
Stankiewicz*, A., B. Bennett, O. Wint, N. Ionkina, B. Motherwell and M. Mastalerz (2015). Kerogen density revisited–lessons from the Duvernay Shale. Unconventional Resources Technology Conference, San Antonio, Texas, 20-22 July 2015, Society of Exploration Geophysicists, American Association of Petroleum ….
Stasiuk, L. and L. Snowdon (1997). "Fluorescence micro-spectrometry of synthetic and natural hydrocarbon fluid inclusions: crude oil chemistry, density and application to petroleum migration." Applied Geochemistry **12**(3): 229-241.
Stephenson, M. H. (2016). "Shale gas in North America and europe." Energy Science & Engineering **4**(1): 4-13.
Sui, H. and J. Yao (2016). "Effect of surface chemistry for CH4/CO2 adsorption in kerogen: A molecular simulation study." Journal of Natural Gas Science and Engineering **31**: 738-746.
Sun, H. (1998). "COMPASS: an ab initio force-field optimized for condensed-phase applications overview with details on alkane and benzene compounds." The Journal of Physical Chemistry B **102**(38): 7338-7364.
Sun, H., P. Ren and J. Fried (1998). "The COMPASS force field: parameterization and validation for phosphazenes." Computational and Theoretical Polymer Science **8**(1-2): 229-246.
Tan, J., P. Weniger, B. Krooss, A. Merkel, B. Horsfield, J. Zhang, C. J. Boreham, G. van Graas and B. A. Tocher (2014). "Shale gas potential of the major marine shale formations in the Upper Yangtze Platform, South China, Part II: Methane sorption capacity." Fuel **129**: 204-218.
Tang, L., Y. Song, Z. Jiang, X. Pang, Z. Li, Q. Li, W. Li, X. Tang and A. Pan (2019). "Influencing factors and mathematical prediction of shale adsorbed gas content in the Upper Triassic Yanchang Formation in the Ordos Basin, China." Minerals **9**(5): 265.
Tang, X., N. Ripepi, N. P. Stadie, L. Yu and M. R. Hall (2016). "A dual-site Langmuir equation for accurate estimation of high pressure deep shale gas resources." Fuel **185**: 10-17.

Tang, X., N. Ripepi, K. A. Valentine, C. Keles, T. Long and A. Gonciaruk (2017). "Water vapor sorption on Marcellus shale: measurement, modeling and thermodynamic analysis." Fuel **209**: 606-614.
Tesson, S. p. and A. Firoozabadi (2019). "Deformation and swelling of kerogen matrix in light hydrocarbons and carbon dioxide." The Journal of Physical Chemistry C **123**(48): 29173-29183.
Thommes, M. and K. A. Cychosz (2014). "Physical adsorption characterization of nanoporous materials: progress and challenges." Adsorption **20**(2-3): 233-250.
Thommes, M., K. Kaneko, A. V. Neimark, J. P. Olivier, F. Rodriguez-Reinoso, J. Rouquerol and K. S. Sing (2015). "Physisorption of gases, with special reference to the evaluation of surface area and pore size distribution (IUPAC Technical Report)." Pure and Applied Chemistry **87**(9-10): 1051-1069.
Tian, H., L. Pan, X. Xiao, R. W. Wilkins, Z. Meng and B. Huang (2013). "A preliminary study on the pore characterization of Lower Silurian black shales in the Chuandong Thrust Fold Belt, southwestern China using low pressure N2 adsorption and FE-SEM methods." Marine and Petroleum Geology **48**: 8-19.
Tissot, B. (1984). "Recent advances in petroleum geochemistry applied to hydrocarbon exploration." AAPG Bulletin **68**(5): 545-563.
Tissot, B. (1984). "WELTED. H.(1984) Petroleum Formation and Occurrence." Berlin (Sprin gcr—Verlag).
Tissot, B., B. Durand, J. Espitalie and A. Combaz (1974). "Influence of nature and diagenesis of organic matter in formation of petroleum." Aapg Bulletin **58**(3): 499-506.
Tissot, B. P. and D. H. Welte (2013). Petroleum formation and occurrence, Springer Science & Business Media.
Uguna, C. N., A. D. Carr, C. E. Snape, W. Meredith, I. C. Scotchman, A. Murray and C. H. Vane (2016). "Impact of high water pressure on oil generation and maturation in Kimmeridge Clay and Monterey source rocks: Implications for petroleum retention and gas generation in shale gas systems." Marine and Petroleum Geology **73**: 72-85.
uk, A. M. C. v. t. c. (2006). "Evaluation of analytical instrumentation. Part XIX CHNS elemental analysers." Accreditation and Quality Assurance **11**(11): 569-576.
Ungerer, P., J. Collell and M. Yiannourakou (2015). "Molecular modeling of the volumetric and thermodynamic properties of kerogen: Influence of organic type and maturity." Energy & Fuels **29**(1): 91-105.
Ungerer, P., V. Lachet and B. Tavitian (2006). "Applications of molecular simulation in oil and gas production and processing." Oil & Gas Science and Technology-Revue de l'IFP **61**(3): 387-403.
Van Bergen, F., C. Spiers, G. Floor and P. Bots (2009). "Strain development in unconfined coals exposed to CO2, CH4 and Ar: effect of moisture." International Journal of Coal Geology **77**(1-2): 43-53.
Vandenbroucke, M. and C. Largeau (2007). "Kerogen origin, evolution and structure." Organic Geochemistry **38**(5): 719-833.
Vassoyevich, N., Y. I. Korchagina, N. Lopatin and V. Chernyshev (1970). "Principal phase of oil formation." International Geology Review **12**(11): 1276-1296.
Wang, M. and D. Zhang (2020). "Influences of moisture on adsorption and desorption of methane on gas shales." Energy Sources, Part A: Recovery, Utilization, and Environmental Effects: 1-19.
Wang, R., J. Li, L. Gibellia, Z. Guo and M. K. Borg (2021). "Sub-nanometre pore adsorption of methane in kerogen." Chemical Engineering Journal: 130984.

Wang, R., N. Zhang, X. Liu, X. Wu, J. Chen and L. Ma (2015). "Characteristics of pore volume distribution and methane adsorption on shales." Adsorption Science & Technology **33**(10): 915-937.
Wang, S., F. Javadpour and Q. Feng (2016). "Confinement correction to mercury intrusion capillary pressure of shale nanopores." Scientific reports **6**: 20160.
Wang, S., X. Yao, Q. Feng, F. Javadpour, Y. Yang, Q. Xue and X. Li (2021). "Molecular insights into carbon dioxide enhanced multi-component shale gas recovery and its sequestration in realistic kerogen." Chemical Engineering Journal **425**: 130292.
Wang, T.-Y., S.-C. Tian, Q.-L. Liu, G.-S. Li, M. Sheng, W.-X. Ren and P.-P. Zhang (2021). "Pore structure characterization and its effect on methane adsorption in shale kerogen." Petroleum Science **18**(2): 565-578.
Wang, T., S. Tian, G. Li, M. Sheng, W. Ren, Q. Liu and S. Zhang (2018). "Molecular simulation of CO2/CH4 competitive adsorption on shale kerogen for CO2 sequestration and enhanced gas recovery." The Journal of Physical Chemistry C **122**(30): 17009-17018.
Wang, Y., Y. Zhu, S. Chen and W. Li (2014). "Characteristics of the nanoscale pore structure in Northwestern Hunan shale gas reservoirs using field emission scanning electron microscopy, high-pressure mercury intrusion, and gas adsorption." Energy & Fuels **28**(2): 945-955.
Wang, Y., Y. Zhu, S. Liu and R. Zhang (2016). "Pore characterization and its impact on methane adsorption capacity for organic-rich marine shales." Fuel **181**: 227-237.
Wang, Z. and Z. J. LI XQ (2016). "Longmaxi formation shale gas geochemical features comparison between different blocks in Sichuan Basin." Coal GeologyofChina **28**(2): 22-27.
Wang, Z., W. Su, X. Tang and J. Wu (2018). "Influence of water invasion on methane adsorption behavior in coal." International Journal of Coal Geology **197**: 74-83.
Washburn, E. W. (1921). "The dynamics of capillary flow." Physical review **17**(3): 273.
Webb, P. A. (2001). "Volume and density determinations for particle technologists." Micromeritics Instrument Corp **2**(16): 01.
Webb, P. A. and C. Orr (1997). Analytical methods in fine particle technology, Micromeritics Instrument Corp.
Wenger, L. M., C. L. Davis, J. M. Evensen, J. R. Gormly and P. J. Mankiewicz (2004). "Impact of modern deepwater drilling and testing fluids on geochemical evaluations." Organic geochemistry **35**(11-12): 1527-1536.
Whitelaw, P., C. N. Uguna, L. A. Stevens, W. Meredith, C. E. Snape, C. H. Vane, V. Moss-Hayes and A. D. Carr (2019). "Shale gas reserve evaluation by laboratory pyrolysis and gas holding capacity consistent with field data." Nature communications **10**(1): 1-10.
Williams, D. B. and C. B. Carter (1996). The transmission electron microscope. Transmission electron microscopy, Springer**:** 3-17.
Winterton, R. (1970). "Van der Waals forces." Contemporary Physics **11**(6): 559-574.
Xiong, J., X. Liu, L. Liang and Q. Zeng (2017). "Adsorption of methane in organic-rich shale nanopores: An experimental and molecular simulation study." Fuel **200**: 299-315.
Young, J. F. (1967). "Humidity control in the laboratory using salt solutions—a review." Journal of Applied Chemistry **17**(9): 241-245.
Zafeiropoulos, N. E. (2011). Interface engineering of natural fibre composites for maximum performance, Elsevier.
Zhang, H. and D. Cao (2016). "Molecular simulation of displacement of shale gas by carbon dioxide at different geological depths." Chemical Engineering Science **156**: 121-127.
Zhang, J., M. Clennell, D. Dewhurst and K. Liu (2014). "Combined Monte Carlo and molecular dynamics simulation of methane adsorption on dry and moist coal." Fuel **122**: 186-197.

Zhang, T., G. S. Ellis, S. C. Ruppel, K. Milliken and R. Yang (2012). "Effect of organic-matter type and thermal maturity on methane adsorption in shale-gas systems." Organic geochemistry **47**: 120-131.
Zhang, Y. and Z. Xu (1995). "Atomic radii of noble gas elements in condensed phases." American Mineralogist **80**(7-8): 670-675.
Zhao, T., X. Li, Z. Ning, H. Zhao and M. Li (2018). "Molecular simulation of methane adsorption on type II kerogen with the impact of water content." Journal of Petroleum Science and Engineering **161**: 302-310.
Zhao, T., X. Li, H. Zhao and M. Li (2017). "Molecular simulation of adsorption and thermodynamic properties on type II kerogen: Influence of maturity and moisture content." Fuel **190**: 198-207.
Zhou, J., Q. Mao and K. H. Luo (2019). "Effects of moisture and salinity on methane adsorption in kerogen: a molecular simulation study." Energy & Fuels **33**(6): 5368-5376.
Zhou, W., R. Apkarian, Z. L. Wang and D. Joy (2006). Fundamentals of scanning electron microscopy (SEM). Scanning microscopy for nanotechnology, Springer**:** 1-40.
ZHU, Y. and X. XIA (2013). "Comparison and explanation of the absorptivity of organic matters and clay minerals in shales." Journal of China Coal Society **38**(5): 812-816.
Zolfaghari, A., H. Dehghanpour and J. Holyk (2017). "Water sorption behaviour of gas shales: I. Role of clays." International Journal of Coal Geology **179**: 130-138.
Zolfaghari, A., H. Dehghanpour and M. Xu (2017). "Water sorption behaviour of gas shales: II. Pore size distribution." International Journal of Coal Geology **179**: 187-195.
Zou, C., D. Dong, S. Wang, J. Li, X. Li, Y. Wang, D. Li and K. Cheng (2010). "Geological characteristics and resource potential of shale gas in China." Petroleum exploration and development **37**(6): 641-653.
Zou, C., Z. Yang, J. Dai, D. Dong, B. Zhang, Y. Wang, S. Deng, J. Huang, K. Liu and C. Yang (2015). "The characteristics and significance of conventional and unconventional Sinian–Silurian gas systems in the Sichuan Basin, central China." Marine and Petroleum Geology 64: 386-402.
Zou, J., R. Rezaee and K. Liu (2017). "Effect of temperature on methane adsorption in shale gas reservoirs." Energy & Fuels **31**(11): 12081-12092.
Zou, J., R. Rezaee, Q. Xie, L. You, K. Liu and A. Saeedi (2018). "Investigation of moisture effect on methane adsorption capacity of shale samples." Fuel **232**: 323-332.

APPENDIX A

Table A1. Basic information of shales used for sample selection and their corresponding carried out experiments.

Sample type	Sample ID	Depth (m)	TOC (%) by EA or Rock-eval	Sample weight (g)	Dry&wet density by HP	BET	XRCT	MIP	Dry&wet HPVA	Demineralization	Solvent extraction	GC-MS (for Oil)	VR or Rock-eval	SEM
Shale from China	SH1	4119	5.13	333.6	√	√	√	√	√	√	√	√	√	√
	SH2	4098	2.44	587.9	√	√	√	√	√	√	√	√	√	√
	SH3	3911	0.40	302.7	√	√								
	SH4	4035	2.55	233.6	√	√		√	√				√	√
	SH5	4037	2.65	190.6	√	√		√	√				√	
	SH6	4073	3.48	261.2	√	√								
	SH7	4083	2.13	269.1	√	√								
	SH8	2245	0.92	200.0	√	√								
	SH9	2261	1.66	328.6	√	√	√							
	SH10	2296	1.07	288.7	√	√								
	SH11	2332	3.72	199.4	√	√	√	√	√				√	√
	SH12	2349	6.17	206.5	√	√			√				√	
	SH13	2353	3.84	238.9	√	√								
	SH14	2262	0.85	229.5	√	√								
	SH15	2317	2.79	164.5	√	√		√	√				√	
	SH16	2322	1.84	151.2	√	√		√	√				√	√
	SH17	2326	0.75	310.2	√	√								
	SH18	3821	0.49	275.9	√	√	√							
	SH19	3827	0.56	205.8	√	√								
	SH20	3844	1.44	294.0	√	√								
	SH21	3870	3.01	206.0	√	√		√	√				√	
	SH22	3910	1.93	223.8	√	√	√	√	√					√
	SH23	3931	3.92	200.7	√	√								
	SH24	3935	4.04	257.6	√	√		√	√				√	
	SH25	3939	4.19	254.0	√	√			√				√	
Shale from UK	BS3	2143	2.48	NA	√	√		√	√		√	√	√	
	GH4	3113	3.37	NA	√	√		√	√	√	√	√	√	
Sample mass for each analysis			3g		3.5g	4g	1g	4g[a*]	10g	60g	60g[b*]	NA	1.5 g[c*]	1g[c*]

There are fourteen China shales that have the higher TOC (>2%), while two of them (SH1 and SH2) have enough weight (>296 g) for all the experiments. At least 148 g sample with the proper required size is needed for the above experiments, which means at least 296 g (double weight) virgin shales are required considering the sample loss during sample smashing, crashing, and milling. Sample mass for each analysis is indicated in the thesis chapter 2. a* is 4 g as duplicated MIP is carried out for the particle and bulk shales, each 2 g. b* is 60 g as duplicated extraction is carried out for 2-4 mm particles shale, and 20 g sample with < 250 µm is used for comparison. c* is around 1-1.5 g as the prepared sample at least needs 1-1.5 g, while the sample procedure for the corresponding experiment could be less than 1 g.

Table A2. The moisture, volatiles, fixed carbon, and ash contents of the three kerogen samples from TGA analysis.

Sample ID		Moisture content (%)	Volatile content (%)	Fixed carbon content (%)	Ash content (%)
K1	Wet base-fraction (%)	29.96±0.48	6.22±0.39	24.35±0.49	39.46±0.99
K2		11.47±7.04	44.38 ±5.47	19.91 ±1.49	24.24 ±1.67
GHK3		2.53±0.06	23.93±0.38	30.08±0.36	43.45±0.50
K1	Dry base-fraction (%)	—	9.55±0.47	37.74±0.79	52.72±1.04
K2		—	49.99 ±3.0	22.55±1.41	27.46 ±1.61
GHK3		—	24.56±0.40	30.87±0.36	44.57±0.49

The mean of the TGA result is from triplicate experiments (Section 2.3.2), and the errors represent the dispersion of a dataset relative to its mean.

APPENDIX B

Table B1. The maturity, TOC, micropore volume, and equilibrated methane adsorption capacities (Qm) of the isolated kerogens.

Publications	Sample code	Maturity (Tmax/VR)	TOC (wt.%)	Qm (mg/g)	Vmicro (mm^3/g)	Qm (mg/g TOC)	Vmicro (mm^3/g TOC)
(Rexer, 2014)	WIC7145	425°C	73	37	22	65	30
	WIC7155	429°C	73	56	24	97	33
	HAR7038	449°C	97	35	25	46	26
	HAR7060	447°C	99	41	33	53	33
	HAD7090	464°C	83	60	42	93	51
	HAD7119	459°C	79	80	51	130	64
(Wang, 2015)	RW	na	63	45	24	72	39
(Li)	K1	2.95 %Ro	36	27	14	76	39
（Li, 2021）	K2	2.58 %Ro	19	17	14	90	75
	GHK3	1.95 %Ro	26	5.5	2.6	21	10

The data of K1, K2, and GHK3 in (Li) and (Li, 2021) are presented in chapter 5.

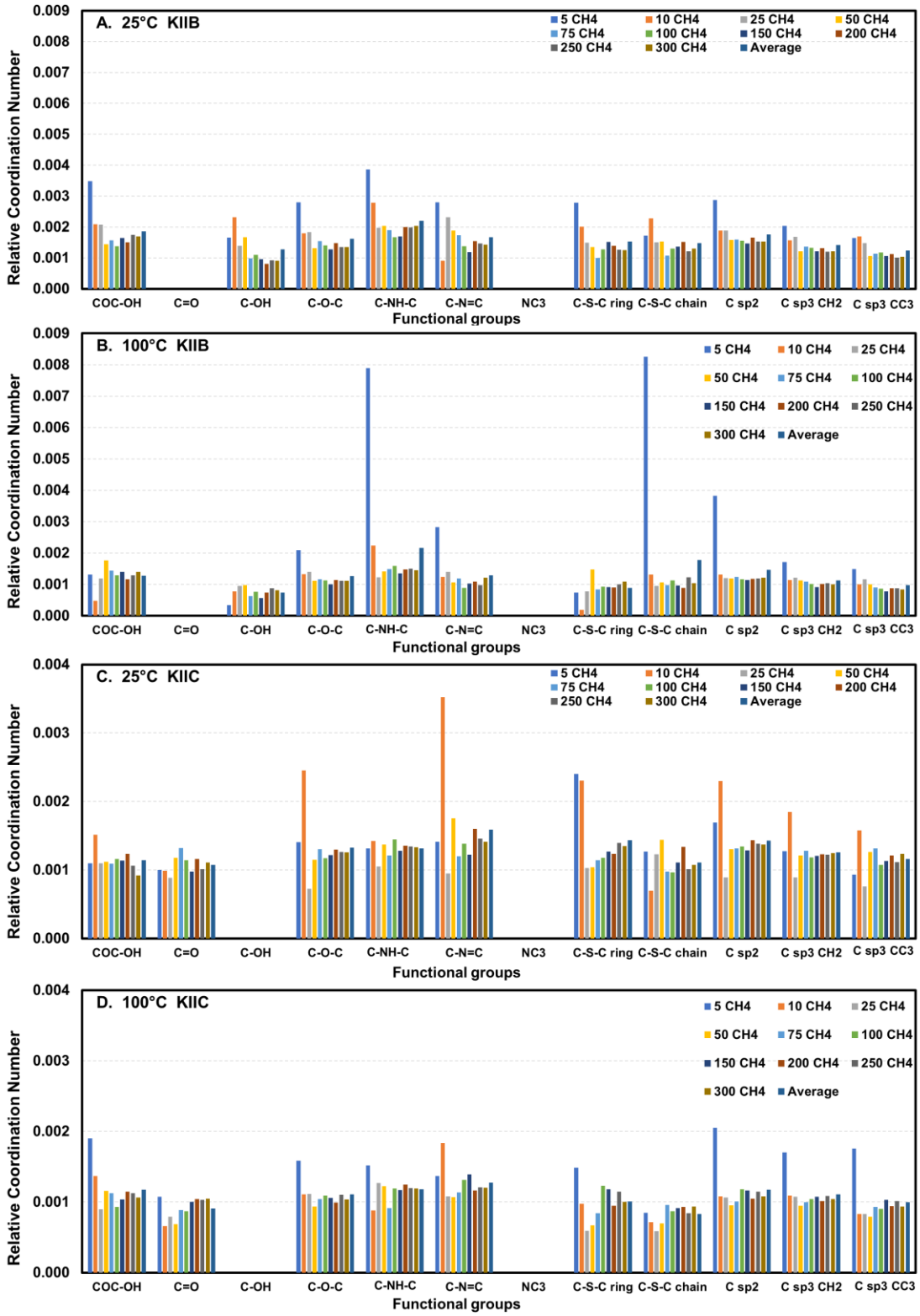

Figure B1. The relative coordination number of methane around the functional groups in kerogens KIIB and KIIC at 25 and 100 °C.

APPENDIX C

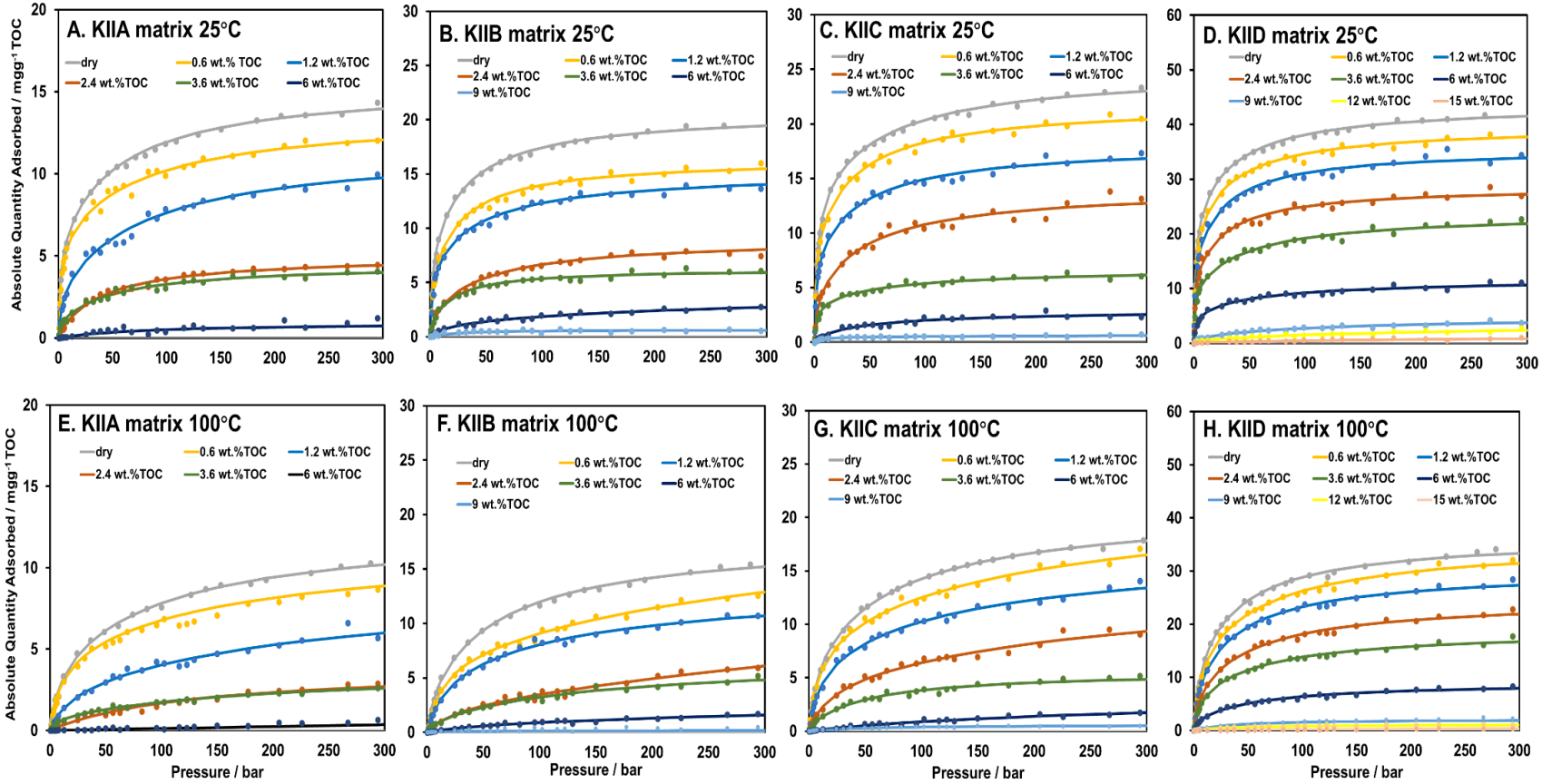

Figure C1. Methane adsorption isotherms of KIIA, KIIB, KIIC, KIID matrices with different moisture contents (wt.% TOC) at 25°C (A, B, C, and D) and 100°C (E, F, G, and H).

Table C1. Micropore volumes of the KIID matrix and slits models measured with d=0.33 nm (for dry kerogen) and d=0.36 nm (for moist kerogen) probes in the simulation.

	Micropore volume (mm^3/g TOC)															
Moisture content (wt.% TOC)	0	0.6	1.2	2.4	3.6	6	9	12	15	18	21	24	27	30	33	36
KIIA matrix	0.93	0.44	0.042	0.0037	0.0036	0	0	0	0	0	0	0	0	0	0	0
KIIB matrix	2.2	1.3	0.43	0.015	0.012	0.0026	0	0	0	0	0	0	0	0	0	0
KIIC matrix	2.3	0.97	0.59	0.13	0.097	0.0026	0.0011	0	0	0	0	0	0	0	0	0
KIID matrix	19	12	8.5	3.4	2.9	0.37	0.0078	0.0088	0	0	0	0	0	0	0	0
KIID 0.5 nm slit	54	42	40	32	29	14	5.8	1.1	0.74	0.052	0.011	0	0	0	0	0
KIID 1.0 nm slit	109	95	94	82	70	57	35	21	13	2.2	0.25	0.11	0.0017	0	0	0
KIID 1.5 nm slit	191	179	177	161	149	124	87	67	59	25	11	3.8	0.59	0.083	0	0
KIID 2.0 nm slit	261	247	245	234	210	169	152	119	96	69	49	36	22	9	0.12	0

The micropore volume for the dry samples is measured by the dummy probe with a diameter of 0.33 nm, same as CO_2, while the micropore volume for the moist samples is measured by the dummy probe with a diameter of 0.36 nm, same as N_2.

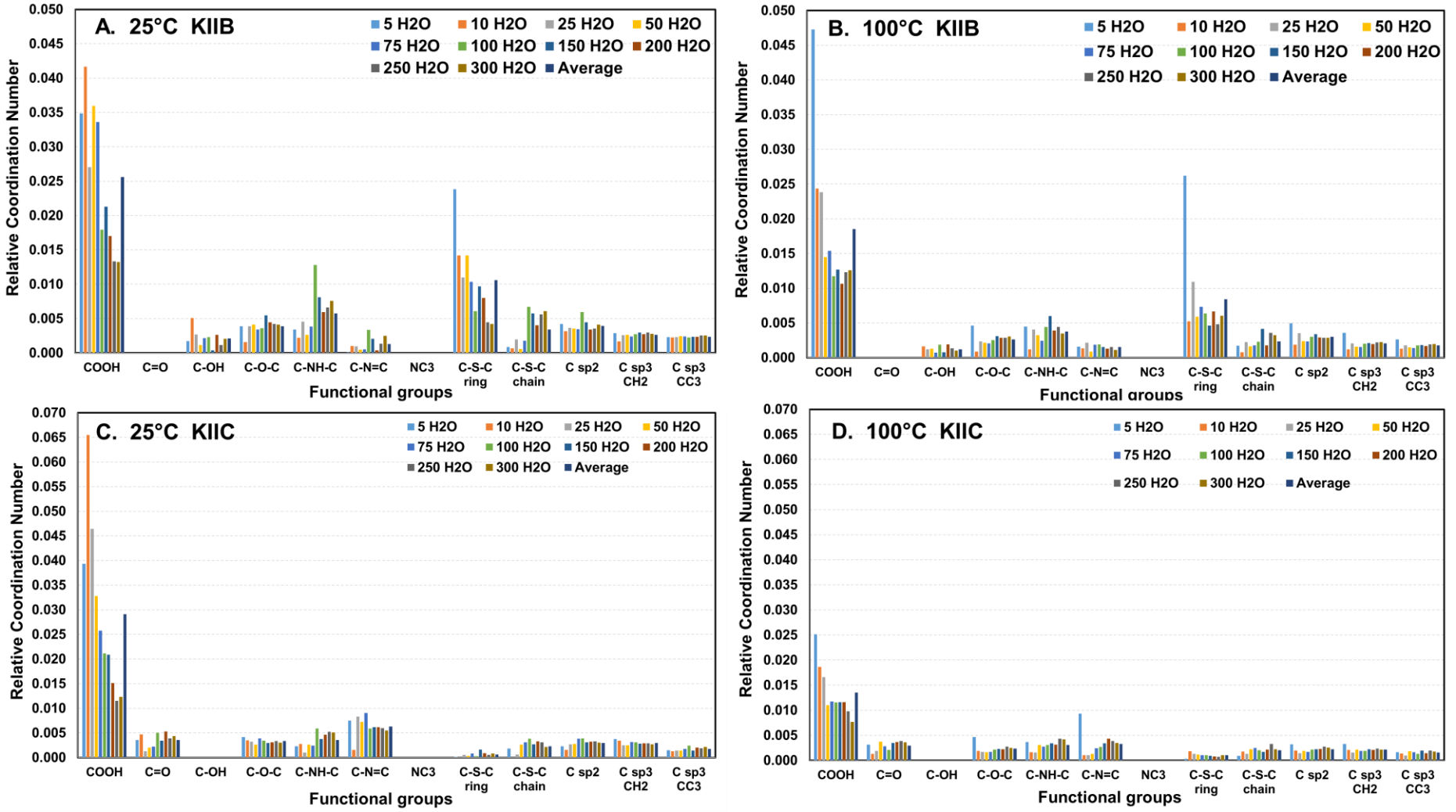

Figure C2. The relative coordination number of water around the functional groups in kerogens KIIB and KIIC at 25 and 100 °C